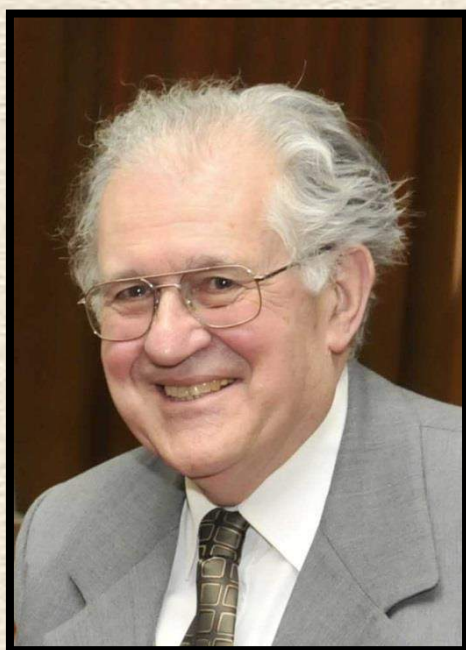


ATOMKI

ANNUAL REPORT

2012



Berényi Dénes
1928-2012



INSTITUTE OF NUCLEAR RESEARCH
OF THE HUNGARIAN ACADEMY OF SCIENCES
DEBRECEN, HUNGARY

INSTITUTE OF NUCLEAR RESEARCH
OF THE HUNGARIAN ACADEMY OF SCIENCES
DEBRECEN, HUNGARY

ANNUAL REPORT
2012



ATOMKI

Postal address:

P.O. Box 51
H-4001 Debrecen,
Hungary

Editors:

K. Tótkési
E. Leiter

HU ISSN0 0231-3596

Preface

Dénes Berényi, former director of Atomki, a major figure in Hungarian science passed away in 2012. His life was always connected to Atomki and his positive attitude stays with us.

Atomki is changing. According to the decision of the Hungarian Academy of Sciences, the institute has a slightly modified name: Institute for Nuclear Research, Hungarian Academy of Sciences (MTA Atomki). Subsequently, our internet domain is changed to atomki.mta.hu. A more prominent development can be seen from now in the institute, since all the buildings are renovated, thanks to a major development program. A bit more hidden at the moment is the fact, that a new particle accelerator, a 2MV Tandem is under construction and will be installed in 2013, thanks to a major investment of MTA. This new accelerator will complement the existing ones in the Atomki Accelerator Center while opening up new research possibilities.

2012 was the year of Higgs boson and Atomki researchers had their share in the work and the results as well through the CMS positioning system developed, installed and maintained by Atomki in collaboration with other parties. We believe an active participation in big science can be done only by developing and exploiting high-tech local infrastructure and expertise. This is also demonstrated by the title page of *European Journal of Physics A* in 2012 January, where the studies at underground laboratories using Atomki detectors are shown.

Atomki hosted the most prominent scientists of cluster physics at the 10th International Conference on Clustering Aspects of Nuclear Structure and Dynamics for a week in 2012. The proceedings volume is open access at *IOP Journal of Physics Conference Series* Vol.436.

Természet Világa (the World of Nature), a major Hungarian science magazine established in 1869 devoted its May issue in 2012 entirely to Atomki. About a dozen of laboratories/topics were presented proving the variety of Atomki research topics and introducing the younger generation to modern physics. The younger generation of Atomki physicists also had a large success in 2012: one of the winners of the nationwide Junior Prima Prize was Dr. G.G. Kiss.

The Atomki Annual Report features this year the activities at the Section of Electronics. It is instructing to follow the developments of electronics for the last five decades and see how Atomki engineers stayed in the forefront in such a rapidly changing environment.

The Atomki Annual Report is changing as well. After many years of work Dr. I. Rajta stepped down as the editor, and Dr. K. Tókési takes over. I would like to thank Dr. Rajta his excellent work and wish similar successes to Dr. Tókési.

Further details of Atomki events, and the back issues of the Annual Reports can be found on our homepage: www.atomki.mta.hu

Debrecen, 14 August 2013

Zs. Fülöp
Director

Dénes Berényi

Dénes Berényi, Director of Atomki from 1976 to 1990, died on 27th June, 2012, aged 84.

He studied physics in Debrecen and graduated here in 1953. He joined Prof. Sándor Szalay in the heyday of Szalay's pioneering research, at the best time to become a founding member of Atomki in 1954. He specialized in nuclear spectroscopy, and, as the Institute grew, he became head of the Section of Nuclear Spectroscopy. He was interested in the exotic decay modes of nuclear states. With his pupils, he invoked international recognition, e.g., by his studies of the nuclear Bremsstrahlung accompanying normal decay. From the early seventies his attention was focussed mainly on the behaviour of the atomic electron shell in response to collisions of the atoms, which was a rather obscure field at that time, but expanded enormously later. Since then this has been one of the major research activities of this Institute. He initiated and chaired a biennial conference series, in Debrecen, which were counted among the most important conferences of the field.

For decades, he was teaching at the University as well. He became a Corresponding Member of the Hungarian Academy of Sciences in 1973 and an Ordinary Member in 1985. He was Vice-President of the Academy between 1990 and 1993. This was the transition period from the dictatorship to the democratic regime in this country, a very difficult and sensitive time for the Academy as well. From 1993 to 1999 he chaired the Debrecen Regional Committee of the Academy, and was the coordinator of the connections with the Hungarian and non-Hungarian scientific communities in the neighbouring countries and of the cooperation with Hungarian scholars and scientists all over the world.

He was a public-minded person. In addition to his jobs in his professional activities, he took part in various national and international organizations promoting scientific cooperation. Among other bodies, he was Ord-

nary Member of Academia Europaea; he was Honorary President of Roland Eötvös Physical Society and Editor of its monthly periodical *Fizikai Szemle* for many years. He was also the mastermind behind the local multidisciplinary quarterly *Debreceni Szemle*. He wrote a huge number of articles for the broad public and a few books to increase public awareness of scientific achievements.

He received dozens of various awards, including some of the most prestigious ones that are given to scientists in this country. He received honorary degrees from four universities, three among them from beyond the border. Retirement at his age of 70 was not a retirement from work for him. He was an active member of this Institute up to the last months of his life.

But this obituary would not be appropriate without some subjective aspects. To give an impression of his personality, I should mention what I admired most.

First, I admired his enormous inner thrust for work. He did everything with apparent vigour and zeal; not only what most people like to do but also what is a nuisance to anybody, the administrative chore, the boring meetings and rubbing shoulders with unpalatable people. He was doing these with apparent ease, with serenity and optimism, without any noticeable sign of fatigue or inhibition. What I most envied is that, even while he was a director, he managed to spend a few hours almost every day on physics. He was accessible and actually accessed by colleagues all the time, and he had to suffer interruptions many times a day, and yet he was able to break away, and do some good science. His routine of doing so many things simultaneously was an extraordinary feat of self-discipline.

Second, whatever he was doing, he was able to see it important and convince other people of its importance. This attitude endowed his initiatives with extra importance, and made him a potential leader of all projects he pursued,

and his projects were destined for success.

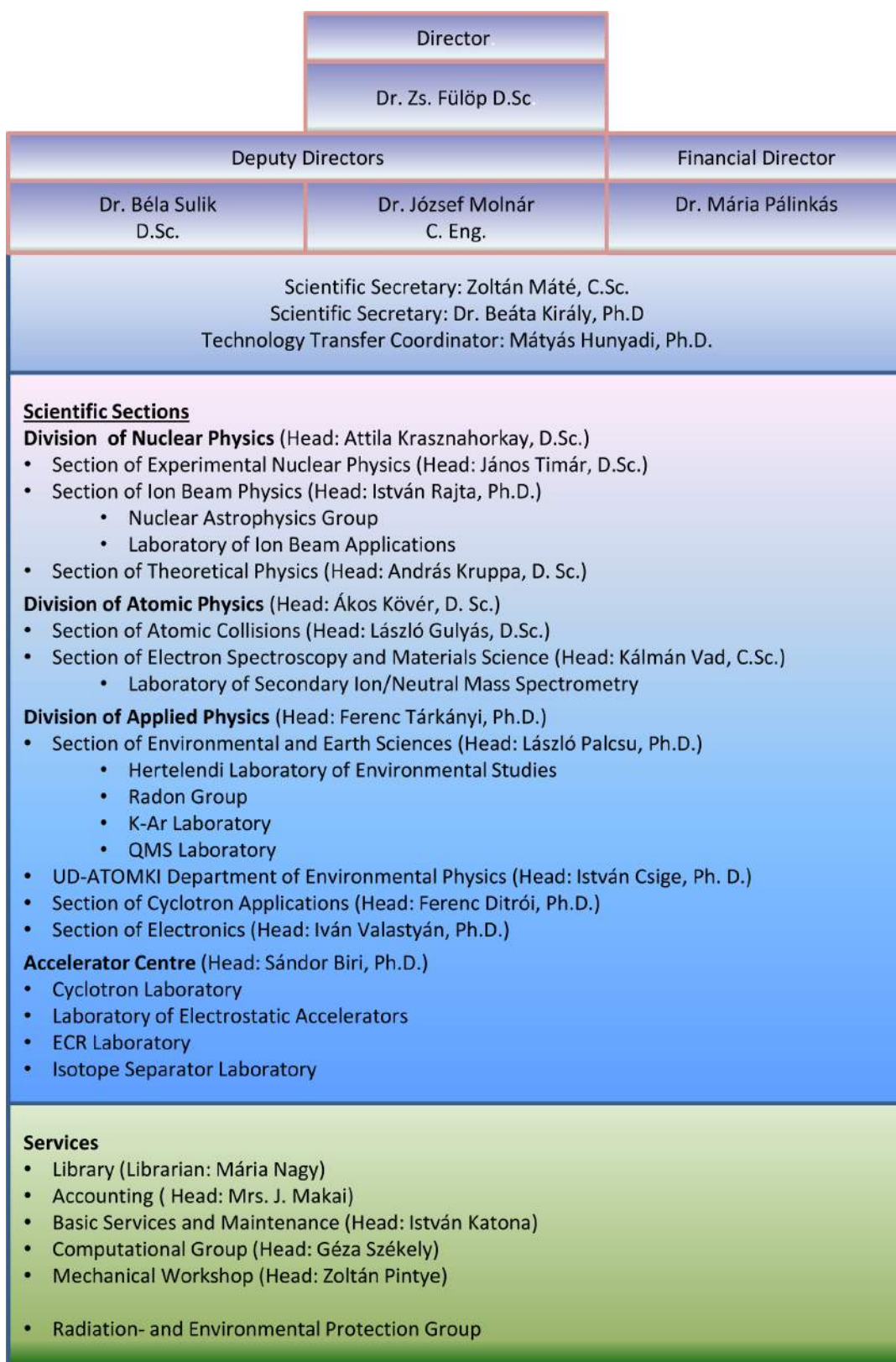
And third, he had a special gift to rally people round him. One secret in his success was that whoever joined him, enjoyed Dénes's full trust, and everybody would reward this with the best performance. Since all his endeavours, from scientific projects to actions for the well-being of the Debrecen region, usually needed collective will and support, this gave the cause an extra push. In our age such a gift is invaluable since both the material and the spiritual attractiveness of the homeland, the home institution and even the home hearth has enormously diminished. The result is atomization in all re-

spects. Dénes fought atomization with all his might both in society and in the scientific community.

The fifteen years of Professor Berényi's directorship was a period of prosperity for the Institute, and I know that a lot of colleagues remember it with great nostalgia. It was in that period that the Institute underwent the most substantial growth, acquired its most significant instrument, the cyclotron, and we all know that Professor Berényi's politics and reputation were key to this success.

R. G. Lovas

Organizational structure of ATOMKI



Data on ATOMKI

At present the Institute employs 197 persons. The affiliation of personnel to units of organization and the composition of personnel are given below.

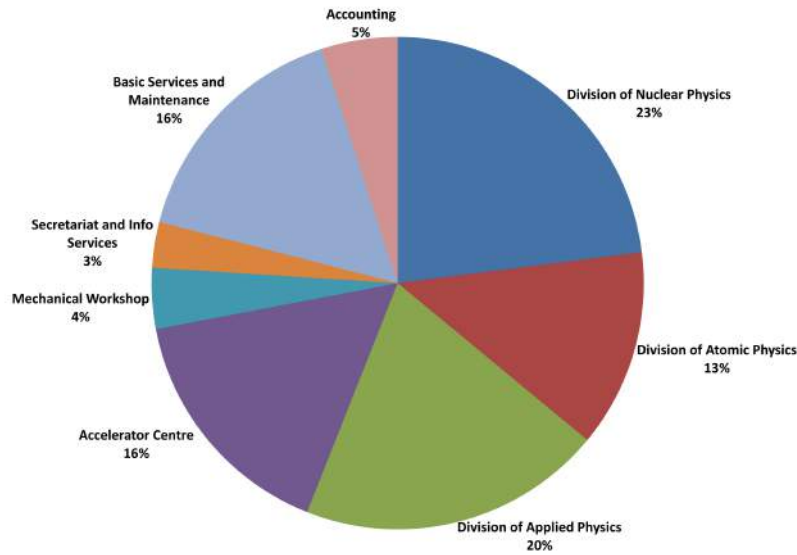


Figure 1. Affiliation of personnel to units of organization

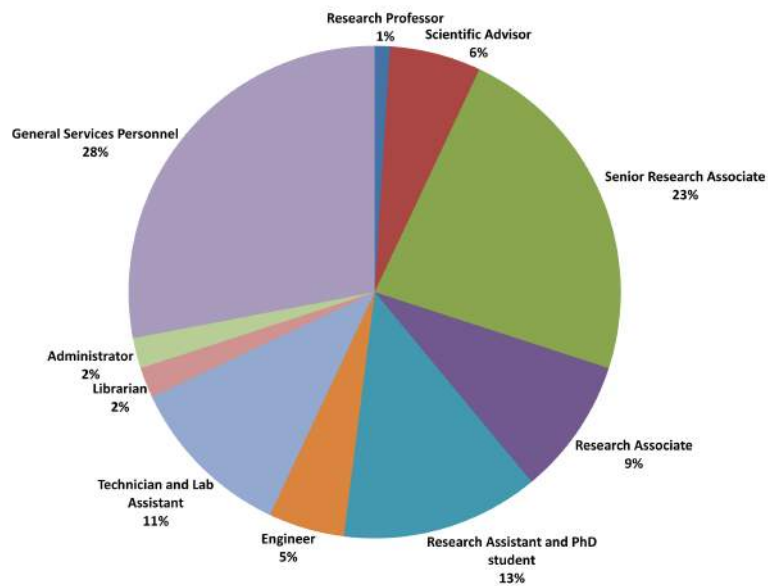


Figure 2. Composition of personnel

International connections

Multilateral international programs: 7

Cooperations based on S&T (TéT) bilateral intergovernmental agreements: 12

Cooperations based on HAS bilateral agreements: 18

Cooperations based on specific collaboration agreements between institutes:

- In nuclear physics and applications with 20 countries in 34 topics
- In atomic physics and applications with 21 countries in 39 topics
- In detection and signal processing technique with 5 countries in 6 topics
- In ion beam analysis with 6 countries in 7 topics
- In environmental research and dating with 13 countries in 15 topics

Membership in international scientific committees: 37

Running research projects, grants

European Research Council (ERC) Starting Grant: 1

Other EU projects: 15

European Organization for Nuclear Research (CERN) projects: 2

International Atomic Energy Agency (IAEA) projects: 2

Intercomparison programs (EURATOM): 2

Hungarian National Research Foundation (OTKA) projects: 14

National Office for Research and Technology (NKTH) projects: 5

Higher education activity

Number of researchers teaching at universities: 34

Number of researchers teaching in doctoral (PhD) schools: 32

Gradual and post-gradual teaching: 72 courses, 1146 hours

Number of undergraduate students participating in research work (organized by the Student's Science Association, TDK): 7

Number of students making diploma work: 17

Number of PhD students: 19

Supervision activity by Atomki researchers: 3720 hours

Finance

The total budget of the Institute for the year 2012 was 2042 million Hungarian Forints income, and 1846 million Hungarian Forints expenses. The composition of the budget and the share of personnel expenditure within the budget are shown below.

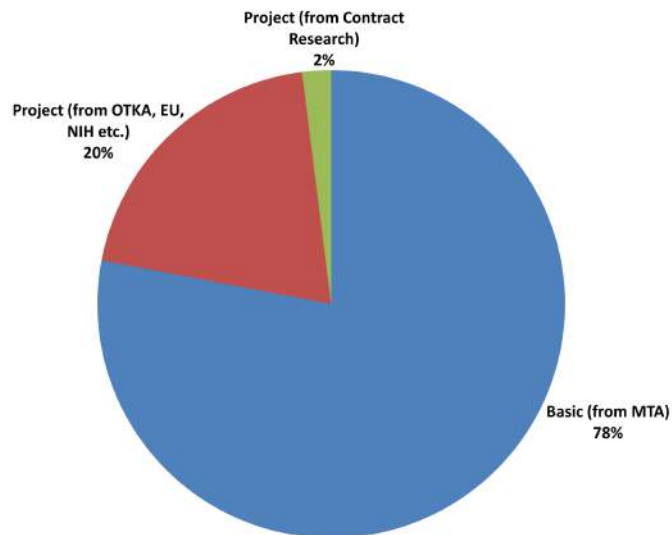


Figure 3. Composition of the budget of the Institute
MTA: Hungarian Academy of Sciences
OTKA: Hungarian Scientific Research Fund
EU: European Union
NIH: National Innovation Office

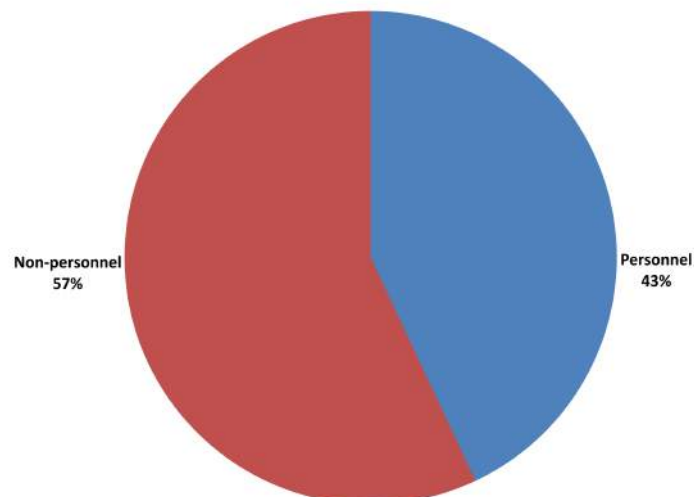


Figure 4. Breakdown of expenditure into personnel and non-personnel expenditures

Table of contents

Preface	i
Dénes Berényi	ii
Organizational structure of Atomki	iv
Data on Atomki	v
International connections	vi
Running research projects, grants	vi
Higher education activity	vi
Finance	vii
Table of contents	viii

Featured:

Research, Development and Innovation at the Section of Electronics	1
--	---

1. General Physics

1.1 Schrödinger equations with indefinite effective mass	45
--	----

2. Particle Physics

2.1 Smoothing problems in nuclear and particle physics	46
2.2 Quantum chromodynamics on the lattice	47

3. Nuclear Physics

3.1 Extensions of Elliott's SU(3) symmetry	48
3.2 Shape isomers and clusterization in the ^{28}Si nucleus	49
3.3 Direct capture in the $^{130}\text{Sn}(n,\gamma)^{131}\text{Sn}$ and $^{132}\text{Sn}(n,\gamma)^{133}\text{Sn}$ reactions under r -process conditions	50
3.4 Recommended cross section of the $^{16}\text{O}(p,\gamma)^{17}\text{F}$ reaction below 2.5 MeV: a potential tool for quantitative analysis and depth profiling of oxygen	51
3.5 Strictly finite range potential for light PET isotopes	52
3.6 Precise half-life measurement of the ^{66}Ga isotope	53
3.7 Investigation of the α -particle induced nuclear reactions on natural molybdenum	54
3.8 Activation cross-sections of deuteron induced reactions on natural palladium	55
3.9 $\gamma\gamma$ -coincidence in the neutron rich nucleus ^{25}F	56
3.10 Investigation of α -induced reactions on ^{127}I for the astrophysical γ process	57
3.11 $^{106,110,116}\text{Cd}(\alpha,\alpha)^{106,110,116}\text{Cd}$ elastic scattering and systematic investigation of the elastic α scattering cross sections along the $Z = 48$ isotopic and $N = 62$ isotonic chains	58
3.12 In-beam γ -spectroscopic study of rotational bands in ^{103}Rh	59
3.13 Investigation of α -induced reactions on ^{130}Ba	60
3.14 $^{64}\text{Zn}(\alpha,\alpha)^{64}\text{Zn}$ elastic scattering experiment, a progress report	61

4. Atomic and Molecular Physics	
4.1 The signature of the Fermi-shuttle type multiple ionization in collision between carbon ions and neon atoms	62
4.2 Interaction of light particles with capillaries	63
4.3 Blocking effect for ions and neutrals in guided transmission of 3 keV Ar ⁷⁺ through dense polycarbonate nanocapillary arrays	64
4.4 The guiding of 3 keV Ar ⁷⁺ ions through a glass microcapillary array	65
4.5 Fragmentation of small molecules induced by 46 keV/amu N ⁺ and N ₂ ⁺ projectiles	66
4.6 Probing scattering phase shifts by attosecond streaking	67
4.7 Single and multiple ionization of noble gas atoms by H ⁰ impact	68
4.8 Universal functional formula of atomic elastic cross sections. The case of the hydrogen target.	69
4.9 Spatial and temporal interference during the ionization of H by few-cycle XUV laser pulses	70
4.10 Energy and angular distribution of electrons transmitted through a single glass microcapillary	71
4.11 Temperature control of ion guiding through insulating capillaries	72
4.12 Investigation of the conductivity of the borosilicate glass	73
5. Condensed Matter	
5.1 Investigation of diffusional intermixing in Si/Co/Ta system by Secondary Neutral Mass Spectrometry	74
5.2 Thermoelasticity and interdiffusion in CuNi multilayers	75
5.3 Structural and magnetic properties of the periodic [Fe(5nm)/V(5nm)] ₁₀ and [Fe(3nm)/V(3nm)] ₂₀ systems	76
5.4 Analysis of InGaP/Ge heteroepitaxy	77
5.5 Evolution of the structure and hydrogen bonding configuration in annealed hydrogenated a-Si/a-Ge multilayers and layers	78
6. Materials Science and Analysis	
6.1 Time-resolved photoelectron emission from surfaces	79
6.2 Interface study by SNMS	80
7. Earth and Cosmic Sciences, Environmental Research	
7.1 Improvement and optimization of sealed tube graphitization	81
7.2 Stable isotopes and noble gas constraints on the genesis of therapeutic waters, SE Poland	82
7.3 One year aerosol fossil carbon trend in Debrecen city air	83
7.4 Pilot study of nitrogen utilisation in maize	84
7.5 Egg origin determination efforts	85
7.6 ¹⁴ C measurement from dissolved organic carbon of groundwater at the Püspökszilágy RHFT	86
7.7 A new combustion and CO ₂ purification line for AMS C-14 measurement	87
7.8 Validation of organic sample pre-treatment method for AMS C-14 measurement in Atomki	88
7.9 Experimental technique to measure thoron generation rate using RAD7 detector	89
7.10 AMS ¹⁴ C performance test of a new automated bone preparation system	90
7.11 Novel methods for AMS C-14 analyses of Dissolved Inorganic Carbon (DIC) of groundwater	91

8. Biological, Chemical and Medical Research	
8.1 Production and radiochemical separation of ^{64}Cu and ^{67}Cu radioisotopes	92
8.2 Biodistribution, pharmacokinetics and uptake ratio of ^{131}I -4-Iodo-phenyl-acetic acid in normal and tumour implied animals	93
8.3 Production and radiochemical separation of ^{203}Pb radioisotope for nuclear medicine	95
8.4 The potential of materials analysis by electron Rutherford backscattering as illustrated by a case study of mouse bones and related compounds	96
8.5 Identification of bisphosphonate from phosphate ion on functionalised carbon nanotube by X-ray photoelectron spectroscopy (XPS)	97
8.6 Dramatic effect on Selenium concentration in blood serum due to the difference between the Hungarian and Indian dietary habits	98
9. Developments of Methods and Instruments	
9.1 Overview of cross sections of proton and deuteron induced nuclear reactions for production of ^{163}Ho radioisotope	99
9.2 Tritium calorimetry	100
9.3 Wear measurement using radioactive tracer technique based on proton, deuteron and α -particle induced nuclear reactions on molybdenum	101
9.4 Production of fully-stripped neon beam with the ECR ion source	102
9.5 Experimental setup for studying guiding of proton microbeam	103
9.6 Status Report on the accelerators operation	104
9.7 Thin target gamma ray yields induced by 0.65–2 MeV deuterons for nitrogen	108
9.8 Constructing an European Low Energy Neutron Spectrometer (ELENs)	109
9.9 Porting VIRTEX4 data acquisition design to SPARTAN6 FPGA	110
9.10 Time over threshold readout method of SiPM based small animal PET detector	111
10. Appendix	
10.1 Report on the 10th International Conference on Clustering Aspects of Nuclear Structure and Dynamics	112
10.2 Events	114
10.3 Hebdomadal Seminars	116
10.4 Awards	120
10.5 List of Publications (Highlights)	121
Author index	134

Research, Development and Innovation at the Section of Electronics

I. Valastyán, J. Molnár, J. Gál, K. Tőkési, G. Hegyesi, G. Pintér, K. Kiss, J. Szádai, Zs. Kertész, B. Szabó, V. Sass, Z. Szillási, N. Béni, A. Makovecz, A. Bükki-Deme, P. Bojtos, J. Sütő, D. Nagy, F. Nagy, B. Rubovszky, G. Székely, A. Sipos, O. Feró, J. Szalka



Panoramic photo of the Atomki from the Section of Electronics

1 Introduction

The main task of the Section of Electronics is to solve electronic measurement problems emerging in the various fields of experimental research of the institute. Beside this, the section has its own research and development activities. We study new methods to improve measurement accuracy and take part in several projects from CERN to space applications and nuclear medical imaging. The Computational Group of this section takes care of the computing resources of the institute.

2 History of the section

Professor Sándor Szalay, the founder of the Institute, realized in the 60's that the performance, stability and quality of electronic devices used in the Institute can be improved only if those are produced by professionals. Since the country was behind the iron curtain, buying such high precision power supplies, analyzers, control units and computers were impossible. He created a new group in 1967, the Section of Nuclear Electronics, in order to solve the electronic measurement problems and design, develop and maintain electronic devices for the Institute. In the next years, thanks to the robust design and high performance and quality of the devices, colleagues could fulfill not only the internal requests, but developed a successful product line for nuclear measurement applications. Products were sold in several countries, not only in the eastern bloc but also in western countries. The most of the customers were research institutes who often needed dedicated instruments. A taste of the wide product range is shown in the tree in Figure 1.

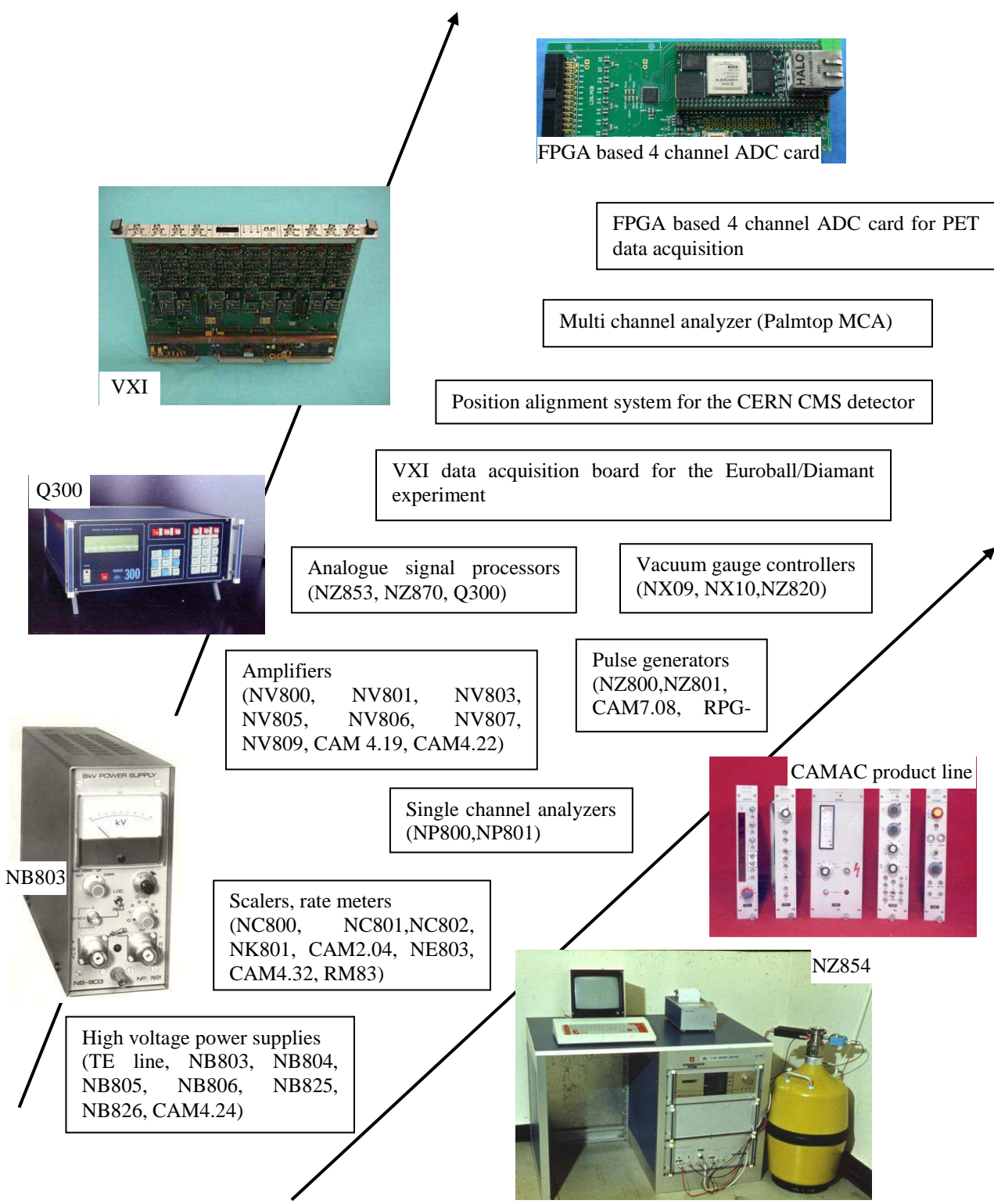


Figure 1: Product range of the Section of Electronics from 1970's to today.

2.1 Early years, the 60's and 70's

The group members were three engineers (head: Béla Sebestyén, Imre Csuka, Lajos Csánki) two physicist (István Török, Tamás Lakatos), one designer, two technicians (Zsolt Kertész, Elek Molnár) two skilled and one unskilled labourers. The first tasks were the developing of low voltage power supplies, type TE-1 and TE-2 (most are still in operating), and a general purpose 2 kV high voltage power supply (type TE-5). These units are based on germanium solid state components, which have high leaking current and low temperature stability.

The section took an active part in the building of the 1MV and 5MV Van de Graaf generators. After Béla Sebestyén, György Máthé became the head of the section. Not only the expertise and the enthusiasm, but friendly colleagues and physical fitness and humor also played an important role in the daily life. Figure 2 shows Zsolt Kertész during load test of a power supply. Old 8kV power supply designed by Atomki (T. Lakatos) after approx. 15 years of operation is visible in Figure 3.



Figure 2: Load test of a power supply by Zs. Kertész.



Figure 3: CAMAC 8kV power supply after 15 years of continuous operation at ^{14}C dating laboratory.

At the beginning of the seventies the main task of the Electronic Section was to develop nuclear measuring instruments for different nuclear detectors, including semiconductor detectors, proportional counters and scintillation detectors. First the instruments for energy measurement were developed and in the second stage of this work those instruments which make it possible coincidence measurements. A whole family of measuring devices was designed and they were realized in a mechanical and electronic standard used by the Comecon countries that time. Selection guides (shown Figure 4 in and in Figure 5) for the energy as well as the coincidence measurements illustrate the available Atomki instruments.

With the help of these instruments different measuring setups could be assembled. As it can be seen high voltage power supplies are available for biasing the nuclear radiation detectors.

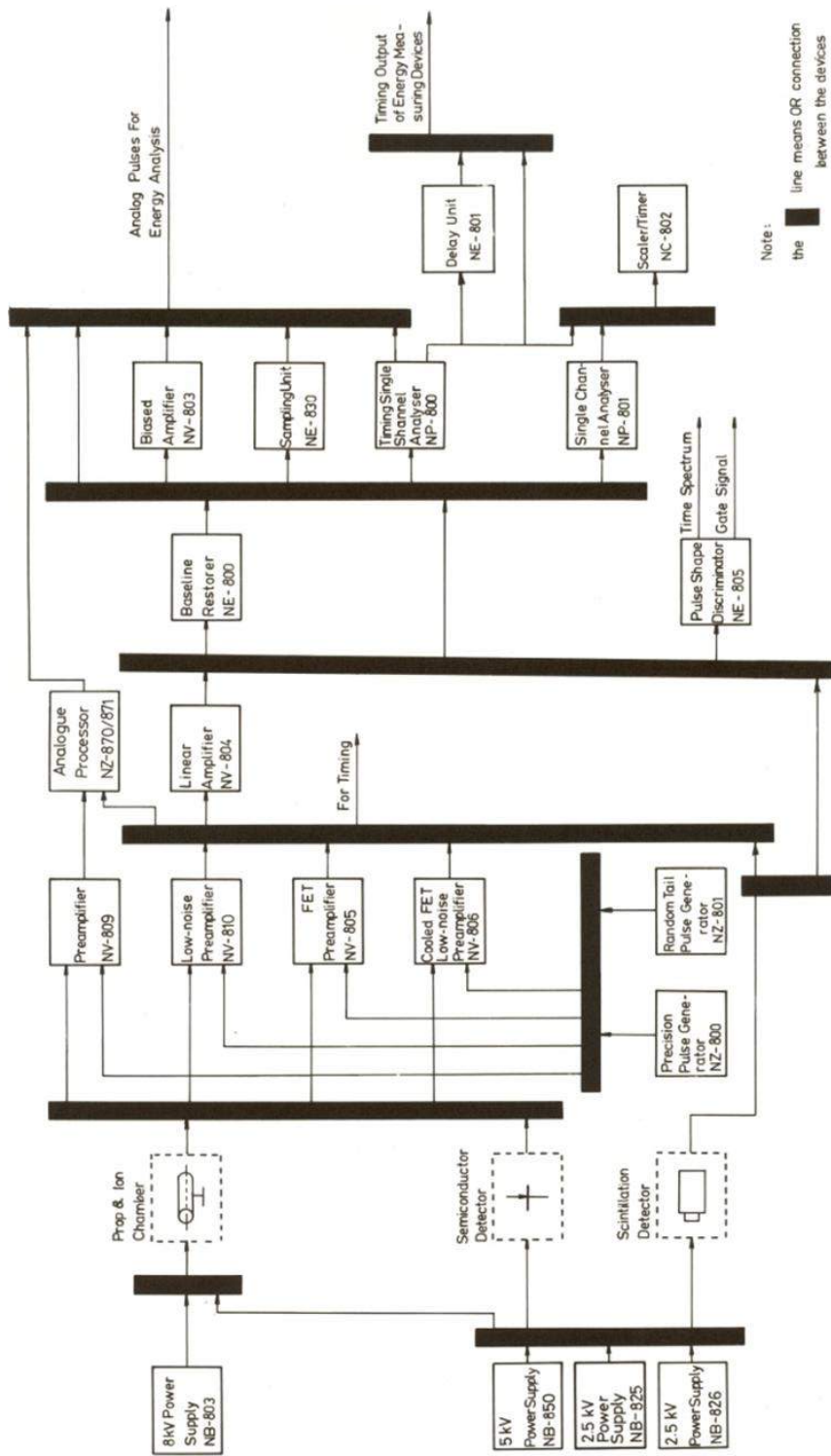
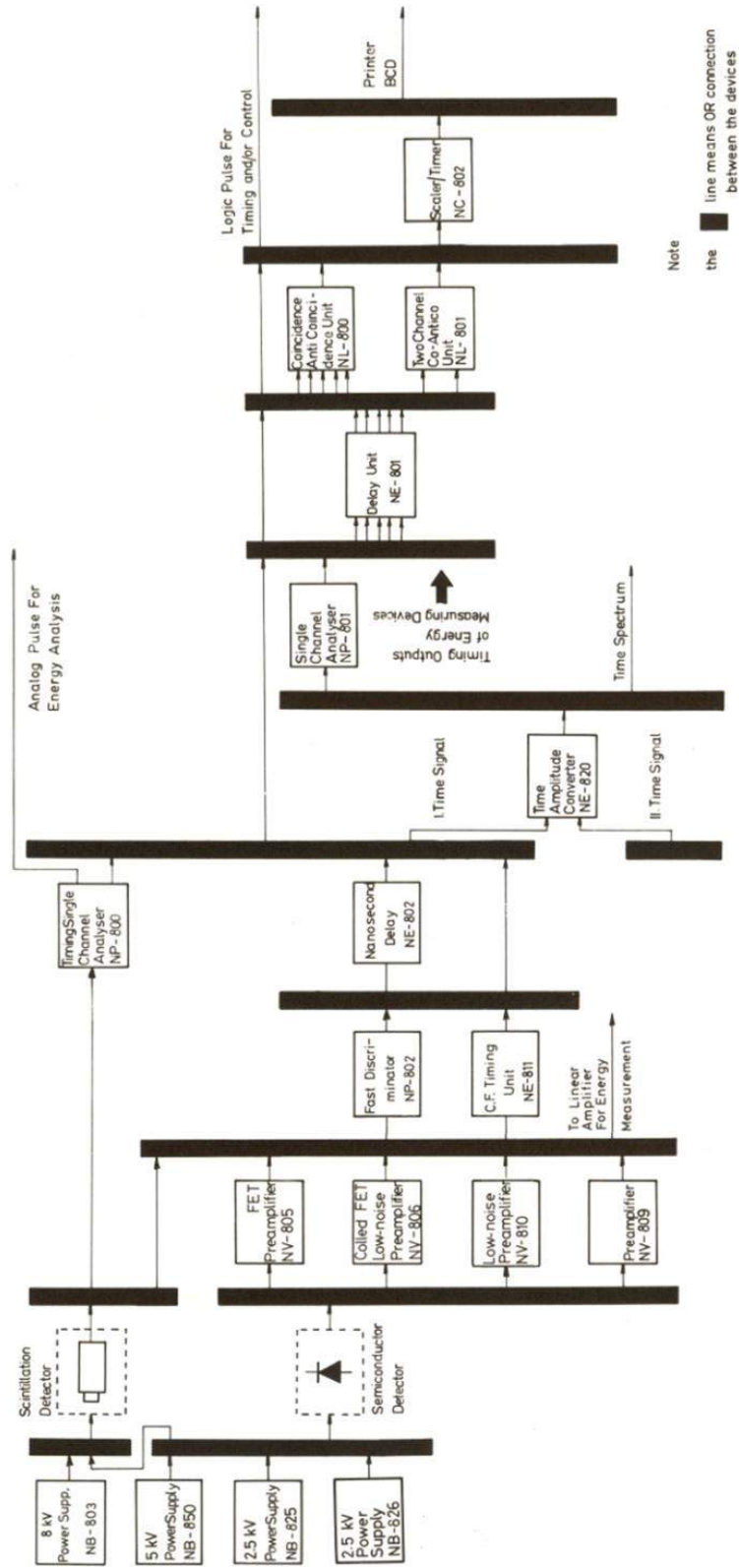


Figure 4: Selection guide for energy measurement with Atomki instruments



Note
 the line means OR connection
 between the devices

Figure 5: Selection guide for coincidence measurement with Atomki instruments

Those detectors, where the signal level is low (semiconductor detectors, proportional counters) can be connected to charge sensitive preamplifiers. The charge sensitive preamplifier is a device which integrates the detector current signals, and it produces a voltage pulse the amplitude of which is proportional to the total charge generated by the nuclear radiation detector. All of the charge sensitive preamplifiers use field effect transistors (FET) at their inputs. Usually the FETs are in room temperature, but for extremely low noise applications (X-ray silicon detectors) they can be cooled. The usual solution for the amplifier circuitry of the charge sensitive preamplifier was a cascode stage with a current generator load followed by a high input impedance follower. The negative feedback with a small value capacitor ($\sim 1\text{pF}$) realizes the charge sensitive (integrator) operation. The accumulated charge on the feedback capacitor must be removed. This can be done continuously with a high value ($\sim 1\text{G}\Omega$) resistor connected parallel with the feedback capacitor or using a pulsed mode discharge. The output pulse shape of the charge sensitive preamplifier is a fast rising pulse, where the rising is determined by the charge collection time of the detector. In the case of resistive discharging the fast rising is followed by a slow decay ($\sim 1\text{ms}$) determined by the feedback capacitor and resistor. This first stage of the preamplifier is usually complemented with a second voltage amplifier stage which partly amplifies the amplitude of the first stage, and at the same time it decreases the decay time of the pulse, using pole zero compensated high pass filter. The purpose of shortening the decay time is to diminish the piling up the pulses.

The output signal of the charge sensitive preamplifier is led to the input of the shaping amplifier. The role of the shaping amplifier is threefold: (i) amplifies the signal, increasing its amplitude to such an extent which makes it possible to measure the signal amplitude easily, (ii) shapes the signal in order to minimize the noise-to-signal ratio, (iii) shortens the signal diminishing the probability of the pile-up effect further. The shaping amplifier applies semi-Gaussian shaping, which is realised with a pole zero compensated high pass filter and two cascaded second order active low pass filter. All the filters have the same time constants which can be varied. By choosing the appropriate value of the time constants the noise-to-signal ratio could be minimized.

The output signal of the shaping amplifier is suitable to measure its amplitude directly. The accuracy of the amplitude measurement is highly influenced by the stability of the baseline of the output signal. High counting rates or external low frequency noises cause baseline fluctuations. These effects deteriorate the amplitude measurement accuracy. This deterioration can be avoided using baseline restorer between the shaping amplifier and the amplitude measuring unit (single or multichannel amplitude analyzer).

The width of the output pulses from the shaping amplifier varies in a wide range, correspondingly the actually chosen shaping time constant. Some of the multichannel analyzers measures the amplitude correctly only if the width of the pulse is in a given range. The sampling unit solves this problem by unifying the width of the pulses but conserving the pulse amplitude. Such a sampling unit is built from a stretcher circuit and a linear gate. The stretcher circuit holds the maximum value of the signal during a well determined time interval and the linear gate produces a constant width ($\sim 1\mu\text{s}$) sample taken from the stretched signal. The timing of the sampling is done by a slow constant fraction discriminator realized by comparison the original semi-Gaussian shaped signal and the stretched and attenuated one [1][2].

For timing purposes the fast discriminator and constant fraction discriminator can be used. The fast discriminator is a leading edge discriminator, where the discrimination level can be set below the noise level in order to diminish the amplitude walking of the discriminator (noise suppressed leading edge timing). Distinguishing the timing signals originating from the noise and the signal could be done on the basis that average width of the noise signal is smaller than that of the real signals.

The traditional constant fraction discriminator uses delay line in order to produce a bipolar signal by subtracting the delayed signal from the original attenuated signal. The zero crossing of the bipolar signal will be a constant fraction (determined by the attenuation factor) of the pulse amplitude, assuring a walk free timing signal. It is also possible to construct so called non-delay line constant fraction timing by the subtraction of a low pass filtered signal from a high pass filtered signal [3][4].

For testing the different nuclear instruments or nuclear measuring setups a special pulse generator (Figure 6) the random tail pulse generator was developed. The generator produces a tail pulse which resembles to the pulse shape of the charge sensitive preamplifier output: it has a fast rise time and a slow exponential decay. It could work in both periodic and random mode. The mean rate of the generator output is adjustable from 10 Hz-1 MHz in decade steps with continuous adjustment within each decade.

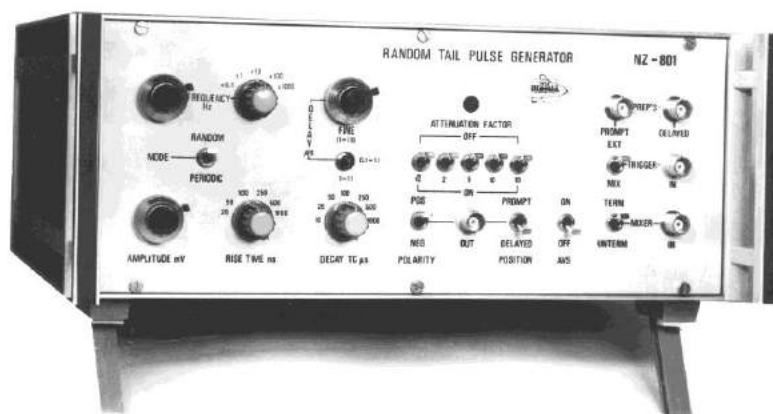


Figure 6: NZ-801 random tail pulse generator, designed and developed by the Section of Electronics.

The time interval distribution in random mode is verified to be Poissonian. Minimum spacing between adjacent tail pulses can be smaller than 100 ns. Rise time can be set from 25–1000 ns in six steps. The decay time constant is also adjustable in the range of 10–1000 μ s. Double tail pulses can be produced by using a mixed triggering facility. Spacing between these two pulses is continuously variable from 0.1–100 μ s [5].

Besides the modular instruments complete signal processing units (Figure 7) also were developed. They contained shaping amplifier, baseline restorer, pile-up eliminator, and dead time and pile-up loss corrector circuitry [6][7][8][9].



Figure 7: NZ-871 Analogue signal processor

2.2 Period 1980-1990

Due to the increasing number of external demands and export possibilities of the special nuclear electronics, the number of employees was also increased rapidly in this period. The section had its own mechanical workshop with turner and miller, chemical lab for printed circuit board production, designers and developers. The maximum number of staff was 39. This period was the era of the computers, microcontrollers. More than 40 different instruments were designed and developed by the colleagues during the decades and this established the future of the modern nuclear electronics at Atomki and enabled the

CERN and other international collaborations, described later. Wide range of serial products, in various form factors, such as Kontaset, CAMAC, NIM, VXI were available for internal and export purposes. The strengths and the main research field in electronics of the section are high precision timing, amplitude and energy measurement.

The Section takes part in the development ^{14}C dating laboratory from the beginning. All the electronics necessary for the large volume proportional counters were developed: high precision high voltage power supplies, charge sensitive preamplifiers, signal processing units (designed by G. Hegyesi and L. Záborszky), which include shaping amplifiers, coincidence and anticoincidence unit and pulse shape discriminators. It was a challenge to assure the long term stability of this electronics.

In the end of seventies and in the beginning of eighties all the modular nuclear electronics were redesigned in CAMAC standard. The laboratories of atomic power plant of Paks were equipped with these instruments.

In the eighties another field of development placed a very important role in the activity of the Electronic Section. This work was closely related to the vacuum technique. We dealt with the development of vacuum measuring units such as Pirani and ionization vacuum meters and automatic vacuum control units. The development of the control unit of the quadrupole mass spectrometers with different mass ranges was a mile stone in the activity of the Electronic Section. The control unit consisted of different parts: power supply system and emission stabilizer for the ion source, RF-DC unit of quadrupole rods and a fast electrometer for measuring very low currents (down to the pA range). The application of the quadrupole mass spectrometer has a wide range: it was used for industrial, agricultural and medical research but it was applied for military purposes, too [10][11][12][13]. Several quadrupole mass spectrometers were sold in Hungary and abroad. The Q300 type quadrupole mass spectrometer is shown in Figure 8.



Figure 8: The QMS 300 quadrupole mass spectrometer controller and the electronic units and measuring head on left and the Q300C on right. Some parameters are adjustable by computer control in Q300C. Its mass range is 1-300.

Digitrack, the first CCD based system for automatic counting and analyzing etched nuclear tracks in solid state nuclear track detectors, was also developed by the section (J. Molnár, G. Somogyi). The video signals were processed by a Fairchild CCD line array sensor (with 1728 pixels). The object was scanned row-by-row and analyzed by two Intel 8080 microprocessors and interfaced to a PDP-11/40 computer. The automatic evaluation of the solid state nuclear detectors means the solution of the following tasks: counting of tracks; measurement of x-y coordinates, track axes and area; record and evaluation of measured track data. The system consists of the following components:

- Leitz Ortholux microscope equipped with the CCD sensor.

- Main processing unit: handles the user interactions and displays the results (keyboard, graphic display 256x256 resolution), evaluates the track configurations, controls the peripherals (serial and parallel communication to the PDP-11/40 and to the Intel 8255 image processor, X-Y plotter interface, Seiko 101F printer).
- Image processor unit: controls the motion of the microscope stage, collects CCD data, recognize patterns with area of single tracks and sends the separated track images to the main processor.

The software tasks were split among the two processors in accordance with the hardware. The system was able to evaluate coordinates areas and spatial densities of etched nuclear tracks and their statistical distributions in solid state detectors using a new type of video sensor [14][15].

Another important development was the RM-83 type rate meters, designed by J. Gál, (Figure 9) and the power supplies for monitoring the emitted radioactivity around the Institute. Rate meters are connected to detectors placed different locations in Atomki and record the activity in 24h/day. The system is still working after more than 25 years of continuous operation.



Figure 9: Rack of RM-83 rate meters and the maintenance of the power supplies.

Pictures in Figure 10, Figure 11, Figure 12 and Figure 13 show the daily life at the section not only in the eighties but in the recent past.



Figure 10: J. Gál on left (later head of the section) and Z. Urszin.



Figure 11: B. Szabó technician has been receiving Atomki award for the contribution to the development of the K/Ar dating system.



Figure 12: J. Szádai, E. Hertelendi and their colleagues moving a heavy component of a water sampler.



Figure 13: J. Molnár (second from the left) received the Dénes Gábor award in 2011 for achievements in CERN and for state of the art nuclear electronics for medical imaging systems, i.e. the miniPET-I and miniPET-II.

3 Diamant detector / VXI data acquisition system

In the beginning of ninetieth the Electronic Section has begun the development of the electronics of the DIAMANT particle detector system. The DIAMANT detector array was originally developed in CENBG (Bordeaux) and it can be used inside large γ -ray detector systems, like EUROBALL. The individual detectors of the DIAMANT are scintillation detectors built of CsI(Tl) scintillator and PIN photodiode. The application of this scintillator makes it possible to separate the particle signals from the γ -photons and the different type of particles (proton, alpha, etc.) can also be distinguished, due to the fact that the scintillation decay time depends on the detected particles. Since the signal processing electronics of the EUROBALL was built in VXI standard, we also decided to construct our diamante electronics in VXI, too.

During the development of this electronic we used several new solutions.

Since the charge signal from the described scintillation detector is very small (2.6 fC for 1MeV α -particle), the noise pick off from the environment could deteriorate the noise to signal ratio. Therefore we used such a solution where the charge sensitive preamplifiers are mounted directly on the detector array and together with the detector array it can be put into the vacuum chamber. For this purpose we developed a charge sensitive amplifier consisting of a junction FET and a current feedback operational amplifier [16]. The charge sensitive preamplifier is built using surface mounting technology. The power consumption of this amplifier altogether is 25 mW. This low power prevents it to overheat itself in the vacuum.

In order to separate between the different particles we used pulse shape discrimination technique. The current pulse from the detector follows the scintillation decay. Since the charge sensitive preamplifier integrates this pulse, therefore the rise time constant of the output signal will be equal to the decay time constant of the scintillation light. This means that we have to discriminate between the signals according to their rise time constant. For the solution of the pulse shape discrimination we developed a technique, based on the ballistic deficit effect [17][18]. The ballistic deficit is a phenomenon when the amplitude of a pulse at the output of a pulse shaping circuit is degraded due to the finite rise time of the input pulse. In the case of a given filter the larger the rise time constant is the larger degradation will be. The pulse shape discrimination based on the ballistic deficit phenomenon uses two filters with different shaping time constant. The ballistic

deficit of a small time constant filter output will be larger than that of a large time constant filter output. Therefore making the ratio of the two filter outputs one can get a signal which is amplitude independent and it depends only on the ballistic deficit, consequently on the rise time constant of the input signal.

During the practical realization of the ballistic deficit method for the large ballistic deficit filter we used low time constant bipolar shaping. The bipolar signal has even larger ballistic deficit than the unipolar signal with the same time constant. For the small ballistic deficit shaping a semi-Gaussian shaped signal followed with a delayed switched gated integrator [19] is used. The output of this integrator practically has extremely low ballistic deficit. The bipolar signal is suitable to realize the zero crossing pulse shape discrimination technique at the same time, too. It is possible to combine the two pulse shape discrimination technique. It was shown experimentally that this mixed method gives better figure of merit than either the ballistic deficit method or the zero crossing method alone.

For the correct functioning the total signal processing unit a very precise timing is necessary. Since the CsI(Tl) is a slow detector comparing it to semiconductor detectors, the traditional constant fraction timing using delay line cannot be used. Therefore we used a non delay line constant fraction timing which applies a tripolar signal. The first zero crossing of this signal is used as time reference point.

In Figure 14 a VXI module is shown, which contains eight identical channels. The block diagram of one channel of the analogue part of the VXI channel [20] is shown in Figure 15. It consists of the following blocks:



Figure 14: VXI module with eight identical channels.

3.1 Amplifier and Shaper

It has seven inputs: positive and negative signal inputs, a test input and four control inputs: one for the baseline, one for the pole-zero and two for the gain. Controlling the baseline of this amplifier section allows to connect to a preamplifier the output DC level of which is between -5V and +5V. This control signal is an analog signal and it is automatically generated by the baseline restorer. The pole zero control signal is an analog signal, generated by a DAC and can be varied from software. The gain control is a two bit digital code, which can be set from software. The block has three outputs: a unipolar signal, a bipolar signal, and a tripolar signal. The unipolar signal is used to measure the energy, the bipolar and tripolar signals are used for timing purposes.

3.2 Baseline Restorer and Gated Integrator

It has four inputs: the unipolar signal input and two control inputs of the integrator (integration time, discharge/inhibit). The control signals for the integrator are generated by the local trigger. The baseline restorer stabilizes the baseline of the unipolar signal before its integration in the gated integrator. The block has two outputs: the energy signal, which is the integrated unipolar signal and the baseline control signal which is produced by the baseline restorer.

3.3 Bipolar Stretcher and Divider

It has six inputs: the energy signal input, the bipolar signal input, the TAC input, a control signal for the bipolar stretcher (discharge/inhibit) and two control signals for selection of the discrimination mode. The control signal for the bipolar stretcher is generated by the local trigger, and the two selection signals can be set from software. The block has one output: the particle output. If the ballistic deficit method is selected the particle output is the ratio between the amplitude of the energy signal and that of the first lobe of the bipolar signal. If the zero crossing method is selected the particle output is the TAC output. If the mixed method is selected the particle output is the weighted sum of the two previous signals.

3.4 Signal Recognition and Timing

It has four inputs: the bipolar and tripolar signal input and two control inputs. One of the control inputs is for setting the signal recognition level. The control signal is an analog signal generated by DAC, and can be set from software. The block has three outputs: signal recognition (SIG. REC.), which is generated when the bipolar signal exceeds the signal recognition level and two timing signals generated at the crossover point of the tripolar and at that of the bipolar signals separately. The timing signal generated at the bipolar signal zero crossover (BIP. TIMING) is used for particle discrimination purposes. The timing signal generated at the tripolar signal first zero crossover point is delayed in order to realize time alignment between the channels, since this signal (TRIP. TIMING) is used for time reference purposes. The delay range is 20-200ns. The second control signal to this module serves to set this delay. It is generated by DAC and can be set from software.

3.5 Particle Discriminator TAC

It has three inputs: start and stop inputs and discharge/reset input. The start signal is the coincidence signal (COINC) from the local trigger. The stop signal is the BIP. TIMING signal. The discharge/reset input is the DISCH. signal from the Local Trigger. The output is an analog signal containing information about the particle type.

3.6 Time Reference TAC

It has three inputs: start and stop inputs, discharge/reset input. The start signal is the TRIP. TIMING signal, and the stop is the delayed FT ($2.7\mu\text{sFT}$), which is delayed by $2.7\mu\text{s}$. The discharge/reset input is the DISCH. signal from the Local Trigger. It has one output signal, which is an analog signal and it is used to reject random coincidence events.

3.7 Dual ADC1

It has five inputs: two analog inputs for the energy (ENERGY) and the particle type (PARTICLE) signals, a third analog input for the sliding scale (S. SCALE) control, a clock input (CLOCK) and the convert command input (CONVERT). It has two outputs: energy and particle type.

3.8 Dual ADC2

It is a similar block to the Dual ADC1, but only one of its channels is used. This channel is for conversion of time reference information, produced by Time Reference TAC.

3.9 Local Trigger

It controls the signal processing of the particular channel and synchronizes it with the Ge detector system. It accepts two global (external) signals: the delayed fast trigger ($2\mu\text{sFT}$) and the validation (VAL), which are produced by the Master Trigger Unit. The delay for FT is common for all channels of one card. The delay range is $0.1 - 2\mu\text{s}$. A further external signal to the Local Trigger is the external reset signal (EXT. RES.). The block accepts two internal signals: signal recognition (SIG.REC.), and the time aligned tripolar crossover timing (TRIP.TIMING) pulse. A further input accepts analog control signal, which serves to control the integration time (INT.TIME). The local trigger contains a coincidence circuit, which investigates the coincidence between FT and TRIP. TIMING. The coincidence resolving time is set to 600 ns. The sum of the FT delay (including the external delay related to the event) and of the integration time determines the “peaking time”. The adjustment range of the integration time is $3 - 10 \mu\text{s}$. One input accepts a 1 bit digital control signal for changing between the standard/standalone mode.

If SRC is generated the signal processing starts, which continues if coincidence is detected between FT and TRIP. TIMING. The coincidence signal (COINC) appears at the leading edge of the delayed FT signal. COINC is the start signal for the integration process and it starts a pulse (INTEGR. TIME) which determines the integration time. At the same time a pulse (SUMBUS) is generated for the analog sumbus driver. The falling edge of INTEGR. TIME in appropriate order initiates two signals: a pulse, which indicates that the analog signal shaping is finished (PEAKHOLD) and a second pulse, which is the discharge/reset signal (DISCH) for the integrator, the stretcher and the time amplitude converters. The rising edge of the COINC signal starts the channel busy time which is an $8\mu\text{s}$ long internal signal (BUSY) in the Local Trigger. The back edge of the BUSY resets the Local Trigger. When external reset (EXT. RES.) is applied, it the BUSY signal.

If the VAL and the BUSY are in coincidence the validation acknowledge signal (VALACK) is generated. The VALACK initiates the readout process.

If SRC is generated, but no COINC signal appears, then TRIP. TIMING initiates the DISCH signal.

The signal recognition circuit works on the bipolar signal, therefore the pulse pair resolution of this circuit cannot be shorter than the first lobe width of the bipolar pulse, which is approximately $3 \mu\text{s}$. (It has to be noted that signal rise time at the preamplifier output is $1.6 - 1.8 \mu\text{s}$ depending on the particle type. If one shape a pulse, the width of which is shorter than this rise time the signal to noise ratio will significantly decrease. Because the signal recognition level has to be raised above the noise level in this case a useful part of the energy spectrum can be lost.) This means that we cannot construct an effective “counting type” pile-up eliminator. Fortunately the pulse shape discriminator which is used for particle separation can detect pile-up with $0.5\mu\text{s}$ resolution. If a dead time event occurs, the signal recognition circuit detects it, and the channel busy time is extended. The first event can be processed and the second event is lost. In the case of dead time event the channel busy time can be longer than the system busy time. If in a subsequent event, occurring during the channel busy time, this channel is also involved zero energy and particle value or alternatively a flag shows that the channel was dead.

Summarizing the above described things, the local trigger has the following output signals: COINC for starting the integration process and to start the particle discriminator TAC, DISCH for discharging, inhibiting and resetting the integrator, the stretcher and the TACs, SUMBUS for driving the sumbus, PEAKHOLD for starting the analog to digital conversion, VALACK to initiate the readout process.

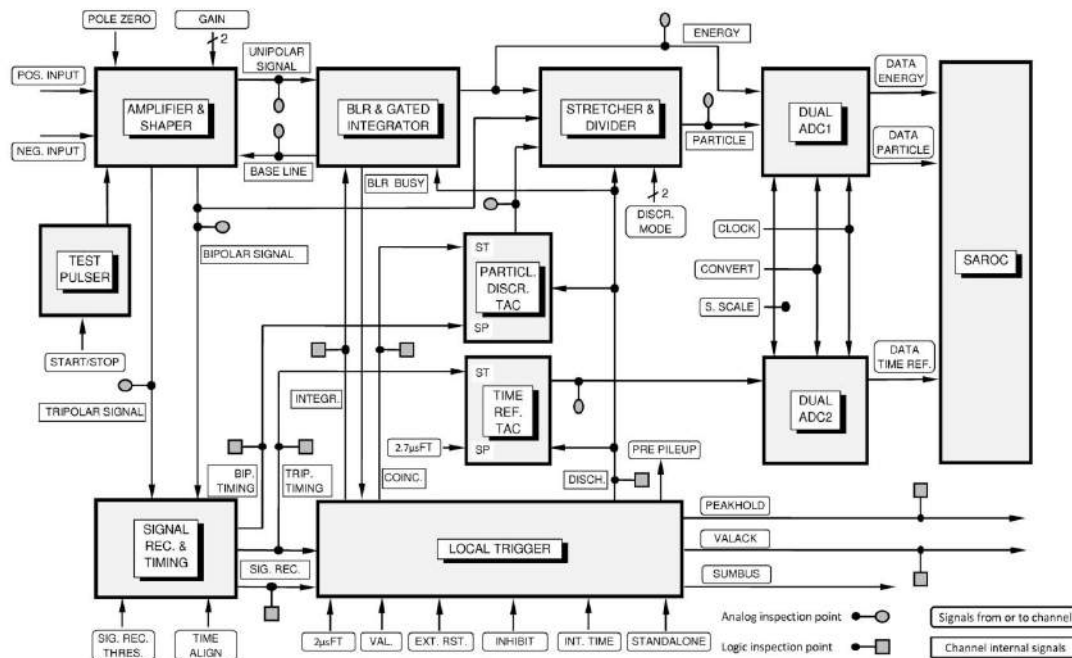


Figure 15: Block diagram of one analogue channel of the VXI card.

The DIAMANT detector (see Figure 16) and its VXI electronics (the boards connected to the experiment's data acquisition system is shown in Figure 17) were used in number of experiments [21][22][23] not only with the EUROBALL but with the EXOGAM at GANIL and with the AFRODITE detector in the iThemba LABS in South Africa.

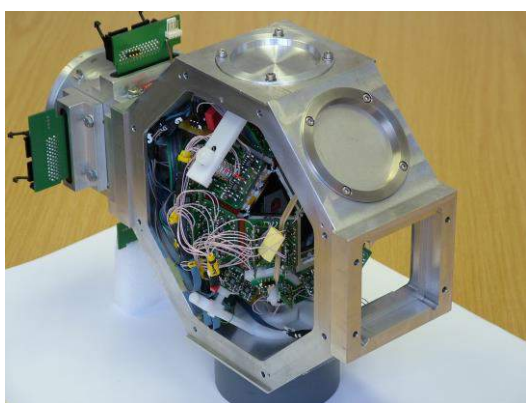


Figure 16: The DIAMANT detector in the AFRODITE scattering chamber.

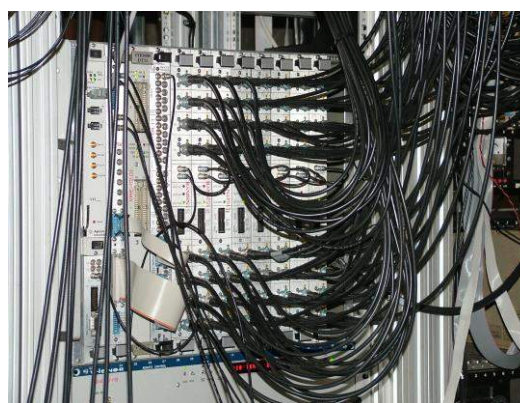


Figure 17: VXI modules in rack.

4 CERN

The section has been playing an important role in various CERN experiments and developments related to the NA49 experiment, DELPHI (DEtector with Lepton, Photon and Hadron Identification) at LEP and CMS (Compact Muon Solenoid) at the Large Hadron Collider (LHC), see Figure 18.

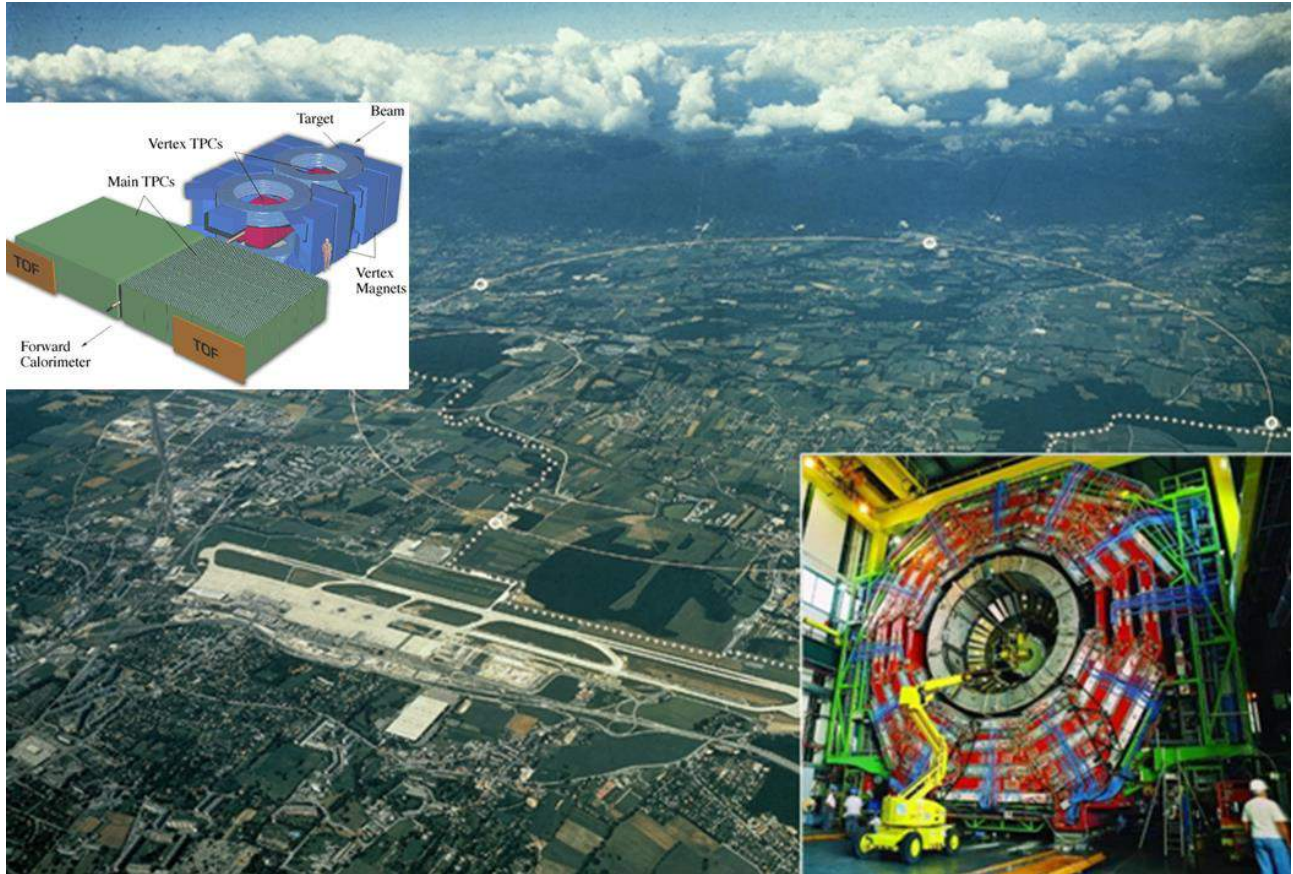


Figure 18: CERN, the CMS detector (bottom right) and the layout of the NA49 experiment (top left).

4.1 Contribution to the NA49 experiment, the Buda Trigger Unit

The NA49 experiment is designed to perform inclusive as well as single event measurements of a variety of observables for ^{208}Pb induced reaction at 158 GeV/nucleon energy. Its experimental configuration includes a fine granularity Time Projection Chamber (TPC), and two high resolution intermediate size TPCs as tracking devices, a Time Of Flight system (TOF, Budapest Wall) and a set of Calorimeters for transverse and forward energy flow measurements.

The tracking of charged particles is performed by the TPCs. Main TPC has a readout surface of $3.9 \times 3.9 \text{ m}^2$ and a depth of the field cage of about 1.1 m. The track signals are read out by 25 proportional chambers providing up to 90 measured points and ionization samples on each particle trajectory. Vertex TPCs have gasboxes with $2.0 \times 2.5 \text{ m}^2$ surface area and 0.67 m depth. The readout is performed by 6 proportional chambers which provide up to 72 measurements and ionization samples on the particle trajectories. The Vertex TPC's are mounted inside the two 450 ton 1.5 Tesla superconducting magnets.

The TPC's are read out by the front-end electronics. They each perform time and charge measurement. The data from up to 18 front-end cards are multiplexed on the control boards and transmitted via a single optical fiber to the data recording building. Flight time was measured between the production target and two 2.2 m² scintillation counter walls (TOF). Each wall consists of 891 closely stacked scintillators connected to photon multiplier tubes.

A Ring Calorimeter and a Veto Calorimeter were used to measure the energy flow due to the particles produced in Pb+Pb collisions and to let pass only those fragments of the beam nuclei which have not interacted in the target foil, respectively.

Colleagues (J. Molnár, J. Gál, K. Kiss) at the Section developed a trigger unit[24] BUT (Budatrigger Unit), which produced the control signals for the TOF. Three variants have developed (in 1994, in 1995 and in 1997). The BUT is intended to control the different parts of the data acquisition system (detectors and front-end electronics, VME daq, ALEPH event builder) built around the TOF spectrometer. The module accepts different input signals and according to the experimental requirements it produces control and timing signals. Since TOF has <60 ps time resolution, it was a requirement that BUT does not cause any additional resolution degradation. In order to satisfy this requirement the BUT was designed using fast ECL integrated circuits.

4.2 ASACUSA – Atomic Spectroscopy And Collisions Using Slow Antiprotons

We joined to the ASACUSA (Atomic Spectroscopy And Collisions Using Slow Antiprotons) collaboration. The aim of ASACUSA is to learn more about fundamental differences between matter and antimatter. At first we had theoretical contribution in the study of creating either anti-atoms or exotic atomic formation of He atom, when one of the electrons in the He is replaced by antiproton. We performed classical simulations for the interpretation of the experimental observations. The agreement between our model calculations and the experiments was reasonable good [25]. We presented theoretical singly- and doubly-differential ionization cross sections in collisions between antiprotons and helium atoms at 50 and 100 keV impact energies. The calculations were performed within the frame work of the three-body classical trajectory Monte Carlo method. We found clear evidence for the formation of the anti-cusp in the differential distributions [26].

However, our activity is mostly focus on to experimental study the ionization of atoms and molecules by slow antiprotons. The group leader of the international collaboration of atomic collision experiments (see the Figure 19) is Prof. Helge Knudsen from the University of Aarhus, Denmark. In our experiment we use the Antiproton Decelerator (AD). The AD is a unique machine providing low-energy antiprotons for studies of antimatter. The starting point, surprisingly, is a beam of protons from the Proton Synchrotron, which is fired into a block of metal. The energy of the collisions is enough to create a new proton-antiproton pair about once in every million



Figure 19: Some members of the atomic collision group after the successful night shift.

collisions. The antiprotons are produced travelling at almost the speed of light. They also have a range of energies and move randomly in all directions. The job of the AD is to tame these unruly particles into a useful, low-energy beam.

Using the CERN facility connected to our ionization apparatus AIA (Aarhus Ionization Apparatus) we have performed our accurate measurements of ionization of atoms and molecules at very low impact energy of antiprotons.

The total cross sections for single ionization of helium and single and double ionization of argon by antiproton impact have been measured in the kinetic energy range from 3 to 25 keV using a new technique for the creation of intense slow antiproton beams [27]. The data which are obtained via absolute measurements show a nice overlap with our earlier data at the highest energies. Moreover, the new data provide benchmark results for the development of advanced descriptions of atomic collisions and we show that they can be used to judge, for the first time, the validity of the many recent theories.

We also measured the double ionization cross section of helium in these energies of antiproton impact and compare our data with the various calculations as well as with previously published experimental data. Our present results can be used to discern between many advanced theoretical calculations. Earlier measurements of the ratio R between the double and single ionization cross sections for antiproton impact on helium show a persistent increase for the projectile energy decreasing from 10 MeV to 10 keV. The present data show that below 10 keV this increase stops and we give an upper limit to R [28]. For double ionization of helium by slow antiproton impact, the mutual disagreement between various published theoretical calculations is even worse - amounting to as much as a factor of 20 at 1 keV.

Recently we presented measurements of the cross section for single, nondissociative ionization of molecular hydrogen for impact of antiprotons with kinetic energies in the range 2-11 keV, i.e., in the velocity interval of 0.3-0.65 a.u. We find a cross section which is proportional to the projectile velocity, which is quite unlike the behavior of corresponding atomic cross sections, and which has never previously been observed experimentally [29].

4.3 CMS – Compact Muon Solenoid

Colleagues have been playing an active role in the position alignment of the CERN Compact Muon Solenoid (CMS) detector system. Performance of the CMS detector of the Large Hadron Collider (LHC) at CERN is affected by the position and orientation of the individual detectors. Therefore, the CMS detector has an alignment system that consists of: the internal alignment of the inner tracker, which measures any deformation of the tracker, the link system, which transfers the position of the tracker to linking points located between the barrel and the end-cap muon regions and the barrel and end-cap internal alignments, which measure the positions of the muon detectors with respect to the linking points.

Colleagues (J. Molnár, G. Székely, Z. Szillási, N. Béni, J. Imrek) are responsible for the designing, manufacturing and maintaining of the muon barrel alignment system. As it follows from the construction and parameters of the CMS experiment [30][31][32][33][34][35][36], the positions of the 250 barrel muon chambers have to be known (measured) with 150-350 micrometer accuracy depending on their radial distance from the interaction point in order to be able to determine the muon momentum with 5-20% accuracy depending on the muon energy. The muon path and the block schema of the CMS are shown in Figure 20. The barrel muon chambers have a typical size of $2.5 \times 3 \times 0.3 \text{ m}^3$ embedded in the return yoke of the detector magnet. The size and configuration of the chambers as well as the additional circumstances and

requirements - like radiation background, high magnetic field, long-term autonomous operation, and an acceptable price - have made it necessary to develop new methods to build the position monitoring system. The measurements of the position of the muon chambers are performed by means of about 10000 light sources mounted on the chambers and observed by an opto-mechanical network composed of 36 rigid structures called MABs (Module for Alignment of the Barrel) holding 600 CMOS video cameras.

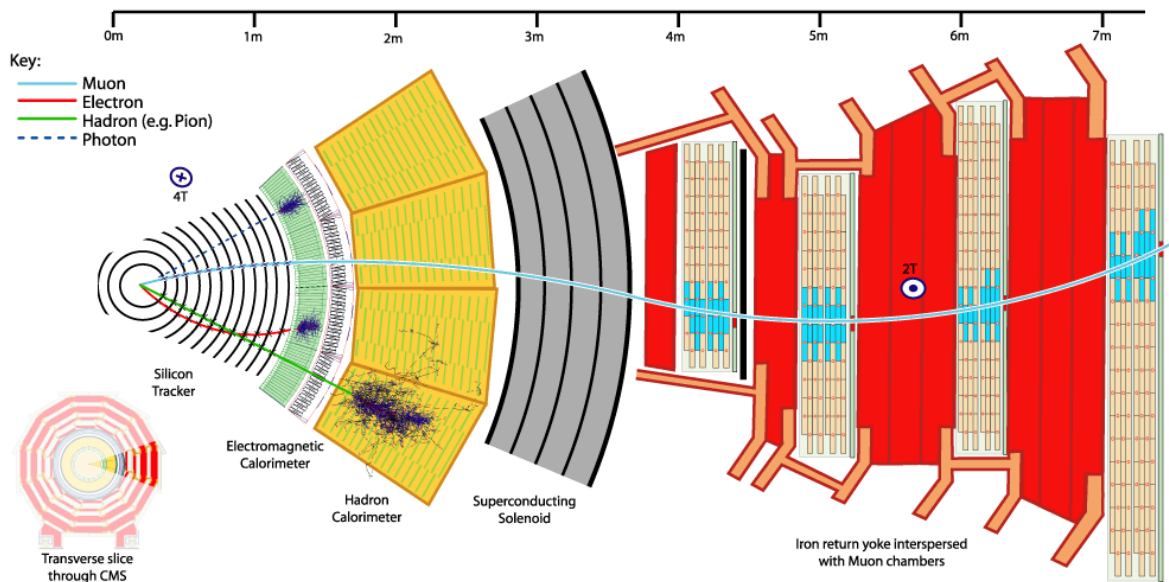


Figure 20: The CERN CMS block schema and the muon track.



Figure 21: Components of the CMS position alignment system: MABs, LEDs, and video sensor left to right.

The operation and synchronization of the elements of the system and the data taking and preliminary evaluation of the collected data are executed by 36 PC-modules mounted on the detector and connected to each other and to the main control computer via an Ethernet network. Block schema, and location of the components (Figure 21) and MABs related to the muon chambers are shown in Figure 22. Radiation hardness tests and magnet tests of the components were crucial, because most of the electronic components are sensitive to the charged particle radiation. Tests were performed at the Theodor Swedberg Laboratory (TSL) Uppsala, Sweden. LEDs were irradiated with neutrons in order to estimate the intensity loss because more than 40% relative intensity loss was observed during the 10 years of operation of the LHC. PC-104

computers were also irradiated by protons to test the reliability of the built in memories and processor. The setup at TSL is shown in Figure 23.

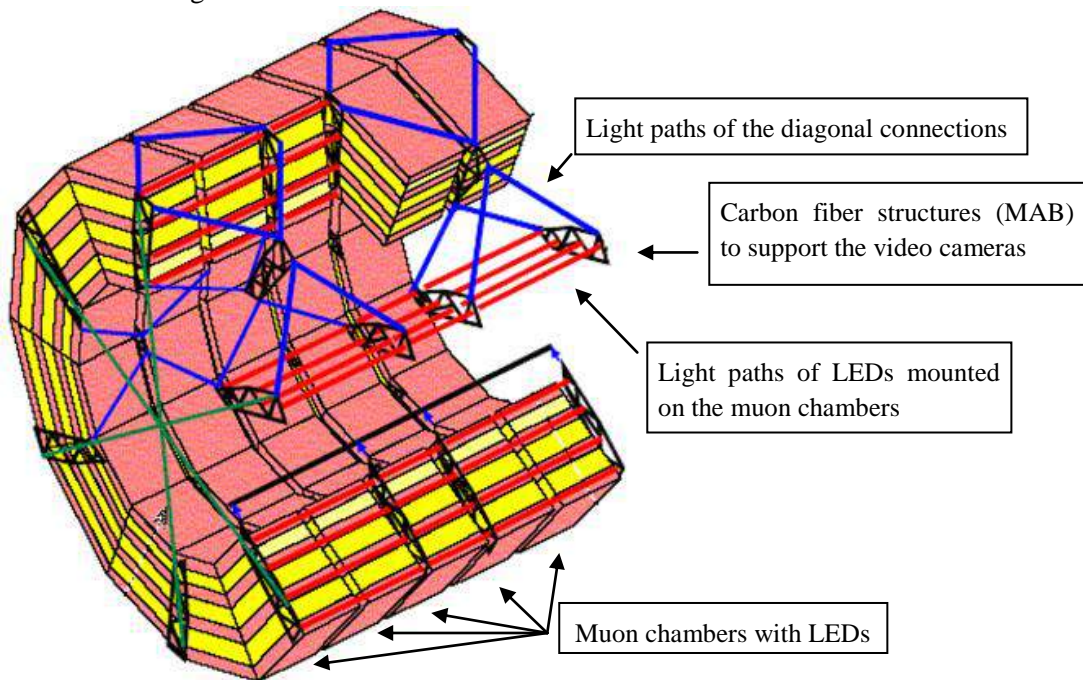


Figure 22: Position of the MABs and LEDs.



Figure 23: PC-104 irradiation setup at TSL, Uppsala. The experiment was carried out by D. Novák, A. Kerek and L-O. Norlin.

One of the most important experiments nowadays in CERN is the observation of new boson at mass 125 GeV. Colleagues (J. Molnár, Z. Szillási, N. Béni and S. Czellar and others from Atomki) also contribute to this experiment. The results [37][38][39] show that a new type of boson (probably the Higgs) exists.

4.4 Irradiation experiments and proton beam dosimetry with silicon CMOS sensor.

The advanced processing techniques of required to manufacture modern microelectronic devices often utilize energetic particles or photons and thus may cause significant radiation damage. In this regard, the practical objective of the research is to control and remove the radiation damage in order to ensure proper functionality of the circuits after they are fabricated. In daily practice, when working with well-known devices, we can sometimes observe unusual effects, for example in the case of a commercial CMOS Active Pixel Sensor (APS) image sensor used as part of the Compact Muon Solenoid (CMS) Muon Barrel Alignment system of the Large Hadron Collider (LHC) accelerator at CERN. The radiation tolerance of this component was tested in a radiative environment. When testing the radiation hardness of the video camera with protons and neutrons, it became obvious that the device has a potential for usage in other applications. During hardness testing bright spots of different size were noticed on the sensor image. These bright spots were interpreted as the results of different nuclear interactions caused by proton and neutron irradiation. A nuclear reaction in silicon initiated by a neutron or proton frequently results in emission of a light particle and the bright spots.

The investigation of the above mentioned observation has split into different directions:

- using the CMOS image sensor as a radiation detector in the energy range of therapeutic proton beams,
- the effects of the secondary particles in the image sensor as a function of energy and type of ion,
- using the CMOS image sensor as a Radiation Field Detector for clinical dosimetry in advanced proton therapy.

4.4.1 Proton irradiation of the CMOS sensor

The CMOS sensor (Figure 24) was irradiated with a 180MeV proton beam at the TSL Laboratory Uppsala, Sweden. The output signal of the sensor was recorded on a videotape. The recorded video images from the tape showed intermittent bright white spots and from time to time long tracks. Every bright spot indicates where a nuclear reaction has occurred and a charged particle has reached the sensitive volume of the pixel. For automated and detailed evaluation, all pixels of the picture are scanned for each frame to assemble the frequency of the possible 256 gradation intensity values.

The resulting brightness frequency histogram is created for each individual frame. In Figure 25 the outcome of this type of analysis is illustrated for a data set that is collected during approx. 2 min with two beam intensities. Within this 2-min time segment, the beam appeared after a few seconds and its intensity is gradually decreased after 30 seconds. The number of bright pixels seems to follow the beam current.

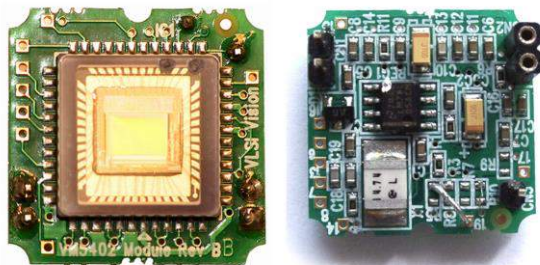


Figure 24: CMOS sensor (front and back) irradiated by protons and heavy ions.

The experiments have proven that the CMOS sensor (even without evaluation software) can be used as simple, inexpensive, but qualitative radiation detector, to detect charged particles for educational purposes, for radiation monitoring in tumor therapy, etc., and also after removal of the protecting glass window, to detect heavy charged particles [40].

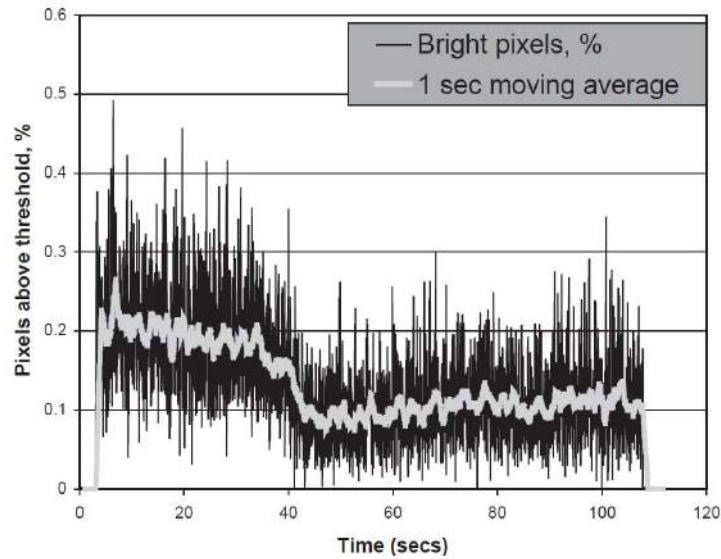


Figure 25: Brightness frequency histogram of the irradiated CMOS sensor.

4.4.2 Heavy ion irradiation of the CMOS sensor

Because the spots in the output signal of the CMOS sensor are caused by the charges created by the interaction of the secondary particles with the detector material, one analyzes the effect of some mixture of secondary projectiles. It was therefore decided to study the effect of individual secondary particles at different energies. The heavy ion irradiations were performed at the Tandem Laboratory at Uppsala, Sweden.

In order to design the measurement and also to help interpret the results, a simple model of the image sensor was used. For automated and detailed evaluation all pixels are scanned for each frame to find the bright spots. The bright spots are defined as a cluster of pixels, where each of the pixels have brightness above some threshold level and the pixels have at least one neighbor joining it side by side from the same cluster. After identifying the individual clusters (spots), different types of statistical analysis can be performed.

In Figure 26 the ranges of proton projectiles with different energy in the image sensor as calculated for the simple model by SRIM (left part), and the experimental brightness distributions as function of proton energy (right part) are illustrated. The limited thickness of the sensitive layer still enables the chip to be used as a particle detector with high spatial resolution ($<100\mu\text{m}$) and with limited energy resolution for particle identification. These features enable the use of the image sensor for energy selection of projectiles, while simple counting of the bright spots can be used in dosimetry applications [41].

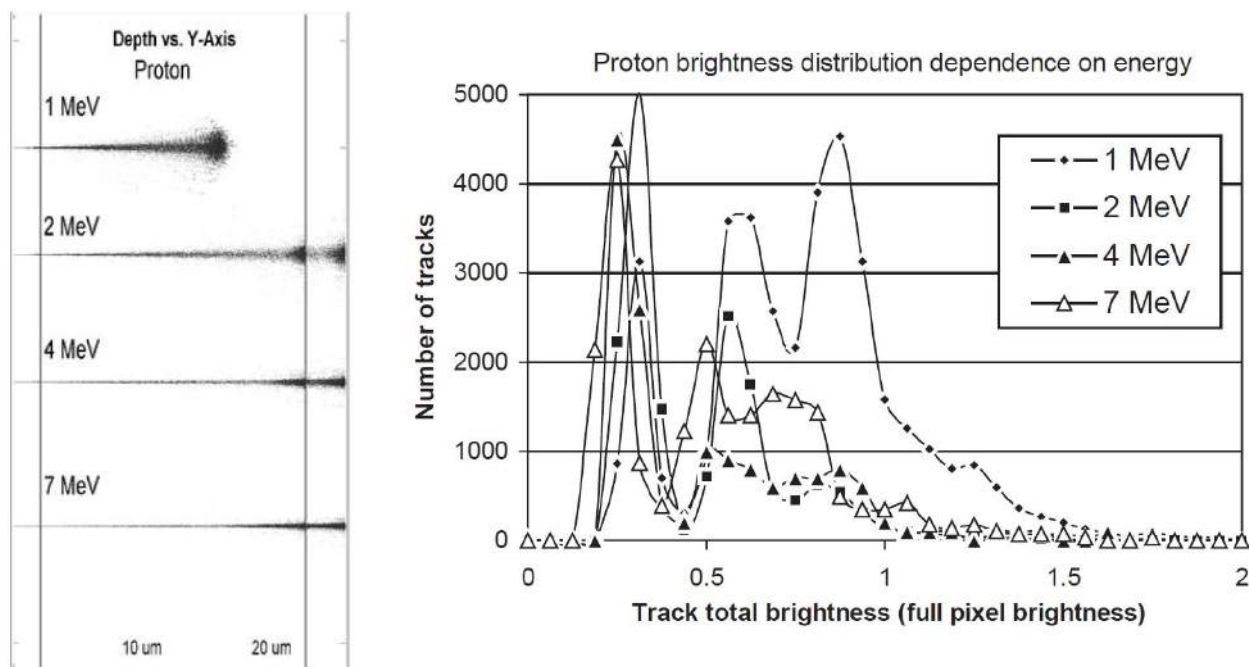


Figure 26: SRIM simulation of the irradiation on left and the measured brightness functions as a function of proton energy on right.

4.4.3 Proton therapy beam dosimetry with CMOS image sensors

The aim of this experiment was to investigate the use of the CMOS image sensor as a Radiation Field Detector for clinical dosimetry in advanced proton radiotherapy. The CMOS sensor was irradiated with 48, 95 and 180MeV protons at the TSL Laboratory. The detector efficiency, linearity, and angular dependence for proton beams of different therapeutic energy and current were studied.

Figure 27 shows the cumulative histogram distribution of the experimentally determined number of recoil nuclei per video frame as a function of proton beam and intensity for perpendicular incidence (including Gaussian fits). Figure 27 present the probability distributions obtained for 48 and 95 MeV proton irradiation. In Figure 28 the corresponding most-probable number of recoil nuclei per image frame as obtained from the Gaussian fits is shown as function of proton current and energy. Finally Figure 29 shows the cumulative histogram distributions of the number of heavy recoils as a function of the incidence angle at approximately constant beam current for 180 MeV protons.

Si-diode detectors used in proton beam dosimetry require a suitable level of pre-irradiation to stabilize the detector signal. Since the use of this CMOS image sensor is based on detection of nuclear reactions, the radiation hardness of this device is high. During the present experiments, which lasted for more than 20h, no serious damage of the chip was found and the analysis method also eliminates the influence of damaged

pixels. In addition to other well-established detectors, the CMOS detector could make a good candidate for proton radiation dosimetry, and has the following advantages (or due to the following factors): direct read out, lack of pile up effects, the well-established proton interaction cross-sections, the stability of the signal, the detector linear response with proton energy and current and the very low cost [42].

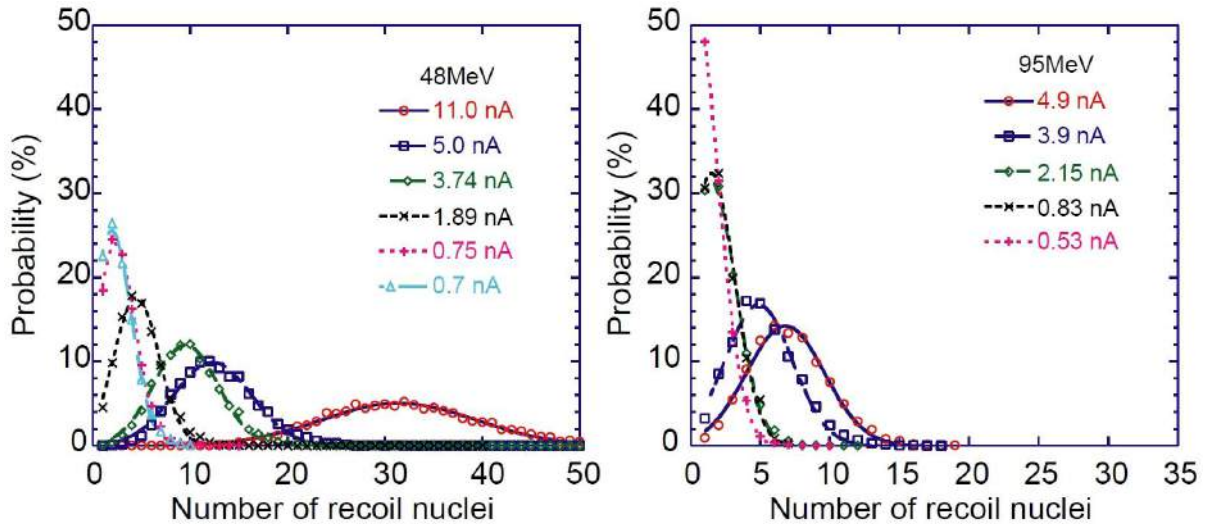


Figure 27: Histogram distribution of the experimentally determined number of recoil nuclei per video frame as a function of proton beam and intensity for perpendicular incidence.

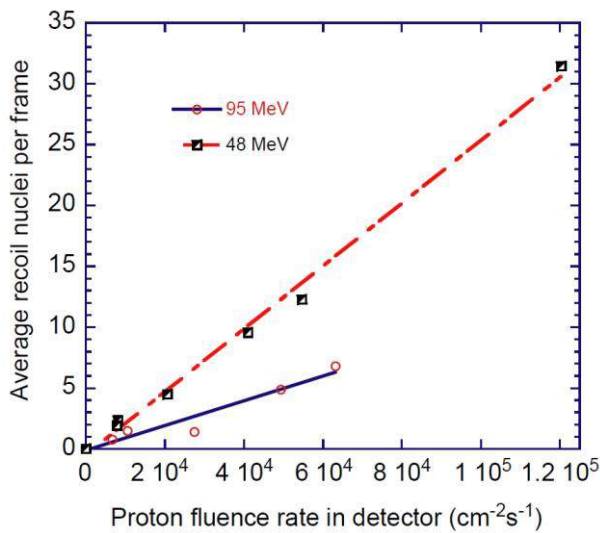


Figure 28: Most-probable number of recoil nuclei per image frame.

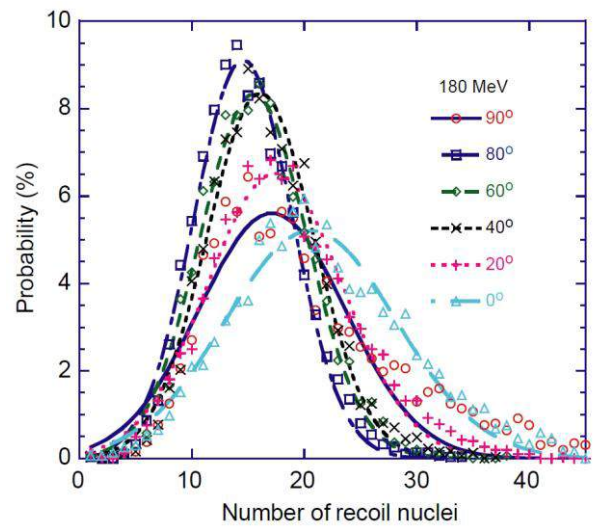


Figure 29: Cumulative histogram distributions of the number of heavy recoils as a function of the incidence angle.

5 From the earth to the space – Satellite Radiation Hardness Tests

5.1 The SMART-1 satellite

The first spacecraft in the series of Small Mission for Research and Technology, SMART-1 (see Figure 30, [43]), was launched on 27th September 2003 by the European Space Agency. This satellite is used to perform in flight tests of some cutting edge technologies for future missions. The approx. 1 m³ spacecraft was placed into a Geostationary Transfer Orbit as a piggyback on an Ariane 5 rocket. It has traveled to an orbit around the Moon driven by its own ion engine in about one year. One of the main technologies tested on SMART-1 is this ion engine using Xe-gas as propellant. Only 15 kg of the total 350

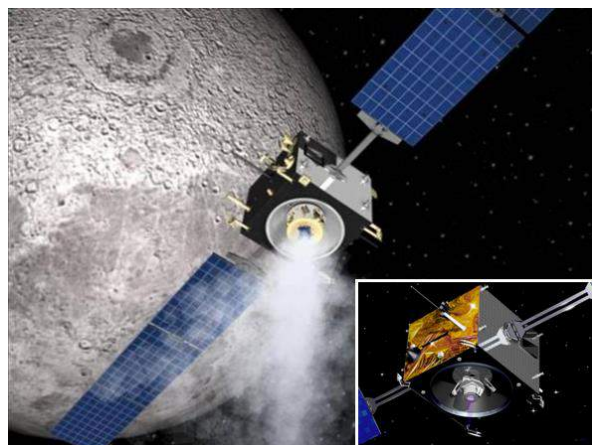


Figure 30: SMART-1 satellite.

kg consist of scientific payload, mainly to examine the composition of the Moon. The aim was to keep the satellite as small as achievable. The prime contractor for SMART-1 was the Swedish Space Corporation (SSC). The characteristics of the ion engine and the low budget requirements put specific demands on the onboard electronics. The ion engine is efficient in using the fuel but its thrust is very low. Therefore it required many revolutions to reach the Moon and, consequently, the time to pass through the radiation belts around the Earth was significant. These belts consist mainly of trapped protons and therefore there was a need of proton irradiation tests to verify the radiation hardness properties of the on board electronic circuits. In addition to the protons of the Van Allen belts the satellite is exposed to solar protons throughout its mission. Smart-1 arrived in lunar orbit on 15 November 2004. After having conducted lunar orbit science operations, its mission ended through lunar impact on 3 September 2006.

5.1.1 Radiation hardness tests

Three different types of memory circuits, that were intended to be used on board of the SMART-1, were radiation hardness tested according to ESA's specification at Atomki. The aim of the study was to test the ability of the selected commercial DRAM memory circuits to meet the SMART-1 requirements and for the SRAM and FIFO memory, to verify the radiation tolerance that was expected from the production process. Since the expected flux of protons during the mission was extreme, one of the main was to test the behavior of the components during proton irradiation. Total dose and heavy ion tests were also performed. Total dose tests on a special coating foil were also performed. This material was intended for helping the thermal balance of the satellite. The memory components passed the tests but the coating foil had to be replaced based on out tests.

5.2 Component tests for PRISMA spacecraft

The PRISMA satellite program containing two satellites (Figure 31), which constitutes a test bed for Guidance, Navigation and Control algorithms and sensors for advanced formation flying and rendezvous operations, ranging from 200 km to 1 m, at 700 km altitude. The project mainly runs by the Swedish Space Corporation.

The designers of the satellite used Commercial Off The Shelf (COTS) approach to be able to use modern components. However, radiation hardness data did not exist for all the selected COTS components. It was necessary to determinate the radiation hardness properties for the selected components and verify their radiation tolerance that is required for the PRISMA mission.

The expected total ionizing dose radiation environment has been calculated with SPENVIS. The electronic components in the System Unit of the satellite will experience 1.0krad on component level after 10 months of mission. This goes up to 2.4krad after 24 months. Considering the required safety factor and the desire to be able to use the parts in future projects with higher radiation levels, it was decided to test every component at least up to a total dose of 20krad. Our aim was to irradiate one sample of each IC type up to a higher dose than the minimum requirement to check the overall progress of damage. The dose rate used in all tests fell in the Standard Rate range (3.6krad-36krad). The total dose rate measurements of the components were done at the Atomki, using a ^{60}Co gamma source. The proton irradiation was performed at the TSL Laboratory. Figure 32 shows one of the oscillator chips of the satellite before the proton irradiation and the experimental setup at TSL. All measurements were carried out according to the ESA requirements. During the test no errors were found [47].

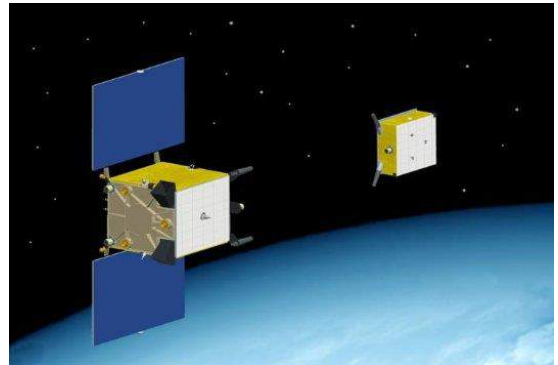


Figure 31: Prisma satellites.

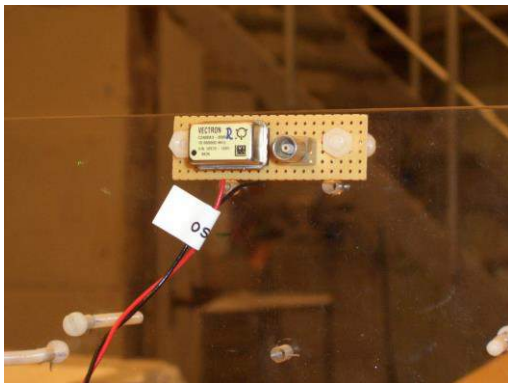


Figure 32: The irradiated oscillator chip on left and the experiment setup at TSL on right (D.Novák and A. Sipos from Atomki and A. Kerek and L-O. Norlin from Royal Institute of Technology, Stockholm, Sweden).

5.3 The Radi-Cal Project

The aim of the project was the development of a new Innovative Dosimeter for Quick and Efficient IMRT Dose Verification. The introduction of intensity-modulated radiotherapy (IMRT) has significantly increased the success rate in the treatment of cancers. IMRT allows to modulate the intensity of the radiation beam and to thus apply higher radiation doses to regions within the tumor while minimizing the dose to the surrounding healthy tissue. Conventional dosimeters which are used to measure the radiation dose only provide single-point measurement. They require considerably more time for dose verification measurements and are therefore less adequate for this new treatment technique.

As a result there is a demand, especially in very small fields, for dosimetry to be done more efficiently and significantly faster using detector arrays with very high resolution. Ordinary ionization chamber or diode arrays cannot always provide adequate solutions.

The key objective of the two-year RadiCal project [48] is to therefore develop a low-cost, high-resolution, high-speed radiation dosimeter that will bring down IMRT set-up times towards that of conventional techniques. To achieve this ambitious goal, the €1.1 million project which is supported by the 7th Framework Programme of the European Commission, brings together expertise from Chemical Vapour Deposition (CVD) diamond growth, radiation measurement and data communication from across six European countries. From Hungary the Electronic Section of the Atomki was involved in the project. Figure 33 shows the neutron irradiation of the diamond sample.

After profound research into suitable CVD diamond material, the project group recently presented the first prototype of the new monolithic 2D CVD diamond-based dosimeter, thus successfully completing a major milestone in this challenging pan-European project. Prototype of the newly developed monolithic 2D CVD diamond-based dosimeter can be seen on Figure 34.



Figure 33: Neutron irradiation of a CVD diamond sample at Atomki (A. Sipos).

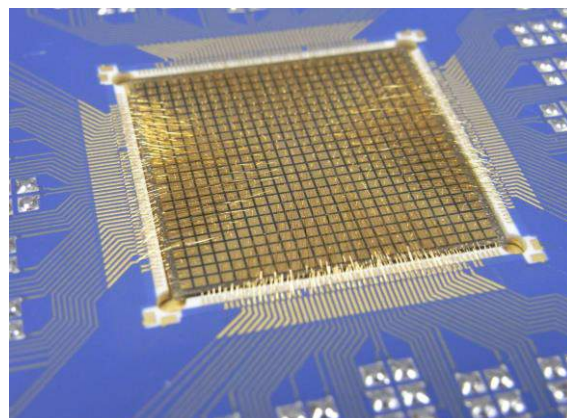


Figure 34: 2D CVD diamond based dosimeter developed by the consortium.

6 Multi Channel Analyzer: Palmtop MCA

Colleagues (J. Gál, G. Hegyesi) developed a small hand held multi channel analyzer in order to support the fast and easy spectrum measurements of nuclear detectors.

The MCA8k-01 Multichannel Analyzer (MCA) is intended to collect spectra coming from nuclear radiation detectors such as scintillation detectors, HPGe, Si, and CZT. It accepts positive going unipolar or bipolar semi-Gaussian shaped pulses with shaping time constants >100 ns. The application of an operational transconductance amplifier in the peak detect and hold circuit and a new dual sliding scale ADC provide excellent differential and integral nonlinearity.

A unique dead-time and pile-up loss correction circuitry assures precise intensity measurement even at very high counting rate. A built in pile-up rejection circuit removes pile-up events from the spectrum. A computer with a USB interface is necessary to operate the MCA8k-01 (Figure 35 shows the MCA unit and Figure 36 the screen shot of the software). No external power or battery is required since it is powered by the USB port. These features and its small dimensions assure the portability of the instrument. The features of the Palmtop MCA [49] are summarized in Table 1.

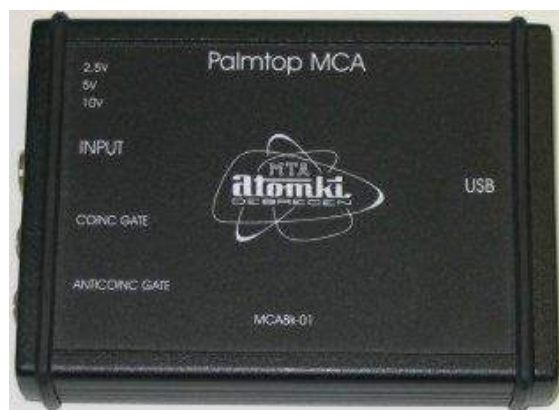


Figure 35: Photo of the Palmtop MCA.

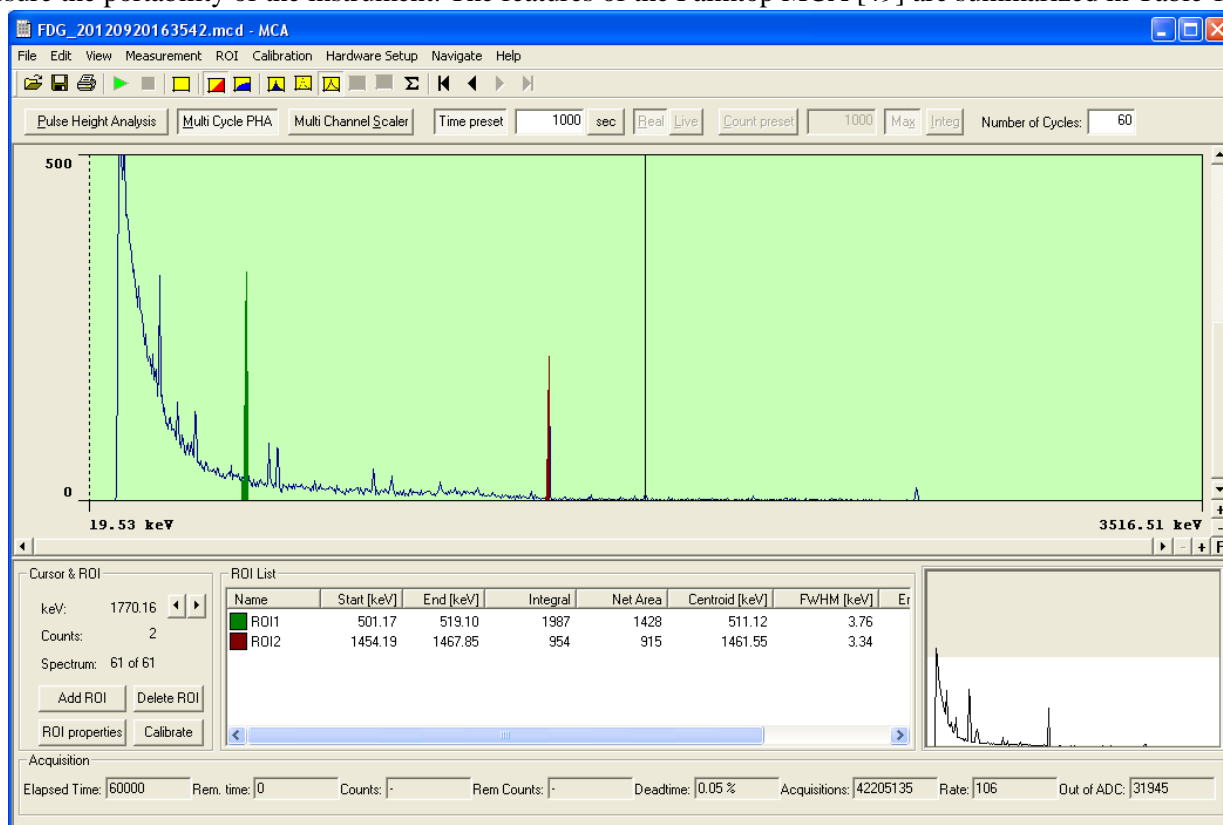


Figure 36: The graphical user interface of the Palmtop MCA.

Table 1: Features of the Palmtop MCA 8k-01

Interface	USB
Data channels	8k (4096)
Conversion time	< 6 μ s
Differential nonlinearity	< 1% (sliding scale linearization)
Integral nonlinearity	< 0.02%
Selectable input ranges	0V to 2.5V, 0V to 5V, 0V to 10V
Peak detection modes	- First peak (nuclear spectroscopy) - Absolute peak after the threshold (aerosol particle detection)
Corrections	- Dead time - Pile-Up
Inputs	Two TTL for coincidences and anticoincidences

7 Positron Emission Tomography and nuclear medical imaging

The PET technique is widely used in human clinical studies and the recent developments of image resolution have made it suitable for small animal research. In-vivo imaging of small laboratory animals is a valuable tool in the development of new drugs. The PET scanners designed for this purpose should exhibit high and possibly uniform spatial resolution and high sensitivity over a field of view, allowing to image mice or other animals of similar size.

7.1 miniPET-I

A small animal PET device, the miniPET-I, was the result of an NKFP project. It has been designed and built at the Section of Electronics. Other consortium members were the PET Center of the University of Debrecen, Mediso Ltd, Budapest, Semmelweis University, University of Kaposvár, Hungarian National Institute of Psychiatry and Neurology, Huniko Ltd, Optilab Ltd., Royal Institute of Technology, Stockholm, Sweden and University of Groningen, The Netherlands.

The miniPET-I consists of 4 detector blocks mounted on a rotatable gantry. The distance between the detector blocks is 93 mm. A photo and drawing of the miniPET-I are shown in Figure 37. Each detector block is built up of an 8x8 array of LSO scintillation crystal needles (see Figure 38), each with a size of 2x2x10 mm³. The crystal array is optically coupled to a Hamamatsu R8520 00 C12 PSPMT. The signal outputs of the PSPMTs are connected to a Nallatech based data acquisition system, using 4 ADCs.

The digital part of the data acquisition hardware is manufactured by Nallatech Ltd. It is a PCI card and can be plugged directly into one of the slots of a PC. The card consists of two modules named BallyRiff and Strathnuey. The Strathnuey module is the main board with PCI and USB interfaces to transfer data directly to the PC. The BallyRiff daughter module is mounted directly on the Strathnuey card. It contains a

XCV1000E-6 Xilinx Virtex II FPGA processor and four 12 bit ADC circuits. The FPGA is programmed in VHDL language.

The two modules, Strathnuey and BallyRiff, contain all the electronic circuits required to digitize four analog signals and send the digitized events to the PC. The block diagram of the Nallatech card is shown in Figure 39. This system also contains an external communication module with Ethernet interface.

The DSP (Digital Signal Processing) technique, the fast free running 50 MHz ADCs and the high data transfer speed of the PCI bus makes it possible to achieve a high count rate in data collection. Each detector module is a network unit, thus the Ethernet based distributed acquisition system [50] collect data from each module. The idea of the network based acquisition is shown in Figure 40. The detector module with the PSPMT, analogue front end electronics and the digital front end is shown in Figure 41.

The miniPET-I system acquires single data and no hardware coincidence is built in. The coincidence sorting is performed off-line directly from the single events in the acquisition computer. The evaluation of events in the line of response (LOR) is based on the topological information and the offline coincidence sorting. The coincidence time window can be varied between 2-20 ns. The final tasks are the image reconstruction using the ML-EM [51] algorithm and the attenuation correction.



Figure 37: The assembly of the miniPET-I small animal PET scanner (J. Molnár).

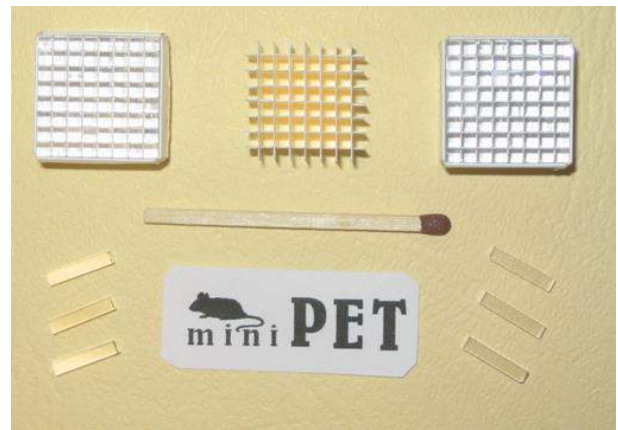


Figure 38: LSO crystal needles ($2 \times 2 \times 10 \text{ mm}^3$), the LuMirror grid for the optical separation between the crystals and the assembled 8×8 crystal matrix.

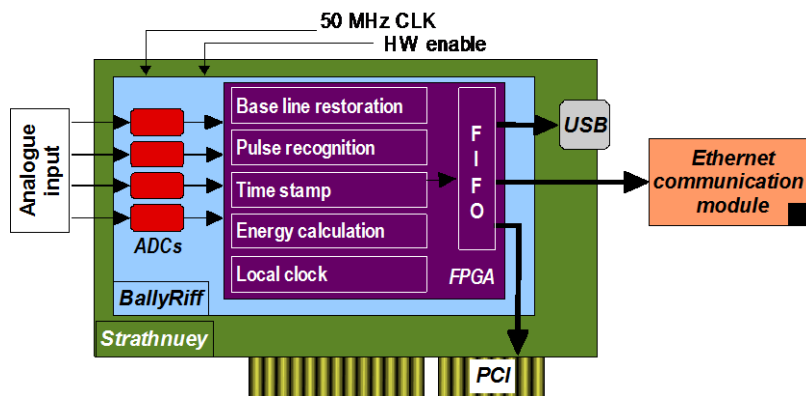


Figure 39: The block schema of the Nallatech DSP based acquisition system.

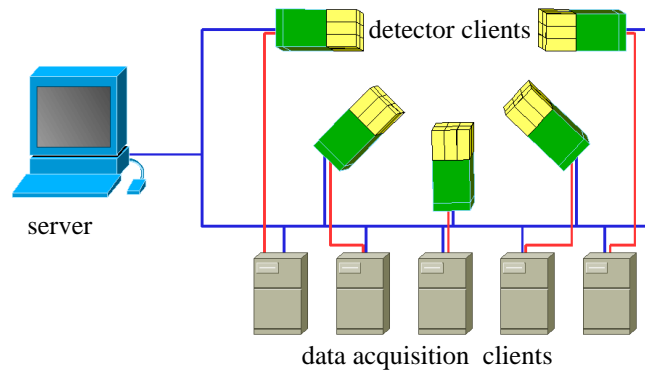


Figure 40: The client server architecture of the network based data acquisition system. The command channel between the clients and server is marked with a blue line and the data channels between the detectors and data acquisition clients are red.

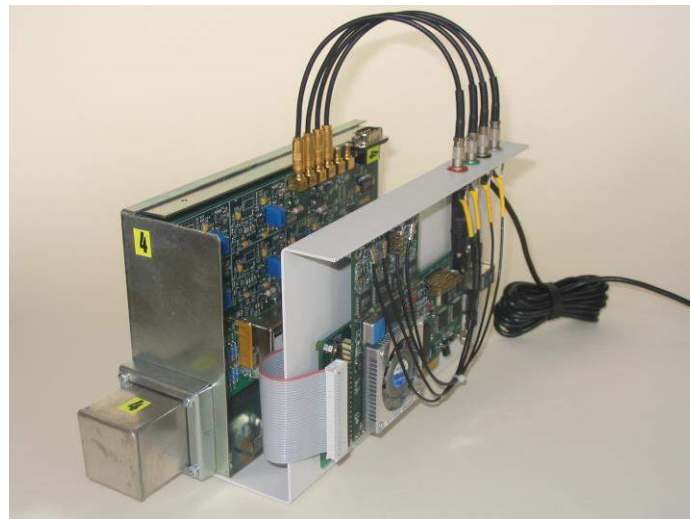


Figure 41: Detector module of the miniPET-I. The PSPMT and the LSO crystal array is placed in the metal box, the analogue front end is in the back and the Nallatech card with the Strathnuey and BallyRiff modules are located in front.

7.1.1 Mice and rat studies

Mice are animals small enough to fit into the limited FOV of the *miniPET-1* scanner. Mice injected with human pancreas tumor were investigated in collaboration with University of Szeged, Hungary. The purpose of the studies was the testing of the effectiveness of a new experimental drug, developed at University of Szeged, and at the same time the presentation of the applicability of the *miniPET-1* scanner.

The mice were injected with ^{18}F FDG and after 30 minutes relaxation time, data were acquired in 8 gantry positions from 0° to 180° with 22.5° angular steps and an 8 min/position acquisition time. A photo from the study and the results are shown in Figure 42. The tumor is located on the back of the mouse. A small tear of FDG was placed close to the tumor to show the orientation in the pictures. High FDG uptake in the tumor was detected.

Rat brain was also studied with the miniPET-I camera. It was injected and evaluated by the PET Center, Debrecen. Axial slices show clear FDG uptake in the brain. Results are shown in Figure 43.

Spatial resolution of the system was measured with the most commonly used isotope, ^{18}F FDG. The phantom, which was a hypodermic needle (inner diameter < 0.5 mm) attached to a syringe, was filled with 11.1 MBq of activity. To minimize scattering the needle was surrounded by air. Images were acquired in the center of the field of view and at distances of 1, 3 and 6 mm from the center in the X direction. The resolution was 1.5 mm, 1.75 mm, 2.1 mm, respectively. The acquisition time was 5 minutes for each angle, with a total of 40 minutes.

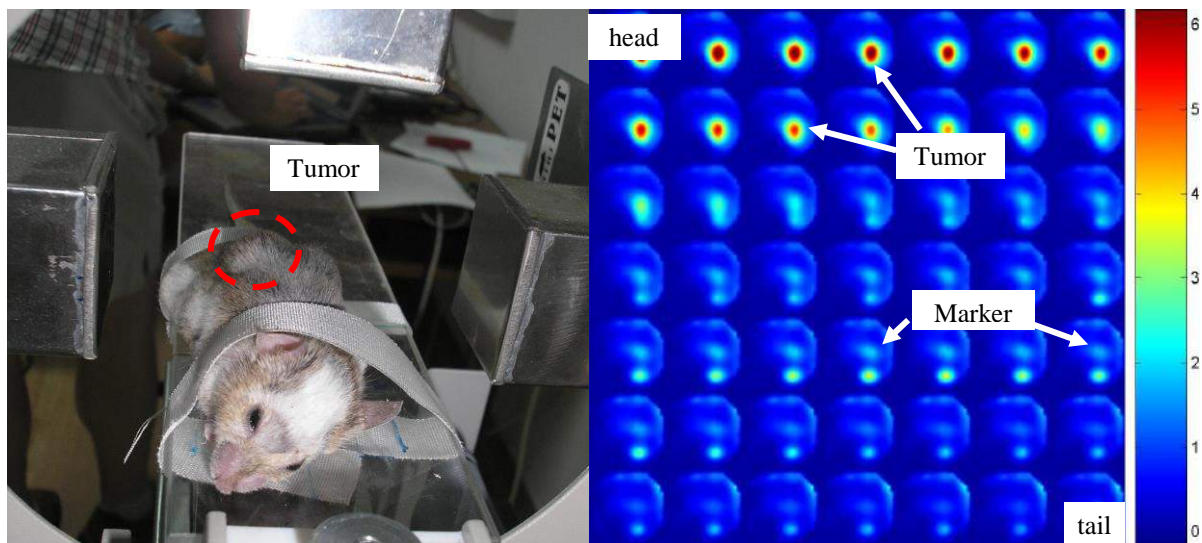


Figure 42: The photo on the left shows a mouse in the miniPET-1 scanner and the corresponding reconstructed axial slices are displayed on the right. Each slice shows the tracer distribution in the 16 mm diameter FOV. The tumor is shown in the top images and the FDG marker is shown in the lower part. The red circle on the photo shows the location of the tumor.

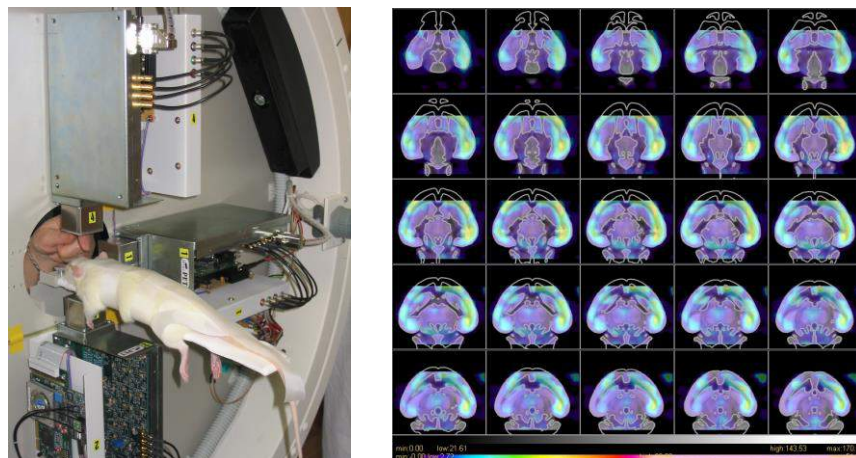


Figure 43: Rat brain study. FDG uptake of the brain is visible on right. The rat brain atlas (grey) shows the anatomical position of the images.

7.2 miniPET-II

The aim of the miniPET-2 project was to develop a full ring small animal PET scanner with an FOV large enough for mice and rat imaging using the acquired knowledge from miniPET-1. The consortium members of the projects were Atomki, University of Debrecen, Mediso Ltd., Technical University, Budapest.

The second generation of our small animal PET scanner, called miniPET-2, consists of 12 individual detector modules.

The port diameter of the scanner is 206 mm and the FOV is 75 mm in diameter and 48 mm deep. A photo of the miniPET-2 scanner is shown in Figure 44.

Each detector module is composed of 1225 pieces of LYSO scintillation crystals (in a 35x35 array configuration, crystal size: $1.27 \times 1.27 \times 12\text{mm}^3$) and one Hamamatsu H9500 PSPMT. The crystal matrix and the PSPMT are shown in Figure 45. The 256 anode outputs of the H9500 PSPMT are connected to the analog front-end with the resistor grid, which determines the four Angler signals. These corner signals are connected to the Memec minimodule based data acquisition system. An external clock generator provides the modules with a 50 MHz central clock signal. The PC processes the incoming list mode data, and performs coincidence sorting energy, windowing and image reconstruction.



Figure 44: Photo of the miniPET-II full ring small animal PET scanner.

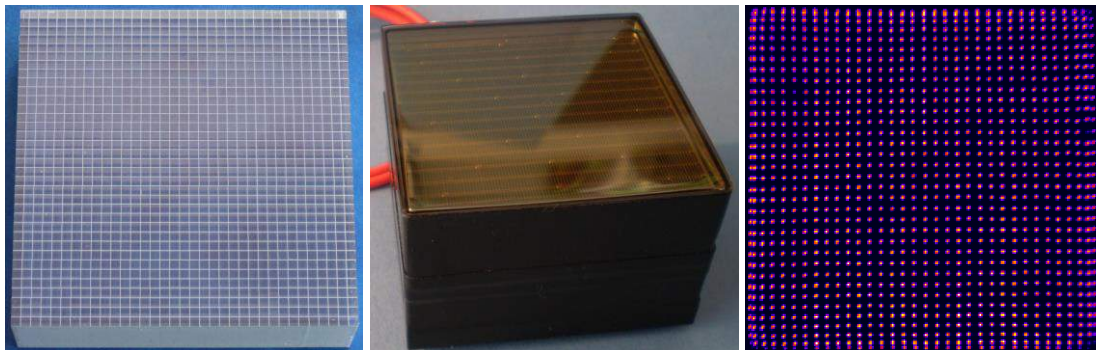


Figure 45: The 35x35 LYSO scintillator array, the H9500 PSPMT and the acquired crystal position map.

The analogue front end, the high voltage module and the DSP card is mounted directly on the PSPMT. Each detector module is individual and the system has the same advantages as the miniPET-I, such as flexible geometrical arrangement, scalability, distributed Ethernet based data acquisition system (Figure 40).

The detector module with the 4 channel ADC card and the Xilinx Virtex4 FPGA (Field Programmable Gate Array) is shown in Figure 46. The block schema (Figure 47) of the detector module system is similar to the Nallatech system (Figure 39), but here the ADC is separated and connected to the FPGA via LVDS (Low-Voltage Differential Signaling).

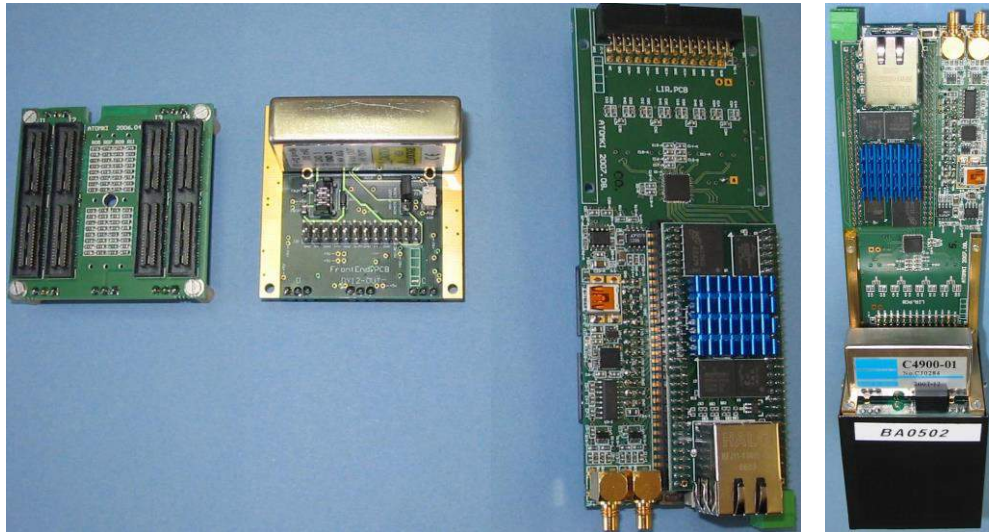


Figure 46: The analogue front end, the high voltage module and the 4 channel DSP card (from left to right) developed at the Section of Electronics. The piggyback module with the FPGA is designed by Avnet Inc. The assembled module is shown in the right. It also contains the LYSO crystal matrix and the PSPMT.

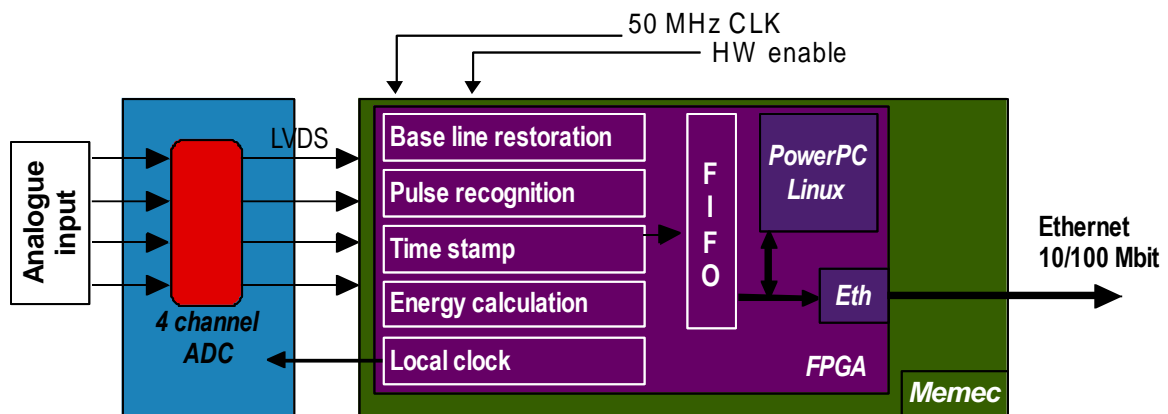


Figure 47: Block schema of the Xilinx Virtex4 FPGA based data acquisition system.

The crystals and the PSPMT were tested during the detector development. The detector module was mounted on a precision table and was moved with the crystal pitch period in order to test the coupling, the sensitivity and intrinsic resolution of the PSPMT. The radiation source was a narrow collimated beam. The setup is shown in Figure 48.

The test of the individual modules was based on acquiring flood field images (with 256x256 matrix size), while list mode events are used in the energy uniformity corrections and coincidence tests. The individual tests, like the determination of the uniformity of the PSPMTs or the quality check of the crystal coupling to the PSPMT, are relatively simple tasks.

The detector module tester software was developed for the assessment of the quality of the modules. It is able to acquire flood field images, present the energy spectrum in a given region, perform energy windowing, store the list mode data, as well as perform crystal identification and crystal based energy correction.

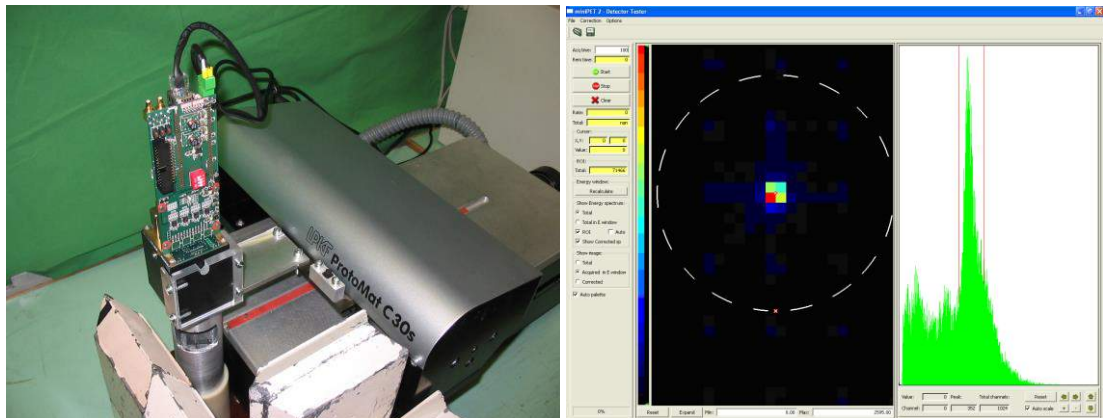


Figure 48: The precision table with the detector module on left and the acquisition program. Response of a single crystal and the energy spectrum is displayed.

To test the central clock generator and the timestamp algorithm, implemented in the FPGA of the Memec module, list mode data were recorded and the coincidence timing spectrum was determined between facing detectors, using a 40 ns wide coincidence window. The measured coincidence timing spectra and the corresponding values are presented in [52]. The mean FWHM of the coincidence timing spectrum of the opposite detector pairs was found to be 2.76 ns.

To illustrate the performance of *miniPET-2* for its intended purpose, results of a cardiac study of a rat is shown in Figure 49. The spatial resolution of the system proved to be the expected 1.4 mm. The images were collected at the Institute of Nuclear Medicine, University of Debrecen (INM).

Besides the phantom and rat measurements the applicability of *miniPET-2* for industrial studies was also investigated in collaboration with colleagues at Atomki. The PET technique is able to follow chemical processes, wherein positron emitter isotopes can be used as a marker. One of these processes is the absorption of gases in catalysts. The goal of this project was to study the applicability of the PET technique and *miniPET-2* scanner for 3D imaging of the structure of a heterogeneous catalyst.

Heterogeneous catalysis is fundamentally important in the petrochemical industry using small metal particles supported on a solid surface. Synthetic materials, made from the catalysts, are used every day in products ranging from fuels to fertilizers or as a catalytic converter in cars.

The imaging of the catalytic reaction helps in understanding the kinetics and surface dynamic of catalysis i.e. the choice of the catalyst type. Different experimental conditions influence the speed of a chemical reaction and yield, as well as adding to the understanding of the reaction's mechanism on surface sites.

Heterogeneous absorber, granulated ascarite, was packed into small glass tubes. The length of the samples was 30 mm. Ascarite is a sodium hydroxide coated non-fibrous silicate which absorbs CO₂ gas. The

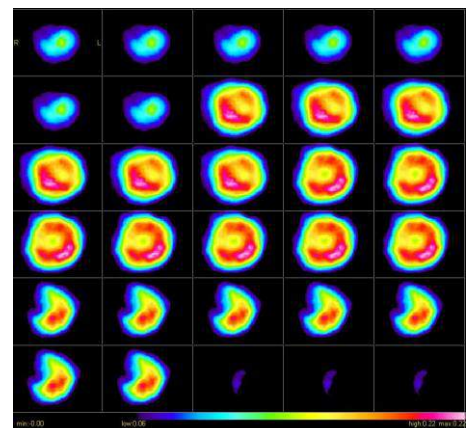


Figure 49: Short axis view of a rat heart (Images were taken by the INM).

two samples, a thin (3 mm inner diameter) and a thick (10 mm inner diameter) glass tube, were tested in the *miniPET-2*.

^{11}C ($T_{1/2}=20.4$ min) labeled CO_2 gas was flowed in the tube. The total absorbed activity was 500 μCi in each sample. After 15 minutes of data acquisition, coincidence events were decay corrected and the images reconstructed using the ML-EM iterative reconstruction algorithm. Photos of the thick and the thin samples and the results of the PET study are shown in Figure 50. The analysis of recorded images shows the binding of the radioactive gas molecules in the catalyst. The activity is higher in the front part of the absorbers, which means most of the gas molecules are absorbed in this region, while the back part remains clean.

The study of heterogeneous catalytic processes requires quantitative information on the concentration of ^{11}C -labeled reactants, intermediates and products as a function of reaction time, catalyst temperatures and position along the catalyst bed. The high resolution *miniPET-2*, as shown above, is a feasible tool for the visualization of these factors.

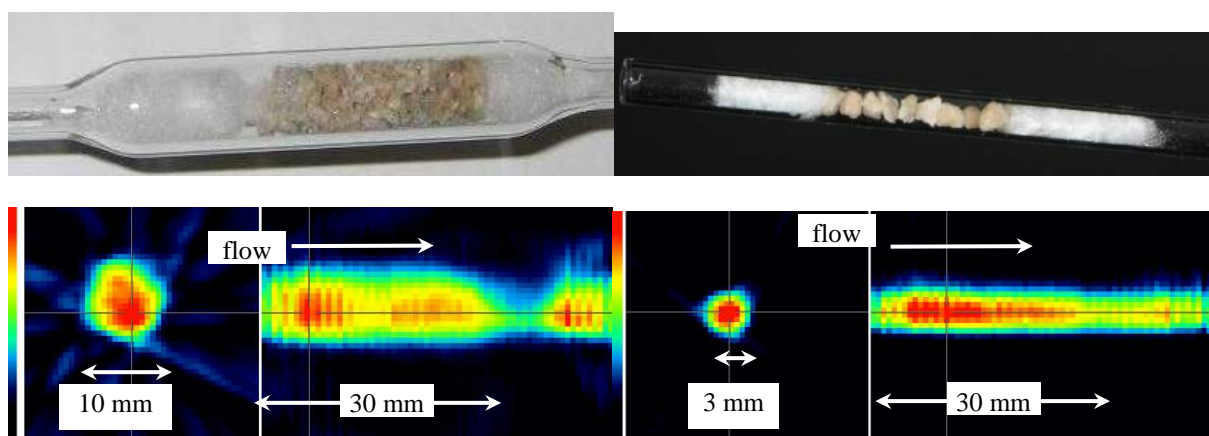


Figure 50: Photos and PET images of the thick (on left) and thin absorbers (on right) respectively. The radioactive ^{11}C -methanol gas was flowed across the tubes. PET reconstruction of the sample is presented in the bottom pictures. The cross-sectional and the longitudinal slices in the position of the cursor are shown on the left and right, respectively.

7.3 *miniPET-III*

The *miniPET-III* small animal PET scanner project is has been carrying out in the ENIAC-CSI (Central Nervous System Imaging) EU project. The unavoidable process of aging of the European population demands for a comprehensive technology support to the diagnostic and therapy of central nervous system diseases. These serious illnesses call for the most expensive diagnosis/therapy procedures in the western countries. Furthermore, central nervous system's diseases are among those with the fastest growing impact on society. They include degenerative brain diseases ranging from Alzheimer and Parkinson to circulatory problems including strokes. The project will pursue the simultaneous capturing/extraction of data produced by new generation's imaging devices, in order to provide the best correlated information to the physician through an innovative and intelligent merging both in timing (i.e. EEG) and spatial resolution (i.e. PET).

This combined and synergistic approach can only be made possible through advances in various technology fields that include sensors, integrated equipments and systems for data fusion and novel data

processing platforms that support Teraflop-range computing capability right at the doctor’s desktop. As a whole the project will anticipate new perspectives to improve patient’s support and treatment for central nervous system’s diseases.

The members of the consortium are ST Microelectronics, Italy; Philips Ltd., The Netherlands; Austria Microsystems A. G.; G-TECH GmbH., Austria; MAT-TECH b.v., The Netherlands; University of Bologna, Italy; Politecnico di Torino, Italy; IMEC-NL, The Netherlands; Austrian Institute of Technology, Kempenhaeghe Clinics, The Netherlands; University of Debrecen, University of Pannonia and Atomki.

The Section of Electronics is responsible for the small animal PET development. The new scanner is based on technologies developed for miniPET-II, e.g. DSP technology, scalable individual detector modules, network based data acquisition system. The design of the detector modules is similar to the miniPET-II; however the bulky H9500 PSPMTs were replaced with silicon photomultipliers (SiPM). SiPMs are insensitive to the high magnetic field thus the development of a PET-MRI insert or a PET-MRI scanner is feasible.

Since SiPMs are one of the latest state of the art photon detecting devices, the development also includes the characterization of the newly developed sensors. SiPM tile, used in miniPET-III, is shown in Figure 51. The tile contains 9x9 SiPM quad pixel sensors, i.e. 324 individual channels. The disadvantage of the SiPM, compared to conventional PMTs, is its high dark current, thus conventional Anger based readout method does not provide sufficient intrinsic spatial resolution.

Digitizing the 324 SiPM channels is a straightforward way to obtain proper crystal position maps. However handling hundreds of analogue input channels and the required DSP resources cause large racks of data acquisition electronics. Therefore a more advanced and coded readout electronics was designed.

The detector module contains the same 35x35 LYSO crystals as the miniPET-II, the new SiPM sensors and the required front end electronics, while the FPGA based 4 channel ADC card, used in miniPET-II also remains the same. The newly designed front-end electronics are shown in Figure 52 and Figure 53.

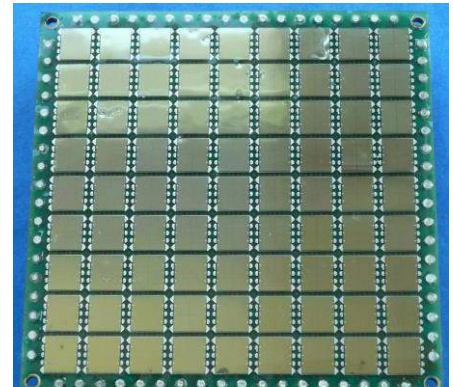


Figure 51: SiPM tile of the miniPET-III detector module, manufactured by ST Microelectronics.

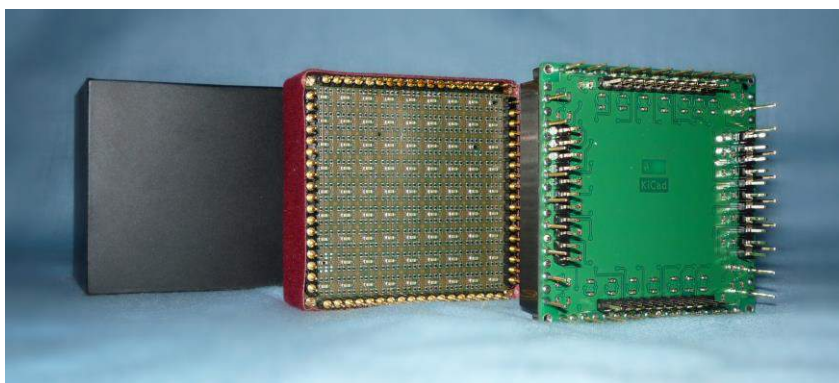


Figure 52: The light shielding the back of the SiPM tile (with the passive front-end, designed by G. Hegyesi and J. Gál) and the analogue front end module from left to right.

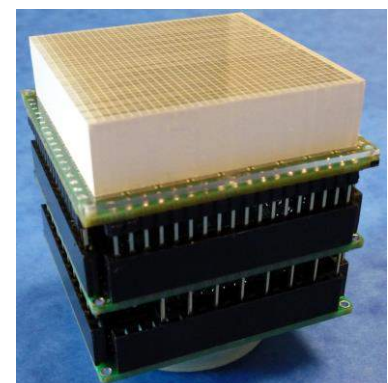


Figure 53: The LYSO crystal matrix, the SiPM tile and the front-end before the final assembly.

Good homogeneity (and its correction), energy response and intrinsic spatial resolution have an important role in high resolution imaging thus optical and nuclear characterization of the tile was performed in order to determine the differences between the SiPM pixels in each quad sensor on the tile.

The SiPM with 1 mm light guide was optically characterized, because this tile has the best crystal position resolution. In order to achieve the best result, a PicoQuant PDL-200B type pulse diode laser was used as a light source. The laser emits 420 nm light and this light was detected by the SiPM tile. Since the diameter of the laser beam (126 μm) is much smaller than the active area of a SiPM pixel (1.95x2.2 mm^2) a light guide is needed between the SiPM tile and the beam. The 35x35 LYSO crystal array was used as a light guide. The laser was positioned over each crystal during the measurement and data were taken in each position.

The computer controllable 3D precision motorized stage manufactured by Zaber Inc. was used for moving the head of the laser source. The whole setup, the motorized stages, the SiPM tile, the analogue front end electronics were placed in a light shielding black box. The measurement setup is shown in Figure 54.

Dedicated software was also developed for the automatized measurement of the SiPM tiles.

In order to perform the nuclear characterization of the SiPM tile, pixelated LYSO scintillation crystal array (crystal needle dimension: 1.27x1.27x10 mm^3 in a 35x35 arrangement) optical grease between the crystal matrix and the SiPM tiles, ^{22}Na positron emitter radiation source and CAEN DT5740 32 channels digitizer were used. External PL303 QMD quad mode dual power supplies were also used for providing the required voltage and current for the SiPM tiles. The measurement setup is shown in Figure 55. The ^{22}Na source was placed 50 cm far from the crystal front face to ensure homogenous irradiation. Analogue pulses were recorded using the CAEN DT5740 digitizer and post processed off line in the PC. Anger signals were calculated from the analogue pulses, using the DSP technique. The crystal position map was calculated by the so called fully digital gamma camera processing method. This method allows only those pulses which are above a certain level (above the dark noise level from the SiPM pixels) around the excited scintillation crystal.

The results of the optical and nuclear characterizations showed that a 1mm light guide between the SiPM tile and the LYSO crystal array produces good spatial resolution and sensitivity over the dead zones between the SiPM quad sensors. Sensitivity correction of the tile's SiPM quad pixel sensors is necessary for proper data acquisition. The SiPM tiles using 1 mm light guide are a feasible solution for small animal PET imaging. The crystal position and sensitivity maps are shown in Figure 56 and Figure 57, respectively. Most of the SiPM pixels have the same sensitivity; however the sensitivity is smaller on the edges, which correlates to the nuclear characterization. Furthermore, the SiPM tile has superior homogeneity than the conventional PSPMTs, because the most of the pixels have ~50% sensitivity difference, while PSPMTs often have more than 1:5 sensitivity ratio in different positions.

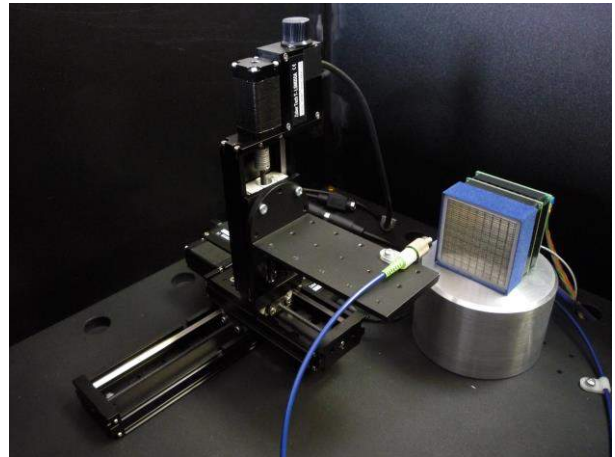


Figure 54: The setup of the optical characterization of the SiPM tile. The 3D position stages, the tile with the LYSO crystal matrix and the laser were placed in a black

light shielding black box. The measurement setup is shown in Figure 54.

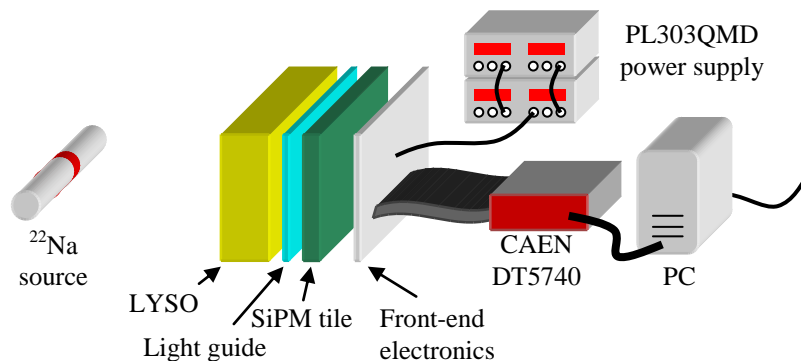


Figure 55: Schematic view of the nuclear characterization setup.

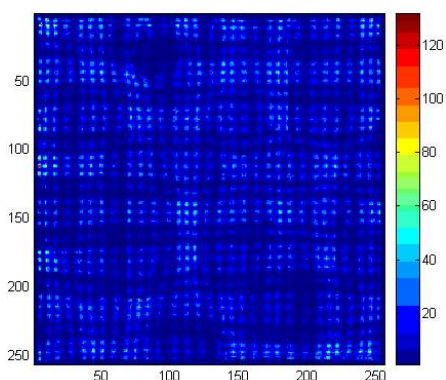


Figure 56: Crystal position map of the SiPM with 1 mm light guide.

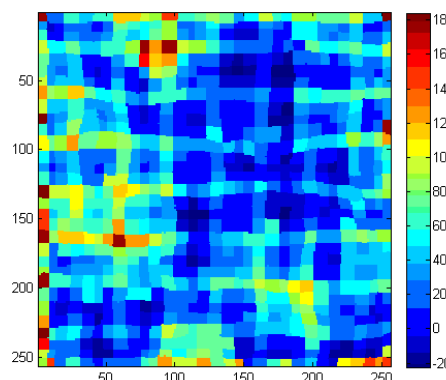


Figure 57: Relative sensitivity map of the tile, it is normalized to the highest sensitivity (100%).

Further developments are the construction of the whole ring using the new detector modules (in the same geometrical arrangement as exists in miniPET-II), carry out performance measurements according to the NEMA-NU-4 standard, and compare the new scanner to the miniPET-II.

7.4 Cardiotom

The Cardiotom system is a mobile gamma camera for 3D imaging. It is based on ectomography, which is an alternative method to SPECT. Ectomography, has been developed and implemented in the Cardiotom systems at the Division of Medical Engineering, Karolinska Institute. The system has been designed to provide a tomographic unit that can be used bedside, when it is not possible to move a patient to the section equipped with a standard SPECT system. Indeed, the Cardiotom suits the emergency environment thanks to its relatively small size and simplicity compared to SPECT systems. The device is designed primarily for early diagnosis of myocardial and cerebral infarction studies in the emergency room.

The Cardiotom uses the limited view-angle technique of ectomography and a rotating slant hole collimator to perform tomographic imaging (see Figure 58). In SPECT, the direction of the collimator holes is perpendicular to the axis of rotation, whereas in ectomography, this angle is less than 90 degree. Since only the collimator rotates, the camera can be positioned very close to the patient (approximately 10 mm).

In limited view angle tomography the volume imaged is not covered by all projections. This results in missing data and an incomplete reconstruction of the volume imaged. The volume that can be reconstructed from tomographic projections is conical as shown in Figure 58 with green.

The Cardiotom systems, Mark 2 and Mark 3, have been introduced earlier, but performance was lacking in the areas of data acquisition speed and image reconstruction capabilities. Colleagues at the Section of Electronics replaced the Cardiotom hardware with high performance fast electronics and developed new dedicated software for data acquisition and image reconstruction [53]. The original mechanics with the rotating collimator, the camera head with the NaI crystal, the PMTs and the analog resistor grid are the only parts of the old systems that remained unchanged. The new Mark 4 (Figure 59) was developed by Inter Medical GmbH, Germany, but the developed reconstruction software (screen shot of the software is shown in Figure 60) was installed on the new camera.

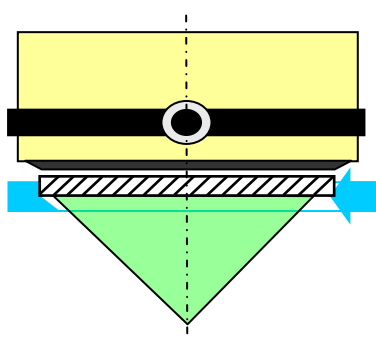


Figure 58: Limited view angle tomography using rotating collimator. Cardiotom uses a 3 segment collimator in order to increase the sensitivity and decrease the acquisition time.



Figure 59: Photo of the Mark 4.

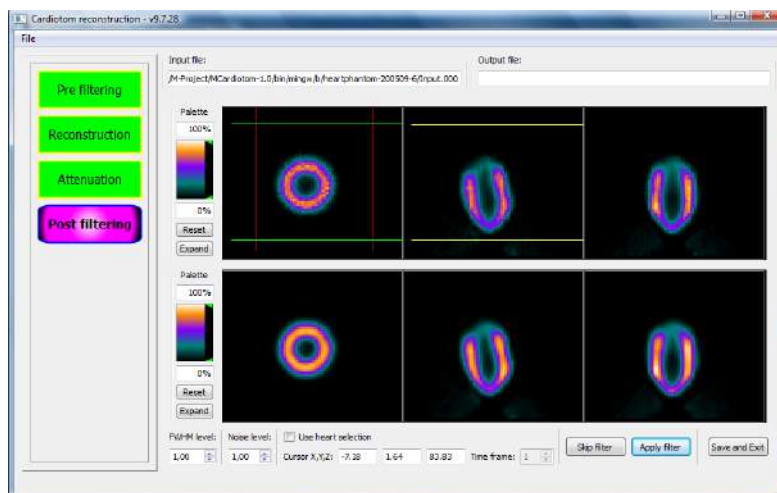


Figure 60: Screen shot of the Cardiotom image reconstruction program. Three orthogonal slices of a heart phantom is displayed after the reconstruction process.

8 Environment monitoring systems

Our colleague, J. Szádai, together with Isotopetech Zrt. and Hertelendi Laboratory of Environmental Studies has been playing an active role in the development of environmental monitoring and sampling systems, such as carbon, air and water samplers and dose rate meters for the nuclear waste storage located at Bataapati, for Radioactive Waste Reprocessing Treatment and Disposal Facility, Puspokszilagyi and for the nuclear power plant in Paks. Figure 61 show the developed and installed systems on the sites.



Figure 61: Air monitoring station installed in Bataapati and water monitoring station in Puspokszilagyi.

9 Education

To get an insight into the different imaging modalities, lectures and laboratory exercises are an important part of a university course in medical imaging and are necessary for understanding the principles of complex imaging systems.

Colleagues at the section take an active part in education, such as Nuclear Imaging 1-2 course at the University of Debrecen and supervise master student's diploma work as well as design and develop laboratory equipment for undergraduate courses.

9.1 Nuclear Imaging course

The course covers the nuclear medical imaging field, especially basic radiation physics, photon interaction with matter, photo detectors, signal processing methods and the working principles of different medical imaging and therapy devices, such as X-ray and Computed Tomographs, Positron Emission Tomographs, Gamma cameras, SPECT systems, MRI, radiotherapy systems and Gamma knife. Besides the lectures, laboratory exercises help the students to get acquainted with the state of the art imaging devices. Photos from the lectures and laboratory exercise are shown in Figure 62 and Figure 63, respectively.



Figure 62: Nuclear imaging lecture in Atomki's lecture hall.



Figure 63: PET laboratory exercise.

9.2 Cosmic ray detector

A cosmic muon ray detector (originally used for laboratory exercises at the Institute of Experimental Physics, University of Debrecen, Faculty of Science and Technology) was refurbished by the Section. New signal processing electronics (see Figure 64) was designed and developed and the three GM tubes were also refilled and recalibrated. The analogue output signals were acquired and processed by the sound card of a computer. PC software was also developed for demonstrating the cosmic rays and the detected muons. The system was presented on physics day at the Institute (Figure 65), when pupils visit Atomki. The system today serves the education at the Institute of Experimental Physics.

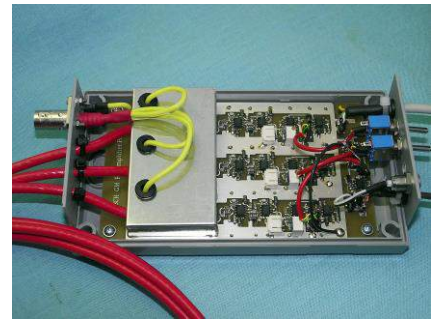


Figure 64: The new coincidence electronics of the detectors.



Figure 65: The muon detector system and the demonstration software in physics day.

9.3 KTH-miniPET and KTH-helicalCT

Demonstrators for the medical imaging course at Royal Institute of Technology, Stockholm, Sweden, have been designed. The data acquisition system and the required acquisition, reconstruction and presentation are based on the technologies developed for the miniPET-II small animal PET system. The devices [54] demonstrate the principles of PET and CT imaging modalities for undergraduate students as laboratory exercise. In order to make the demonstrators more attractive, the phantoms are Barbie dolls.

The KTH-miniPET (Figure 66) contains two opposite mounted detector blocks (8x8 LSO crystals, similar to miniPET-I) that do not surround the whole field of view. However if we rotate the doll between the two stationary detector modules the whole field of view (FOV) can be covered. The scintillator light is detected by a PSPMT connected to FPGA based digital data acquisition systems. Memec minimodule based data acquisition electronics (the same as implemented in the miniPET-II) and data acquisition software, were installed to serve the modularity and transparency of the systems. Two ^{22}Na positron emitter point sources are placed into the head, which simulates tumors in the FOV. Figure 66 also shows the reconstructed radioactivity distribution.

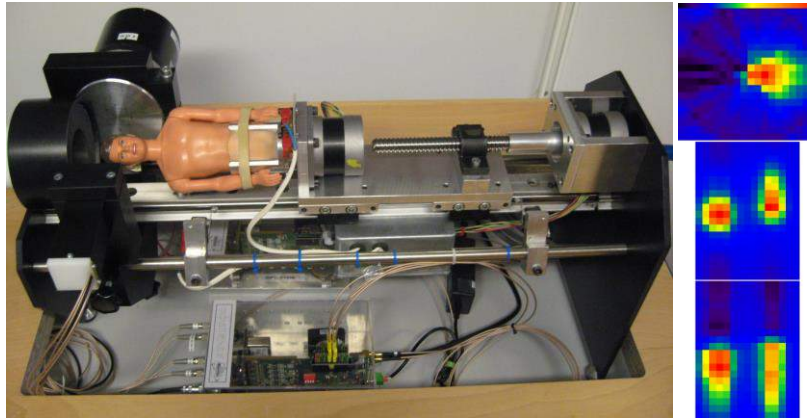


Figure 66: Photo of the KTH-miniPET on left. The two stationary PSPMTs are mounted close to the head of the doll. Reconstructed orthogonal slices of two ^{22}Na point sources (mounted in doll's head) are visible on right. Axial, coronal and sagittal slices are displayed top to bottom. The star shape pattern of the FBP is visible in the left picture.

The aim of the KTH-helicalCT was to demonstrate the working principles of computed tomography in general and especially the design of a helical CT. The X-ray source is the USB controlled mini-X X-ray tube by Amptek, Inc. with a silver target and with a focal spot size of ~ 2 mm. The detector is a Hamamatsu photodiode array (type S8865-256G). The data acquisition board is a mini2440 computer with ADC and PWM support on board and with embedded Linux OS. The driver for the photodiode array and the control software of the detector front-end as well as the data acquisition program was carried out at the Section of Electronics. The photo of the KTH-helicalCT and a reconstructed slice from the doll's head are shown in Figure 67.

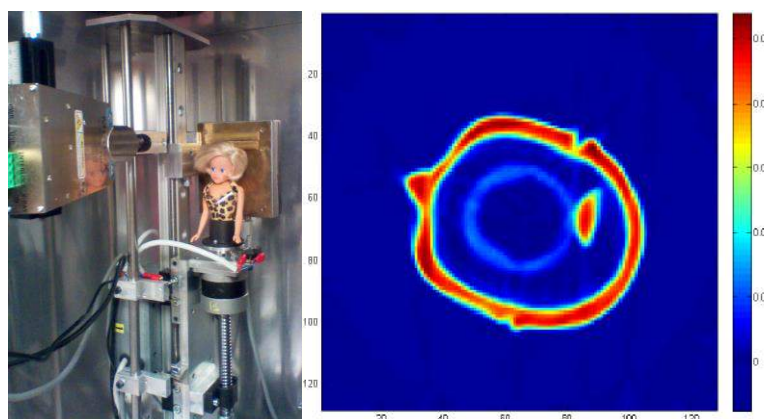


Figure 67: Photo of the KTH-helical CT and the filtered back projection of a cross sectional slice of the doll's head.

Acknowledgements

- Radical: This work was supported by the FP7-SME-2008-1 "RADI-CAL" under contract No: 231753.
 miniPET-I: This work was supported by the National Fund for Research and Development tender under contract No. NKFP-1A/0010/2002.
 miniPET-II: This work was supported by the National Fund for Research and Development tender under contract No. NKFP-A1-2006-0017.
 miniPET-III: This work was supported by the ENIAC Joint Undertaking under contract No. #120209.

We express our gratitude to the former members and heads of the Section of Electronics and to all colleagues at Atomki, who helped to establish and to keep the R&D&I rolling and provide us interesting tasks and problems.

References

- [1] Lakatos T., et al.: Nuclear Instruments and Methods 123 (1975)579
- [2] Gál J.: Nuclear Instruments and Methods 133 (1976)341
- [3] Bibok Gy., et al.: Atomki Közlemények 22 (1980)365
- [4] Gál J., et al.: Nuclear Instruments and Methods 163 (1979)535
- [5] Gál J., et al.: Nuclear Instruments and Methods 171 (1980)401
- [6] Bibok Gy., et al.: Atomki Közlemények 19 (1977)365
- [7] Gál J., et al.: Atomki Közlemények 19 (1977)373
- [8] Gál J., et al.: Atomki Közlemények 24 (1982)95
- [9] Gál J., et al.: Nuclear Instruments and Methods in Physics Research 206 (1983)465
- [10] Berecz I., et al.: Vacuum 33 (1983)69
- [11] Berecz I., et al.: Vacuum 37 (1987)85
- [12] Langer G. A., et al: Periodica Polytechnica, Chemical Engineering 34 (1990)1-3:251-254
- [13] Bohátka S., et al.: Vacuum 44 (1993)669
- [14] K. Mahesh, D.R. Vij: Techniques of Radiation Dosimetry, Wiley Eastern Limited, ISBN 0 85226 578 6 1985
- [15] J Molnár et. al: 12 Int. Conf. on SSNTDs 4-10 Sept 1983, Acapulco, Mexico

- [16] Gál J., et al.: Nuclear Instruments and Methods in Physics Research Section A 366 (1995)145
- [17] Gál J., et al.: Nuclear Instruments and Methods in Physics Research Section A 366 (1995)120
- [18] Gál J., et al.: Nuclear Instruments and Methods in Physics Research Section A 399 (1997)407
- [19] Gál J., et al.: Nuclear Instruments and Methods in Physics Research Section A 397 (1997)399
- [20] Gál J., et al.: Nuclear Instruments and Methods in Physics Research Section A 516 (2004)502-
- [21] B. Cederwall, et al.: Nature 469 (2011)7328:68-
- [22] Papka P., et al.:Physical Review C Nuclear Physics 81 (2010)5:4308(9)
- [23] Petri M. et al.: NIM-A 607 (2009)412-420
- [24] Páll G. et. al: Atomki Annual Report 1995 (1996)92-
- [25] K. Tökési, et al.: Journal of Physics B 38 (2005) 401.
- [26] K. Tökési, et al.: Hyperfine Interact 194 (2009) 45.
- [27] H. Knudsen, et al.: Phys. Rev. Lett 101 (2008) 043201-1 - 043201-4.
- [28] H. Knudsen, et al.: Nucl. Instr. and Meth. Phys. Res. B267 (2009) 244–247.
- [29] H. Knudsen, et al.: Phys. Rev. Lett. 105 (2010) 213201.
- [30] T. Muller et al.:Nuclear Instruments and Methods in Physics Research Section A 408 (1998)119-
- [31] P. Zotto, et al.: Nuclear Instruments and Methods in Physics Research Section A: 408 (1998)274
- [32] V. Hagopian et al.: Nuclear Physics B Proceedings Supplement 61 (1998)47-
- [33] M. de Palma M et al.: Nuclear Physics B Proceedings Supplement 61 (1998)32-
- [34] J. P. Ernenwein et al.: Nuclear Physics B Proceedings Supplement 78 (1999)186-
- [35] F. Martin et al.: Nuclear Physics B Proceedings Supplement 78 (1999)192-
- [36] M. C. Fouz M. C. et al.: Nuclear Instruments and Methods in Physics Research Section A 446 (2000)366-
- [37] A. A. Savin et al.: European Physical Journal Web of Conferences 28 (2012)9004(3)
- [38] S. Chatrchyan et al.: Journal of High Energy Physics 2012 (2012)4:36(36)
- [39] S. Chatrchyan et al.: Physics Letters B 716 (2012)1:30-61
- [40] A. Sipos, et al.:Nuclear Instruments and Methods in Physics Research Section A 509 (2003) 328-
- [41] J. Végh, et al.: Nuclear Instruments and Methods in Physics Research A 525 (2004) 229–
- [42] A. Sanchez-Crespo, et al.: Nuclear Instruments and Methods in Physics Research A 525 (2004) 289–
- [43] SMART-1 satellite homepage: <http://sci.esa.int/science-e/www/area/index.cfm?fareaid=10>
- [44] Simon A., et al.: Nuclear Instruments and Methods in Physics Research Section A 546 (2005) 33-
- [45] Imrek J., et al. : IEEE Nuclear Science Symposium Conference Record, 2009. Proceedings (2010) 2434-
- [46] Valastyán I., et al.:IEEE Nuclear Science Symposium Conference Record. Proceedings (2009) 3846-
- [47] D. Novák, et al.: 9th European Conference on Radiation and Its Effects on Components and Systems, 2007. (10-14 September 2007), Deauville, Poster presentation
- [48] <http://radical.pera.com/>
- [49] http://www.atomki.hu/atomki/Electr/palmtopmca_en.html
- [50] Gy. Hegyesi, et al.: IEEE Trans. Nucl. Sci., Vol 53. No. 4 (2006) 2112-
- [51] I. Valastyán, et al.: Nucl. Instr. and Meth. A 571 (2007) 219-
- [52] I. Valastyán, et al.: IEEE Nuclear Science Symposium and Medical Imaging Conference Record (2008) 3846
- [53] I. Valastyán, et al.: Nuclear Instruments and Methods A580 (2007) 1097
- [54] I. Valastyán, et al.: Nuclear Instruments and Methods A Supplement 633 (2011)1:S300-

1.1 Schrödinger equations with indefinite effective mass

G. Lévai, M. Znojil^{a)}

The interaction of a particle with the medium around it is usually described by some potential function $V(x)$. It is also often necessary to take into consideration the effects of this medium using a position-dependent effective mass. A wide variety of effective masses $m(x)$ have been used in methodological studies and applications mainly restricted to one-dimensional problems, including mass functions that vanish at certain locations or those reaching infinity in some limit. The common feature of these $m(x)$ functions was that they were all non-negative.

In our recent study on the \mathcal{PT} -symmetric version of the Coulomb potential we found that an asymptotically negative effective mass is necessary for the stability of the energy spectrum. This result inspired us to investigate under which conditions can one apply mass functions that are negative at least in some domains of the coordinate space [1]. For the sake of simplicity we considered the infinitely deep square-well potential in one dimension

$$V(x) = \begin{cases} +\infty, & |x| > L > 1, \\ 0, & |x| < L \end{cases} \quad (1)$$

with a piece-wise constant effective mass

$$m(x) = \begin{cases} 1, & |x| \in (1, L), \\ m_0, & |x| < 1. \end{cases} \quad (2)$$

After prescribing the appropriate continuity requirements at the boundaries, the energy eigenvalues of this system can be obtained from the roots of a transcendental equation on k . It turned out that for negative values of m_0 the energy spectrum becomes unbounded from below. This is not surprising considering that with a negative mass the kinetic energy also becomes negative.

In order to stabilize the spectrum we considered energy-dependent effective mass functions that kept the mass finite even for increasing values of the energy. Our first choice was

$$m(x, E) = \begin{cases} 1, & |x| \in (1, L), \\ -\tanh(E), & |x| < 1. \end{cases}$$

The energy eigenvalues of this problem are obtained from another transcendental equation

$$\sqrt{\tanh k^2} \tanh \lambda(k) \tan k(L-1) = -1,$$

where $\lambda(k) = k\sqrt{\tanh k^2}$. With this choice the energy spectrum was found to be bounded from below.

Qualitatively similar results were found for our second example, where we considered a threshold energy E_{thr} by

$$m(x, E) = \begin{cases} 1, & |x| \in (1, L), \\ -1, & E \geq E_{thr} \\ +1, & E < E_{thr} \end{cases}, \quad |x| < 1.$$

In our final example we introduced another parameter in the original toy model (1) replacing Eq. (2) with

$$m(x) = \begin{cases} 1, & |x| \in (a, L), \\ -1/b^2, & |x| < a \end{cases}$$

such that $a > 0$ and $b = b(E) > 0$. This led to the rescaled secular equation

$$\tan \frac{\kappa a}{b} \times \tanh \kappa(L-a) = b. \quad (3)$$

This setting allowed the investigation of the special limit in which the $m(x)$ turns into the Dirac delta function. We found that in this limit only a single bound state remains in the energy spectrum.

In conclusion, our study revealed that indefinite effective mass functions can lead to regular energy spectrum if one introduces also energy dependence such that $m(x, E)$ takes on negative value only in a limited coordinate and energy domain.

^{a)} Nuclear Research Institute of the Academy of Sciences of the Czech Republic, Řež, Czech Republic

[1] M. Znojil, G. Lévai, Phys. Lett. A **376** (2012) 3000.

2.1 Smoothing problems in nuclear and particle physics

I. Nándori, P. Salamon, T. Vertse

Mathematics is the universal language of all natural sciences, in particular, of theoretical physics. Thus, the same mathematical problem, e.g. the smoothing can appear in various fields, namely in Nuclear and Particle physics. A new type of smoothing of the nuclear level density was introduced in Ref. [1]. The weight function of the new smoothing function was also used in a new phenomenological nuclear potential the so called Salamon–Vertse (SV) potential [2], which becomes zero smoothly at finite distance. The use of the same weight function of the smoothing of the level density seems to be a good idea in particle physics too.

At the heart of every quantum field theory there is the need for renormalization. This procedure is required to obtain measurable physical quantities. Renormalization is usually performed perturbatively, however, in some cases a non-perturbative treatment is a necessity which can be realized by e.g. the functional renormalization group (RG) method by using approximations. The approximated RG flow depends on the choice of the so called regulator function, i.e. on the renormalization scheme and physical results could become scheme-dependent. Therefore, a general issue is the comparison of results obtained by various RG schemes (i.e. various types of regulator functions). In order to optimize the scheme-dependence an optimization procedure has already been worked out and in the leading order of the derivative expansion, an explicit form for the optimized regulator was provided,

$$r_{\text{opt}}(y) = a \left(\frac{1}{y^b} - 1 \right) \theta(1 - y) \quad (4)$$

where $\theta(y)$ is the Heaviside step function. It

was also shown that this simple form of the optimized regulator does not support a derivative expansion beyond second order because it is a function of class C^0 with compact support thus it is a continuous function and it has a finite range but it is not differentiable. It was argued the general criterion for optimization has to meet the necessary condition of differentiability to the given order. In Ref. [3] we give an example for a regulator function of class C^∞ (it has derivatives of all orders i.e. it is a smooth function) with compact support. A specific form of the compactly supported smooth (CSS) regulator reads as,

$$r_{\text{css}}(y) = \frac{\exp[cy_0^b/(1 - y_0^b)] - 1}{\exp[cy^b/(1 - y^b)] - 1} \theta(1 - y) \quad (5)$$

which becomes exactly zero at $y = 1$ and its derivatives are continuous everywhere. It was also shown [3] that in an appropriate limit the CSS regulator recovers the optimized one,

$$\lim_{c \rightarrow 0} r_{\text{css}}(y) = \frac{y_0^b}{1 - y_0^b} \left(\frac{1}{y^b} - 1 \right) \theta(1 - y) \quad (6)$$

with $a = y_0^b/(1 - y_0^b)$. Therefore, the CSS regulator provides us a scheme to approximate a regulator which fulfills the general criterion for optimization at any order of the derivative expansion.

Similarly to the CSS regulator, the nuclear SV potential also falls into the C^∞ class.

- [1] P. Salamon, A. T. Kruppa, T. Vertse, *Phys. Rev.* **C81**, 064322 (2010).
- [2] P. Salamon, T. Vertse, *Phys. Rev.* **C77**, 037302 (2008).
- [3] I. Nándori, e-Print: arXiv:1208.5021 [hep-th].

2.2 Quantum chromodynamics on the lattice

T.G. Kovács, F. Pittler

Quantum chromodynamics (QCD) is the generally accepted theory of the strong interactions that bind quarks into hadrons like the proton and the neutron. The only systematic way of computing low-energy observables starting from the theory is to discretize it on a space-time lattice and perform large-scale Monte Carlo numerical simulations. In the past years lattice QCD did not only provide more and more precise numerical data to be compared to experimental data but also contributed to a better intuitive understanding of the phenomena occurring in strongly interacting systems.

One of the most interesting of these phenomena is the transition of ordinary strongly interacting matter to the so called quark-gluon plasma phase occurring at high temperature and already observed in heavy ion collisions. Quarks that are all confined into hadrons at low temperature become liberated above the critical temperature characterizing the transition. At the same time the chiral symmetry that is spontaneously broken at low temperatures also gets restored.

Chiral symmetry is intimately connected to the density of low-lying quark states. At low temperature these states are known to follow Wigner-Dyson random matrix statistics. This has been successfully exploited to compute the parameters of the effective chiral Lagrangian describing strongly interacting systems in the low energy limit. In contrast, up to a few years ago there was no generally accepted understanding of the statistical properties of low-lying quark states above the critical temperature. We showed that in simplified models of QCD the low quark eigenmodes obey Poisson statistics that gradually crosses over to Wigner-Dyson statistics higher up in the spectrum. This also implies that the low modes are highly localized which can have significant physical consequences.

In this year, for the first time we could verify Poisson statistics for the low quark modes in full dynamical QCD without any simplifica-

tions [1,2]. In figure 1 we show the unfolded level spacing distribution, a commonly used statistic that can clearly distinguish between Poisson and Wigner-Dyson behavior. We also studied the details of the transition in the spectrum from Poisson to Wigner-Dyson statistics. We found that in systems with larger spatial volumes the transition becomes sharper, indicating that it might be analogous to a genuine phase transition. We also studied the scaling properties of the so called mobility edge, separating localized (Poisson statistics) states from delocalized (Wigner-Dyson statistics) states in the spectrum. We found that the mobility edge scales properly and as a result it is a well-defined quantity in the continuum limit. We also studied the temperature dependence of the mobility edge and found that it increases sharply with the temperature. Thus at higher temperatures more quark states become localized. The transition we found in the spectrum from localized to delocalized states is analogous to the so called Anderson transition, well known in conductors containing impurities.

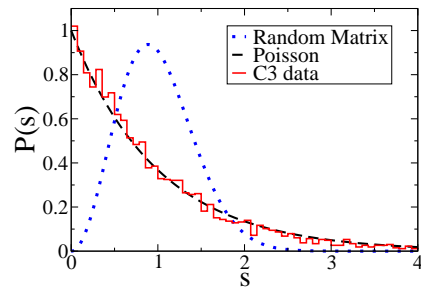


Figure 1. The unfolded level spacing distribution of low quark modes.

Acknowledgments

This work was supported by the Hungarian Academy of Sciences under “Lendület” grant No. LP2011-011 and also partly by the EU Grant (FP7/2007-2013)/ERC No. 208740.

- [1] T. G. Kovacs and F. Pittler, Poisson to Random Matrix Transition in the QCD Dirac Spectrum; *Phys. Rev. D* **86** (2012) 114515.
- [2] T. G. Kovacs and F. Pittler, Is there a gap in the QCD Dirac spectrum above T_c ?, *PoS (Lattice 2012)* 078.

3.1 Extensions of Elliott's SU(3) symmetry

J. Cseh

The SU(3) model by Elliott [1] derived the quadrupole deformation and collective rotation from the spherical shell model. Very soon the SU(3) symmetry proved to be the important link between the shell and cluster models, too [2]. This model is applicable in its original form to light nuclei ($12 \leq A \leq 28$), and it describes a single major shell. This symmetry is a dynamical (ly broken) one in the sense that the Hamiltonian is not symmetric (scalar), but its eigenvectors are symmetric (transform according to a single irreducible representation).

Due its essential role in connecting the fundamental models of nuclear structure several extension of the SU(3) symmetry has been invented. In Fig. 1. we consider some of them [3].

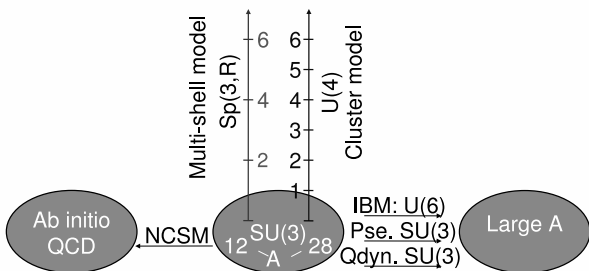


Figure 1. Extension of Elliott's SU(3) symmetry along the dimensions of the mass number and excitation energy. (The scale along the vertical axes is measured in $\hbar\omega$).

The symplectic model (with Sp(3,R) group structure) incorporates major shell excitations in the algebraic shell model, and it describes the quadrupole collectivity, too [4]. The (semimicroscopic) algebraic cluster model (with $U_C(3) \otimes U_R(4)$ group structure, where C stands for the cluster internal structure, while R for relative motion) accounts for the dipole (i.e. cluster) collectivity [5].

Several generalizations have been worked out in order to extend the powerful algebraic

description to heavy nuclei. We mention here three of them (probably the best-known ones). In the interacting boson model [6] the description is based on (monopole and quadrupole) pairs of nucleons of the valence shells. This model contains other symmetries as well: in addition to the SU(3) rotational limit it has an U(5) vibrational one, and a O(6) gamma-unstable one, too. The pseudo-SU(3) model incorporates several major shells, in each of them the normal and intruder parity states are separated, the former ones are described by the pseudo SU(3) symmetry [7]. The quasi-dynamical SU(3) symmetry [8] accounts for many major shells, too, and describes all the single-particle orbitals in a unified way, due to the conceptual generalization of the symmetry: neither the Hamiltonian, nor its eigenvectors are symmetric [9].

Towards the very light nuclei, where no-core shell model and QCD-inspired bare nucleon-nucleon interactions are applied, the quasi-SU(3) extension [10] (not to be confused with the quasi-dynamical SU(3)!) proved to be useful [11].

- [1] J.P. Elliott, Proc. Roy. Soc. A **245** (1958) 128, 562.
- [2] B.F. Bayman, A. Bohr, Nucl. Phys. **9** (1958/59) 596.
- [3] J. Cseh, J. Phys. Conf. Ser. **381** (2012) 012081.
- [4] G. Rosensteel, D.J. Rowe, Phys. Rev. Lett. **38** (1977) 10.
- [5] J. Cseh, Phys. Lett. B **281** (1992) 173; J. Cseh, G. Lévai, Ann. Phys. (NY) **230** (1994) 165.
- [6] F. Iachello, A. Arima, The interacting boson model, Cambridge University Press 1987.
- [7] J.P. Draayer, Nucl. Phys. A **520** (1990) 259c.
- [8] P. Rochford, D. J. Rowe, Phys. Lett. B **210** (1988) 5.
- [9] J. Cseh, Proc. IV Int. Symp. on Quantum Theory and Symmetries (Varna) (Sofia: Heron Press) p. **918** (2006).
- [10] A.P. Zuker, et al., Phys. Rev. C **52** (1995) R1741.
- [11] T. Dytrych et al., J. Phys. G **35** (2008) 123101.

3.2 Shape isomers and clusterization in the ^{28}Si nucleus

J. Darai^{a)}, *J. Cseh*

The shape isomers of light nuclei attract much attention from different structure studies, and provide a close connection to nuclear reactions as well. Superdeformed (SD) bands in ^{36}Ar and ^{40}Ca have been well-established through gamma-ray spectroscopy. In addition, candidate hyperdeformed states have been suggested from reaction studies [1].

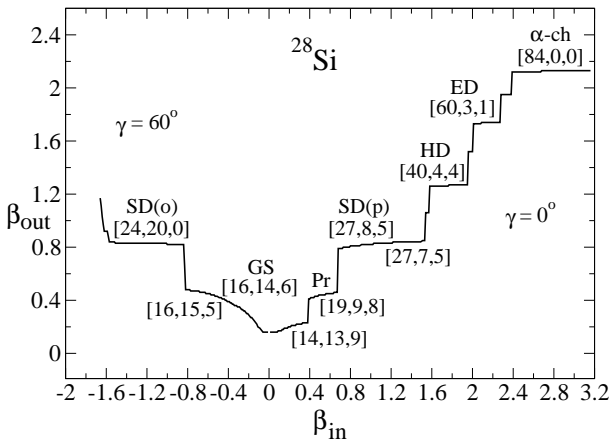


Figure 1. Quadrupole deformation of ^{28}Si nucleus from the Nilsson model using effective $U(3)$ quantum numbers. The horizontal axis shows the β_{in} input parameter, and the vertical axis indicates the absolute value of β_{out} . The left-hand side corresponds to $\gamma_{in} = 60^\circ$ while the right hand side represents $\gamma_{in} = 0^\circ$.

There has been considerable theoretical effort, recently, in considering superdeformed and other highly deformed configurations in ^{28}Si . From the experimental side, there are a set of states in ^{28}Si identified in the $^{12}\text{C}(^{20}\text{Ne},\alpha)^{28}\text{Si}$ reaction which have been attributed to the superdeformed band by Kubono et al. [2]. This sequence does not, however, have the smooth characteristics expected for such a band, and the moment of inertia is not in line with the result of a recent AMD calculation.

Jenkins et al. [3] have reviewed the available experimental data, and extended them with new γ -transitions. As a result they propose a new candidate for the SD band.

Inspired by this exciting situation with open questions on the SD state, we have carried out an independent theoretical analysis of highly-deformed structures in ^{28}Si . [4]. In particular we performed a Nilsson-calculation, combined with quasi-dynamical $U(3)$ considerations, and determined the allowed binary clusterization of the shape isomers.

We have found eight shape isomers ranging from the ground state up to a linear alpha-chain configuration (see Fig. 1).

In searching for the allowed clusterizations the clusters were considered to have deformations, like the ground states of the corresponding nuclei, and no constraint was applied for their relative orientation. The alpha-like clusterizations proved to be energetically favoured. The hyperdeformed state allows only a single binary clusterization (of intrinsic ground state clusters): $^{20}\text{Ne}+^8\text{Be}$, the ground state can have core+alpha, as well as core+ ^8Be . The prolate and the superdeformed state allow several clusterizations. For the SD state, which is the focus of the present work, we find that the $^4\text{He}+^{24}\text{Mg}$, and the $^{12}\text{C}+^{16}\text{O}$ cluster configurations are the most probable, taking account of both the selection rules and energetic preference. Our result on the SD state supports the new candidate state proposed by Jenkins et al. [3].

^{a)} *Dept. Experimental Physics, Univ. Debrecen*

- [1] W. Scianiet al., Phys. Rev. C **80** (2009) 034319; J. Cseh et al., Phys. Rev. C **80** (2009) 034320.
- [2] S. Kubono et al., Nucl. Phys. A **457** (1986) 461.
- [3] D. Jenkins et al., Phys. Rev. C **86** (2012) 064309.
- [4] J. Darai et al., Phys. Rev. C **86** (2012) 064310.

3.3 Direct capture in the $^{130}\text{Sn}(n,\gamma)^{131}\text{Sn}$ and $^{132}\text{Sn}(n,\gamma)^{133}\text{Sn}$ reactions under r -process conditions

P. Mohr^{a)}

The neutron capture cross sections of the $^{130}\text{Sn}(n,\gamma)^{131}\text{Sn}$ and $^{132}\text{Sn}(n,\gamma)^{133}\text{Sn}$ reactions play an important role in r -process nucleosynthesis [1,2]. Recently, single-particle properties of the residual ^{131}Sn and ^{133}Sn nuclei have been studied using the (d,p) reaction in inverse kinematics [3,4]. A series of states has been identified, and it has been noticed that the fragmentation of strength is very similar in both nuclei which is a surprising result because larger fragmentation is expected for the semi-magic ^{130}Sn target.

The information from the (d,p) transfer experiments [3,4] has been used to adjust all parameters of the direct capture (DC) model to local experimental results. This leads to relatively small uncertainties for the calculated DC cross section. The results and the contributions of the different final states are shown in Figs. 1 and 2.

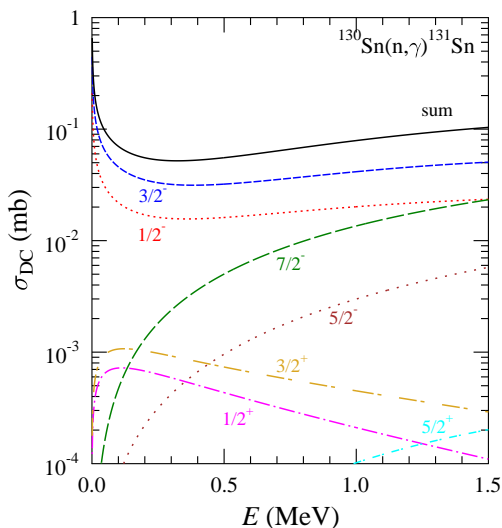


Figure 1. Cross section of the $^{130}\text{Sn}(n,\gamma)^{131}\text{Sn}$ reaction from the DC model.

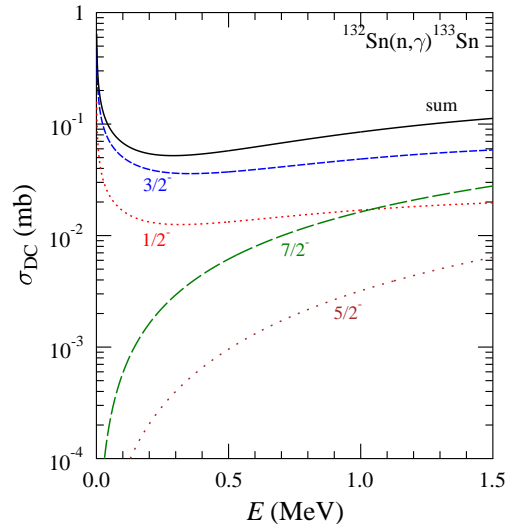


Figure 2. Cross section of the $^{132}\text{Sn}(n,\gamma)^{133}\text{Sn}$ reaction from the DC model.

It is found that the DC cross sections of both reactions are very similar. They could be determined with relatively small uncertainties of about a factor of two. Because of the larger Q -value of the $^{130}\text{Sn}(n,\gamma)^{131}\text{Sn}$ reaction it is possible that resonant contributions may enhance the stellar reaction rate by up to a factor of five. Such an enhancement is not expected for the $^{132}\text{Sn}(n,\gamma)^{133}\text{Sn}$ reaction. Further details and comparison to earlier calculations can be found in [5].

This work was supported by OTKA (NN83261).

a) Diakonie-Klinikum Schwäbisch Hall, D-74523 Schwäbisch Hall, Germany

[1] R. Surman *et al.*, Phys. Rev. C **79**, 045809 (2009).

[2] J. Beun *et al.*, J. Phys. G **36**, 025201 (2009).

[3] R. L. Kozub *et al.*, Phys. Rev. Lett. **109**, 172501 (2012).

[4] K. L. Jones *et al.*, Phys. Rev. C **84**, 034601 (2011).

[5] P. Mohr, Phys. Rev. C **86**, 068803 (2012).

3.4 Recommended cross section of the $^{16}\text{O}(p,\gamma)^{17}\text{F}$ reaction below 2.5 MeV: a potential tool for quantitative analysis and depth profiling of oxygen

P. Mohr^{a)} and C. Iliadis^{b),c)}

The $^{16}\text{O}(p,\gamma)^{17}\text{F}$ reaction has been studied experimentally at low energies by many authors. Because of the relatively low Q -value, it is a textbook example for non-resonant external capture, and relatively simple models are able to describe the energy dependence of the cross section with good accuracy.

In an earlier study we have investigated the cross section and astrophysical S-factor at very low energies [1]. The study has been restricted to the few experimental data sets which have been measured absolutely [2-4]. The present work [5] extends the energy range under study up to about 2.5 MeV. Here the $^{16}\text{O}(p,\gamma)^{17}\text{F}$ reaction can be used for analytical purposes. The cross section is non-resonant in this energy region (see Fig. 1).

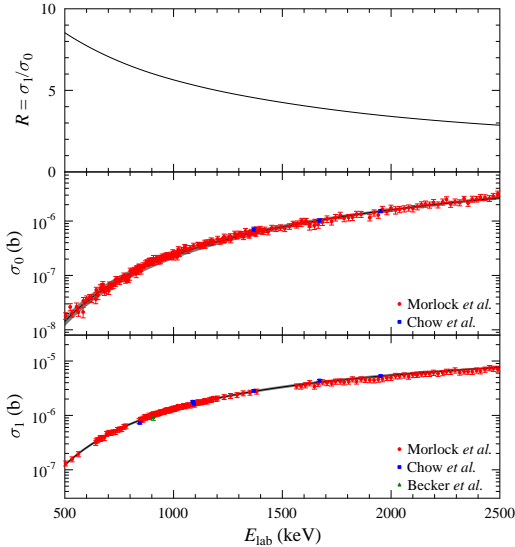


Figure 1. Recommended cross section of the $^{16}\text{O}(p,\gamma)^{17}\text{F}$ reaction and branching ratio R .

The recommended cross section has been determined by the following procedure. In a first step the absolute value of a direct capture (DC) calculation has been adjusted to the experimental σ_0 and σ_1 cross sections to the ground state and first excited state in ^{17}F from [2-4], i.e. for each transition 3 adjustment factors were determined. Next, a weighted average of the adjustment factors was calculated, and the weights were derived from the abso-

lute uncertainties of the experimental results [2-4]. The above procedure has been repeated for a R-matrix calculation. Both calculations are able to reproduce the energy dependence of the experimental data with $\chi^2 \leq 1.0$ but do not show exactly the same energy dependence. Thus, in a final step the DC calculation and the R-matrix calculation with their corresponding adjustment factors) were averaged. The deviation between the recommended σ_0 and σ_1 cross sections and the experimental results [2-4] is shown in Fig. 2. The result of a further recent R-matrix calculation [6] is also shown.

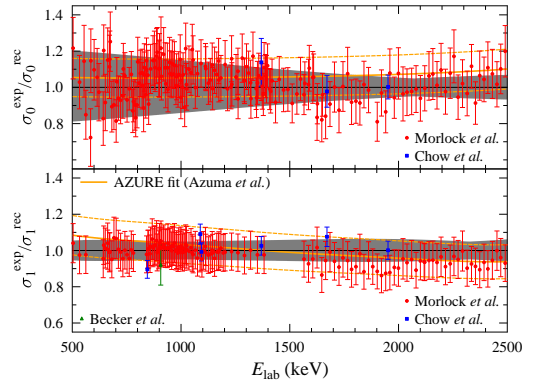


Figure 2. Ratio $\sigma^{\text{exp}}/\sigma^{\text{rec}}$ for the $^{16}\text{O}(p,\gamma)^{17}\text{F}$ reaction and prediction of further recent R-matrix calculation [6].

This work was supported by OTKA (NN83261).

- a) Diakonie-Klinikum Schwäbisch Hall, D-74523 Schwäbisch Hall, Germany
- b) Department of Physics and Astronomy, University of North Carolina, Chapel Hill, North Carolina, 27599-3255, USA
- c) Triangle Universities Nuclear Laboratory, Durham, North Carolina, 27708-0308, USA

- [1] C. Iliadis *et al.*, Phys. Rev. C **77**, 045802 (2008).
- [2] H. C. Chow *et al.*, Can. J. Phys. **53**, 1672 (1975).
- [3] R. Morlock *et al.*, Phys. Rev. Lett. **79**, 3837 (1997).
- [4] H. W. Becker *et al.*, Z. Phys. A **305**, 319 (1982).
- [5] P. Mohr and C. Iliadis, NIMA **688**, 62 (2012).
- [6] R. E. Azuma *et al.*, Phys. Rev. C **81**, 045805 (2010).

3.5 Strictly finite range potential for light PET isotopes

P. Salamon, T. Vertse, L. Balkay^{a)}

Adjusting the potential parameters of the new phenomenological nuclear potential introduced recently by P. Salamon and T. Vertse [1] (SV) to the global potential set of Perey and Becchetti–Greenlees showed that for the light nuclei the first term of the SV potential approximate well the cut-off Woods–Saxon (CWS) form. Both CWS and SV potential have strictly finite ranges [2] since both become zero at finite distance. Trajectories of the poles of the S -matrix are compared for the two potentials and a potential in R. G. Newton’s book for which analytical formulae for the starting points of the trajectories are given. The accuracy of the numerical calculations were tested against these formulae. The numerical calculations were performed for a light nucleus $A = 18$ playing important role in reaction producing a β^+ decaying residual nucleus used in positron emission tomographs (PET). See Fig. 1.

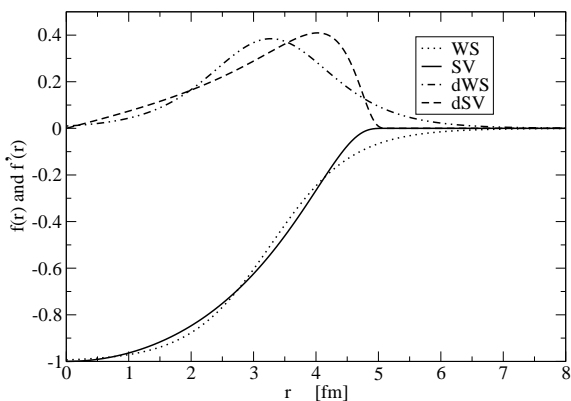


Fig. 1. Radial shapes of the WS and first term of the SV potentials and its derivatives for ^{18}F .

We calculated the neutron single particle spectrum for other PET nuclei e.g. the nuclei ^{13}N , ^{15}O and ^{18}F nuclei in CWS potential and the SV potential with its first term. The single particle energies calculated in the two potentials agree reasonably well for the same nucleus [3].

n, l, j	Energy (CWS)	Energy (SV)
$0s_{1/2}$	-38.926	-38.119
$0p_{3/2}$	-23.998	-23.610
$0p_{1/2}$	-22.0674	-21.640
$1s_{1/2}$	-7.697	-7.697
$0d_{5/2}$	-8.985	-9.048
$0d_{3/2}$	-5.779	-5.769

Table. I. Neutron single particle energies (in MeV) in the CWS and the first term of the SV potentials outside the ^{18}F core.

- a) University of Debrecen, Institute of Nuclear Medicine, Medical and Health Science Center, PO Box 12, H-4010 Debrecen, Hungary
- [1] P. Salamon, and T. Vertse, Phys. Rev. **C77**, 037302 (2008).
- [2] J. Darai, A. Rácz, P. Salamon, and R. G. Lovas, Phys. Rev. **C86**, 014314 (2012).
- [3] P. Salamon, T. Vertse, and L. Balkay, e-Print: arXiv:1210.1721 [nucl-th].

3.6 Precise half-life measurement of the ^{66}Ga isotope

Gy. Gyürky, J. Farkas, Z. Halász, T. Szücs

The ^{66}Ga radioisotope is important e.g. in the high energy efficiency calibration of γ -detectors. Therefore, the precise knowledge of its half-life is crucial. In 2004 a critical review was published about the half-lives of radionuclides considered to be important for detector efficiency calibrations [1]. It was found that the precision of the ^{66}Ga half-life is by far not enough for the requirements posed by the International Atomic Energy Agency [2]. Since 2004 two new high precision half-life measurement of ^{66}Ga became available [3,4] whose results disagree by about six standard deviations. This strong deviation indicates that the knowledge of the ^{66}Ga half-life is still very far from the required precision, therefore, new experiments are clearly needed.

In the present work the half-life of ^{66}Ga has been measured based on counting the γ -radiation following the β^+ decay. Special emphasis was put to the experimental implementation of the measurements to reduce the systematic uncertainties and to increase the reliability of the measured half-life value.

Six sources were produced at the cyclotron of Atomki by the $^{66}\text{Zn}(p,n)^{66}\text{Ga}$ and $^{63}\text{Cu}(\alpha,n)^{66}\text{Ga}$ reactions. Evaporated Zn targets and thick Cu disks were used for these two reactions, respectively.

The γ -radiation following the β^+ decay of ^{66}Ga was measured with three shielded HPGe detectors. A sufficiently long waiting time was inserted between the source preparation and the beginning of the counting in order to reduce the initial dead time of the counting setups below 2%. The reliability of the dead time values provided by the data acquisition system was checked by measuring the decay

of one source in parallel with two different acquisition systems. In order to check the long-term stability of the counting systems, long-lived reference sources were measured together with the ^{66}Ga sources. The reference isotopes were ^{56}Co , ^{65}Zn and ^{137}Cs .

The ^{66}Ga half-life was determined based on the analysis of the seven strongest γ -transitions. The decay was followed for up to 87 hours (about 9 half-lives) and the spectra were recorded in every 30 minutes. The half-life was determined from the parameters of the exponential curve fitted to the peak area vs. time function. The final value was calculated as the weighted average of 37 individual half-life values (six sources with six or seven γ -transitions).

The obtained half-life value is $t_{1/2} = (9.312 \pm 0.032)$ h. The quoted uncertainty include the statistical uncertainty as well as systematic uncertainties from the stability of the counting systems, dead time determination and peak integration.

Further details of the experiments and the data analysis can be found in [5]. The obtained half-life value supports the validity of one of the recent measurements [4] while it is in contradiction with the other one [3].

- [1] M.J. Woods, , S.M. Collins, *Appl. Radiat. Isot.* 60, (2004) 257.
- [2] IAEA, 1991. In X-ray and gamma-ray standards for detector calibration. IAEA-TECDOC-619, International Atomic Energy Agency, Vienna, Austria, pp. 112-124.
- [3] K. Abbas, K., *et al.*, *Appl. Radiat. Isot.* 64, (2006) 1001.
- [4] G.W. Severin, L.D. Knutson, P.A. Voytas, E.A. George, *Phys. Rev. C* 82, (2010) 067301.
- [5] Gy. Gyürky, J. Farkas, Z. Halász, T. Szücs, *Appl. Radiat. Isot.* 70, (2012) 278.

3.7 Investigation of the α -particle induced nuclear reactions on natural molybdenum

F. Ditrói, A. Hermanne, F. Tárkányi, S. Takács, A.V. Ignatyuk

Cross-sections of alpha particle induced nuclear reactions on natural molybdenum have been studied in the frame of a systematic investigation of charged particle induced nuclear reactions on metals for different applications [1]. The excitation functions of ^{93m}Tc , $^{93g}\text{Tc}(m+)$, ^{94m}Tc , ^{94g}Tc , ^{95m}Tc , ^{95g}Tc , $^{96g}\text{Tc}(m+)$, ^{99m}Tc , ^{93m}Mo , $^{99}\text{Mo}(cum)$, $^{90}\text{Nb}(m+)$, ^{94}Ru , ^{95}Ru , ^{97}Ru , ^{103}Ru and ^{88}Zr were measured up to 40 MeV alpha energy by using a stacked foil technique and activation method. The main goals of this work were to get experimental data for accelerator technology, for monitoring of alpha beam, for thin layer activation technique and for testing nuclear reaction theories [2-4]. The experimental data were compared with critically analyzed published data and with the results of model calculations, obtained by using the ALICE-IPPE, EMPIRE and TALYS codes (TENDL-2011).

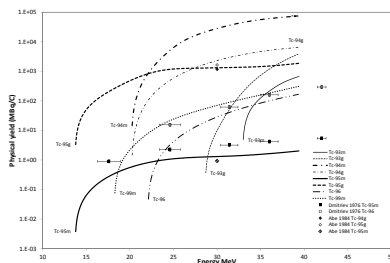


Figure 1. Calculated integral yields of the produced technetium radioisotopes compared with the available literature data

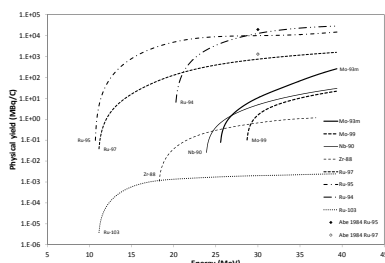


Figure 2. Calculated integral yields of the produced molybdenum, niobium, zirconium and ruthenium radioisotopes compared with the available literature data.

Yield versus energy curves are calculated from the measured data (Figs. 1-4) for the radioisotopes having special importance in one of the application fields.

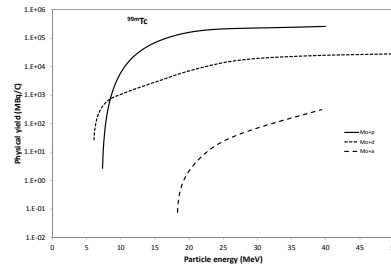


Figure 3. Comparison of integral yields for ^{99m}Tc by proton, deuteron and α -particle irradiation

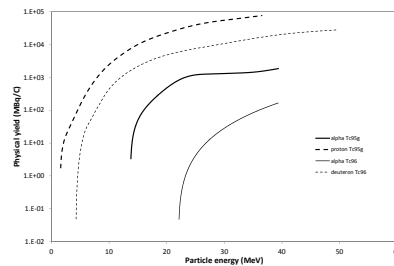


Figure 4. Comparison of integral yield for ^{95g}Tc by proton and α -particle irradiation and for $^{96g}\text{Tc}(m+)$ by deuteron and α -particles.

- [1] F. Tárkányi, F. Ditrói, A. Hermanne, S. Takács, A.V. Ignatyuk, Nucl. Instr. Meth. B 280 (2012) 45
- [2] M. Herman, R. Capote, M. Sin, A. Trkov, B.V. Carlson, P. Oblozinsky, C. Mattoon, H. Wienke, S. Hoblit, Y.-S. Cho, V. Plujko, Z. V., Nuclear Reaction Model Code EMPIRE-3.1 (Rivoli), in: <http://www.nndc.bnl.gov/empire/index.html>, 2012.
- [3] A.J. Koning, S. Hilaire, M.C. Duijvestijn, TALYS-1.0, in: O. Bersillon, F. Gusing, E. Bauge, R. Jacqmin, S. Leray, in: (Ed.) International Conference on Nuclear Data for Science and Technology, EDP Sciences, Nice, France, 2007, pp. 211
- [4] M. Blann, Recent progress and current status of pre-equilibrium reaction theories and computer code ALICE, in: LLNL, Report UCRL-JC-109052, 1991.

3.8 Activation cross-sections of deuteron induced reactions on natural palladium

F. Ditrói, F. Tárkányi, S. Takács, A. Hermanne, A.V. Ignatyuk, M. Baba

Activation cross-sections for deuteron induced reactions were measured on natural palladium up to 40 MeV with the activation method using a stacked-foil irradiation technique and high resolution gamma-spectrometry. Excitation functions are reported for the reactions producing the radionuclides ^{111}Ag , ^{110m}Ag , ^{106m}Ag , ^{105}Ag , ^{111m}Pd , ^{109}Pd , ^{101}Pd , ^{100}Pd , ^{105}Rh , ^{102g}Rh , ^{101m}Rh , ^{100}Rh and ^{99g}Rh . Comparisons with earlier published data and theoretical results of ALICE-IPPE, EMPIRE and the TALYS codes are presented. Calculated yield curves and activity versus depth distributions are also presented for practical applications such as isotope production or thin layer activation.

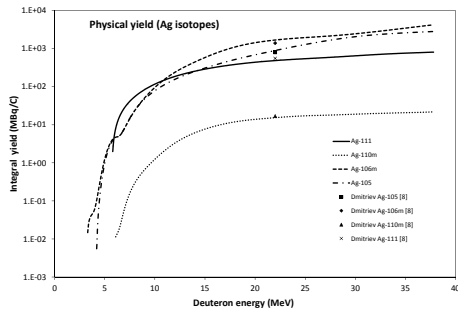


Figure 1. Integral yield graphs of the Ag isotopes.

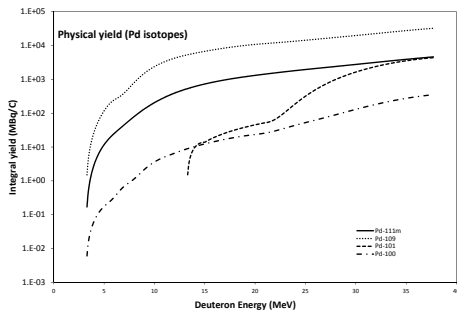


Figure 2. Integral yield graphs of the Pd isotopes.

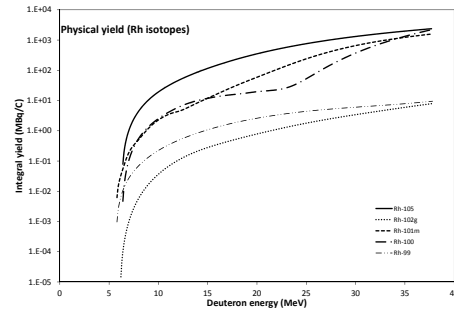


Figure 3. Integral yield graphs of the Rh isotopes.

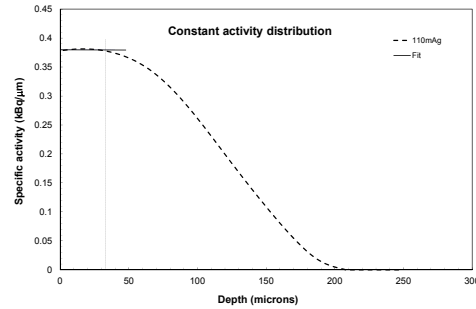


Figure 4. TLA curve of the ^{110m}Ag isotope with constant activity distribution (within 1%) in the first 30 μm (see vertical dotted line) (14.1 MeV deuterons; perpendicular irradiation, 2 μA beam current; 1 h irradiation time).

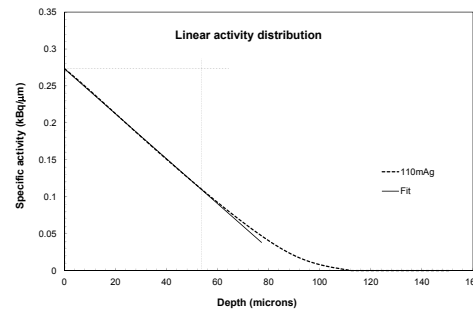


Figure 5. TLA curve of the ^{110m}Ag isotope with linear activity distribution (within 1%) in the first 53 μm (see vertical dotted line) (10.1 MeV deuterons; perpendicular irradiation, 2 μA beam current; 1 h irradiation time).

3.9 $\gamma\gamma$ -coincidence in the neutron rich nucleus ^{25}F

Zs. Vajta, M. Stanoiu^{a)}, D. Sohler, F. Azaiez^{b)}, Zs. Dombrádi, O. Sorlin^{c)}, B.A. Brown^{d)}, F. Becker^{e)}, M. Belleguic^{b)}, C. Borcea^{a)}, C. Bourgeois^{b)}, Z. Dlouhy^{f)}, Z. Elekes, S. Grévy^{g)}, D. Guillemaud-Mueller^{b)}, F. Ibrahim^{b)}, M. Lewitowicz^{c)}, S.M. Lukyanov^{h)}, S. Mandal^{g)}, P. Mayet^{c)}, J. Mrázek^{f)}, F. Negoita^{a)}, Yu.-E. Penionzhkevich^{h)}, Zs. Podolyákⁱ⁾, P. Roussel-Chomaz^{c)}, M.G. Saint-Laurent^{c)}, H. Savajols^{c)}, J. Timár, C. Timis^{h)}

The ^{25}F isotope, having a valence proton in addition to the doubly closed shell ^{24}O core, is expected to have a rather simple structure: its energy spectrum can be described as a few single proton states coupled to the ground and excited states of the neighboring oxygen nucleus, ^{24}O . However, states arising from cross shell excitations may also be present. According to theoretical calculations intruder states may appear in ^{25}F somewhat above the neutron separation energy. To see if any of these states is bound the structure of ^{25}F was studied at GANIL by in-beam γ -spectroscopic technique in the double step fragmentation reaction.

In the experiment the primary beam of ^{36}S delivered by the two GANIL cyclotrons at an energy of 77.5 MeV·A and an intensity of 400 pnA hit a carbon target of 348 mg/cm² thickness placed in the SISSI device. The produced nuclei were selected through the ALPHA spectrometer. The secondary beam was mainly composed of ^{24}F , $^{25,26}\text{Ne}$, $^{27,28}\text{Na}$ and $^{29,30}\text{Mg}$. The fragments produced by reactions of the secondary beam on an 'active' target made of a plastic scintillator sandwiched by two carbon foils were collected and identified at the focal plane of the SPEG spectrometer by the combined use of ΔE , E , TOF infor-

mation. 74 BaF₂ scintillators surrounding the secondary target detected the γ rays from the fragments. The γ -spectra were corrected for the Doppler-shift caused by the large fragment velocity. As the detectors were closely packed, the γ rays could easily scatter from one detector to another. To decrease the background caused by the scattered particles, we used the array in anti-Compton mode.

On the basis of the analysis of γ -ray spectrum taken for ^{25}F 6 γ lines are assigned to the studied nucleus between 750 and 4200 keV. To help the level scheme construction, $\gamma\gamma$ -coincidence matrices were created. Putting a gate on the most intense 1720-keV γ line, it was found to be in coincidence with itself, as well as with the 750-keV line. Furthermore, the 750-keV transition is in mutual coincidence with the 3440-keV γ ray as it can be seen in Fig. 1.

- a) IFIN-HH, Bucharest-Magurele, Romania
- b) Inst. de Phys. Nucl., IN2P3-CNRS, Orsay, France
- c) GANIL, Caen, France
- d) NSCL, MSU, East Lansing, USA
- e) GSI, Darmstadt, Germany
- f) Nucl. Phys. Inst., Rez, Czech Republic
- g) Lab. de Phys. Corp., Caen, France
- h) FLNR, JINR, Dubna, Moscow region, Russia
- i) Dept. of Phys., Uni. of Surrey, Guildford, UK

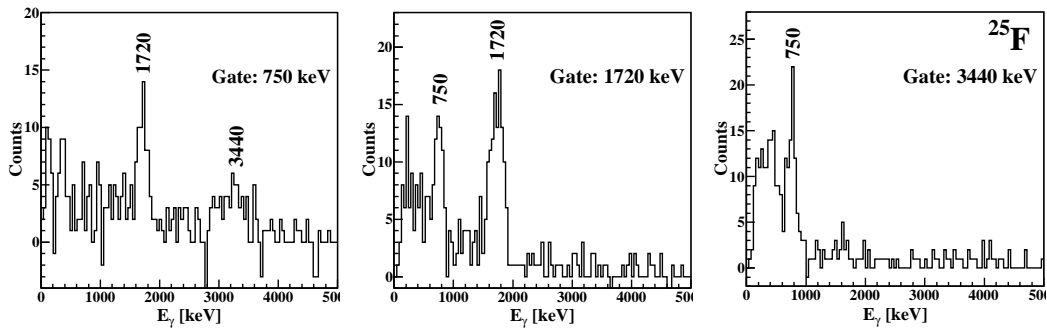


Figure 1. $\gamma\gamma$ -coincidence spectra of ^{25}F .

3.10 Investigation of α -induced reactions on ^{127}I for the astrophysical γ process

T. Szücs, G. G. Kiss, Zs. Török, Z. Korkulu^{a)}, Gy. Gyürky, Z. Halász, Zs. Fülöp, E. Somorjai, T. Rauscher^{b)}

The main stellar mechanism synthesizing the stable proton-rich nuclei with charge number $Z \geq 34$ is the so-called γ process. It is initiated by (γ, n) photodisintegration reactions on preexisting more neutron-rich seed nuclei. As the neutron separation energy increases along the (γ, n) path, (γ, p) and (γ, α) reactions become dominant and push the material towards lower masses. Recently, consistent studies of the γ process nucleosynthesis proved that in the production of the heavy proton-rich nuclei (γ, α) reactions play a crucial role. To predict the stellar (γ, α) rates measurements of (α, γ) cross sections are required [1].

Our systematic study of reactions relevant for the γ process was continued with the cross section measurement of $^{127}\text{I}(\alpha, \gamma)^{131}\text{Cs}$ and $^{127}\text{I}(\alpha, n)^{130}\text{Cs}$ reactions using the activation method. Both reactions have been studied close to the astrophysically relevant energy range. The decay of the (α, n) reaction product is followed by emission of γ -rays. By counting these, the reaction cross section can be derived. The (α, γ) reaction product decays exclusively by electron capture followed by the emission of characteristic X-rays, but no γ -rays. For determination of the radiative α -capture cross sections the yield of these characteristic X-rays was measured, using the technique described in Ref. [2]. For the target preparation KI compound was evaporated onto thin Al foils. The target thickness was determined by PIXE method using the 5-MV VdG accelerator of ATOMKI. The targets were irradiated with α beams from the MGC20 cyclotron of ATOMKI. The investigated energy range between 9.8 MeV and 15.5 MeV was covered about 0.5 MeV steps. For the γ counting a shielded HPGe detector was used, while the X-ray countings were carried out using a shielded low-energy photon spectrometer (LEPS). The obtained results were compared with statistical model predictions calculated by the code SMARAGD (version 0.8.4s). It is found that

the calculations overestimate the experimental values by a factor of 2 at the upper end of the investigated energy range and a factor of about 6 at the lower end. (see fig 1.) In the measured energy range the predicted (α, γ) cross sections are sensitive to the α , neutron and γ widths. Therefore it is impossible to further disentangle the different contributions of the widths to the total deviation from experiments and to draw strong conclusions on the basis of the experimental capture data alone. The predicted (α, n) cross sections at the upper part of the measured energy range is only sensitive to the α width. Here the predictions and the measurements are in good agreement. It is to be concluded, therefore, that the α width is predicted well by the SMARAGD code. The deviations in the (α, γ) case are caused by problems in the neutron and/or γ widths.

Further details of the experiment, the data analysis and the astrophysical discussion can be found in Ref. [3].

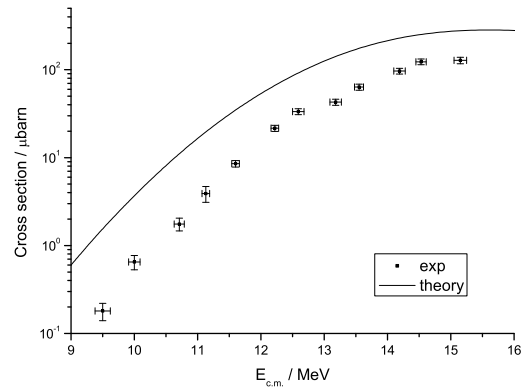


Fig. 1. Measured cross sections compared to theoretical prediction for the $^{127}\text{I}(\alpha, \gamma)^{131}\text{Cs}$ reaction.

- a) Department of Physics, University of Kocaeli, Umuttepe 41380, Kocaeli, Turkey,
- b) Department of Physics, University of Basel, CH-4056 Basel, Switzerland

[1] T. Rauscher, *et al.*, PRC **80**, 035801 (2009)

[2] G. G. Kiss, T. Szücs, *et al.*, NPA **867**, 52 (2011)

[3] G. G. Kiss, T. Szücs, *et al.*, PRC **86**, 035801 (2012)

3.11 $^{106,110,116}\text{Cd}(\alpha, \alpha)^{106,110,116}\text{Cd}$ elastic scattering and systematic investigation of the elastic α scattering cross sections along the $Z = 48$ isotopic and $N = 62$ isotonic chains

G. G. Kiss, P. Mohr^a, Zs. Fülöp, Gy. Gyürky, J. Farkas, Z. Elekes, E. Somorjai, D. Galaviz^b, N. Özkan^c, R.T. Gürayf, C. Yalcin^c, J. Görres^d

Alpha-nucleus optical potentials are basic ingredients for the calculation of reaction cross sections with α particles in the entrance or exit channel. These reaction cross sections are included in stellar reaction rate calculations in nuclear astrophysics. To test the global alpha-nucleus optical potential parameterizations several (α, α) reactions have been studied at ATOMKI (see e.g. [1]). Recently, the angular distributions of the $^{106,110,116}\text{Cd}(\alpha, \alpha)^{106,110,116}\text{Cd}$ reactions at $E_{c.m.} \approx 15.6$ MeV and 18.8 MeV between 20° - 170° were measured. The experimental data are compared to calculations performed with global and regional alpha nucleus optical potentials and in some cases reasonable agreement was found [1]. However, a global alpha-nucleus optical potential must be able not only to provide a correct prediction for the elastic scattering cross sections but also to describe the variation of the angular distributions along

isotopic and isotonic chains. In this work the ratios of the Rutherford normalized cross sections were used to test further the global potential parameterizations used in astrophysical calculations. We found that all optical potential parameterizations failed to reproduce the amplitude and/or phase of the oscillations of the ratio of the Rutherford normalized cross sections as can be seen in Fig. 1. In order to improve our current understanding of the α -nucleus optical potential, further experimental data as well as theoretical improvements are essential.

- a) Diakonie-Klinikum, Schwäbisch Hall, Germany
- b) Instituto de Estructura de la Materia, Madrid, Spain
- c) Kocaeli University, Department of Physics, Kocaeli, Turkey
- d) University of Notre Dame, South Bend, Indiana, USA

[1] G. G. Kiss *et al.*, *Phy. Rev. C* **83**, 065807 (2011).

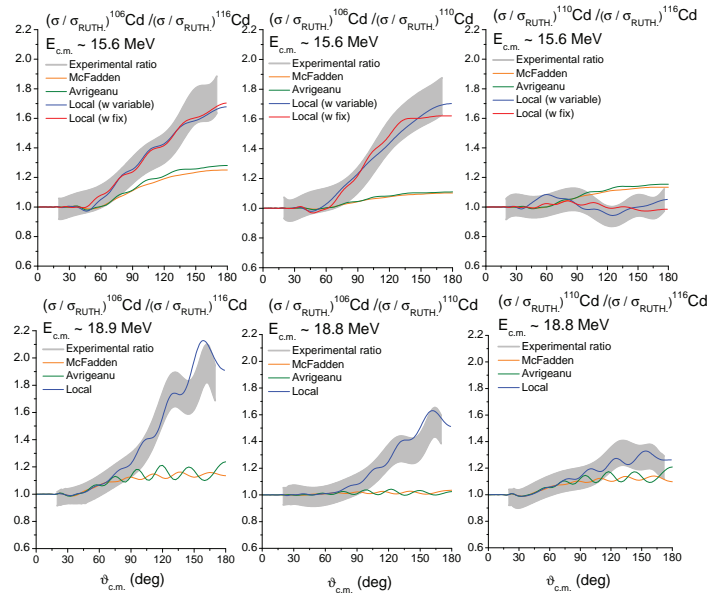


Figure 1. Ratio of the Rutherford normalized elastic scattering cross sections of $^{106,110,116}\text{Cd}(\alpha, \alpha)^{106,110,116}\text{Cd}$ reactions at $E_{c.m.} \approx 15.6$ and 18.8 MeV versus the scattering angle. The lines correspond to the predictions using different local and global optical potential parameter sets (for details, see [1]).

3.12 In-beam γ -spectroscopic study of rotational bands in ^{103}Rh

I. Kuti, J. Timár, D. Sohler, K. Starosta,^{a)}, C. Vaman,^{b)}, D. B. Fossan^{b)}, T. Koike^{c)}, I. Y. Lee^{d)}, A. O. Machiavelli^{d)},

Earlier studies revealed the existence of chiral partner candidate bands in ^{103}Rh [1]. In order to construct a more complex level scheme, and to collect more information on the band structure, we studied the experimental properties of the rotational bands of this nucleus. For this analysis, excited states of ^{103}Rh were populated through the $^{96}\text{Zr}(^{11}\text{B},4n)$ reaction at a beam energy of 40 MeV. The beam, provided by the 88-in. cyclotron of the Lawrence Berkeley National Laboratory (LBNL), impinged on a $500\ \mu\text{g}/\text{cm}^2$ self-supporting target foil. For detection of the emitted γ -rays, the GAMMASPHERE spectrometer was used. Out of a sum of 9×10^9 events, about the 65% could be assigned to ^{103}Rh .

In the present phase of the study, the level scheme was constructed based on $\gamma\gamma$ -coincidence relationships, as well as energy and intensity balances of the observed γ -rays. The analysis included the evaluation of 2-

and 3-dimensional histograms, using the RADWARE software package. Three typical $\gamma\gamma\gamma$ -coincidence spectra are shown in Figure 1.

We doubled the number of transitions assigned to ^{103}Rh and we established five new bands to the formerly known six ones [2]. In order to assign firm spin-parities to the states, we plan to make an angular correlation (DCO) analysis for the observed transitions.

[1] J. Timár et al., Physical Review C 73, 011301(R) (2006).

[2] D. de Frenne, Nuclear Data Sheets 110, 2081 (2009).

a) Department of Chemistry, Simon Fraser University, Burnaby, BC, Canada

b) SUNY, Stony Brook, NY, USA

c) Graduate School of Science, Tohoku University, Sendai, Japan

d) Nuclear Science Division, LBNL, Berkeley, CA, USA

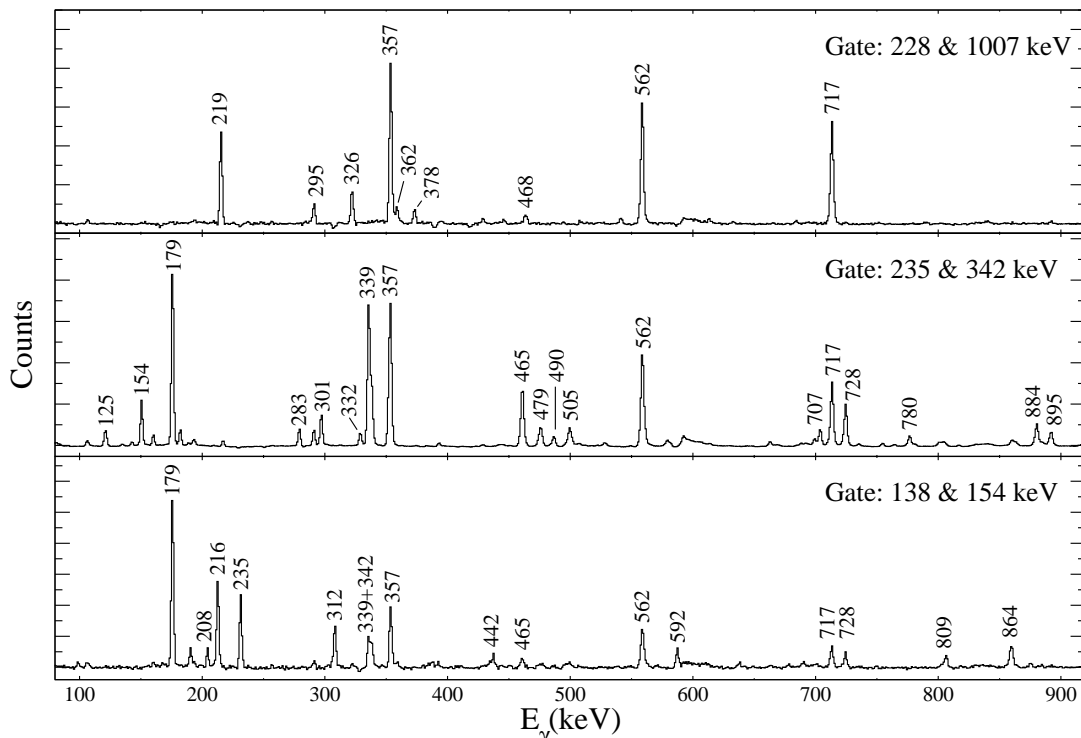


Figure 1: Sample $\gamma\gamma$ -coincidence spectra for ^{103}Rh .

3.13 Investigation of α -induced reactions on ^{130}Ba

Z. Halász, Gy. Gyürky, J. Farkas, Zs. Fülöp, T. Szücs, E. Somorjai and T. Rauscher

The synthesis of the chemical elements heavier than iron is the focal point of nuclear astrophysics. The origin of about 99% of the heavier elements observed in the Universe are well described by the classical r- and s-processes. Nevertheless, the genesis of the remaining 1% is rather interesting: because of the shielding effect of the stable elements, they can not be created via neutron-capture reactions. These are the so-called p-isotopes and their producing mechanism is referred to as the astrophysical p-process. The validation of nucleosynthesis theories are based mainly on experiments, *i.e.* on the extensive knowledge about the reaction cross sections. For this reason there is a great demand to high precision measurements. Particularly, among the p-elements there are some, where the experimental results are totally missing.

This report shows some results of the α -induced reaction cross section measurements on ^{130}Ba , which is one from these above mentioned isotopes.

In the astrophysical relevant energy range - in the Gamow-window, in this case between 5.3 and 8.1 MeV - the ^{130}Ba 's (α,γ) and (α,n) reaction cross sections are very low, thus they are non-measurable in laboratory environment. The cross section must be measured "higher" energy and the results must be interpolated to the lower range. The α -capture on ^{130}Ba leads to the radioactive ^{134}Ce and decays to ^{134}La with 75.9h half-life. The produced ^{134}La decays to the stable ^{134}Ba with a half-life of 6.67min. Besides this radiative capture, the $^{130}\text{Ba}(\alpha,n)^{133}\text{Ce}$ can be measured parallel, because both the ground state and the isomeric state of the ^{133}Ce also have a suitable half-life (5.3h, 97min respectively).

The natural abundance of the p-nucleus ^{130}Ba is very low, consequently, enriched target should be used. Targets have been prepared by evaporating BaCO_3 onto thin Al foils. The target stability was continuously monitored dur-

ing the irradiation process.

The uncertainty of the measured values has been calculated from the following components: counting statistics ($\leq 15\%$), number of target atoms ($\leq 8\%$), detector efficiency and summing correction ($\leq 5\%$) and current integration ($\leq 3\%$).

^{131}Ce	^{132}Ce	^{133}Ce 5.3h, 97m 58 keV γ	^{134}Ce 75.9h Weak γ 's	^{135}Ce	^{136}Ce	^{137}Ce
^{130}La	^{131}La (α,n) (α,γ)	^{133}La 3.9h 278.8 keV	^{134}La 6.7m 604.7 keV	^{135}La	^{136}La	
^{129}Ba	^{130}Ba Stable	^{131}Ba	^{132}Ba	^{133}Ba 39h, 10.5y 356.0 keV	^{134}Ba Stable	^{135}Ba
^{128}Cs	^{129}Cs	^{130}Cs	^{131}Cs	^{132}Cs	^{133}Cs	^{134}Cs

Figure 2: The investigated Ba reactions and the decays of the reaction products.

The experimental cross sections were compared to theoretical predictions based on the Hauser-Feshbach statistical model. The predictions overestimates the experimental values by factors 2-3 in the measured energy range.

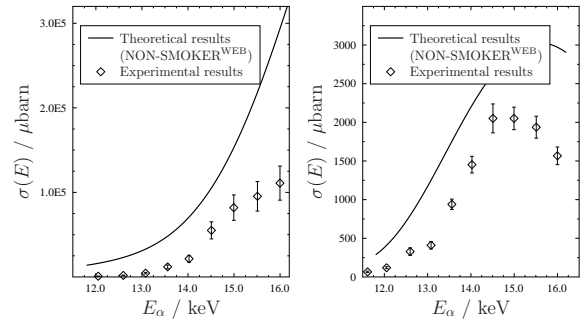


Figure 3: Comparison of experimental cross sections for $^{130}\text{Ba}(\alpha,\gamma)^{134}\text{Ce}$ and $^{130}\text{Ba}(\alpha,n)^{133}\text{Ce}$ reactions with the theoretical predictions of NON-SMOKER^{WEB}.

- [1] J. Jose and C. Illiadis, Rep. Prog. Phys. **74**, 096901 (2011).
- [2] S. E. Woosley and W. M. Howard, Astrophys. J. Suppl. Ser. **36**, 285 (1998).
- [3] Z. Halász *et al.*, PRC **85**, 025804 (2012).

3.14 $^{64}\text{Zn}(\alpha, \alpha)^{64}\text{Zn}$ elastic scattering experiment, a progress report

M.P. Takács, Gy. Gyürky, G.G. Kiss, Z. Halász, T. Szücs, Zs. Fülöp, E. Somorjai, A. Ornelas^{a)}, D. Galaviz, ^{a)}, P. Mohr^{b)}, R.T. Güray^{c)}, Z. Korkulu^{c)} N. Özkan^{c)}, C. Yalcin^{c)},

The 35 stable nuclei located on the proton rich side of the valley of stability whose production cannot be explained in the framework of the slow and rapid neutron capture process are called the p-nuclei. In order to reproduce the abundance distribution of these isotopes, an extensive reaction network is needed, in which reactions with alpha particles in their entrance or exit channels play an important role. Therefore, the determination of the alpha-nucleus optical potentials is essential for the calculation of reaction cross sections. The experimental data, which is obtained by alpha elastic scattering, can provide a direct test for the global alpha-nucleus optical potential parameterizations and thus makes the improvement of the statistical models possible.

In previous years several (α, α) reactions on heavy nuclei have been studied at ATOMKI. As a continuation of this systematic study, we measured the angular distribution of the $^{64}\text{Zn}(\alpha, \alpha)^{64}\text{Zn}$ reaction at laboratory energies: 12.00 MeV and 16.15 MeV. The experimental setup was an updated version of the scattering chamber which is presented e.g. in [1]. The angular distribution of the scattered alpha particles was recorded by 9 Si particle detectors. The physical dimensions of experimental setup made the investigation of 20-175° angular range possible.

During the experiment around 700 spectra were acquired by the 9 detectors. The evaluation of the spectra was done with the help of commercial and self-developed programs. The angular distribution of scattering cross section was first calculated in the laboratory frame then it was converted into the center of mass system and normalized to the Rutherford scattering. The results at energies of 12.00 and 16.15 MeV can be found in Fig. 1 and 2 respectively. Due to the high precision measurements

the overall uncertainties of the obtained data were less than 5 %.

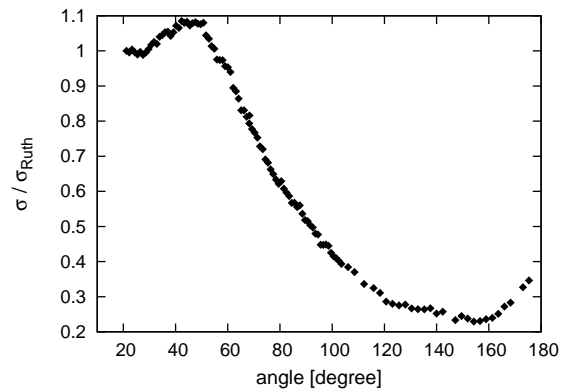


Figure 1. Rutherford normalized scattering cross section at 12.00 MeV

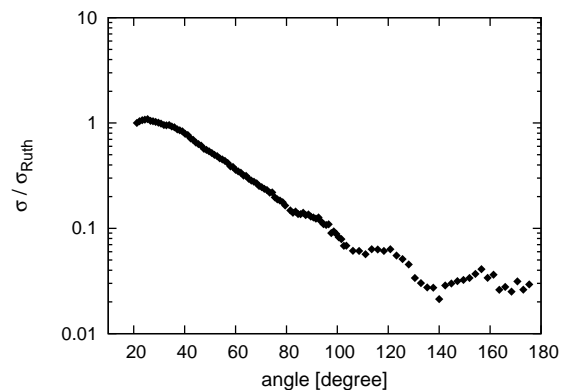


Figure 2. Rutherford normalized scattering cross section at 16.15 MeV

The next stage of the analysis will involve the comparison of the experimental data with cross sections supplied by global optical potentials and the construction of a local optical potential.

a) Centro de Física Nuclear, University of Lisbon, 1649-003 Lisbon, Portugal

b) Diakonie-Klinikum, D-74523 Schwäbisch Hall, Germany

c) Department of Physics, Kocaeli University, TR-41380 Umuttepe, Kocaeli, Turkey

[1] G.G. Kiss *et al.*, Phys. Rev. C **83** 065807 (2011)

4.1 The signature of the Fermi-shuttle type multiple ionization in collision between carbon ions and neon atoms

K. Tőkési, L.H. Toburen^{a)}, and J.L. Shinpaugh^{a)}

During the past few years there has been increasing interest in ionization of atomic and molecular targets by intermediate-energy dressed and partially dressed ions. Ionization is one of the fundamental phenomena studied in atomic collision physics. The energy and angular distributions of the ejected electrons carry detailed information about the dynamics of this break-up type process. Characteristic structures in these doubly differential spectra can be associated with different collision mechanisms. Some of the observed high energy tails, bumps or peaks have been recently identified as produced by an accelerating multiple electron scattering process, often referred to as Fermi-shuttle acceleration. Originally, Fermi proposed the mechanism as a possible source of energetic cosmic rays [1] where weak but giant magnetic fields, moving in outer space, can accelerate charged particles with extremely high energies in long sequences of reflection. Similarly, a light electron can be scattered forward and backward by heavy target atoms and an incoming projectile ion.

In this work, the ionization of Ne by 2.4 MeV C⁺ ion is studied both experimentally and theoretically [2]. The energy distributions of the ejected electrons as a function of the scattering angle were measured and compared with the calculations obtained using the classical trajectory Monte Carlo method. The system is a challenge to describe theoretically owing to screening of the projectile nuclear charge by bound electrons, interactions of projectile electrons with target electrons, and the large number of possible exit channels. The calculation separates the process into ionization of the target by the screened incident projectile ion and the ionization of the projectile by the screened target atom. By summing these components in the rest frame of the target we can compare the theoretical predictions to the measured electron spectra. Figure 1 shows the doubly differential cross sections for ejection of electrons

in 2.4 MeV C⁺ - Ne collisions at 130°. There is remarkably good general agreement between experiment and theory. We obtained significant electron emission yields at the binary encounter peak (2V, where V is the velocity of the projectile) and even higher energies. One of the explanations of this unexpected yield of electrons with velocities greater than 2V is the so-called Fermi shuttle acceleration indicating that this multiple scattering mechanism is important for describing the energetic electrons produced in low energy ion-matter interactions.

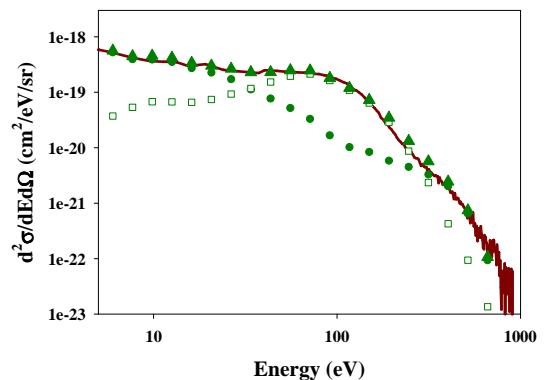


Figure 1. Energy distribution of electrons ejected in collision between 2.4 MeV C⁺ ions and Ne atoms with impact velocity of $V=2.83$ a.u. The emission angle is 130°. Solid line: experiment, solid circle: CTMC data, contribution from the target ionization, open square: CTMC data, contribution from the projectile ionization, solid triangle: the sum of target and projectile ionization.

Acknowledgements

This work supported by the Hungarian Scientific Research Fund OTKA No. NN 103279 and in part by East Carolina University.

a) Department of Physics, East Carolina University
Greenville, NC 27858, USA

[1] E. Fermi, Phys. Rev. **75** (1949) 1169.

[2] K. Tőkési, L.H. Toburen, and J.L. Shinpaugh, 22nd International Conference on the Application of Accelerators in Research and Industry. Fortworth, USA, 5-10 Aug., 2012. CAARI 2012. Proceedings. New York, AIP, 2013 in press.

4.2 Interaction of light particles with capillaries

K. Tókési, R.D. DuBois^{a)}

Since the discovery of the new phenomenon, namely guiding of charged particles through insulating capillaries, the research activities in the field of charged particle physics have turned to the investigation of charged particle interactions with inner surfaces of various insulating capillaries from nano- to micrometer size. The fact that most of the guided ions keep their initial charge state suggests that the ions do not touch the inner wall of the capillary during the transport process, i.e. a surprisingly well-tuned electric field is formed within each capillary. Ion guiding through the capillary ensues as soon as a dynamical equilibrium of self-organized charge-up by the ion beam, charge relaxation and reflection is established.

When electrons, instead of highly charged ions (HCI), are used to test the guiding conditions for various targets, this simple and straightforward explanation, however, fails for several reasons. It was found experimentally that a dominant fraction of electrons escaping from the capillary have energies smaller than the incident energy. This is in sharp contrast with the HCI transmission when the particles pass through the capillary with almost loss free transmission. Since electrons do not change their charge state a clear distinction between transmission of the original projectiles (primaries) and secondary electrons generated with the interaction of primaries with the capillary inner surface, is impossible. Furthermore, secondary electron production also implies that the inner capillary surfaces can be either positively charged (the secondary electron emission coefficient larger than 1) thereby attracting rather than deflecting subsequently arriving electrons or negatively charged (the secondary electron emission coefficient smaller than 1) generating the same conditions as obtained for HCI. We note here, that the velocities of the light particles in the measurements so far are much larger than that of the parti-

cle velocity in the HCI experiments. We believe that our knowledge of guiding by highly charged ions (HCI) is adequate. At the same time, however, although during the past few years many research groups contributed to this field of research many details of light particle guiding are still unknown.

Our studies demonstrated that a portion of the entering beams were transmitted and that the emerging intensities followed the direction of the capillary and depended on the tilt angle [1]. Both of these indicate guiding. However, we were unable to definitively rule out the possibility that the transmitted beams observed experimentally could result from different input angles associated with our diffuse beams. Although our 2D simulations also indicate that guiding will occur, measurements of the transmitted intensity as a function of charge entering the capillary did not show any major increases in the transmitted intensity with time, as has been seen in HCI guiding experiments. This could mean that insufficient charge was deposited or that charge patches were not able to form because the charging rate was too small with respect to the discharging rate. To investigate these aspects further, additional simulations plus additional measurements using positrons and electrons as well as low intensity positive ion beams are in progress.

Acknowledgements

This work supported by the Hungarian Scientific Research Fund OTKA No. NN 103279 and by the National Science Foundation. We are very grateful to P. Gunacker, C. Lemell and J. Burgdörfer for useful discussions.

a) Department of Physics, Missouri University of Science and Technology, Rolla, MO, USA

[1] K. Tókési, and R.D. DuBois, 22nd International Conference on the Application of Accelerators in Research and Industry. Fortworth, USA, 5-10 Aug., 2012. CAARI 2012. Proceedings. New York, AIP, 2013 in press.

4.3 Blocking effect for ions and neutrals in guided transmission of 3 keV Ar⁷⁺ through dense polycarbonate nanocapillary arrays

Z. Juhász, P. Herczku, S.T.S. Kovács, R. Rácz, S. Biri, I. Rajta, G.A.B. Gál, S.Z. Szilasi, J. Pálinkás^a), B. Sulik

Ion guiding through insulating capillaries is a topic of increasing interest. This self-organizing process is governed by the guiding electric fields created by the deposited charges on the inner capillary walls [1].

In the present work we investigated the dynamic properties of 3 keV Ar⁷⁺ ions guided through polycarbonate (PC) nanocapillaries at different tilt angles ranging from 1° to 7° together with the transmitted neutrals [2]. Two-dimensional transmission profiles were measured with a position sensitive detector. The guided ions and the transmitted neutrals were separated by an electrostatic deflector. The intensity of ions started from zero, and, after a short delay, increased rapidly (see Fig. 1). After reaching a maximum, it strongly decreased in time, showing a blocking effect, similarly as in previous measurements with other PC capillaries. The time dependence can be approximately described by the formula:

$$f(Q_d) = \begin{cases} 0 & \text{if } Q_d < Q_s \\ f_0(1 - \exp[-\frac{Q_d - Q_s}{Q_c}]) (\exp[-\frac{Q_d - Q_s}{Q_b}] + K) & \text{if } Q_d \geq Q_s \end{cases}$$

Here, Q_d is the deposited charge, Q_s is a threshold value introduced to describe the period until there is no transmission. The first term in brackets describes the rising part [3] with Q_c as a characteristic charge constant. The second term is for describing the blocking effect. This is an exponentially decaying function with characteristic charge Q_b . Since the intensities seem to approach a non-zero constant value at the end, an additive K constant was introduced in the blocking term, too.

The time dependence of the intensity of neutrals was similar to that of ions except that it started from a finite value, and the final yield was relatively larger than in the case of ions. These observations indicate that neutrals originate from multiple sources. They can be created in the entrance region, where ions are impinging and neutralized at the capillary wall, and they can also be created from the guided ions at the exit region. The latter mechanism

results in similarities in the time dependences of ions and neutrals.

The characteristic deposited charge value for blocking, Q_b was higher for larger tilt angles showing that blocking is faster for smaller tilting.

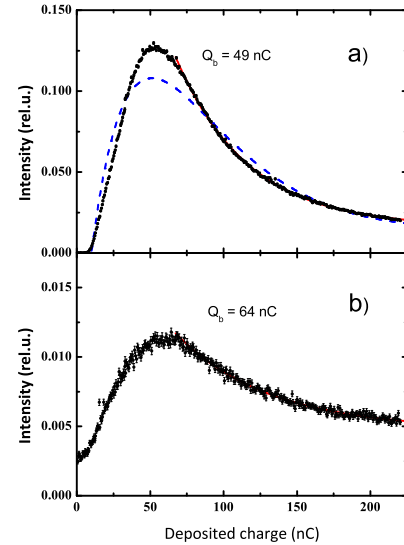


Figure 1. Intensity of transmitted Ar⁷⁺ ions (a), and Ar atoms (b) as function of deposited charge on the sample surface [2]. The primary beam was of 3 keV Ar⁷⁺ ions. The tilt angle of the capillaries was 5.5°. Fitting by the function $f(Q_d)$ for ions is plotted by a (blue) dashed line. Fitting of the decreasing parts by an exponential decay function is plotted by (red) solid lines. The resulting characteristic values for blocking Q_b are indicated in the panels.

In summary, blocking effect was observed for both the guided ions and for the neutrals with similar dynamic behavior. From this we concluded that neutral creation at the exit region is significant. Discrepancies in the fitting of $f(Q_d)$ indicate the need for better theoretical models.

Acknowledgements

This work was supported by the Hungarian National Science Foundation OTKA (Grant No: K83886). Work is supported by the TÁMOP-4.2.2/B-10/1-2010-0024 project, co-financed by EU and the European Social Fund.

a) Dept. of Exp. Phys., Univ. Debrecen, Hungary

[1] N. Stolterfoht, *et al*, Phys. Rev. Lett. **88** (2002) 133201

[2] Z. Juhász, *et al*, Nucl. Inst. Meth. B **279** (2012) 177-181

[3] N. Stolterfoht, *et al*, Nucl. Inst. Meth. B **235** (2005) 460

4.4 The guiding of 3 keV Ar⁷⁺ ions through a glass microcapillary array

P. Herczku, Z. Juhász, S.T.S. Kovács, R. Rácz, S. Biri, B. Sulik

The investigation of ion guiding phenomena attracts increasing interest since its discovery. The incident ions deposit their charge on the inner capillary walls hereby forming an electrostatic field which is able to deflect the ions along the capillary axis. This is a self-organizing process [1].

Within the frame of the present work we investigated a new type of capillary arrays. The material of the sample was glass. The diameter of the capillaries was about 5 μm and its length was 1 mm. The length to diameter ratio was even higher (about 200:1) than that of the nanocapillary samples studied earlier. In the present work we measured the transmission of 3 keV Ar⁷⁺ ions guided through the microcapillaries at 5° tilt angle together with the transmitted neutrals. Two-dimensional transmission profiles were collected with a position sensitive detector. The guided ions and the transmitted neutrals were separated by an electrostatic deflector [2]. The time evolution of the transmission was found to be very slow compared to nanocapillary samples. The ion intensity was zero for a long time and, only after that delay, started to increase slowly (see Fig. 1). The transmitted ion intensity remained under 0.6 percent during the few hours measuring period. To accelerate the process we tried to use higher beam current, however it led to overexposure problems in counting, so we could not follow that way. While the transmission of ions exhibits a threshold behavior, the yield of the neutrals starts from a finite value at the moment of letting the beam to the sample (see fig. 1 (b)). Its increase is also very slow. Neither of the transmitted intensities reached the maximum, when the dead time of the detector was already too high. In order to observe the full charge up process, we plan to repeat this experiment with other detection

technique, which is able to record higher intensities accurately, for instance sensitive current measurement.

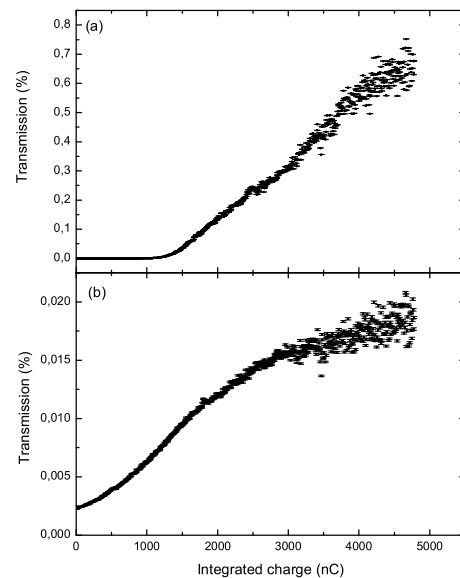


Figure 1. The transmitted intensity of Ar⁷⁺ ions (a), and Ar atoms (b) as function of deposited charge. The sample was tilted by 5° relative to the beam. The points with error bars represent the experimental data.

We note that the development of guiding for a single borosilicate capillary with 4.5 keV Ar⁹⁺ impact at 150 pA [3] appeared to be much faster than that of our present sample. Therefore the present results may be explained by collective effects of the neighboring capillaries in the high density sample.

Acknowledgements

This work was supported by the Hungarian National Science Foundation OTKA (Grant No: K83886). Work is also supported by the TÁMOP-4.2.2/B-10/1-2010-0024 project, co-financed by EU and the European Social Fund.

- [1] N. Stolterfoht, *et al*, Phys. Rev. Lett. **88** (2002) 133201
- [2] Z. Juhász, *et al*, Nucl. Inst. Meth. B **279** (2012) 177-181
- [3] G. Kowarik *et al*, Nucl. Inst. Meth. B **267** (2009) 2277

4.5 Fragmentation of small molecules induced by 46 keV/amu N^+ and N_2^+ projectiles

S.T.S. Kovács, Z. Juhász, P. Herczku, B. Sulik

Collisional molecule fragmentation experiments has gain increasing attention in several research and applied fields. In order to understand the fundamental processes of molecule fragmentation one has to start with collisions of small few-atomic molecules. Moreover, fragments of small molecules such as water can cause damages of large molecules (DNA) very effectively in living tissues.

In the last few years a new experimental setup was developed at Atomki. It was designed especially for molecule fragmentation experiments [1]. Now the measurements using this system are running routinely.

In 2012 the studied targets were water vapor, methane and nitrogen gases, injected into the collision area by an effusive molecular gas jet system [2]. 650 keV N^+ and 1,3 MeV N_2^+ ions were used as projectiles produced by the VdG-5 electrostatic accelerator. The velocity of the two types of projectiles was the same. Energy and angular distribution of the produced fragments was measured by an energy dispersive electrostatic spectrometer [3].

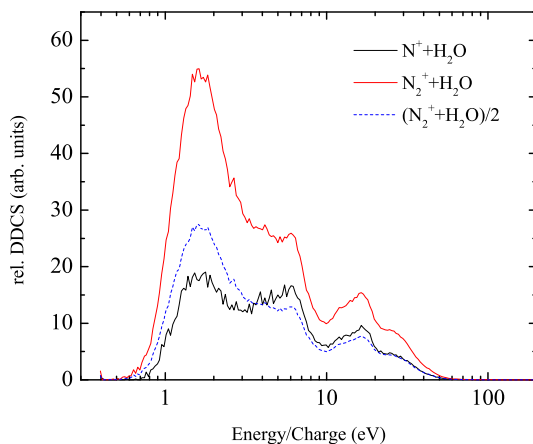


Figure 1. Normalized spectra of fragment ions from H_2O target integrated over the observation angle

For atomic ionization a symmetric, diatomic molecular projectile (e.g. N_2^+) yields

about twice more electrons compared to those of singly charged ion projectiles of the same atom (N^+) at the same velocity. In such cases the two atomic centers in the molecular ion can be considered as two individual atomic centers. For the fragmentation of molecular targets the picture is not so simple because in this case close collision of two extended systems is investigated.

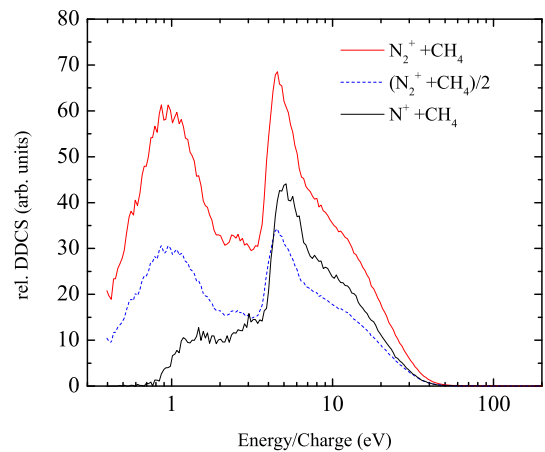


Figure 2. Normalized spectra of fragment ions from CH_4 target integrated over the observation angle

As figure 1 and 2 show, the measured yields for molecular projectile is not simply twice of the ones for atomic projectile. The shape of the energy spectra are different. The measured data are under evaluation.

Acknowledgements

This work was supported by the Hungarian National Science Foundation OTKA (Grant: K73703) and by the TAMOP-4.2.2/B-10/1-2010-0024 project. The project is co-financed by the European Union and the European Social Fund.

- [1] S. T. S. Kovács, P. Herczku, Z. Juhász, L. L. Horváth, ATOMKI Annual Report 2010 (2011) 57
- [2] S. T. S. Kovacs, ATOMKI Annual Report 2010 (2011) 56
- [3] P. Herczku, ATOMKI Annual Report 2010 (2011) 55

4.6 Probing scattering phase shifts by attosecond streaking

R. Pazourek^{a)}, S. Nagele^{a)}, K. Doblhoff-Dier^{a)}, J. Feist^{b)}, C. Lemell^{a)}, K. Tórkési, and J. Burgdörfer^{a)}

The emerging field of attoscience enables the investigation of electron dynamics as well as timing information of photoionization processes. Attosecond streaking has developed into a powerful tool to achieve temporal-resolution on the sub-100 attosecond time scale. It is based on a pump-probe setting with an extreme ultraviolet (XUV) pulse of a few hundred attoseconds duration serving as pump and a phase-controlled few-cycle infrared (IR) pulse as probe. Temporal information about the photoionization process can thus be mapped onto the energy axis in analogy to conventional streaking.

We studied attosecond streaking of the release time of electrons in atomic photoemission by solving the time-dependent Schrödinger equation (TDSE) for effective one-electron systems. We presented calculations also employing a restricted ionization model (RIM) in the TDSE. We verified that the trajectory effects on the time shift resulting from the interaction between the outgoing electron and the combined Coulomb and IR laser fields can be described classically.

We have shown that Eisenbud-Wigner-Smith (EWS) time shifts (or energy variation of the scattering phase) for short-ranged potentials become accessible by attosecond streaking provided both initial-state dependent entrance channel and final-state exit channel distortions are properly accounted for. For Coulomb potentials the coupling between the IR streaking field and the Coulomb field which depends on the final energy of the free electron dominates the extracted streaking time shift but can be accounted for classically. In addition we have identified considerable state-dependent time shifts for easily polarizable initial states which are of quantum mechanical origin. Accounting for polarization of the initial state, the remaining difference of time de-

lays between ionization from states with different angular momentum can be related to the EWS delay of the centrifugal potential.

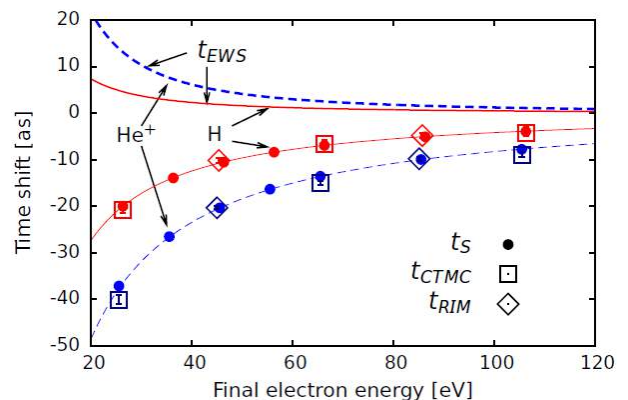


Figure 1. Temporal shifts T_S extracted from quantum mechanical streaking simulations with the full TDSE (full circles) and RIM (open diamonds), classical (Classical Trajectory Monte Carlo, CTMC) streaking simulations (open squares), and for comparison, the EWS time shift $T_{EWS} = d\sigma/dE$ for the Coulomb phase σ of an outgoing electron moving in an ionic core potential H^+ (red solid line) and He^{2+} (blue dashed line).

Acknowledgements

This work was supported by the FWF-Austria, Grants No. SFB016 and P21141-N16, the TeT under Grant No. AT-2/2009, and in part by the National Science Foundation through TeraGrid resources provided by NICS and TACC under Grant TG-PHY090031. The computational results presented have also been achieved in part using the Vienna Scientific Cluster (VSC). JF acknowledges support by the NSF through a grant to ITAMP.

a) Institute for Theoretical Physics, Vienna University of Technology, 1040 Vienna, Austria, EU

b) ITAMP, Harvard-Smithsonian Center for Astrophysics, Cambridge, Massachusetts 02138, USA

[1] R. Pazourek, S. Nagele, K. Doblhoff-Dier, J. Feist, C. Lemell, K. Tórkési, and J. Burgdörfer, *Journal of Physics: Conference Series* **388** (2012) 012029.

4.7 Single and multiple ionization of noble gas atoms by H^0 impact

L. Sarkadi, L. Gulyás, P. Herczku, S.T.S. Kovács, Á. Kövér

The understanding of the mechanisms of collisions between energetic charged particles and neutral atoms is of fundamental significance, and it has large importance in many research fields (plasma physics, astrophysics, materials science, etc.), as well as in number of practical applications.

In the present work we measured total direct ionization and electron loss cross sections for the collisions of H^0 atoms with noble gas atoms (He, Ne, Ar, Kr) in the energy range 75-300 keV. The experiment was carried out at the 1.5 MV Van de Graaff accelerator of Atomki by coincident detection of the recoil target ions and the charge-state analyzed scattered projectiles. With this study we wished to obtain information about the role played by the electron of the H^0 projectile in the process of the single and multiple vacancy production induced by the collision. For this purpose we repeated the measurements also with proton projectile under the same experimental conditions. For calibration of the measuring system and normalization of our data we used the cross section values of Ref. [1]. The experimental results were analysed with using the classical trajectory Monte Carlo (CTMC) method. CTMC describes well the experimental data for both projectiles for the single vacancy creation, however we observed increasing deviation between the theory and experiment with increasing number of the created vacancies, as well as with decreasing atomic number of the target atoms.

Fig. 1 shows our results obtained for the single, double and triple ionization ($q = 1, 2, 3$) of Kr at H^0 impact for the two cases when the outgoing projectile is H^0 (a) and H^+ (b), i.e., for pure ionization of the target, and ionization of the target with simultaneous electron loss of the projectile. The curves in the figure were obtained by two versions of the three-body CTMC theory: a conventional model [2,3] (dashed curves); and a model taking partially account of the many-body charac-

ter of the collision (a simplified version of the nCTMC theory [4], solid curves).

Further theoretical calculations in the framework of the Continuum Distorted Wave (CDW) theory are in progress.

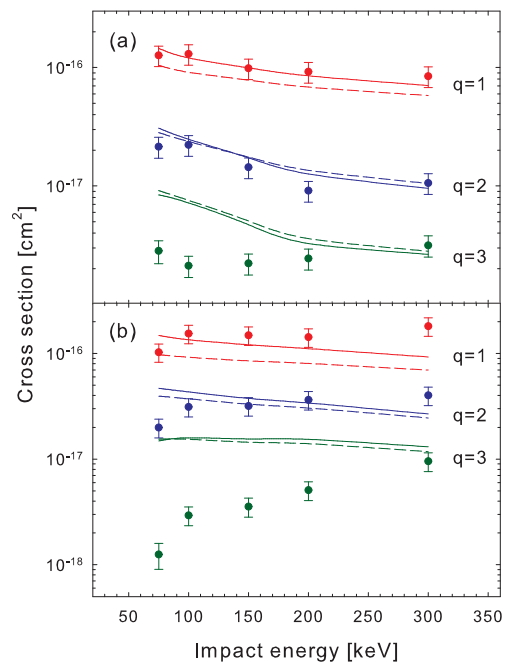


Figure 1. Cross sections for ionization of Kr by H^0 impact as a function of the collision energy. The full circles with errors bars are the measured data obtained for H^0 (a) and H^+ (b) outgoing projectiles. q is the charge state of the recoil target ions. The curves are results of CTMC calculations (for explanation see text).

Acknowledgments

This work was supported by the National Scientific Research Foundation and the National Office for Research and Technology of Hungary (NKTH-OTKA, Grant No. K67719) and the TÁMOP-4.2.2/B-10/1-2010-0024 project, co-financed by EU and the European Social Fund.

- [1] R.D. DuBois and Á. Kövér, *Phys. Rev. A* **40** (1989) 3605.
- [2] R. Abrines and I. C. Percival, *Proc. Phys. Soc. London* **88** (1966) 861.
- [3] B. Sulik and K. Tőkési, *Advances in Quantum Chemistry* **52** (2007) 253.
- [4] R. E. Olson, J. Ullrich and H. Schmidt-Böcking, *J. Phys. B* **20** (1987) L809.

4.8 Universal functional formula of atomic elastic cross sections. The case of the hydrogen target.

P. Salamon, D. Tskhakaya^{a)}, D. Coster^{b)}, and K. Tókési

Mathematics is the universal language of all natural sciences, in particular of the theoretical physics. Since the same mathematical problem, e.g. for example the smoothing of either the measured or calculated data can appear in various fields of sciences.

In this work the angular differential electron elastic cross sections of hydrogen atoms for a wide range of incident electron energy and in the entire angular range were calculated using the code described in Ref. [1], where the partial expansion method is applied to obtain cross sections. The aim of the present work was to develop a universal functional form of elastic cross sections for the case of hydrogen target.

We have the following system of three column "block" basic points which comes from cross section calculations:

$$\tilde{z}_1 \quad x_1 \quad \tilde{y}_{1,1} \quad (7)$$

$$\vdots \quad \vdots \quad \vdots \quad (8)$$

$$\tilde{z}_1 \quad x_n \quad \tilde{y}_{1,n} \quad (9)$$

$$\tilde{z}_2 \quad x_1 \quad \tilde{y}_{2,1} \quad (10)$$

$$\vdots \quad \vdots \quad \vdots \quad (11)$$

$$\tilde{z}_2 \quad x_n \quad \tilde{y}_{2,n} \quad (12)$$

$$\vdots \quad \vdots \quad \vdots \quad (13)$$

$$\tilde{z}_m \quad x_1 \quad \tilde{y}_{m,1} \quad (14)$$

$$\vdots \quad \vdots \quad \vdots \quad (15)$$

$$\tilde{z}_m \quad x_n \quad \tilde{y}_{m,n} \quad (16)$$

This means that we have m blocks and each block has the same x_k ($k = 1, \dots, n$) basis points. Our sample is made up $m \cdot n$ triples. We would like to fit our sample with a two variables continuous $\tilde{y} = F(x, \tilde{z})$ function using the method of least squares. For that we require that $\tilde{y}_{i,k} \approx F(x_k, \tilde{z}_i)$ for all $i = 1, \dots, m$ and $k = 1, \dots, n$. In our case $\tilde{z}_i \in [10^0, 10^5]$, $i = 1, \dots, m$ and $x_k \in [0^\circ, 180^\circ]$, $k = 1, \dots, n$ and $m = 201, n = 251$. According to our fitting

procedure the best fit function $y = F(x, z)$ is given as:

$$F(x, z) = \sum_{j=0}^p C_j(z) x^j, \quad (17)$$

where

$$C_j(z) = \sum_{l=0}^q d_{l,j} z^l \quad (j = 0, \dots, p). \quad (18)$$

Fig. 1 shows the elastic cross sections at 100 eV and 10 keV to verify the goodness of our universal functional form.

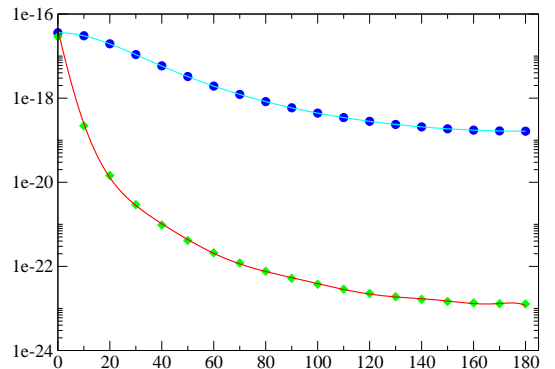


Fig. 1. Elastic scattering cross section as a function of the scattering angle. The symbols represent the calculations according to Ref. [1]. Circles: E=100 eV, Diamonds: E=10 keV. The solid lines: cross sections according to Eq. (1).

Acknowledgements

This work, supported by the European Communities under the contract of Association between EURATOM-HAS, was carried out within the framework of the Task Force on Integrated Tokamak Modelling of the European Fusion Development Agreement.

- a) Institute for Theoretical Physics University of Innsbruck, Innsbruck, Austria
- b) Max-Planck-Institut für Plasmaphysik, Garching, Germany

[1] F. Salvat, R. Mayol, *Comput. Phys. Commun.* **74** (1993) 358

4.9 Spatial and temporal interference during the ionization of H by few-cycle XUV laser pulses

A. Tóth^{a)}, S. Borbély^{a)}, K. Tőkési, L. Nagy^{a)}

We have studied the ionization of H atoms by two-cycle XUV laser pulses in the tunneling and over-the-barrier regimes, by following the time evolution of our system.

Beside the dominant ionization processes, secondary processes may occur. These are interferences between different electronic wave packets. From the numerous possible scenarios two have a significant impact on the final momentum distribution of the free electrons.

In the first case, the interference between wave packets emitted at different time moments during the action of the laser pulse leads to circular interference minima and maxima in the final momentum distribution.

In the second scenario, electronic wave packets emitted at the same time follow different paths, accumulating different final phases, leading to a radial fringe structure in the electron spectra. This process can be viewed as the interference between a direct and a scattered wave, so its pattern in the momentum distribution can be interpreted as the holographic mapping (HM) of the target system's state [1].

In our work we have used the time dependent close-coupling method [2] to solve numerically the time dependent Schrödinger equation. For the investigation of the temporal interference we used also the strong field approximation, and we showed that the concentric extremas are the result of the interference between wave packets emitted at opposite half-cycles of the same laser field cycle.

In case of the spatial interference, first, we have confirmed the existence of the two types of electron trajectories using classical trajectory Monte Carlo calculations [3]. According to the simple two-path model of [1], the spatial interference pattern is mainly influenced by only one parameter, z_0 , which is the maximum distance reached by the free wave packet before it is redirected towards the parent ion by the laser field. By performing TDCC cal-

culations for different laser pulse parameters (implicit modification of z_0) we confirmed this presumption. The discrepancies between the exact TDCC calculations and the simple two-path model can be explained with the fact that the later one neglects the effect of the parent ions Coulomb potential on the scattered wave.

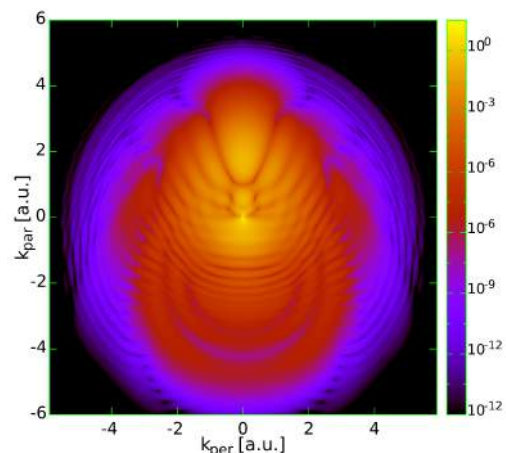


Figure 1. Momentum distribution of the continuum electrons as a function of parallel and perpendicular momentum components. Laser pulse parameters: $\omega = 0.4445$ a.u., $E_0 = 1$ a.u., and $\tau = 28.26$ a.u.

Acknowledgements

This work was supported by the Sectoral Operational Programme for Human Resources Development 2007-2013, co-financed by the European Social Fund, under Projects No. POSDRU 89/1.5/S/60189 and No. POSDRU/107/1.5/S/76841, by a grant of the Romanian National Authority for Scientific Research, CNCS UEFISCDI Project No. PN-II-ID-PCE-2011-3-0192, and partially the Hungarian Scientific Research Fund OTKA No. NN 103279.

a) Faculty of Physics, Babeş-Bolyai University, Cluj-Napoca, Romania

[1] Y. Huismans *et al.*, Science **331** 61 (2011)

[2] J. Colgan and M. S. Pindzola, Phys. Rev. Lett. **88** (2002) 173002.

[3] K. Tőkési and G. Hock, Nucl. Instrum. Methods Phys. Res., Sect. B. **86**, 201 (1994)

4.10 Energy and angular distribution of electrons transmitted through a single glass microcapillary

A. R. Milosavljevic ^{a)}, R. J. Bereczky, M. Kovacevic ^{a)}, K. Tőkési, B. P. Marinkovic ^{a)}

The transmission of electrons through insulating (micro) nanocapillaries with high aspect ratio has been attracting large interest in recent years [1]. This research is motivated both by potential application of low-energy electron manipulation at (micro) nanometer scale in highly developing bionanotechnology. The processes of electron transmission through insulating capillaries appeared to be more complex than in the case of highly charged ion (HCI) guiding, where the guiding is dominantly due to the Coulomb deflection. In the case of electrons the close electron-surface interaction and secondary electron emission, as well as Coulomb deflection, must be taken into account. In this work we investigate the transmission of low-energy electrons of 200 eV through a single glass capillary of high aspect ratio. We study both angular distribution of electrons transmitted with the incident energy and energy distribution of electron escaping the capillary [1].

The glass capillary sample was prepared at the ATOMKI laboratory in Debrecen, Hungary. The capillary has the inner diameter of $d=0.15$ mm and the length of $l=12.4$ mm, therefore, the aspect ratio (l/d) is 82.6. The measurements of transmission of electrons through the single glass microcapillary were performed in the Laboratory for atomic collision processes at the Institute of Physics Belgrade, Serbia. The system allows measurements of transmitted current at incident electron energies from about 100 eV to 350 eV, variation of both tilt and observation angles and an energy analysis of transmitted electrons. The electron gun produces a well collimated electron beam, with a diameter and an angular divergence estimated to be approximately 1 mm and 1° at 200 eV of the incident energy, and with an energy spread of about 0.5 eV.

Figure 1(a) shows the angular distributions of electrons transmitted through the single glass capillary at the incident energy of 200 eV, at three different tilt angles of the incident

electron beam with respect to the capillary direction.

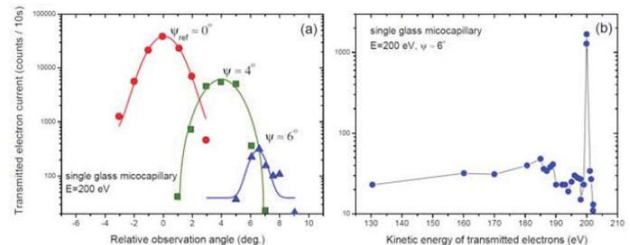


Fig1. (a) Angular distribution of electrons transmitted through the capillary at the incident energy, for different tilt angles (Ψ). (b) Kinetic energy distribution of electrons escaping the capillary at the tilt angle of 6° .

The measurements were performed by fixing the angle between the capillary and the incident beam and then by recording the signal intensity of transmitted electron current as a function of the observation angle, the angle between the capillary direction and the axis of the entrance electron lens of the analyzer. The results show transmission of electrons even at large tilt angles, where direct transmission should be geometrically prevented, thus suggesting an existence of the guiding effect. Figure 1(b) shows the measured kinetic energy distribution of electrons escaping the capillaries at large tilt angle. Except the dominant peak at about 200 eV corresponding to elastic transmission, there is a significant fraction of electrons that suffer inelastic collisions. Further works are in progress in the topic.

Acknowledgements

The work was supported by the Ministry of Education and Science of Republic of Serbia (Project No. 171020) and by the Hungarian Scientific Research Fund OTKA No. NN 103279.

a) Laboratory for atomic collision processes, Institute of Physics, University of Belgrade, Serbia

[1] A. R. Milosavljevic, R. J. Bereczky, M. Kovacevic, K. Tőkési and B. P. Marinkovic, 26th International Symposium on the Physics of Ionized Gases 79 (2012).

4.11 Temperature control of ion guiding through insulating capillaries

E. Gruber^{a)}, R. J. Berezky, G. Kowarik^{a)}, F. Ladinig^{a)}, J. P. Waclawek^{a)}, D. Schrempf^{a)}, K. Tőkési, F. Aumayr^{a)}

First experiments on guiding of highly charged ions (HCI) through straight insulator nano-capillaries showed a remarkable effect: after an initial charge up phase, the ion beam could be steered by tilting the capillary axis while remaining in the initial charge state indicating that the transmitted ions never touched the inner walls. Subsequent experiments confirmed this guiding effect also for macroscopic glass capillaries, both straight and tapered ones. Microscopic simulations revealed that a self-organized charge up of the capillary walls due to preceding HCI impacts leads to an electric guiding field, which guides the incoming projectile ions along the capillary axes. Ion guiding ensues as soon as a dynamical equilibrium of charge-up by the ion beam and charge relaxation by bulk or surface conductivity is established.

In our measurements [1] we investigated the temperature dependence of ion guiding through a single glass macrocapillary. The sample had an inner diameter of 160 μm , a length of 11.4 mm and made of Borosilicate for which the guiding effect has been previously established. The current experimental set-up allows for a controlled and uniform temperature variation of the glass capillary between -30°C and $+90^\circ\text{C}$. Within such a moderate variation of the temperature the conductivity changes by almost five orders of magnitude. In Figure 1 we show the intensity of the transmitted ions as a function of capillary tilt angle as measured for different capillary temperatures. The experimental points are taken under steady-state conditions, i.e. after reaching a time-independent value of the transmitted intensity. Our experiments show that increasing the temperature of a glass capillary and therefore its conductivity leads to a reduction of guiding and, eventually, to a complete disappearance of the guiding effect.

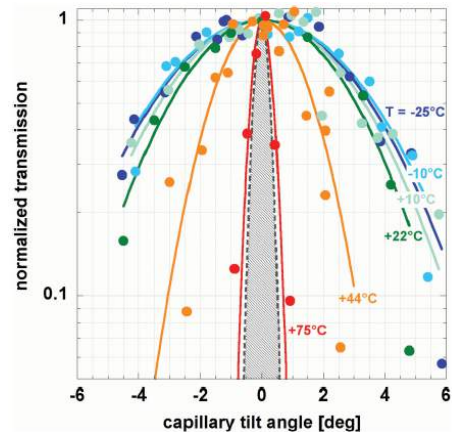


Fig1. Normalized transmission curves $I(\varphi, T)$ for 4.5 keV Ar^{7+} ions guided through a glass capillary for different temperatures ranging from 25°C to 75°C (248 - 348 K). The flux of the incident projectiles was kept constant at about 5000 counts on the position sensitive detector in the $\varphi = 0^\circ$ direction. Gaussian fits through the data points are shown as solid lines. The shaded area indicates the geometric limit of transmission in the absence of guiding.

This strong temperature dependence opens the pathway to improved control of ion-beam guiding thereby can be employed to stabilize guiding against Coulomb blocking due to a high incident ion flux. Exploiting the strong temperature dependence of the electrical surface and bulk conductivities (almost one order of magnitude per $\Delta T = 25\text{ K}$ temperature change) allows for optimization of the transmitted beam either for transmitted current or guiding angle of the transmitted beam.

Acknowledgements

This work has been supported by the European Project ITS - LEIF (No. RII3#026015), by Austrian Science Foundation FWF (SFB041 - ViCoM), and in part by the Hungarian Scientific Research Fund OTKA No. NN 103279.

a) Institut für Angewandte Physik, Technische Universität Wien.

[1] E. Gruber, G. Kowarik, F. Ladinig, J. P. Waclawek, D. Schrempf, F. Aumayr, R. J. Berezky, K. Tőkési, P. Gunacker, T. Schweigler, C. Lemell, J. Burgdörfer *Physical Review A* **86** 062901 (2012).

4.12 Investigation of the conductivity of the borosilicate glass

E. Gruber^{a)}, R. J. Berezky, G. Kowarik^{a)}, J.P. Waclawek^{a)}, D. Schrempf^{a)}, K. Tőkési, F. Aumayr^{a)}

Guiding of highly charged ions through tilted capillaries promises to develop into a tool to efficiently collimate and focus low-energy ion beams to sub-micrometer spot size. While the processes leading to ion guiding are meanwhile conceptually well understood, applications of this technique as a tool for ion-beam formation and the search for tuning parameters to control and optimize highly charged ion transmission are still in their infancy.

In our work [1] we investigated the temperature dependence of the electrical conductivity of the capillary material, a borosilicate glass under the trademark Duran. Both bulk conductivity $\sigma_b(T)$ and surface conductivity $\sigma_s(T)$ were monitored. The basic electrical circuit applied during the measurements is shown in Figure 1. Graphite electrodes in a circular shape were applied to the specimen. On one side, one single electrode covers some area, faced on the other by a smaller circular electrode. It is surrounded by a ring of the same outer diameter, as the electrode on the opposite side.

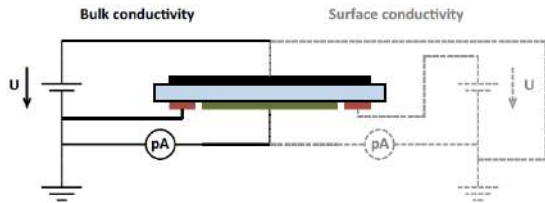


Fig1. Schematic illustration of the electrical circuit used for measuring the bulk conductivity (solid lines) and the surface conductivity (dashed lines). The borosilicate sample (blue) is covered on one side with a circular electrode (black), on the other side a ring electrode (red) is surrounds a central circular electrode (green).

The bulk conductivity is measured by grounding the outer ring, and applying a voltage between the other electrodes. The current is measured with a pico-ampere-meter. We applied voltages between a few volts and 1 kV with an external power supply. To determine the surface conductivity, the measuring volt-

age is applied between the ring and the inner circular electrode. A second kind of geometry was also used, where the electrodes were applied to the inside and the outside, respectively, of a glass tube. There again, three electrodes were used to determine the bulk and surface conductivity independently. In order to avoid any influence by the surrounding, the measurements were actually performed in vacuum. The vacuum vessel was heated and cooled later on, respectively, from the outside by electrical heaters on the one hand, or a fridge on the other. By this, a temperature range from about -18°C to 90°C was covered. The actual sample temperature was monitored by a K-type thermocouple, which was attached to the glass sample.

For the conductivity measurement presented, a voltage of 100 V was applied; this has been chosen as a compromise between avoiding high field effects on the one hand and electronic noise problems in the very low current regime, on the other. When applying a voltage to the sample, the measured current starts to drop immediately, showing some exponential-like behavior. An equilibrium value is reached after a few hours.

We found that the conductivity for both bulk and surface transport displays a steep, approximately exponential, increase with temperature. The near-exponential temperature dependence is key to control guiding by only modest variations of the capillary temperature [1].

Acknowledgements

This work has been supported by the European Project ITS - LEIF (No. RII3#026015), by Austrian Science Foundation FWF (SFB041 - ViCoM), and in part by the Hungarian Scientific Research Fund OTKA No. NN 103279.

a) Institut für Angewandte Physik, Technische Universität Wien.

[1] E. Gruber, G. Kowarik, F. Ladinig, J. P. Waclawek, D. Schrempf, F. Aumayr, R. J. Berezky, K. Tőkési, P. Gunacker, T. Schweigler, C. Lemell, J. Burgdörfer *Physical Review A* **86** 062901 (2012).

5.1 Investigation of diffusional intermixing in Si/Co/Ta system by Secondary Neutral Mass Spectrometry

A. Lakatos^{a)}, G. Erdélyi^{a)}, A. Makovec^{a)}, G.A. Langer^{a)}, A. Csik, K. Vad, D.L. Beke^{a)}

Low temperature analysis of diffusion and intermixing of Co-Si systems are very important in applications for microelectronics and Ultra Large Scale Integration (ULSI) technology. Investigations of the properties of silicon/transition metal contacts are particularly crucial. Indeed transitional metals and their silicides are commonly used as interconnects, Schottky contacts and ohmic contacts in the technology of different electronic devices. In most cases the investigations are focusing on the phase formation kinetics. In early stages of the intermixing, the atomic transport along grain boundaries (GBs) of the metal film certainly plays an important role but it is difficult to observe because the experimental methods are not sensitive enough to map the changes in the concentration profiles.

In this work [1] we give a comprehensive report on degradation and diffusion processes in the Si(substrate)//Co(150nm)/Ta(10nm) system, where the Ta was used as a cap layer. In order to study the initial steps of the Si transport into the cobalt layer, we annealed our samples at 200, 280, 310, 330 and 353 °C for various times. Although there are no data in the literature for Si GB diffusion in Co, other GB diffusion results suggested that a considerable atomic transport along Co GBs should take place in the above temperature interval. The time evolution of the concentration profiles were followed by Secondary Neutral Mass Spectrometry (SNMS).

The samples were prepared by DC magnetron sputtering and were annealed in argon ambient at several temperatures. The SNMS depth profiles shows that the degradation/intermixing starts with fast (grain-boundary (GB)) diffusion of the Si into the Co layer. After some incubation time Si atoms appear and spread over the Co/Ta interface. The Si accumulated at the Co/Ta interface acts as a reservoir for back-diffusion into the Co layer from the Co/Ta interface through the slower grain-boundaries. At higher temperatures the formation of a Co-Si phase was detected at the Co/Si and Co/Ta interface. Three different diffusion coefficients were calculated from the SNMS concentration-depth profiles using "Central-gradient" (CG) and "First-appearance" methods. The observed intermixing was interpreted as a mixture of different "C-type" grain boundary diffusion processes. Furthermore, our experimental results are also compared with computer simulations [2] modelling the grain-boundary diffusion through different grain-boundary paths. From the SNMS profiles measured at different temperatures the activation energy of GB interdiffusion coefficients was deduced using the "CG method".

a) University of Debrecen, Department of Solid State Physics, H-4010 Debrecen, P.O. Box 2, Hungary

[1] A. Lakatos *et al.*, *Vacuum* **86**, 724 (2012).

[2] A. Makovec *et al.*, *Thin Solid Films* **520:6**, 2362 (2012).

5.2 Thermoelasticity and interdiffusion in CuNi multilayers

M. C. Benoudia^{a)}, F. Gao^{a)}, J.-M. Roussel^{a)}, S. Labat^{a)}, M. Gailhanou^{a)}, O. Thomas^{a)}, D. L. Beke^{b)}, Z. Erdélyi^{b)}, G.A. Langer^{b)}, A. Csik, M. Kis-Varga

The idea of observing artificial metallic multilayers with x-ray diffraction techniques to study interdiffusion phenomena dates back to the work of DuMond and Youtz. Interestingly, these pioneering contributions even suggested that the approach could be used to measure the concentration dependence of the diffusion coefficient. This remark is precisely the subject of the present work: we aim to revisit this issue in light of recent atomistic simulation results obtained for coherent CuNi multilayers.

More generally, CuNi multilayers have been extensively studied for their magnetic, mechanical, and optical properties. These physical properties depend critically on interfaces and require a good control on the evolution of composition and strain fields under heat treatment. Understanding of how interdiffusion proceeds in these nanosystems should therefore improve these practical aspects. From a theoretical viewpoint these synthetic modulated structures have been also used as valuable model systems to test the various diffusion theories accounting in particular for the influence of the alloying energy, the coherency strain, and the local concentration. Nowadays, this field remains active and has been extended with the development of atomic simulations and many microscopy techniques like atom probe tomography which give details on the intermixing mechanisms.

We have performed x-ray diffraction experiments on coherent CuNi multilayers to probe thermoelasticity and interdiffusion in these samples [1]. Kinetic mean-field simulations combined with the modeling of the x-ray

spectra were also achieved to rationalize the experimental results. We have shown that classical thermoelastic arguments combined with bulk data can be used to model the x-ray scattered intensity of annealed coherent CuNi multilayers. This result provides a valuable framework to analyze the evolution of the concentration profiles at higher temperature.

The typical coherent CuNi multilayers studied in this work have a modulation length of 6 nm and were annealed up to 367 °C. At intermediate temperature in the thermoelastic regime, we first showed that the classical description based on elasticity theory remains valid to evaluate the coherency strain in these nanosized samples. Considering an interdiffusion coefficient that depends on the concentration [of the type $D(c)=D(0)\cdot\exp(-mc)$], our kinetic simulations reproduce well the time evolution of the first order and second order satellite peaks. The m values ranging from 7 to 8 while $D(0)$ is close to $1.26\cdot 10^{-23}\text{m}^2\text{s}^{-1}$ for two samples studied in detail in this work. These values are consistent with extrapolated bulk diffusion data and with the strong diffusion asymmetry expected in this system. More importantly, the resulting composition profiles and the interdiffusion mode correspond to the layer-by-layer one predicted in the past for this system.

a) IM2NP, UMR 6242 CNRS, Université Aix-Marseille, France

b) University of Debrecen, Department of Solid State Physics, H-4010 Debrecen, P.O. Box 2, Hungary

[1] M. C. Benoudia *et al.*, Phys Rev B **85**, 235404 (2012).

5.3 Structural and magnetic properties of the periodic $[\text{Fe}(5\text{nm})/\text{V}(5\text{nm})]_{10}$ and $[\text{Fe}(3\text{nm})/\text{V}(3\text{nm})]_{20}$ systems

Yu. N. Khaydukov^{a)}, A. Csik, N.S. Perov^{a)}

The layered Fe/V heterostructures are widely used in solid state physics research. Variety of fields where these systems are involved is primarily due to the crystallographic "similarity" of lattice parameters of the vanadium and iron crystals. Both metals in bulk are bcc crystals, having difference in crystal parameters not exceeding several percents, which allows to growth epitaxial heterostructures. Iron in bulk is ferromagnetic with the critical temperature 770 °C. Exchange coupling in Fe can be effectively suppressed by alloying with vanadium [1]. Vanadium, in contrary, is not magnetic, but several studies have shown that near the interface with iron it is polarized antiparallel to the magnetization of the iron (the size of the polarized area in order of 1 nm). Magnitude of the magnetic moments depends on the quality of the interface and makes value $(0.1 \div 1)\mu_B$. In addition, it is worth to mention the indirect exchange interaction of iron layers through the vanadium spacer [2] which can lead, at certain thicknesses of vanadium spacers, to the antiferromagnetic coupling of two neighboring Fe layers. This coupling can be affected by absorption of the hydrogen which leads to the effective change of the thicknesses of V layer.

In this work experimental study of structural and magnetic properties of two Fe(d)/V(d) (d=3nm and 5nm) periodic structures have been done. Studies identified a number of structural features of systems that affect

their magnetic properties. It was shown that ferromagnetic islands are formed on the interfaces of Fe and V. These islands have different magnetic properties as sub-layers of pure iron.

Synchrotron diffuse scattering and magnetometry data indicate on the presence of the in-plane anisotropy of structural and magnetic properties in periodic Fe/V structures. In addition, magnetometry data indicate the presence of two magnetic phases in both samples. On this basis, we propose the following model which qualitatively describes our data. It is a well-known fact that the deposition of Fe/V structures with thicknesses of V greater than 2 nm goes in a 3D mode [3]. It means that on the interface between Fe and V layers the formation of islands take place. The presence of steps on the hysteresis loop suggests that the magnetic properties of these islands, especially coercive force, different from those of sub-layer of pure iron. At thicknesses of 2-3 nm of V layer islands are quite isotropic, which is confirmed by magnetometry and synchrotron diffuse scattering. At the further growth of the V layer, islands stretch along one direction. Due to the shape anisotropy, islands are only can be magnetized applying magnetic field along one of the axis of the islands.

a) Moscow State University, Moscow, Russia

[1] J. Aarts *et al.*, Phys Rev B **56**, 2779 (1997).

[2] C. Clavero *et al.*, Phys Rev B **80**, 024418 (2009).

[3] P. Granberg *et al.*, JMMM **186**, 154 (1994).

5.4 Analysis of InGaP/Ge heteroepitaxy

P. Joice Sophia^{a)}, G. Attolini^{a)}, M. Bost^{a)}, E. Buffagni^{a)}, C. Ferrari^{a)}, C. Frigeri^{a)}, K. Vad, A. Csik, Z. Zolnai^{b)}, D. Arivuoli^{c)},

InGaP is the basic material for many electronic and optical devices, such as heterojunction bipolar transistors, metal oxide semiconductor field effect transistors (MOSFETs), light emitting diodes and multi-junction solar cells. High efficiency solar cell germanium junctions are usually realized by diffusion between a Ge substrates and epitaxial GaS or InGaP layers, i.e. by the dopant element diffusion into the Ge at high temperature [1].

In the present work, we report the study of InGaP/Ge heterojunctions grown by metal organic vapor phase epitaxy at different growth temperatures, with the aim to analyze the element diffusion into the p-type germanium substrate, in order to realize n-p junctions. Secondary Neutral Mass Spectrometry (SNMS), Rutherford Backscattering Spectrometry (RBS), High Resolution X-Ray Diffraction (HR-XRD), Transmission Electron Microscopy (TEM) and Atomic Force Microscopy (AFM) have been used to characterize the layers. The InGaP films were grown on a Ge (001) substrate by Metal Organic Vapor Phase Epitaxy (MOVPE) technique in a horizontal reactor without substrate rotation at temperature ranging between 600 to 675 °C and at 60 mbar. The precursors were trimethylgallium (TMG) and trimethylindium (TMI) for the elements of group III and phosphine in a 10% mixture with hydrogen for the elements of group V.

XRD diffraction showed the presence of strain release combined with peak broadening, the latter ascribed to compositional variation. From RBS measurements, it can be stated that a high degree of P diffusion towards Ge does

not occur, even if the detection limit for P is quite high (being several atomic percent, because of the Ge background).

Surface analysis by AFM showed a dependence of surface roughness on temperature, while SNMS technique reported the presence of interdiffusion with no significant temperature dependence. Mutual diffusion of Ga, In, P in the substrate and of germanium in the film can be observed. It is evident that the elements of the film diffuse much more than germanium, in particular phosphorous is present in greater quantities. The trend is similar for all samples, regardless of the growth temperature [2].

The analysis by HRTEM showed the presence of antiphase boundaries, twins and stacking faults: the last were observed to originate preferentially near antiphase boundaries. We observed that twins are preferentially nucleated near antiphase boundaries about 30-50 nm from the interface. This behaviour does not depend on temperature which suggests that this is due to some instability in the gas phase.

Further optimization of growth conditions will be necessary to improve InGaP epitaxy.

a) IMEM-CNR Institute, Parma, Italy

b) Research Institute for Technical Physics and Materials Science, Hungarian Academy of Sciences, Budapest, Hungary

c) Crystal Growth Centre, Anna University, Chennai, India

[1] R.R. King *et al.*, *Progress in Photovoltaics* **20:6**, 801 (2012).

[2] T-Y. Sheong *et al.*, *Appl Phys Lett* **70**, 3137 (1997).

5.5 Evolution of the structure and hydrogen bonding configuration in annealed hydrogenated a-Si/a-Ge multilayers and layers

C. Frigeri^{a)}, M. Serényi^{b)}, A. Csik, Zs. Szekrényes^{c)}, K. Kamarás^{c)}, L. Nási^{a)}, N.Q. Khánh^{b)},

Among the present available renewable energy sources, energy harvesting from sunlight by means of photovoltaic cells is the most attractive one. In order to win over the traditional energy resources both efficiency and cost effectiveness of photovoltaic conversion must be optimized as far as possible. Efficiency is basically improved by the use of multijunction cells containing semiconductors with different band-gap. In this respect, the III-V compounds guarantee the highest efficiency, up to 41.6 %, but they are quite expensive. The latter drawback also affects other compounds like CdTe and $\text{CuIn}_{1-x}\text{Ga}_x\text{Se}_2$ (CIGS). Si based solar devices have lower efficiency but are much more cost effective. They can use either crystalline or amorphous Si thin layers or Si nanoparticles.

As to the thin films, amorphous Si (a-Si) is preferred to crystalline Si as it has a wider band-gap (1.7 instead of 1.1 eV) thus harvesting a larger portion of solar energy. A tandem cell is formed by using a-SiGe which has a smaller band-gap tunable between 1.1 and 1.7 eV depending on the Ge content. The best value should be 1.4 eV since the material properties seem to degrade below this value whilst the photo-conductivity drops after light soaking if the band gap exceeds 1.4 eV. A key issue of amorphous Si, Ge and SiGe is the high density of defects in the band-gap mostly due to dangling bonds whose density is particularly high (even up to $5 \cdot 10^{19} \text{ cm}^{-3}$) since the lattice is significantly disordered with distorted bond angles and lengths. This increases the probability of rupture of the Si-Si (Ge-Ge) bonds, i.e., formation of dangling bonds. Owing to the fact that hydrogen with its single electron structure can close the dangling bonds, their density can be reduced even by 4 orders of magnitude by doping with hydrogen. However, H is unstable in the host lattice. In fact,

several findings showed its evolution from the thin layer upon annealing and that its bonds to Si (Ge) can be broken under strong illumination (Staebler-Wronski effect). Moreover, the H bond to Si (Ge) may have several configurations (mono-, di-, tri-hydride as well as chains of them) that can change in density and type depending on the growth conditions and applied heat treatment.

In this work the relationship between morphological structure and H bonding configuration in sputtered a-Si/a-Ge multilayers (MLs) and a-Si layers submitted to annealing has been studied by AFM (Atomic Force Microscopy) and Fourier transform infrared (FTIR) spectroscopy. After annealing the samples exhibited blisters whose size and height increase with increasing annealing time/temperature and/or H content. Similarly, FTIR showed that the total H bonded to Si and Ge, in the case of MLs, or to Si, for the single a-Si layers, decreased in the annealed samples indicating that H is released from its bonds to the host atoms. In the MLs the H release was quicker in Ge than in Si because of the smaller binding energy of the Ge-H bond with respect to the Si-H one. It is hypothesized that the liberated H atoms gathered into nano-cavities where they could react with each other producing molecular H_2 . The growth in size of the nano-cavities, both by coalescence at the beginning and later also by thermal expansion of the trapped H_2 gas, is argued to eventually produce larger H_2 -containing bubbles that may plastically deform the layer with formation of surface blisters.

- a) IMEM-CNR Institute, Parma, Italy
- b) Research Institute for Technical Physics and Materials Science, Hungarian Academy of Sciences, Budapest, Hungary
- c) Institute for Solid State Physics and Optics, Wigner Research Centre for Physics, Hungarian Academy of Sciences, Budapest, Hungary

6.1 Time-resolved photoelectron emission from surfaces

C. Lemell^{a)}, K. Tókési, and J. Burgdörfer^{a)}

Recent theoretical and experimental investigations have shown that the emission time contained in streaked energy spectra contains a wealth of information which cannot be determined by other spectroscopic means. Even for simple atomic systems extraction of all relevant contributions is challenging. In the case of extended systems such as solid surfaces excited by energetic photons, the situation is further complicated by multiple scattering and dissipative processes.

In this work we have concentrated on emission time delay due to transport effects for core and conduction band levels of metallic systems with electron energies of about 100 eV (see Fig. 1). We model the target as amorphous with bulk values for the atomic and electron densities together with quantum mechanically calculated cross sections providing information about scattering events (i.e. the mean free path). Possible long-range effects of the positive hole left at the point of excitation as well as interface effects are not included in our simulation. The latter can be neglected in the special cases selected for our study as they would cancel out in the determination of the relative delay between lines.

For systems for which preliminary experimental results exist, excellent agreement with simulated data is found [1]. The approximation in terms of an amorphous target appears to be justified for electron energies ≈ 100 eV. Pronounced crystal-structure related effects should appear for smaller excitation energies which, however, are difficult to resolve in experimental investigations due to the ATI background in the energy spectra. Pronounced crystal-momentum effects were originally assumed to cause larger delay times between conduction band and bound state lines in the experiment by Cavalieri et al. [2]. Effects from different timing contributions of electrons interacting with core and conduction band holes such as dynamic screening remain to be accounted

for. Crystal dependent features in the dispersion relation can, in principle, be observed using adlayer systems if the photon energy of the exciting XUV pulse is scanned. Further works are in progress in this line.

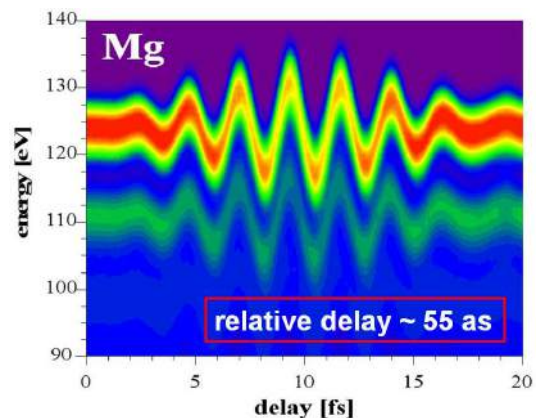


Figure 1. Streaking spectrum of bulk Mg. Two well separated lines from excited conduction band electrons can be observed. Top line: no energy loss; bottom line: electrons have excited a plasmon in the electron gas. The relative delay is about 55 as.

Acknowledgements

This work was supported by the Austrian Fonds zur Förderung der wissenschaftlichen Forschung under grants no. FWF-SFB016 ADLIS, FWF-SFB041 ViCoM, and no. 17449, the European ITS-LEIF network RII3 026015, and the TeT Grant No. AT-7/2007. We thank the group of R. Kienberger (MPQ Garching) for making their latest data available to us prior to publication.

a) Institute for Theoretical Physics, Vienna University of Technology, Wiedner Hauptstraße 8-10, A-1040 Vienna, Austria

[1] C. Lemell, K. Tókési, and J. Burgdörfer, *Journal of Physics: Conference Series* **388** (2012) 012048.

[2] A.L. Cavalieri, N. Müller, Th. Uphues, V.S. Yakovlev, A. Baltuska, B. Horvath, B. Schmidt, L. Blümel, R. Holzwarth, S. Hendel, M. Drescher, U. Kleineberg, P.M. Echenique, R. Kienberger, F. Krausz and U. Heinzmann, *Nature* **449** (2007) 1029.

6.2 Interface study by SNMS

V. Takáts, A. Csik, J. Hakl, K. Vad

Secondary neutral mass spectrometry (SNMS) is a well known destructive method for depth profiling in material science. The depth resolution can achieve several nanometers. Study of surfaces and interfaces in layered structures by depth profile analysis (DPA) help to understand the behaviour of adjacent layers or doping elements. It is also an excellent method to investigate materials and compounds even at nanometer scale. To achieve such results, a correct interpretation of the acquired spectrum is required.

The knowledge of depth concentrations of constituents of layered structures is very important for research and technological developments. An accurate method for the quantitative analysis of depth composition profiles with high depth resolution is essential for investigating the formation conditions, growth kinetics, and stability of thin-film systems with possible concentration gradients. Determination of depth distributions of constituents often uses mathematical methods which are based on approximations. These calculations are based on theoretical estimations for some well defined sample groups or measurements. The Mixing-Roughness-Information-depth (MRI) model of S. Hofmann [1,2] makes it possible also to reconstruct the depth concentration profile determined by AES and SIMS. Its disadvantage is that the MRI model is only applicable partially for SNMS technique. Though AES and SIMS depth profiling yield a good depth resolution, they can have several artefacts as atomic mixing at the sputter surface, preferential sputtering of the specimen components, and implantation [3,4]. Using high energy ions for sputtering, the effect of these undesirable phenomena increases.

Since SNMS strictly separates the emission and ionisation of sputtered constituents, it is an excellent sputtering technique for DPA

[5,6]. In ion sputtering processes the sputtered elements mostly remain in neutral state, only less than 1% is ionised. The ionization happens in the matrix before the particles escape from the sample surface, and the ionization of degree depends on the matrix material. This is called as matrix effect. Contrary to the direct detection of secondary ions, the analysis of neutral particles can effectively eliminate the matrix effect. After a subsequent post-ionization of neutral particles, they are ideally suited for quantitative elemental and DPA of any material. Minimal matrix effect renders a very accurate material analysis possibility.

Since models used to reconstruct depth concentration profiles measured by SIMS or AES are not fully applicable for SNMS analyses, a mathematical model based on statistical and probability calculations of surface morphology is required. Surface roughness, sputtered crater shape, detection rate of different constituent elements, and some other complex nanoscale physical behaviours must be taken into account and studied systematically for sufficient mathematical analysis. The goal is to develop and apply a new procedure for DPA of the samples having high surface roughness. Our experience shows that the depth resolution is mainly determined by the surface roughness and the crater shape.

- [1] S. Hofmann, *Thin Solid Films* **398-399**, 336-342 (2001).
- [2] S. Hofmann *et al.*, *Surf Interface Anal* **30**, 228 (2000).
- [3] D. Briggs *et al.*, *Practical Surface Analysis - Auger and X-ray Photoelectron Spectroscopy* **1-2**, 228 (1990), Ed.: J.Wiley & Sons.
- [4] S. Hofmann *et al.*, *Rep Prog Phys* **61**, 827 (1998).
- [5] H. Oeschner *et al.*, *J Vac Sci Technol A* **17:6**, 3401 (1999).
- [6] K. Vad *et al.*, *Spectroscopy Europe* **21**, 13 (2009).

7.1 Improvement and optimization of sealed tube graphitization

L. Rinyu, G. Orsovski^{a)} M. Molnár, A. Horváth, É. Sarkadi-Pribóczky, M. Veres^{b)}

In this report, we would like to present the status of our sealed graphite preparation line and how we have employed and tuned to serve our new MICADAS system. After we carried out the first successful test measurements on the ETHZ MICADAS AMS [1], we have developed a gas handling line, which is capable to routinely handle eight independent sealed tube reaction units simultaneously.

We investigated how the 3 different (440, 500 and 550 °C) preheating temperatures (in case of sealed tube graphitization process, during preheating hydrogen gas gets released from the solid TiH₂) influences the properties of the formed graphite.

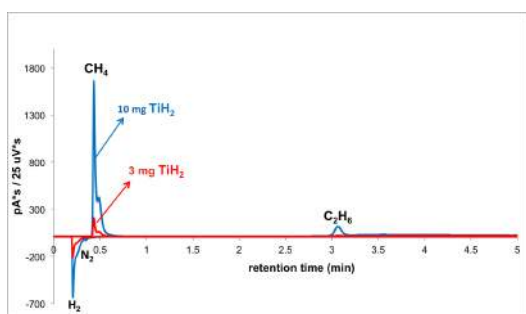


Figure 1. Residual gas constitution after sealed tube graphitization. HP-PLOT Molsieve 5A, 15m · 0.53mm, 0.25 μ m (film thickness). Oven: 35°C (2 min) 40°C/min to 250°C (hold 7.5 min). Carrier: Argon. Injection: 500 μ l loop. Detection method: TCD and FID.

The ratio of the hydrogen and carbon-dioxide is important in the reaction cell, as the higher hydrogen ratio increases the possibility of methane formation. In case of sealed tube graphitization, the determination of the actual hydrogen volume is not simple, since the zinc reagent re-processes the hydrogen from the water vapor. We decreased the amount of the TiH₂ reagent to 3 mg to analyze the ratio of methane in the residual gases by gas chromatography after the graphitization process. The preliminary results indicate that the methane ratio is lower in case of 3 mg TiH₂ than in case of 10 mg TiH₂ (Fig 1.). We found

that the smaller TiH₂ amount decreases the background level in case of every investigated preheating temperature and the smallest blank level was measured at 500 °C. The measured isotopic fractionation is also decreased by the reduced amount of TiH₂ (Fig 2.).

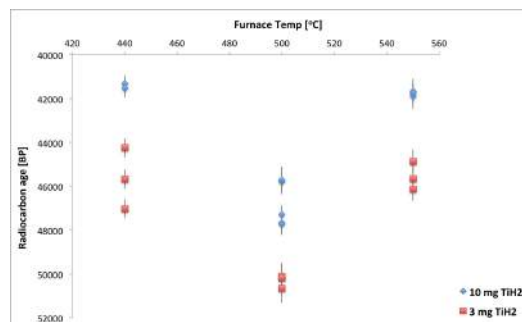


Figure 2. Preheating temperature and TiH₂ quantity influence on blank level.

Another important result is that the scatter of the oxalic acid standards were also smaller in case of 3 mg TiH₂ reagent for each applied preheating temperature. However, the smaller amount of TiH₂ slightly decreases the ion current (Fig3).

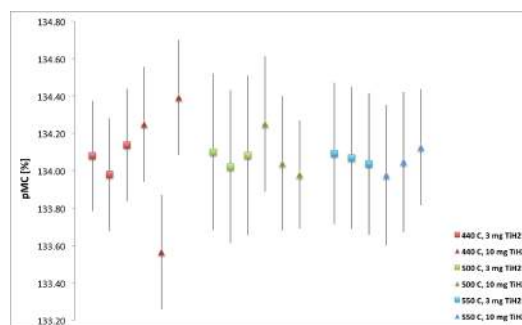


Figure 3. Preheating temperature and TiH₂ quantity influence on the scatter of the oxalic acid standard.

- a) University of Debrecen
- b) Isotoptech Co Ltd., Debrecen, Hungary

[1] L. Rinyu, M. Molnár, I. Major, T. Nagy, M. Veres, Á. Kimák, L. Wacker, H.-A. Synal, NIMB **294** (2013) 270.

7.2 Stable isotopes and noble gas constraints on the genesis of therapeutic waters, SE Poland

L. Palcsu, L. Papp, M. Molnár, Z. Major, G. Koltai, I. Futó, S. Halas^{a)}, A. Baran^{a)}

In the cooperation between Marie-Curie-Sklodowska University, Lublin, Poland and the Hertelendi Laboratory of Studies, the aim was to further investigate the origin of two unique therapeutic water areas of Southern Poland by using noble gas measurements. Water samples were taken into copper tubes equipped with pinch-off clamps. Noble gas measurements were performed in the Hertelendi Laboratory of Environmental Studies, Hungary (for description of the used method see [1]).

Horyniec Spa: Róża-III seems to be groundwater that infiltrated the surface in the middle Holocene (^{14}C content: 25.55 pMC, water age ≈ 6000 years). Using the closed-system equilibration model, a reliable noble gas recharge temperature of 7.6 °C could be calculated.

Iwonicz-Zdrój and Lubatowka: Lubatówka waters are enriched in helium. They are mainly of crustal origin, which is evidenced by the isotope ratios. These low R/R_a ratios (0.012 and 0.014) show that radiogenic ^4He prevails in these waters (Table 1). It is in good agreement with the previous findings of Porowski [2], Baran and Halas [3] who concluded that Lubatowka waters are a mixture of three types of water: meteoric water, pore water (connate water) and dehydration water. The other noble gases, namely neon, argon, krypton and xenon could not be detected in the Lubatówka samples. Most probably the water is in contact with a huge gas phase composed of mainly methane, and the atmospheric noble gases could escape from the water to the gas phase.

Additionally, methane gas bubbling through the saline aquifer could carry away the initially dissolved gases from the water. This water contains methane which also has light carbon isotopic composition, whilst carbon isotope ratio of bicarbonate attained extremely heavy $\delta^{13}\text{C}_{PDB}$ values (+19.9 to +24.0 ‰) as the result of isotope fractionation.

Iwonicz-II, Klimkówka-27 and Elin-7 waters contain relatively low concentrations of He, close to the solubility equilibrium (Table 1). The R/R_a (0.96-0.98) of Iwonicz-II and Elin-7 waters is close to the atmospheric ratio. Klimkówka-27 waters contain a small amount of radiogenic He, which is evidenced by the R/R_a value (0.47). These samples have suffered subsurface degassing. The lack of heavier noble gases concerning Ne-Ar-Kr-Xe concentrations can be explained either by mixed origin with a substantially low saline end-member component or by the dilution of noble gas concentrations in the methane rich waters. Using two degassing models we could calculate recharge temperatures (13.0°C, 14.4°C and 18.4°C), but these temperatures have to be handled with care.

a) Marie-Curie-Sklodowska University, Lublin, Poland

[1] L. Papp, L. Palcsu, Z. Major, L. Rinyu, I. Tóth, *Isotopes in Environmental and Health Studies* **48** (2012) 1-18.

[3] A. Porowsky, *Studia Geologica Polonica* **125** (2006) 5-67.

[2] A. Baran and S.Halas, *Biuletyn Panstwowego Instytutu Geologicznego* **444** (2011) 5-14.

Table 1. The noble gas composition of the sampled waters

	He [ccSTP/g]	Ne [ccSTP/g]	Ar [ccSTP/g]	Kr [ccSTP/g]	Xe [ccSTP/g]	R/R_a (helium)	^{14}C [pMC]	NGT [°C]	Remark
Horyniec Róża-III	3.715E-07	2.792E-07	4.549E-04	1.034E-07	1.462E-08	0.210	25.55	7.6	
Lubatowka-12	6.046E-06	bellow det.	bellow det.	bellow det.	bellow det.	0.012	-	-	Lot of gas (CH_4)
Lubatowka-14	1.049E-06	bellow det.	bellow det.	bellow det.	bellow det.	0.014	-	-	Lot of gas (CH_4)
Iwonicz-II	4.602E-08	1.373E-08	2.419E-04	6.632E-08	1.025E-08	0.978	-	13.0	Contains CH_4
Klimkówka27	5.728E-08	1.294E-07	2.843E-04	6.682E-08	9.212E-09	0.470	-	18.4	Contains CH_4
Elin-7	4.978E-08	9.648E-08	2.377E-04	6.097E-08	9.657E-09	0.961	-	-	-

7.3 One year aerosol fossil carbon trend in Debrecen city air

I. Major^{a)} E. Furu, L. Haszpra, Zs. Kertész, M. Molnár

Inspired by the results of the fossil atmospheric carbon-dioxide measurements our programme was enhanced by including the investigation of atmospheric aerosols to obtain a more representative view regarding anthropogenic contribution of the atmospheric carbon species. For ^{14}C measurements, special sample preparation system and method was developed for the tiny total carbon content of the aerosol samples collected at the same location (ATOMKI backyard) synchronously with the carbon dioxide observations. The radiocarbon measurement of the aerosol samples was performed by a high-sensitivity accelerator mass spectrometer (AMS) of ATOMKI dedicated to environmental samples (EnvironMICADAS).

During the winter heating period, due to the meteorological conditions (frequent thermal inversion, decreasing rate of mixing and upwelling), significantly higher total $\text{PM}_{2.5}$ concentrations can be observed close to the surface, which is also reflected in the quantity of the total carbon. The trend of the fossil CO_2 excess is very similar to the fossil carbon content of the total $\text{PM}_{2.5}$. On the other hand during the winter time heating periods the extreme high observed aerosol concentrations in the city air seems to be caused by biomass com-

bustion. It is well-visible from the aerosol C-14 measurements that the relative ^{14}C content of the aerosol increases in the heating period in the $\text{PM}_{2.5}$, even compared to the summer period.

It can be stated that the fossil carbon content of the atmospheric CO_2 and the $\text{PM}_{2.5}$ show similar trend during the monitoring period, however, on a different scale. In absolute terms, the fossil part of the $\text{PM}_{2.5}$ increased as well in the heating period, however even this value was exceeded by the increment of the modern carbon from the biomass combustion showing the dominant role of the high aerosol emission due to the municipal wood combustion.

The project was performed in part of the New Hungary Development Plan under Project No. GOP-1.3.1-09/A-2009-0032. The research was supported by the Hungarian NSF (OTKA-81515 and OTKA-77550). The publication is supported by the TÁMOP-4.2.2/B-10/1-2010-0024 project. The project was co-financed by the European Union and the European Social Fund.

a) University of Debrecen, Debrecen, Hungary

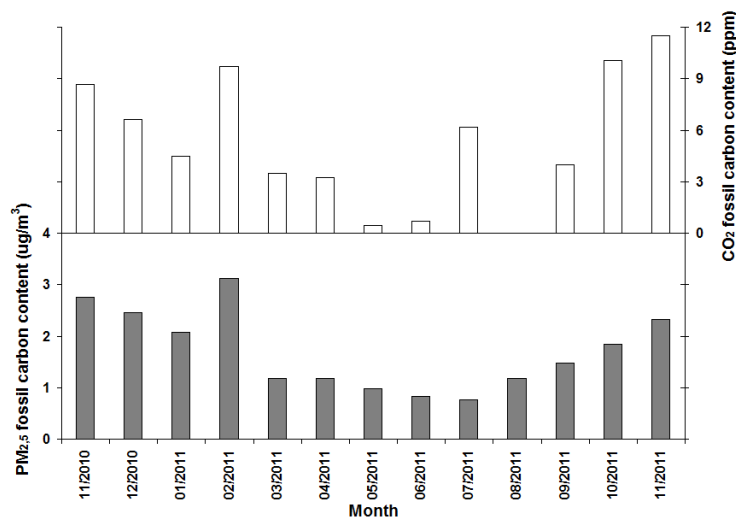


Figure 1 Trends of the $\text{PM}_{2.5}$ and excess CO_2 fossil carbon content in 2010

7.4 Pilot study of nitrogen utilisation in maize

I. Futó, L. Palcsu, E. Heim^{a)}, A. Czébel^{a)}, G. Vodila

In the cooperation between KITE Ltd., Nádudvar, Hungary and the Hertelendi Laboratory of Environmental Studies, the aim was to determine the ideal locations of fertilising, the ideal distance of rows for the ideal production yield.

To track the nitrogen utilisation of maize (*Zea mays*) ^{15}N enriched NH_4NO_3 fertiliser [1] was introduced among the usual fertilisers in the maize field of KITE Ltd. Nádudvar, Hungary on 30th March 2012, before sowing. Four maize samples were taken from different areas of different fertiliser treatment (non-fertilised and non-labelled, fertilised and non-labelled, fertilised and labelled between the rows and fertilised and labelled within the rows) and from different development stages of the plant on 22nd May, 8th June, 6th July and 7th September being sampling periods 1-4, respectively. The plant samples were sub-sampled based on organs: root, stem and leaf. Samples were dried to constant mass and pulverised. The ^{15}N measurements were made by a Thermo Finnigan Delta^{PLUS} XP isotope ratio mass spectrometer coupled with an elemental analyser [2].

In case of non-fertilised and non-labelled plants, all the three organs were getting ^{15}N depleted with time, most intensively the stem and the less intensively the root (Figure 1).

For the leaves and stems of the fertilised and non-labelled plants, the tendency in time is very similar to the ones of the non-fertilised and non-labelled plants, however, the roots of the fertilised and non-labelled plants got significantly enriched in the sample of September.

In case of the fertilised and labelled-between-the-rows samples, labelling is slightly seen as the delta values are positive. These values are significantly lower than the ones for the fertilised and labelled-within-the-rows

plants. It is seen that fertiliser got to the vegetation in the largest extent in this layout. Labelling showed its maximum intensity in the second sampling (8th June) showing that the metabolism and the development of the plant is the most intensive in this period of the year, and later these highly enriched $\delta^{15}\text{N}$ values were significantly decreasing showing the lower rate of metabolism.

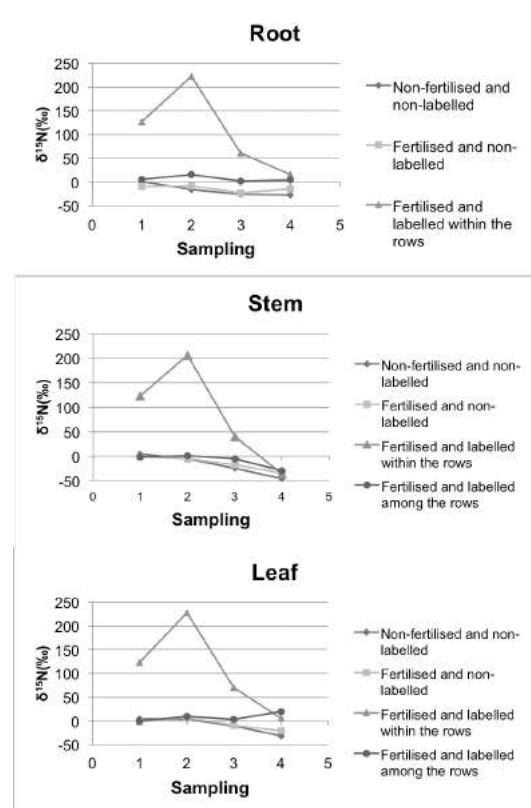


Figure 1. $\delta^{15}\text{N}$ values of the root, leaf and stem samples from different sampling periods (sampling periods 1-4 are for 22nd May 8th June, 6th July and 7th September, respectively).

a) Isotoptech Co Ltd., Debrecen, Hungary

[1] D.L. Karlen, P.G. Hunt and T.A. Matheny Crop Science, **36** (1996) 975-981.

[2] Z. Muccio and G.P. Jackson, Analyst, **134** (2009) 213-222.

7.5 Egg origin determination efforts

A. Horváth, I. Futó, G. Vodila, L. Palcsu

As a co-operation with the Poultry Product Board, egg and drinking water samples were received in order to investigate whether the country of origin of the egg can be determined based on its stable isotope composition with the aim of market protection of the Hungarian eggs against the mislabelled foreign ones. The scientific background is that drinking water of egg laying hens is assumed to reflect the composition of regional precipitation, and it is also an input data in the process of egg formation.

In the first sampling, altogether 23 sets of egg and drinking water samples were received from different production sites covering the whole area of Hungary. The egg white samples were vacuum distilled and frozen out by liquid nitrogen at -196°C . The process was monitored by two vacuum gauges. Water frozen out together with the drinking water samples was measured by a Thermo Finnigan Delta^{PLUS} XP isotope ratio mass spectrometer using a GasBench II peripheral unit equipped with a GC-autosampler. As a second issue, additionally, elemental composition of egg shells were also performed for series of Hungarian, Czech and Polish egg samples by energy dispersive X-ray fluorescence.

The drinking waters fit well to the Global Meteoric Water Line indicating their precipitation origin [1].

It was experienced that the water in egg white gets enriched compared to the drinking water ($\Delta^{18}\text{O} = -4.9 \pm 1.0\text{‰}$ and $\Delta_D = -21.8 \pm 6.4\text{‰}$), however, this shift is independent of the type of the hens, since the mean shifts in the eggs of Tetra and Hy-line hens are similar within error bar.

For more depleted drinking water, the shift of the egg white was higher than for more enriched ones. This can be due to the contribution of the nutriment isotopic composition.

The water isotope composition of the Hungarian eggs investigated was $\delta^{18}\text{O} = -4.8 - -7.3\text{‰}$ and $\delta\text{D} = -46.0 - -70.7\text{‰}$, therefore

egg whites outside this interval, foreign origin can be assumed, since the isotope ratio of the drinking water samples covers natural waters characteristic for Hungary. As a conclusion, the same applies for eggs, as well.

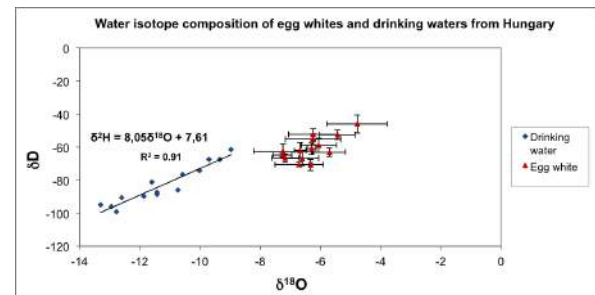


Figure 1. Water isotope composition of egg whites and drinking waters from Hungary

The three foreign egg samples can be separated from the Hungarian ones based on their $\delta^{18}\text{O}$ and δD values, however, differences in the shifts compared to their own drinking water samples masks the region-specific information of the drinking water.

From the micro elemental composition of the egg shells it can be stated that the identification of the samples can be performed with a precision of 97.1%, therefore differences in the elemental composition are large enough to characterise the origin of the eggs by the elemental analysis of the egg shell.

It is recommended from the market protection point of view that to compare the elemental composition data of the shell of the supposedly foreign egg with an information database established for each production plant in Hungary. As on the information stamp of the mislabelled eggs the code of a Hungarian production plant is seen, it would be comparable with the real eggs originating from that plant. In this way, foreign eggs may be filtered out. Of course, to verify this method, further investigations are required.

[1] H. Craig, Science **133** (1961) 1702-1703.

7.6 ^{14}C measurement from dissolved organic carbon of groundwater at the Püspökszilágy RHFT

R. Janovics, A. Molnár^{a)}, J. Orsovszki^{a)}, M. Molnár

Generally radiocarbon content of groundwater is referred to the activity of dissolved inorganic carbon (DIC) which is in the water in the form of mainly HCO_3^- and CO_3^{2-} depending on pH. The dissolved carbon can be found in organic form besides the inorganic form as well. In the surrounding of the Püspökszilágy Radioactive Waste Treatment and Disposal Facility (RWTDF) groundwater monitoring well network is operating, from which radiocarbon measurement occurs systematically from the DIC fraction of the water. On the basis of results of previous measurements it is suspicious that in the monitoring wells besides the inorganic fraction small amount of organic fraction with much higher ^{14}C activity can be found. For this reason we adapted and improved a method [1] for measuring directly ^{14}C from dissolved non-purgeable organic carbon (NPOC). The main point of the method is that water samples are acidified with H_3PO_4 so that the dissolved inorganic carbon can be released as CO_2 . After the acidification the water sample is evaporated down in a 35°C water bath with the help of a membran pump. With this step the inorganic carbon and water content of the water sample are eliminated. Phosphoric acid and NPOC remain in the bulb. Thereafter chromosulfuric acid is given to the sample which oxidizes NPOC to CO_2 . The originating CO_2 is prepared to AMS measurement. The elaborated method is validated with international ^{14}C reference materials (IAEA-C6 and IAEA-C9). During the experiments the DIC, total carbon (TC) and NPOC ^{14}C activity of the same water sample were measured and compared. The results of the DIC and TC measurements do not differ from each other sig-

nificantly (Table 1).

Table 1. ^{14}C content of different fractions of groundwater (pMC) (uncertainty: $<0.5\%$)

sample	DIC (pMC)	TC (pMC)	NPOC (pMC)	NPOC (Bq/dm ³)
Psz-11	87.9	86.4	324.6	0.0011
Psz-55	88.5	83.0	387.9	0.0022
Psz-57	34.6	35.2	232.6	0.0018
Psz-54	473.3	480.2	151920.0	1.0700
Némedi-creek	100.5	98.6	96.0	0.0012

NPOC results show unexpected values compared to the control TC and DIC measurements. The NPOC fraction of Psz-54 well gave the most extreme value (151.920 pMC). Moreover in every examined groundwater monitoring well (Psz-11, Psz-55 and Psz-57) next to the disposal facility dissolved organic material having 2-3 times higher ^{14}C content (200-300 pMC) than the natural level can be found. Sample from Némedi-creek near the disposal facility gave ^{14}C value around 100 pMC according to the natural level in the case of NPOC measurement. On the basis of our results it can be stated that from the Radioactive Waste Treatment and Disposal facility ^{14}C in the form of dissolved organic carbon is released to the groundwater with occasionally very high specific activity. But these values are represents of very low activity concentration in Bq/dm³ because the NPOC content of groundwater is negligible.

a) University of Debrecen, Debrecen, Hungary

[1] G.S. Burr, J.M. Thomas, D. Reines, D. Jeffrey, C. Courtney and A.J.T. Jull, Radiocarbon **43** (2001) 183

7.7 A new combustion and CO₂ purification line for AMS C-14 measurement

R. Janovics, A.J.T. Jull^{a)}, M. Molnár

In most cases of AMS sample preparation is necessary to produce high purity CO₂ from organic and inorganic samples as well. For this purpose a combustion and CO₂ purification line were designed and constructed at the HEKAL ATOMKI. For combustion of samples, we used a system similar to that at the University of Arizona. Samples can be combusted in the presence of CuO or oxygen gas. The carbon dioxide is cryogenically separated from water at -78°C, passed over Cu/Ag to reduce nitrogen oxides and remove halogens, and trapped in a known volume at liquid nitrogen temperature. The gas is then transferred to a sealed tube for the graphitization. To build the system, Na-borosilicate glass tubes by Pyrex and glass valves by Kontes with Viton sealings. The lubrication of the glass valves are performed with Apiezon vacuum grease, which has a vapour pressure of 10⁻⁹ mbar. The parts are attached by stainless Ultratorr fittings by Swagelok. The final pressure of the system is 3x10⁻⁵ mbar ensured by an SH-110 dry scroll vacuum pump by Varian and a Navigator 301 turbomolecular pump. Between the system and the turbomolecular pump, there is a freeze-out trap frozen by liquid nitrogen. For the measurement of the vacuum, an Edwards WRG vacuum gauge is used. In the case of CuO combustion, the temperature necessary for the oxidation is produced by a gas torch of 1100°C.

In the case of low-temperature controlled stepped combustion, a Watlow tube oven with a precision temperature controller is used. To check the combustion process, a vacuum tight stainless steel Swagelok manometer is used. The gas is passed through a tube at a 1000°C filled by quartz pearls (Fig 1/2), which ensures complete conversion to CO₂. The quartz oven is followed by two spiral freeze-out traps with a functional length of ≈500 mm each. The first freeze-out trap (Fig 1/4.a.) is cooled by the mixture of isopropyl-alcohol and dry ice to -78°C, and removes the water vapour from the combustion process. The next freeze-out trap (Fig 1/4.b.) is frozen by liquid nitrogen to -197°C and is used to freeze out the CO₂ generated and to pump away waste gases. Gases frozen out at -197°C pass through a catalyst oven (Fig. 1/6) at 500°C filled with elemental copper and silver to eliminate sulphur, nitrogen oxides and halogens. After the oven, there is a second -78°C trap to remove the water vapour generated in the course of the reduction. The determination of the quantity of the CO₂ gas is made in a calibrated volume using an MKS Baratron pressure gauge (Fig. 1/9a). The calibrated volume can be split into two equal parts. One half of the sample gets graphitised (Fig 1/9.b.) while the other half gets reserved in a sealed glass tube (Fig 1/9.c.).

a) NSF Arizona AMS Laboratory, University of Arizona, Tucson, USA

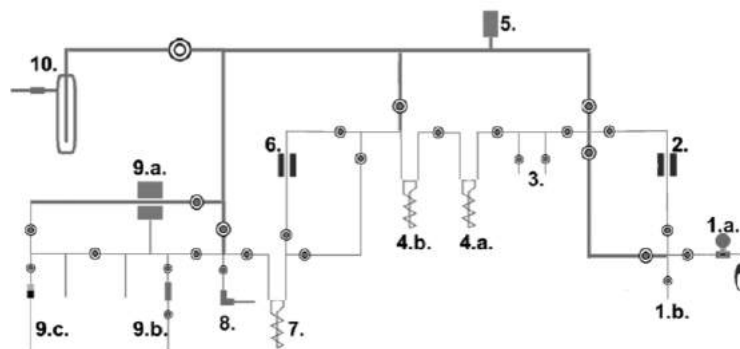


Figure 1 Scheme of the on-line combustion and CO₂ purification line, adopted from UA.

7.8 Validation of organic sample pre-treatment method for AMS C-14 measurement in Atomki

R. Janovics, A.G. Leonard^{a)}, A.J.T. Jull^{a)}, M. Molnár

In the new AMS sample preparation laboratory of Atomki we treat normal organic samples with a sequence of 1N HCl, distilled water, 0.1M NaOH, distilled water and then 1N HCl [1]. After the final acid wash, the sample is washed again with distilled water to neutral pH (4-5) and then dried. It is then ready for combustion. We have also adopted a Soxhlet-extraction protocol similar to that applied by [2] for textiles and art samples. In this case, the samples are extracted in a sequence of solvents: hexane, ethanol and methanol, followed by a distilled water wash. The samples are dried before combustion.

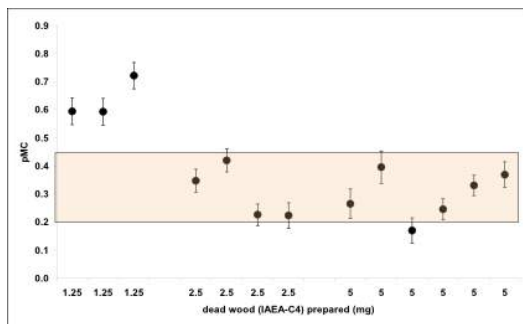


Figure 1 Sample size dependence of processed blank level using IAEA-C4 wood international ^{14}C reference material.

For testing the various organic sample preparation procedures at HEKAL, we have used international ^{14}C reference materials with known ^{14}C activity. IAEA-C4 reference wood samples (very old, no ^{14}C) were prepared using different amounts of sample. In this way, we can investigate the contamination level and its effect on the different sized real samples. The blank results obtained (Figure 1.) showed good results down to the 0.5 mg carbon con-

tent sized samples, the blank in the HEKAL Lab varies not significantly for samples of this size. In case of smaller sized samples (< 0.5 mg C), we prepared blanks of similar size with the real unknown samples to evaluate the proper blank correction.

To investigate reproducibility in the sample-preparation process, known activity ^{14}C reference organic material from IAEA (C5 wood, 23.05 ± 0.02 pMC) was prepared using different sample sizes. The results obtained (Figure 2.) showed excellent agreement with the reference value in case of all samples, regardless of size.

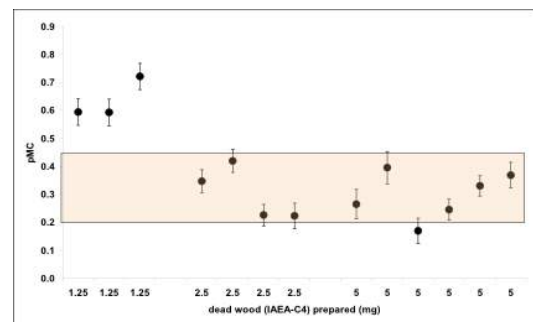


Figure 2 Sample size dependence of ^{14}C results of processed IAEA-C5 wood.

- a) NSF Arizona AMS Laboratory, University of Arizona, Tucson, USA
- [1] A.J.T. Jull, G.S. Burr, J.W. Beck, G.W.L. Hodgins, D.L. Biddulph, J. Gann, A.L. Hatheway, T.E. Lange, N.A. Lifton, *Radioactivity in the Environment* **8** (2006) 3
- [2] I. Hajdas, G. Bonani, H. Thut, G. Leone, R. Pfenniger and C. Maden *Nuclear Instruments and Methods in Physics Research Section B-Beam Interactions with Materials and Atoms* **223-24** (2004) 267

7.9 Experimental technique to measure thoron generation rate using RAD7 detector

I. Csige, Zs. Szabó^{a,b}, Cs. Szabó^a,

Recent studies [1] show that in some cases exhalation of thoron (^{220}Tn) from building materials may result in significant radiation exposure of the public. Therefore, to characterize radiation safety of such building materials we have developed an experimental technique to measure thoron generation rate in building materials using RAD7 detector.

The experimental setup (Fig. 1) consists of a cylindrical shape sample holder with cross-sectional area of A and height of H ; plastic tubing; a gas-drying unit filled with desiccant; an aerosol filter and a RAD7 radon-thoron detector [2].

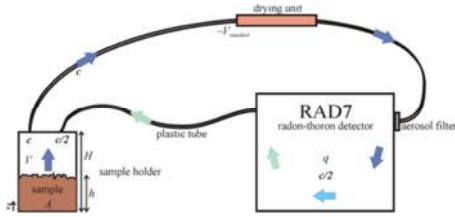


Figure 1. Experimental setup.

The sample with a thickness of h occupies the bottom part of the sample holder. Thoron generation rate (G) is defined as the activity of thoron that is emanated into the pore space of unit bulk volume of the sample in unit time ($\text{Bqm}^{-3}\text{s}^{-1}$). Thoron exhale to the air-filled part of the sample holder from the sample by molecular diffusion and it is sampled by a RAD7 detector, which induces an air circulation through the system at a rate of q . Diffusion of thoron in the sample is described by the steady state transport equation:

$$\frac{d^2C(z)}{dz^2} = \frac{1}{D}(-G + \lambda\beta C(z)), \quad (19)$$

where D is the thoron diffusion coefficient in the sample (m^2s^{-1}), λ is the decay constant of thoron and β is the partition corrected porosity. Thoron concentration in the air-filled

volume (V) of the sample holder can be obtained from the following equation:

$$j/(H-h) - \lambda C - (q/2V)C = 0 \quad (20)$$

where j is the diffusion flux of thoron on the top surface of the sample. This system of equations can easily be solved:

$$C(h) = \frac{G}{\lambda\beta + \frac{\gamma\{\lambda(H-h)+q(2A)\}}{\tanh(\gamma h)}}, \quad (21)$$

where

$$\gamma = \sqrt{\lambda\beta/D}(\text{m}^{-1}). \quad (22)$$

For experimental validation of the method we have used an adobe building material sample and measured the dependence of thoron activity concentration as a function of the sample thickness (Fig. 2).

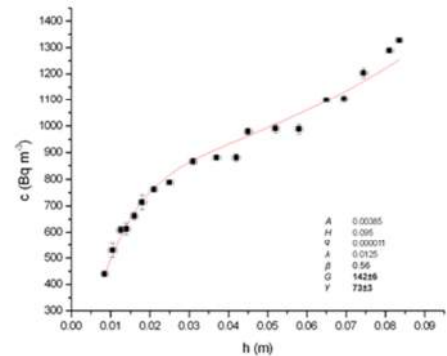


Figure 1. Experimental validation of the method.

For routine measurements, when large number of samples has to be measured, thoron generation rate can be obtained from a single measurement assuming that β and γ is known. The optimum thickness of the sample is in the middle of the height of the sample holder.

a) Lithosphere Fluid Research Lab, Eötvös University, Budapest, Hungary

b) Centre for Energy Research, Hungarian Academy of Sciences, Budapest, Hungary

[1] H. Yonehara et al., Int. Congr. Ser. 1276, 58-61. (1999)

[2] Durrige Co., RAD7 radon detector, Bedford, 49-63. (2000)

7.10 AMS ^{14}C performance test of a new automated bone preparation system

I. Major^{a)} A.J.T. Jull, M. Molnár

Bone is one of the most complex sample materials for radiocarbon dating. After burial, its physical state and chemical composition can be affected by many environmental processes.

In case of our new AMS bone preparation technique, after ultrasonication in distilled water, drying, surface cleaning and grinding, the sample is sieved to get the appropriate sized sample fraction (0.5 – 1 mm) out of which 500 - 1000 mg is measured, depending on the state of the bone. We have developed our own continuous flow bone sample preparation equipment. In this unit OMNIFITTM columns are used as flow cells to construct our own automatic ABA (acid-base-acid) cleaning system. From 3 types of reagent, each one is injected via a 4 way valve and inert plastic tubing to an IsmatechTM IPC 12 channel peristaltic pump to ensure a constant flow rate. Reagents are selectively pumped to the reaction cells containing the powdered bone samples, with a sequence of 0.5 M HCl and 0.1 M NaOH solution, interspersed with flushing with distilled

water. During the sixteen-hour-long process, reagents follow a well-defined sequence that is controlled by a computer program and a special electronic driver device. The cleaned sample is inserted into a test tube containing 5 ml, pH 3 aqueous solutions, and it is placed into a heating block at 75°C for 24 hours. Dissolved collagen is filtered via a 45 μm glass fibre filter (WhatmanTM AUTOVIAL 5) into a clean vial, and after freezing, it gets freeze-dried, a process which takes at least a day.

To investigate the sample-preparation reproducibility and possible extra contamination effect by an optional ultra-filtration process a known-age bone sample, previously dated by an independent method (GPC at HEKAL), was prepared several times using the new AMS preparation line for ^{14}C analyses. The results obtained (Figure 1.) showed very good reproducibility and excellent agreement with the classical GPC measured ^{14}C age in the case of ultra filtration too.

a) University of Debrecen, Debrecen, Hungary

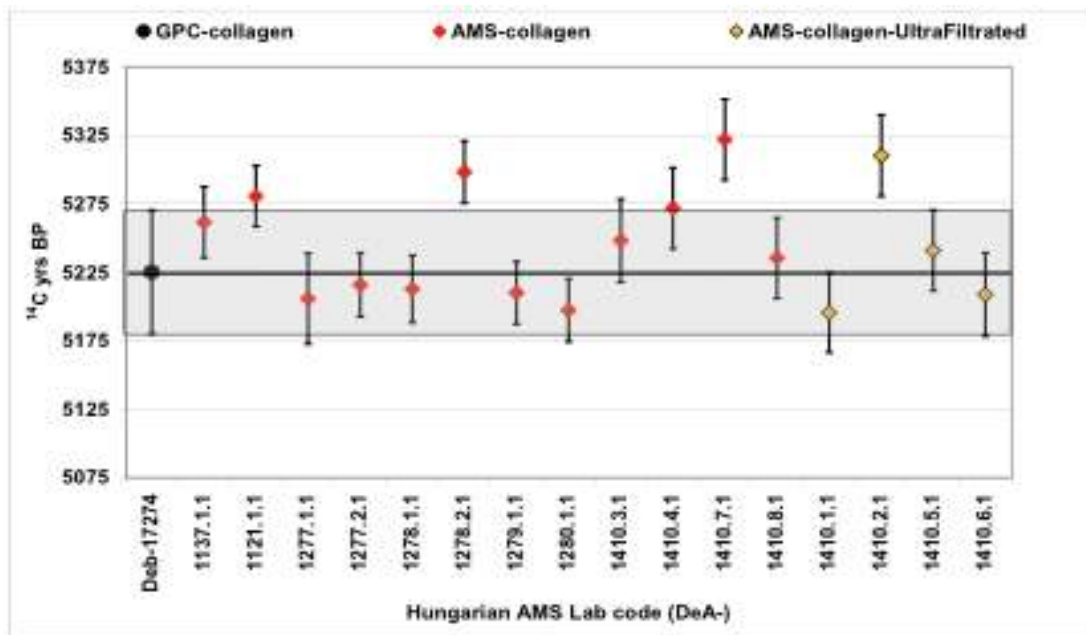


Figure 1. Repeatability and ultra filtration test using a GPC dated bone sample

7.11 Novel methods for AMS C-14 analyses of Dissolved Inorganic Carbon (DIC) of groundwater

M. Molnár, J. Orsovski^{a)}, R. Janovics, A.J.T. Jull

Two different AMS C-14 water sample preparation methods were developed and tested in Hertelendi Laboratory of ATOMKI (HEKAL). The first method is for water samples with Low Dissolved Carbonate content (LDC-method) where up to 500 ml water sample is needed to obtain enough (> 0.5 mg) carbon for graphitization. The second method is for water samples with High Dissolved Carbonate content (HDC-method) where maximum 20 ml water sample is enough to obtain the necessary amount (> 0.5 mg) of carbon for graphitization.

In the LDC method, samples are transferred to a 500 ml round-bottom flask, on top of which a large dry-ice trap is connected. The entire volume is pumped out with the vacuum system of our in-line combustion/ CO_2 purification system. A small amount of phosphoric acid can be injected using a needle and septum arrangement (see Fig 1.). The CO_2 produced from the water sample can be introduced directly into our on-line combustion/ CO_2 purification system.



Figure 1. LDC water preparation setup, adapted from the University of Arizona design.

The preparation of the relatively high dissolved inorganic carbon (HDC) samples is performed by a novel method combining the advantages of the preparation of carbonate and water samples. The setup is basically similar to that used for carbonate samples, but instead of the second sample holder finger, a silicone septum fitting is formed (Fig 2.). The internal volume is about 70 ml. The reaction cell has been previously evacuated, and 10-20 ml water sample is introduced later into the evacuated and closed cell via the septum. Phosphoric acid is also measured and introduced into the reaction cell through a septum.

In this way, the free CO_2 content of the water can also be measured as well as dissolved inorganic carbon. We can also use the same system with an oxidizing acid instead of phosphoric acid to determine organic compounds. The off-line produced CO_2 from the water sample can be introduced into our in-line combustion/ CO_2 purification system.

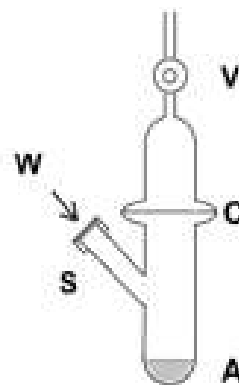


Figure 2. HDC water preparation setup developed by HEKAL (W: water sample injection by a plastic syringe; S: septa silicon sealed cup; A: phosphoric acid; C: glass and O-ring (Viton) vacuum tight connection; V: Kontes glass valve).

a) University of Debrecen, Debrecen, Hungary

8.1 Production and radiochemical separation of ^{64}Cu and ^{67}Cu radioisotopes

Z. Szűcs, R. Dóczi^{a)}

The Copper is one of the most important trace elements in the biosphere. Its importance in blood system and chelate bonds to the bioactive macro-peptides are well known. The nuclear medical applications of Copper radioisotopes such as ^{64}Cu also have wide literature. The ^{67}Cu became the target of the scientific interest due to the optimal nuclear properties for nuclear medicine. The optimal production of these isotopes in quality of high specific activity is different. For production of ^{64}Cu it is more preferable to apply the $^{64}\text{Ni}(p,n)^{64}\text{Cu}$ nuclear reaction by cyclotron, as can be seen in Fig. 1. The production of ^{67}Cu is possible using the $^{67}\text{Zn}(n,p)^{67}\text{Cu}$ nuclear reaction by nuclear reactor (see Fig. 2). Theoretically the $^{64}\text{Ni}(\alpha,p)^{67}\text{Cu}$ and $^{64}\text{Ni}(^7\text{Li},\alpha)^{67}\text{Cu}$ are also useable to produce the ^{67}Cu , but the Atomki's cyclotron isn't dedicated for that reactions. However for that two radioisotopes have two different production routes, both radioisotopes can be separated by the same following chemical method:

The strength of complexation of metal ions with chloride ions depends of the concentration of chloride ion. This is the theoretical background for separation of different transition metal ions by ion-chromatography [3]. In case of Ni target the separation was carried out in 4 moldm⁻³ HCl media, when the Ni²⁺ ions went through the anion-exchanger column as effluent and after that the ^{64}Cu was washed out by water. Due to the extremely expensive price of the enriched ^{64}Ni the natural Ni was used for the irradiation (15 MeV proton beam with 20 μAs intensity). However the contaminating Co radioisotopes originated from the side reaction were also separated when the Co²⁺ also eluted in the effluent together with the Ni²⁺ ions. The 10 times higher dose rate of the Co radioisotopes compared to the dose rate of ^{64}Cu is a real disadvantage of the pro-

cedure. The same anion-exchanger is also suitable for separation of the ^{67}Cu from the irradiated ^{67}Zn , only we have to use different HCl media: 8 moldm⁻³. In this case the ^{67}Cu will be in the effluent.

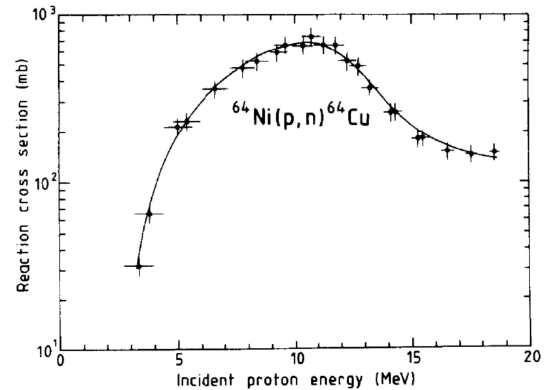


Figure 1. Cross section curve of $^{64}\text{Ni}(p,n)^{64}\text{Cu}$ [1]

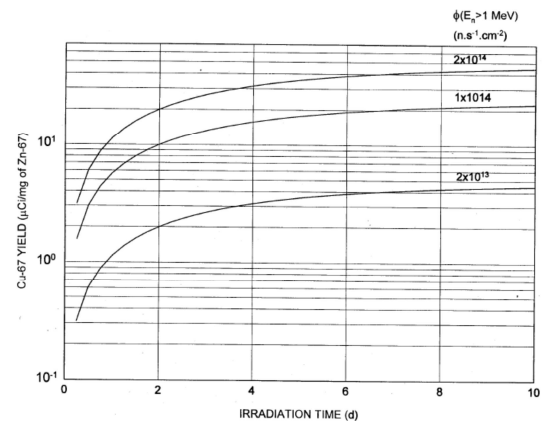


Figure 2. Target yield of $^{67}\text{Zn}(n,p)^{67}\text{Cu}$ [2]

a) Budapest University of Technology and Economics, Institute of Nuclear Techniques

[1] F. Szelecsényi et al., Applied Radiation and Isotopes, 1993, **44**, 575-580

[2] I.A.E.A. TECDOC-1340

[3] F. Nelson, D. C. Michelson, J.Chromatogr. 1966, **25**, 438

8.2 Biodistribution, pharmacokinetics and uptake ratio of ^{131}I -4-Iodo-phenyl-acetic acid in normal and tumour implied animals

Z. Szűcs, J.R. Zeevaart^{a)}, T. Pulker^{b)}, T. Sello^{c)}, M. Sathekge^{d)}

Phenyl acetate is one of the tumour metabolism compounds that is currently studied in phase II clinical trials targeting brain tumour by reducing plasma levels of glutamine. It has been reported to have a potent anti-proliferative and anti-differentiating effect in haematological malignancies and in solid tumours at non-toxic concentrations. Due to the closeness of its structure compared to phenyl-acetic acid, as well as the reported biological activity of phenyl-acetic acid, it is hypothesized that useful information of the biodistribution of ^{131}I labelled agent can be obtained from experimental animals, especially with regards to its uptake in neoplastic vs normal tissue. The results presented here describe the biodistribution of ^{131}I -4-iodo-phenyl-acetic acid in healthy rats and nude balb c/c mice xenograft with WCHO1 cells accessing its potential as diagnostic imaging and / or therapeutic agent for the treatment of neoplastic conditions.

The radiosynthesis has been described in detail earlier [1]. It was found that the inert atmosphere and the adequate temperature are the key parameters for the synthesis. The fresh preparation of the solution of the ascorbic acid is also essential. The HPLC QC showed that the radiochemical purity of the final product was higher than 98%. The activity of the product was 96 MBq. The calculated specific activity was 355 Ci/mol.

A 1 h dynamic scan was recorded for one of the rats, where after static scans were recorded for all four rats up to 5 h. From the dynamic scan fast excretion from the blood pool was visible as can be seen in Fig. 1. The time activity curves are given in Fig. 1. After completion of the scintigraphy the rats were sacrificed and dissected and the organs counted. The average of the percent-injected dose per gram of tissue (%ID/g) was determined. The xenograft mice were sacrificed after 5h after injection and di-

sected and the organs counted. The average of the percent-injected dose per gram of tissue (%ID/g) is given in Table 1 for nine animals as three were considered outliers predominantly due to a high percentage of activity remaining in the tail after injection. The tumour to background ratio was calculated by comparing the muscle on the left flank as opposed to the right flank where the tumour was induced.

The labeling via isotopic exchange did yield a low specific activity of the tracer which meant that a substantial amount of 4-iodo-phenyl-acetic acid was injected. This would amount to 30 μg per rat or 75 $\mu\text{g}/\text{kg}$ or 1.1 $\mu\text{g}/\text{ml}$ blood (mass of rats 400g and assuming 7% of body weight is blood). The LD50 value for phenyl acetic acid is 1600 mg/kg for intraperitoneal injection in rats [2] which is orders of magnitude higher than the amount injected and therefore one can assume the 0,075 mg/kg injected 4-iodo-phenyl-acetic acid would not adversely interfere with the biological processes in the rat. The amount of phenyl-acetic acid in normal tissue is 16.8 $\mu\text{g}/\text{ml}$ [3] which is also a two orders of magnitude higher than the amount of 4-iodo-phenyl-acetic acid injected. This implies that the biodistribution of the tracer was not influenced by its metabolic product due to equilibrium with phenyl-acetic acid already present in the body.

^{131}I -4-iodo-phenyl-acetic acid was successfully prepared and the biodistribution in rats recorded. As expected no target organ was found after 5 h (although at the early stages a high cardiac blood pool uptake was recorded) with fast excretion from all organs via the kidney into the urine. In xenograft mice study a 4% tumour uptake and a tumour to background ratio of 2 was recorded after 5 h although high activity levels in the blood still remained at this time point.

Organ	Average %ID/g	SD (%ID/g)	% SD
blood	17.6	2.0	11
heart	6.18	0.77	12
spleen	1.73	0.19	11
lung	6.27	2.28	36
liver	3.58	0.49	13
kidney	5.09	0.58	11
fat	2.30	0.53	23
trachea	9.73	1.29	13
GI tract	1.94	0.32	16
bladder	13.1	7.5	57
muscle	2.04	0.18	9
tumour	4.10	0.43	10
T:B #	2.0		
excretion*	32	10	

Table 1. Biodistribution of ^{131}I -4-iodo-phenyl-acetic acid in normal rats.

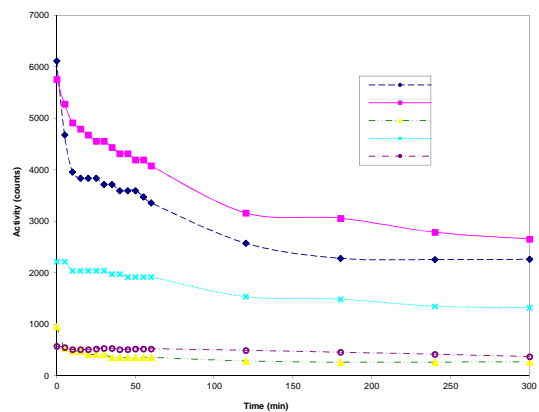


Figure 1. Dinamic scan of rat by organs.

- a) Drug Research and Development, North West University, South Africa
 - b) University of Pretoria, Biomedical Research Centre, Pretoria, South Africa
 - c) Necsca, Radiochemistry, Pretoria, South Africa
 - d) University of Pretoria/Steve Biko Academic Hospital, Pretoria, South Africa
- [1] Z. Szűcs, M. Sathekge, B. Marjanovic-Painter, J. Wagener, T. Sello, C. Wagener, J. R. Zeevaart. J. Labelled Compound and Radiopharmaceuticals, 2011, **54**, 54-58
 - [2] CHEMTOX [®] online 2005 Atrion Internat. Inc.
 - [3] S. Hoda et al Biol. Pharm. Bull. 2002, **25**, 1244-1246.

8.3 Production and radiochemical separation of ^{203}Pb radioisotope for nuclear medicine

Z. Szűcs, S. Takács, D. Andrászi^{a)}, B. Kovács^{a)}

The heavy metal pollution due to their industrial production, waste repository or accident as the cyanide spill in river Tisza in 2002, increase the scientific interest for using an ideal trace isotope for monitoring these type of events. The lead is one of the most toxic and commonly used heavy metal, its poisoning is often deadly because very difficult to recognize and identify. The neuro-scientific study of biodegradation effect of lead could be an impressive scientific field of application of ^{203}Pb radioisotope. However the targeted radionuclide therapy especially the α -emitting radioisotope therapy is also strongly interested to find an ideal tracer for the ^{213}Bi and ^{212}Pb therapy [1,2]. Therefore the ^{203}Pb is a potential radioisotope for this role due to its radiation behaviour and as heavy metal element. The $^{203}\text{Tl}(p,n)^{203}\text{Pb}$ nuclear reaction was chosen for the production. The irradiation was done at the compact cyclotron of Atomki with proton beam 14.5 MeV energy and beam current of 7 μAs . The thickness of the target material was 840 μm , the irradiation time was 3 hours and the produced activity was 40 MBq at EOB. It corresponds to 1.87 MBq/ μAh physical yield of the reaction which correlating with the cross section curve. A new technique was developed for target preparation. The metal Tl was pressed into a copper backing and covered with a HAWAR foil with thickness of 11 μm . The covering foil saved the surface of the Tl from the oxidation and also transferred the dissipating heat to the cooling He gas. The back side of the target was cooled with pressured cold water. The irradiated Tl target was pressed out from the copper backing, which

had only the thickness of 0.2 mm. Then the Thallium was dissolved in nitric acid. The excess acid was evaporated slowly. The nitrate form was transferred to chloride form by 8 mol/dm³ HCl and the Thallium was kept in 3+ oxidation stage by hydrogen peroxide. The separation was carried out on the anion exchange column (DOWEX1-4x, 200/400 mesh, 15 cm long and 0.5 cm ID) in 8 mol/dm³ HCl media, based on literature [3]. The radioactive ^{203}Pb was collected in the effluent. The target material Tl remained on the column. The regeneration of the column, i.e. collection of Thallium was made by washing of the column with deionized water. The collected fraction of ^{203}Pb was evaporated to wet dryness and take back with saline of 0.8 ml. The separation yield was 63%+12%. No contaminating radioisotopes were detected in the product. However, the amount of Tl was 0,6 mg, which is higher than the tolerable level for the mice [4]. The next step planned is to decrease the level of Tl and determine the specific activity of ^{203}Pb by ICP-MS.

a) Institute of Food Science, Quality Assurance and Microbiology, Centre for Agricultural and Applied Economic Sciences, University of Debrecen

[1] Y. Miao, S. D. Figueroa, D. R. Fisher, H. A. Moore, R. F. Testa, T. J. Hoffman, T. P. Quinn, *J Nucl Med* May 2008, **49**, 823-29

[2] Y. Miao, M. Hylarides, D.R. Fisher, T. Shelton, H. Moore, D.W. Wester, A.R. Fritzberg, C.T. Winkelmann, T. Hoffman, T.P. Quinn, *Clin Cancer Res.* 2005, **11**, 5616-21

[3] F. Nelson, D. C. Michelson, *J. Chromatogr.* 1966, **25**, 438.

[4] Niosh, Registry of Toxic Effects of Chemical Substances, Washington, DC. 1976

8.4 The potential of materials analysis by electron Rutherford backscattering as illustrated by a case study of mouse bones and related compounds

M. Vos^{a)}, K. Tókési, and I. Benkő^{b)}

Electron Rutherford backscattering (ERBS) has a number of distinct advantages for semi-quantitative analysis of samples. These are for example: a) Its high energy makes it rather insensitive to surface effects. b) The peaks appear well approximated by Gaussian with no obvious problems due to background subtraction. c) All the electrons involved have very similar kinetic energy, and hence one does not need to consider changes of the mean-free path or the analyzer transmission function. d) There are no intrinsic satellites to complicate the quantitative interpretation. On the other hand ERBS has a weak point, peaks tend to overlap. Peak separation is proportional to the incoming energy E_0 , but the intrinsic peak width increases proportional to the square root of E_0 . In practice one has to live with overlapping peaks. In the present work we mainly focus on the measurement and analysis procedure [1], and compare our best estimate of the concentration of the various elements in mouse bone with that obtained in a recent paper [2]. The promise of ERBS as an analytical technique is clear from the successful analysis of the simple case of calcium carbonate and the somewhat more complicated case of hydroxyapatite. Here agreement between the measured and actual composition are on a very respectable 10% level. The actual bone sample showed more variation in outcome and a somewhat less satisfactory agreement between experiment and theory (see Fig. 1). The variation in outcome between the different measurements can be due to the fact that we average over very few grains, and that the grain composition will vary somewhat with its original position in the bone. In summary, ERBS can become a useful tool to study bone mineralization. As our knowledge of bone mineralization is incomplete this is currently an active topic of multidisciplinary research involving people working in physics, chemistry and biological/medical sciences. One of the important conclusion of the present work is that

quantitative analysis is often still possible, but only if one has some knowledge of which elements could be present in the sample and their peak width. More in general this case study has shown that ERBS provides an interesting new avor of microanalysis, a technique that, we think, could have interesting applications, especially if it would be integrated in some kind of electron microscopy.

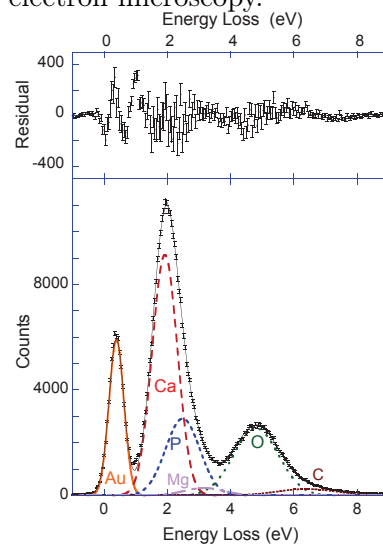


Figure 1. A fit of a mouse bone spectrum with all widths fixed to the corresponding values obtained in hydroxyapatite and CaCO_3 spectra.

Acknowledgements

This research was made possible by a grant of the Australian Research Council the Medical and Health Research Council of Hungarian government (ETT293/2009).

- a) Research School of Physics and Engineering, Australian National University, Canberra ACT Australia
- b) Department of Pharmacology and Pharmacotherapy, Medical and Health Science Center, University of Debrecen, Hungary, EU

- [1] M. Vos, K. Tókési, and I. Benkő, *Microscopy and Microanalysis* **18** (2013) 01123.
- [2] I. Benkő, I. Rajta, A. Csik, J. Tóth, K. Benkő, K. Géresi, É. Ungvári, B. Szabó, G. Sarkadi, B. Paripás, I. Takács, and K. Tókési, *Nucl. Instrum. and Meth. B* **279** (2012) 223.

8.5 Identification of bisphosphonate from phosphate ion on functionalised carbon nanotube by X-ray photoelectron spectroscopy (XPS)

Z. Szűcs, J. Tóth, J.R. Zeevaart^{a,c}, N.L. Dlamini^b X.Y. Mbianda^b

The carbonnanotube (CNT) is one of the most studied nanoparticles in nano science. However the CNT is not only chemically inert but even extremely difficult to moisten due to the carbon-carbon bond hegemony. The importance of moistening is the key question for application of CNT in medicine, where all materials, chemicals and drugs can move in the body within solvated state only. Therefore one needs to build up a "sphere" on the CNT which will create a solvated ring surrounding the CNT. This method is generally called the functionalization process. The CNT with the functionalized group of bisphosphonate is a potential therapeutic drug for metastatic bone cancer [1]. The X-ray photoelectron spectroscopic (XPS) analysis is an uncial device to map not only the elements the CNT consists of, but also their chemical bonds in and on the CNT. As Fig.1 indicates the analysis shows chemically bonded phosphorus, however one has to prove that it's a bisphosphonate, and not the phosphate ion, that was incorporated during the functionalizing process. Fig 2. shows the binding critical energy (E_B)range in XPS spectrum referring for the P2p bond. The XPS analysis was performed on a ESA-31 instrument of Atomki by AlK α energy. The charging effect on specimen was corrected for C1s ($E_B= 284,8$ eV C-C bond). The systematic study of the P2p energy range demonstrated that there is a small EB difference of strength of the P-bond between the phosphate ion and bisphosphonate group. The numerical data are $132,8\pm 0,1$ eV for the pyrophosphate, $133,8\pm 0,1$ eV for the phosphate and $133,9\pm 0,1$ eV for bisphosphonate both in CNT (Fig. 2.) as well as in 1-hydroxy-ethylene diphosphonate (HEDP) used as standard for bisphosphonates.

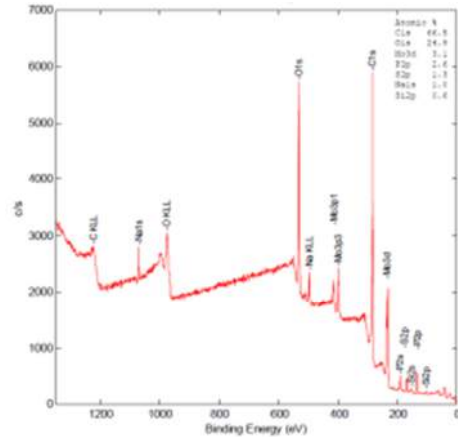


Figure 1. XPS scan of functionalized CNT.

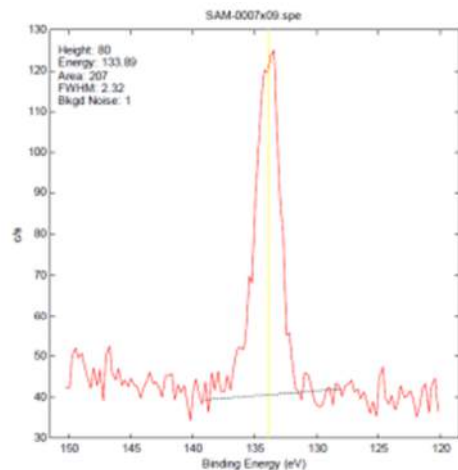


Figure 2. Energy range of P2p bond of XPS spectrum on functionalized CNT

- a) Drug Research and Development, North West University, South Africa
 - b) Dept of Chem. Tech, Univ. of Johannesburg
 - c) Necsa, Radiochemistry, Pretoria, South Africa
- [1] N.L. Dlamini, X.Y Mbianda, Z. Szucs, J.R. Zeervaart, European Cells and Materials, 2010, **19**, Suppl. 1, 21-23

8.6 Dramatic effect on Selenium concentration in blood serum due to the difference between the Hungarian and Indian dietary habits

Z. Szűcs, M. Maiti^{a)}, S. Lahiri^{b)}, D. Andrászi^{c)}, B. Kovács^{c)}

The importance of Selenium as trace element in animals, as well as in humans is well known. The deficiency of Selenium was observed in case of several heavy or fatal clinical events such as high infant mortality, premature, malformations and even prostate cancer. Hungary is in the top of their worldwide statistic with parallel of the low concentration of Selenium in soil as well as in food. The direct correlation can explain in Venezuela [1], where the prostate cancer is "unknown disease". The concentration of Selenium in India is higher than the worldwide level [2]. Under the scientific bilateral cooperation "Speciation dependent studies on physicochemical behavior of some elements in trace scale in natural and synthetic system" the Selenium was determined in human blood serum from the group of Hungarian and group of Indian patients. The samples were given in same time from each group. The main goal of the study was explain the effect of the traditional dietary habit for the level of Selenium. Therefore the samples were taken from the visiting scientist just arrived to the host institute as well as from the host scientists too. After 2 weeks stay the sampling was repeated, when the guest scientists eat the same food as the host scientists. The measurements were done in Thermo-2 ICP-MS from blood-serum separated by centrifuge. The results are summarized in Table 1. Dramatic effect was found for the level of Selenium in blood serum. As it was expected the Hungarian samples showed low concentration of Selenium in starting of the visit, as well as the high concentration was found in Indian sample, comparing to the Hungarian sample. After two weeks the Hungarian sample showed much higher concentration, however it was still less, than in Indian sample. Similar effect was found during the visit the Indian scientists in Hungary, however their Selenium concentration decreased not so spectacu-

lar due to the Selenium "store" in body. The general conclusion of these experiment is that the level of Selenium strongly different between in Hungary and in West-Bengal, India. This difference can be relatively quickly (2 weeks) compensated by the traditional dietary habit: increase in India and decrease in Hungary. The saturation effect was found for the concentration of the Selenium, which could be interpretate with the longer process of incorporation of the Selenium as well as to fill the Selenium store. The additional analysis of the Hungarian and Indian foods will determine which the most potential Selenium source is, as well as for the mysterious concentration of Molybdenum.

Table 1. Concentration of Se and Mo in blood serum due to the traditional Indian and Hungarian food consumption in Hungarian and Indian sample in ppb unit

Sampler	Se in India	Se in Hung	Mo in India	Mo in Hung
Indian 1.	135	110	577	81
Indian 2.	113	93	4143	620
Indian 3.	113	no d.	355	no d.
Hungarian 1.	115	97	990	23
Hungarian 2.	98	93	423	18

Acknowledgements

Authors thank for the support of the Hungarian-Indian bilateral cooperation (OMFB-00742/2008) and the Indo-Hungarian Collaboration.

- a) Indian Institute of Technology Roorkee, India
- b) Chemical Sciences Division, Saha Institute of Nuclear Physics, Kolkata, India
- c) Institute of Food Science, Quality Assurance and Microbiology, Centre for Agricultural and Applied Economic Sciences, University of Debrecen

- [1] A. T. Diplock, Am J Clin Nutr, 1993, **57** 256S-258SY.
- [2] G. F. Combs Jr, British Journal of Nutrition, 2001, **85**, 517-547

9.1 Overview of cross sections of proton and deuteron induced nuclear reactions for production of ^{163}Ho radioisotope

Z. Szűcs, S. Takács

The main goal of the Electron Capture ^{163}Ho (ECHO) project is to determine the mass of neutrino. In view of the ECHO experiment necessity of production of pure ^{163}Ho source has been realized as it offers low Q value ≈ 2.8 keV to the Electron Capture process. However, production of long lived (4570y) ^{163}Ho radionuclides is a challenging task. Very few experimental data are exist in the literature, which could be used to decide which nuclear reactions can be used for production of ^{163}Ho . The cyclotron based nuclear reactions are as follows: $^{163}\text{Dy}(p,n)^{163}\text{Ho}$, $^{163}\text{Dy}(d,2n)^{163}\text{Ho}$, $^{164}\text{Dy}(p,2n)^{163}\text{Ho}$, $^{nat}\text{Dy}(\alpha,xn)^{163}\text{Er} \rightarrow ^{163}\text{Ho}$, $^{159}\text{Tb}(^7\text{Li},3n)^{163}\text{Er} \rightarrow ^{163}\text{Ho}$, $^{159}\text{Tb}(^7\text{Li},p2n)^{163}\text{Ho}$ and the $^{162}\text{Er}(d,n)^{163}\text{Tm}$, $^{164}\text{Er}(p,2n)^{163}\text{Tm}$. ^{163}Tm decays to ^{163}Ho through ^{163}Er . The most potential nuclear reactions among them, are the (d,xn) and (p,xn). The excitation function of these reactions are collected and compared. Thick target yields were deduced for the main as well as the side reactions and the yields of the critical contaminating isotopes are discussed. The highest cross section and thick target yield can be reached using the (p,2n) reactions and enriched ^{164}Dy target. Relevant data are collected in Fig. 1 and Table 1. The $^{164}\text{Dy}(p,2n)^{163}\text{Ho}$ reaction offers the best yield/price value, additionally the amount of potential contaminating stable and radioactive isotopes is the smallest (Fig. 2 and Table 2). The ECHO experiment requires a ^{163}Ho radioisotope source with at least an amount of 10^{17} atoms, i.e. 1 MBq activity,. This activity can be produced by the proton irradiation with energy of 30 MeV and beam intensity of $20 \mu\text{A}$ during a week. Therefore the $^{164}\text{Dy}(p,2n)^{163}\text{Ho}$ reaction provides not only more "clean" source of ^{163}Ho but financially is more effective than the reactor produced ^{163}Ho .

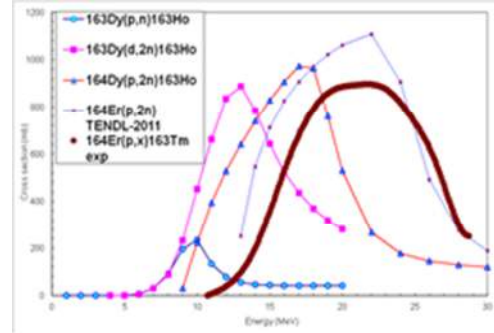


Figure 1. Excitation function of different accelerator based nuclear reactions for production of ^{163}Ho

Nuclear reaction	Energy range [MeV]	Activity [kBq]	thickness [μm]	price of target [kUSD]
$^{163}\text{Dy}(p,n)^{163}\text{Ho}$	6-14	614	471	1,2
$^{163}\text{Dy}(p,n)^{163}\text{Ho}$	2-20	875	1103	2,7
$^{163}\text{Dy}(p,2n)^{163}\text{Ho}$	4-20	3600	661	1,6
$^{163}\text{Dy}(p,2n)^{163}\text{Ho}$	4-30	5000	1350	3,3
$^{164}\text{Dy}(p,2n)^{163}\text{Ho}$	8,5-30	9800	2000	4,9
$^{164}\text{Er}(p,2n)^{163}\text{Tm}$	10,7-28,7	12000+	1620	61,9

Table 1. Thick target yields and prices of target materials (1800 h irradiation, $20 \mu\text{A}$ beam current)

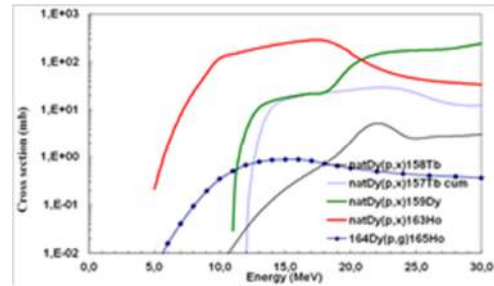


Figure 1. Excitation functions of nuclear reactions of potential contaminating stable and radioactive isotopes.

E-range MeV	^{157}Tb MBq]	^{158}Tb MBq]	^{159}Dy MBq]	^{163}Ho MBq]
5-11	0	0	0	0,20
5-18	3,81	0,04	968	1,74
5-28,7	18,27	1,10	20762	2,93

Table 2. Thick target yields of contaminating radio-isotopes and ^{163}Ho (1800 h irradiation, $20 \mu\text{A}$)

9.2 Tritium calorimetry

András Bükki-Deme

Future deuterium-tritium fusion experiments (like ITER) will use large amount of tritium. Therefore, it is very important to develop better tritium accountancy methods. Tritium calorimetry is used to measure the heat produced by the beta-decay of tritium. If we consider that all the decay energy is converted into thermal heat, we can calculate the tritium activity and mass from calorimetric measurements. The advantages of calorimetry are that it measures absolute activity, and the physical or chemical composition of the sample is not relevant. For example, tritiated structural components can only be measured in a non-destructive way with calorimeters. Disadvantages are: long measurement time for large sample volumes, and offline sampling. The accepted conversion factor is $0.324\text{W/g} \pm 0.3\%$. I have started participation from ATOMKI in an EFDA-GOT program, called TRI-TOFFY (TRITium fOr Fusion Fuel cYcle), in 2010. I have spent 8 months at Tritium Laboratory Karlsruhe (TLK), Germany in 2011, and 9 months in 2012. TLK is a semi-industrial scale facility for processing tritium, the radioactive hydrogen isotope. The main tasks of TLK are fusion research (ITER) and neutrino physics (KATRIN), but also EU projects. The present site inventory is $\sim 25\text{ g T}_2$ (8914 TBq). There are four calorimeters are used for tritium analytics at TLK. My main work was to carry out upgrade on these devices, to deploy new modern control and data acquisition (DAQ) software, and to partly change their hardware. I worked on three calorimeters at the laboratory. The ANTECH-351 is a commercial 20 years old calorimeter. It is a power compensation type isothermal calorimeter. Useful sample volume is 1.2 dm^3 . This is not a sensitive device (power range is $1\text{ mW} - 5\text{ W}$), mainly used for tritium shipment (from Canadian CANDU reactors) validation, but can measure tritium samples very fast: less than 8 hours. The IGC-V0.5 is a custom made heat flow calorimeter, using a special thermostat

design developed by J. L. Hemmerich [1]. This thermostat has about three orders of magnitude better temperature stability ($\pm 30\text{ nK}$ standard deviation in one hour!) compared to conventional thermostats. Among dedicated tritium calorimeters, in this sample volume class (0.5 dm^3), the IGC-V0.5 has the best accuracy in the literature. The IGC-V25 is similar to the IGC-V0.5, also designed by Hemmerich. Its sample holder has a volume of 20 dm^3 . Due to the larger heat capacity, and a more complicated control design, its sensitivity ten times worse compared to IGC-V0.5. Also slower: while the IGC-V0.5 can measure samples in 5-6 days, IGC-V25 needs about 2 weeks to finish only one sample measurement. Note that, such inertial guidance calorimeters (IGC) are custom made, and only available at TLK. I have significantly improved the stability and accuracy of the IGC-V0.5 calorimeter. The original IGC-V0.5 system was able to measure $1\text{ }\mu\text{W}$ with 60 % accuracy. I have developed a new automatic control and DAQ software in LabView, and I have retuned the PID control loops. The results are significant. Now we are able to measure $1\text{ }\mu\text{W}$ with 20 % accuracy. Moreover, the detection limit has been decreased from $1\text{ }\mu\text{W}$ to $0.5\text{ }\mu\text{W}$. In terms of mass, now we are able to measure samples containing $1.5\text{ }\mu\text{g}$ tritium with an accuracy of $\pm 0.5\text{ }\mu\text{g}$. The results are submitted [2].

Acknowledgments

This project was financially supported by EFDA through Mobility Agreements.

- [1] J.L. Hemmerich, J.-C. Loos, A. Miller, Advances in temperature derivative control and calorimetry, *Review of Scientific Instruments* 65, 67, 3877. (1996)
- [2] A. Bükki-Deme, C. G. Alecu, B. Kloppe, B. Bornschein, First results with the upgraded TLK tritium calorimeter IGC-V0.5, *Fusion Engineering and Design* (under review)

9.3 Wear measurement using radioactive tracer technique based on proton, deuteron and α -particle induced nuclear reactions on molybdenum

F. Ditrói, S. Takács, F. Tárkányi,

Excitation functions of light ion induced nuclear reactions on natural molybdenum have been studied in the frame of a systematic investigation of charged particle induced nuclear reactions on metals for various applications. Excitation functions of $^{93,94g,94m,95g,95m,96,99m}\text{Tc}$, $^{90,93m,99}\text{Mo}$, $^{90,91m,92m,95m,95g,96}\text{Nb}$ and $^{88,89}\text{Zr}$ were measured up to 50 MeV deuteron energy [1], $^{93m,93g,94m,94g,95m,95g,96g,99m}\text{Tc}$, $^{90,93m,99}\text{Mo}$, $^{90,92m,95m,95g,96}\text{Nb}$ and $^{88,89}\text{Zr}$ were measured up to 40 MeV proton energy [2] and $^{93m,93g,94m,94g,95m,95g,96g,99m}\text{Tc}$, $^{93m,99}\text{Mo}$, ^{90}Nb , $^{94,95,97,103}\text{Ru}$ and ^{88}Zr were measured up to 40 MeV alpha energy [3] by using the stacked foil technique and activation method. The results for ^3He induced reactions on natural Mo were taken from the literature [4]. According to their half-lives, from the above listed radionuclides the $^{95m,96}\text{Tc}$, $^{91m,92m,95m,95g}\text{Nb}$, ^{99}Mo , $^{103,97}\text{Ru}$ and ^{88}Zr are suitable candidates for wear measurement by using Thin Layer Activation (TLA) method. The goal of this work was to determine the necessary nuclear data for TLA of the above radionuclides and to prove their applicability for wear measurements. As examples we present herewith the specific activity distribution (wear curves) of the ^{95m}Tc , ^{96}Tc , ^{95m}Nb and ^{95g}Nb radioisotopes (see Figs. 1-4).

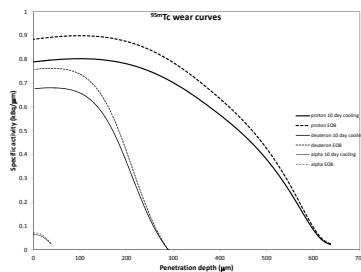


Figure 1. Specific activity distribution (wear curve) of ^{95m}Tc produced by proton, deuteron as well as α -particle irradiation.

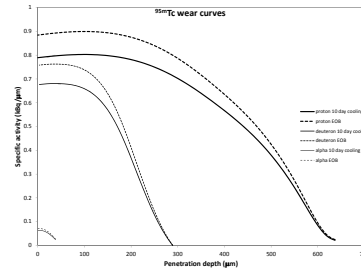


Figure 2. Specific activity distribution (wear curve) of ^{96}Tc produced by proton, deuteron as well as α -particle irradiation.

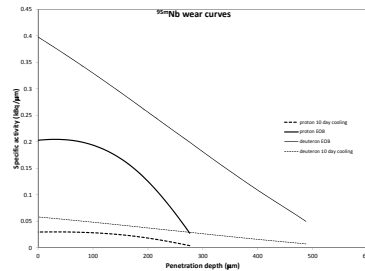


Figure 3. Specific activity distribution (wear curve) of ^{95m}Nb produced by proton and deuteron irradiation.

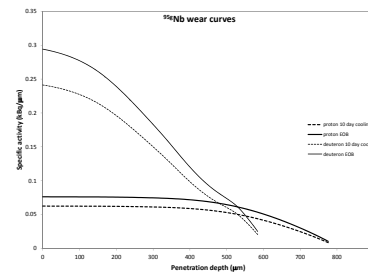


Figure 4. Specific activity distribution (wear curve) of ^{95g}Nb produced by proton and deuteron irradiation.

- [1] F. Tárkányi, F. Ditrói, S. Takács, B. Király, A. Hermanne, M. Sonck, M. Baba, A.V. Ignatyuk, Nucl Instrum Meth B, **274** (2012) 1-25
- [2] F. Tárkányi, F. Ditrói, A. Hermanne, S. Takács, A.V. Ignatyuk, Nucl Instrum Meth B, **280** (2012) 45-73
- [3] F. Ditrói, A. Hermanne, F. Tárkányi, S. Takács, A.V. Ignatyuk, Nucl Instrum Meth B, **285** (2012) 125-141
- [4] G. Comparetto, S.M. Qaim, Radiochim Acta, **27** (1980) 177-180

9.4 Production of fully-stripped neon beam with the ECR ion source

R. Rácz, S. Biri, A.G. Drentje^{a)}

The ATOMKI ECRIS Laboratory [1] celebrated the 20th anniversary of the project starting-up in 1992. Ion beams themselves are being delivered since 1996. The facility is used for low energy atomic physics research, plasma investigations and for applications. There is continuous necessity to increase the quality of the produced ion beams and plasmas in order to satisfy the diversified requirements.

For example high intensity, highly charged neon ion beams with very low kinetic energy (several hundred eV/nucleon) are necessary to measure some aspect of the nowadays very intensively studied physics of nano-capillaries (guiding of highly charged ions through nano-capillaries) [2].

We were motivated to measure the intensity of a fully-stripped neon ion beam (at first time in Hungary) which is impossible with natural neon due to the (always) present molecular hydrogen ions (same charge - to- mass ratio). In order to overcome this difficulty it was decided to use isotopically enriched (99.95 %) ²²Ne gas. The ECR ion source operated in standard mode [1]. The plasma was tuned for the required charge state by changing parameters like the microwave power (klystron amplified), the biased electrode (voltage and position) and the neon-gas flow. The extraction voltage was 10 kV and the analysed beam was measured by a Faraday cup. The size of the beam was defined by (10 mm x 30 mm) slits.

At first the charge state distribution (CSD) of the extracted ion beam was recorded using natural neon gas when the source was tuned for ²⁰Ne⁸⁺ in order to get a benchmark for comparison. The natural neon gas abundances of ²⁰Ne and ²²Ne are 90.48 % and 9.25 %, respectively. By measuring the CSD of both isotopes in one setting we were able to observe (likely for the first time) the so-called isotopic

anomaly, well known for nitrogen and oxygen [3], see figure 1. The CSD for the heavier isotope is shifted to higher charges at the cost of higher losses (output) for low charge states of the lighter isotope.

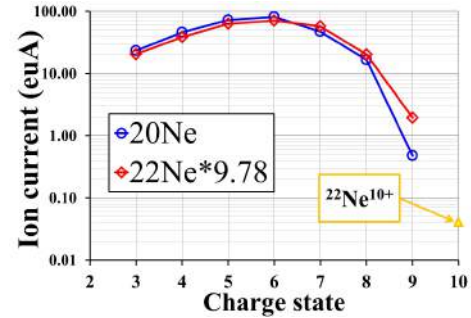


Figure 1. CSDs for ²⁰Ne (blue curve) and ²²Ne (multiplied by the ratio of the ²⁰Ne and ²²Ne compound of the natural neon gas) (red curve) using natural neon. The ²²Ne¹⁰⁺ current was obtained using isotopically enriched ²²Ne gas (yellow triangle).

Then the working gas was changed to the isotopically enriched ²²Ne gas; the source was optimized to maximise the ²²Ne⁸⁺ ion current. The analysed beam current (²²Ne⁸⁺) increased by a factor of 1.3 compared to the ²⁰Ne⁸⁺ current. The main goal was to produce fully-stripped neon beam, which was easily reached when the source was optimised for the ²⁰Ne⁹⁺ production. Result: **20 electrical nA** (i.e. 2 particle nA) of ²²Ne¹⁰⁺ current appeared in the spectra. This value was then further increased up to **43 nA** by tuning the plasma directly to ²²Ne¹⁰⁺ and by mixing helium gas into the neon.

a) NIRS, Chiba, Japan and KVI, University of Groningen, The Netherlands.

[1] S. Biri, R. Rácz, J. Pálkás Rev. Sci. Instrum. **B83** (2012) 02A341

[2] Z. Juhász et al, Phys. Rev. A **82** (2010) 062903

[3] A. G. Drentje, Rev. Sci. Instrum. **74** (2003) 2631

9.5 Experimental setup for studying guiding of proton microbeam

G.U.L. Nagy, I. Rajta, R.J. Berezky, K. Tókési

Charged particles, keeping their initial charge states, can be transmitted through an insulating capillary even if the capillary axis is tilted with respect to the incident beam axis larger than the geometrical limit. This phenomenon is called charged particle guiding.

Although during the past few years many research groups joined to this field of research and carried out various experiments with insulator capillaries many details of the interactions remained unknown. In our forthcoming experiments we would like to try to determine whether the guiding-effect is still observable for 1 MeV proton beam. We note that the velocity of the 1 MeV protons is about 100 times larger than that of the highly charged ions used so far in the previous investigations. We plan to measure the energy distributions of proton microbeam transmission through a single macroscopic capillary as a function of time.

In order to perform ion guiding investigations in single macroscopic capillaries on the scanning nuclear microprobe of Atomki, a new experimental setup was necessary to be introduced. Both the sample positioning and the analysis of the transmitted particles required new features.

In the new setup the sample can be perfectly aligned to the beam axis by observing it with an optical microscope and Rutherford Backscattering technique. A thermal electron source (a lightbulb without its glass housing) is used to ensure neutral sample surface before each measurement.

The time evolution of the current and energy of the transmitted beam can be measured by a Faraday-cup and a STIM detector that are placed on a rotatable disk behind the sample. Since only one of them can be put into the capillary axis at a time, current and energy measurements cannot be performed simultaneously.

Another setup have also been built for de-

flection measurement and charge state identification purposes (see Fig. 1). A fluorescent screen that emits visible light from where the beam have hit it is mounted onto the end of the target chamber. Between the screen and the chamber a 21 cm long drift tube is put, in which a parallel plate deflector is mounted. The plates are connected to a 5 kV power supply, that is enough to deflect charged particles and make them separated from neutrals. The drift tube is long enough to magnify the deflection due to the sample rotation even if the sample is rotated with only 1 degree with respect to the beam. Since the deflection due to the plates is vertical while the sample rotation is horizontal, the two types of deflections can be observed parallel. A digital camera or camcorder is used for taking pictures and video of the beam position.

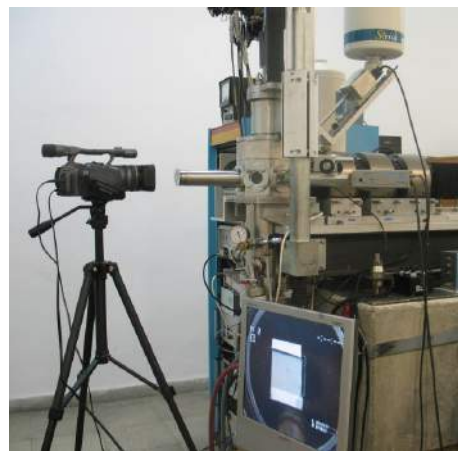


Figure 1. The new setup for deflection and charge state measurements. The fluorescent screen can be seen on the LCD display.

Acknowledgements

This work was supported by the Hungarian Scientific Research Fund OTKA No. NN 103279.

- [1] Nagy G.U.L., Rajta I., Berezky R.J., Tókési K., 22nd International Conference on the Application of Accelerators in Research and Industry. Fort Worth, Texas, USA, 5-10 Aug., 2012. Proceedings. New York, AIP (AIP Conference Proceedings) in press.

9.6 Status Report on the accelerators operation

S. Biri, Z. Kormány, I. Berzi, R. Rácz, Z. Perduk, I. Vajda

In 2012 our particle accelerators operated as scheduled, safely and without major or long breakdowns. The utilization rates of the accelerators slightly increased in comparing to the preceding year (see Fig. 1). The cyclotron delivered 1900 hours and the 40-years old 5 MeV Van de Graaff generator supplied more than 2400 hours. The 1 MeV Van de Graaff accelerator was also operated for short basic physics experiments (160 hours). The plasma and beam-on-target time at the ECR ion source was similar to the preceding years (410 hours). The isotope separator, as ion beam accelerator was utilized only for a few hours in 2012, since the research and development in this lab focused on other fields. Nevertheless it is continuously available for research requiring special deposition techniques and for isotope tracing studies. We developed the first version of an on-line accelerator status display software. Through our homepage anybody from anywhere can now check the current state of the cyclotron, VdG-5 and ECRIS accelerators [1].

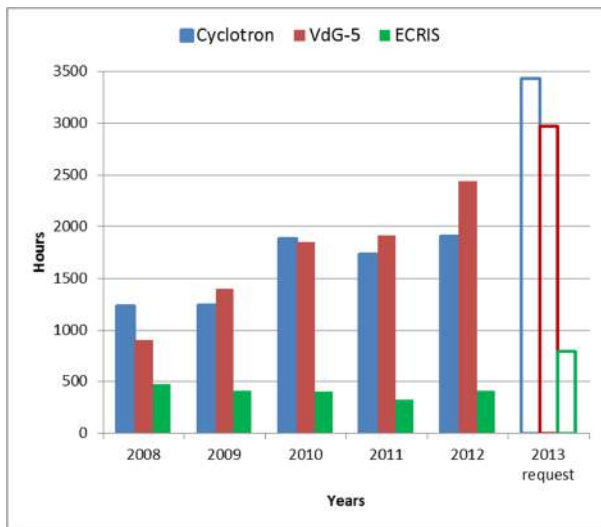


Figure 1. . Delivered and scheduled beamtimes by the main accelerators.

While in 2010 the cyclotron celebrated the 25th anniversary of its regular starting-up, in

2012 two of our other accelerators had also anniversary. The ECR Ion Source project started 20 years ago, in 1992. To celebrate it, a scientific symposium was hold in September. In the symposium - beyond the high number of audience - the leaders of the Hungarian Academy of Sciences, the University of Debrecen and the City of Debrecen attended, as well. The local and national press reported about the event in many form. A short summary of the symposium is in our homepage [2] (in Hungarian). We had the 40th anniversary of the regular use of the 5 MeV Van de Graaff accelerator. Having obtained the final approval of the project the "Electrostatic Accelerator Department" was organized in the Institute in July 1967 with the tasks to perform the planning and construction of the laboratory, to make all the preparations necessary for the intensive scientific use of the accelerator to be built, to adjust the equipments during the test runs and to put them to continuous use in nuclear research. The first nuclear measurements [$^{27}\text{Al}(p,g)$ and $^7\text{Li}(p,n)$] necessary for setting the main directions of the scientific activity were performed in September 1972. The annual running hours of VdG-5 accelerator was continuously increasing until reaching 3368 hours in 1979. From the year 1980 the average running per year was 2000 hours. After a long and careful technical and financial evaluation it was decided that the old 4 MeV used tandetron accelerator (was given as a gift to our institute years ago) will not be installed, instead, it will be disassembled. Many of its parts however can be used at other accelerators. There is a good chance that our institute can buy a new 4 MeV tandetron in 2013 (some details of this project are still under negotiation). If so, many of the beamline elements, vacuum components, power supplies of the old tandetron might be built together with the new tandetron. In the next sub-chapters the 2012 operation and development details at the cyclotron, VdG-5 and ECR accelerators are

summarized.

Cyclotron operation

The operation of the cyclotron in 2012 was concentrated to the usual 9 months; January, July and August were reserved for maintenance and holidays. The overall working time of the accelerator was 2573 hours; the time used for systematic maintenance was 259 hours. The breakdown periods amounted to 23 hours. Therefore, the cyclotron was available for users during 2291 hours from which the effectively used beam time was 1906 hours, summarized in Table 1. Two 140 W solid-state broadband preamplifiers have been built for the cyclotron RF-system. One is for replacing the outdated and partly faulty preamplifier module; the other will serve as the first stage of a new driver amplifier. For this purpose, a new project was started to build a 2 x 2.4 kW solid-state driver amplifier (SSDA) for the final stages of the cyclotron RF-system. Most of the amplifier modules and the control and safety electronics of the SSDA have been built during 2012. The system integration and tests are scheduled for 2013.

Table 1. Statistics of the cyclotron beam time for different research activities.

Projects	Hours	%
Nuclear Spectroscopy	202	10.6
Nuclear Astrophysics	1182	62.1
Radiation tolerance test	16	0.8
Nuclear data	3	0.1
Neutron physics	31	1.6
Isotope production	295	15.5
Thin layer activation(TLA)	177	9.3
Total	1906	100

Van de Graaff electrostatic accelerators

At the VdG-5 accelerator, we faced more beam time requirements than in the preceding year. The accelerator was running 2447 hours in 2012. We had to open the accelerator tank only 5 times during the last year. We had only one scheduled weekly maintenance work that involved the full disassembly of the charging system. In addition, we had several other short-time planned maintenance works in 2012. We had to replace some parts of the ion-source and to change the gas-bottles close to

the ion-source. Besides the beam-time requirements the ion species requirements increased, as well. We accelerated H^+ , D^+ , $^3He^+$, $^4He^+$ and N^+ particles. We solved the handling of the fourth gas-bottle in the ion-source, in order to serve our users with longer continuous beamtimes. With the 5 MV Van de Graff accelerator mainly (61%) proton particles were accelerated. The need for other particles was the following: D^+ 11%, $^3He^+$ 18%, $^4He^+$ 3%, N^+ 7%. The beam time was distributed among different research subjects as shown in Table 2. In the switching magnet we started to use a new generation High Precision Analog Linear Hall Effect Sensor (HE144, Hoeben Electronics) with improved measurement range up to 10 Tesla and excellent linearity.

Table 2. Time distribution among different research activities at VdG-5.

Topic	Hours	%
Atomki physics	183	7
Nuclear physics	445	18
Nuclear astrophysics	34	1
Analytical studies	1603	66
Micromachining	167	7
Machine test	15	1
Total	2447	100

In 2012 the VdG-1 machine was operated 160 hours. There were some test measurements with proton beam for a time-of-flight electron-spectrometer.

ECR ion source

Table 3 shows the beam species the ECRIS supplied in 2012 for users. In this year new beams were produced from solid materials as gold, calcium and silicon. To make plasmas from solids the sputtering technique was applied (see Fig.2). A background oxygen plasma supplied enough positive oxygen ions to sputter the small metal cylinders (made from pressed powder of the given material) which was negatively biased. Middle charged calcium (e.g. 8+) and silicon (e.g. 5+) beams and highly charged gold ion beam (upto 27+) were produced with moderate but extremely stable intensity (1-2 microamper at 10 KV extraction voltage). The method should be further developed to get higher intensity in order to

satisfy the requests of the users. The old computer control system (Pentium-1 motherboard, Windows-95, GPIB-card, VEE software) served well during the last 15 years. Recently a new National Instruments PXI hardware system was installed: controller, digital and analogue inputs/outputs, GPIB and RS232 interfaces, fiber optics coupling. The development of the Labview-based control software is under way. At that moment all the functions operated under the old control system work at the same level or better in the new configuration. New devices are also being included into the system continuously. In figure 3 the present layout of the full hardware assembly is shown.

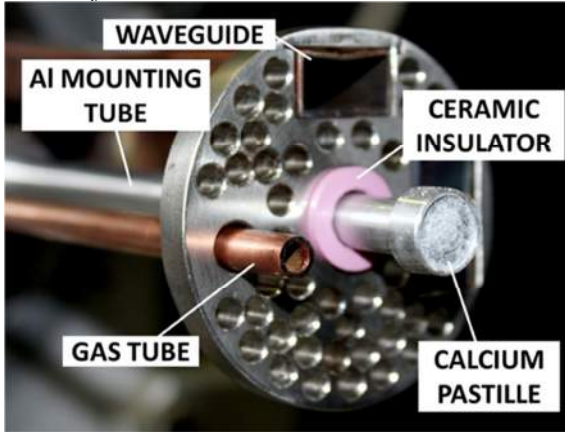


Figure 2. The sputtering assembly to make plasmas and beams from solid materials.

The ECRIS measuring and setting tools that have been included into the computer-based control and data acquisition system, are:

- vacuum gauge controllers
- high voltage power supplies (ion source extraction voltage, beam current, puller electrode voltage, einzel lens voltage, sputtering electrode voltage and current)
- high current bending magnet (setting one required value and scanning a range)
- bipolar power supply (biased disc)
- picoammeter (beam current measured in a Faraday-cup)
- microwave power (klystron amplifier).

The final goals are (1) to include majority of the ECRIS setting tools into hardware-controlled group, (2) to save the setting input/output data together with beam spectra to make a large data library and (3) to shorten the plasma tuning and beam transport time by automatically recalling the saved settings and (4) to stabilize the energy and intensity of the beam on target for long-term measurements.

Table 3. The ion beams delivered by the ECR ion source in 2012. The total energy of the beams is the product of the charge and the extraction voltage. DE: University of Debrecen, IEP: Institute of Experimental Physics, FD: Faculty of Dentistry, DAP: Division of Atomic Physics, ECR: ECR Group.

Research topic	User	Ion species	Extraction	Hours	%
Ion guiding through capillaries	ATOMKI-DAP	Ne ⁷⁺	0.4	144	35
Surface coating and implantation	DE-IEP, DE-FD ATOMKI-ECR	Au ⁹⁺ , Au ¹⁹⁺ , Ar ⁸⁺ , Ne ³⁺ , Si ³⁺	2,5,10	137,5	34
Fullerene (Co ₆₀) research	ATOMKI-ECR	Fe ⁵⁺	1.3, 13.0	33.5	8
Beam development	ATOMKI-ECR	O ^{6+,7+} , Ne ^{4+...10+} , Si ^{3+,5+} , Ar ^{7+...14+} , Fe ⁵⁺ , Au ^{+9+...27+}	0.4-10	95.5	23
Total				410.5	100

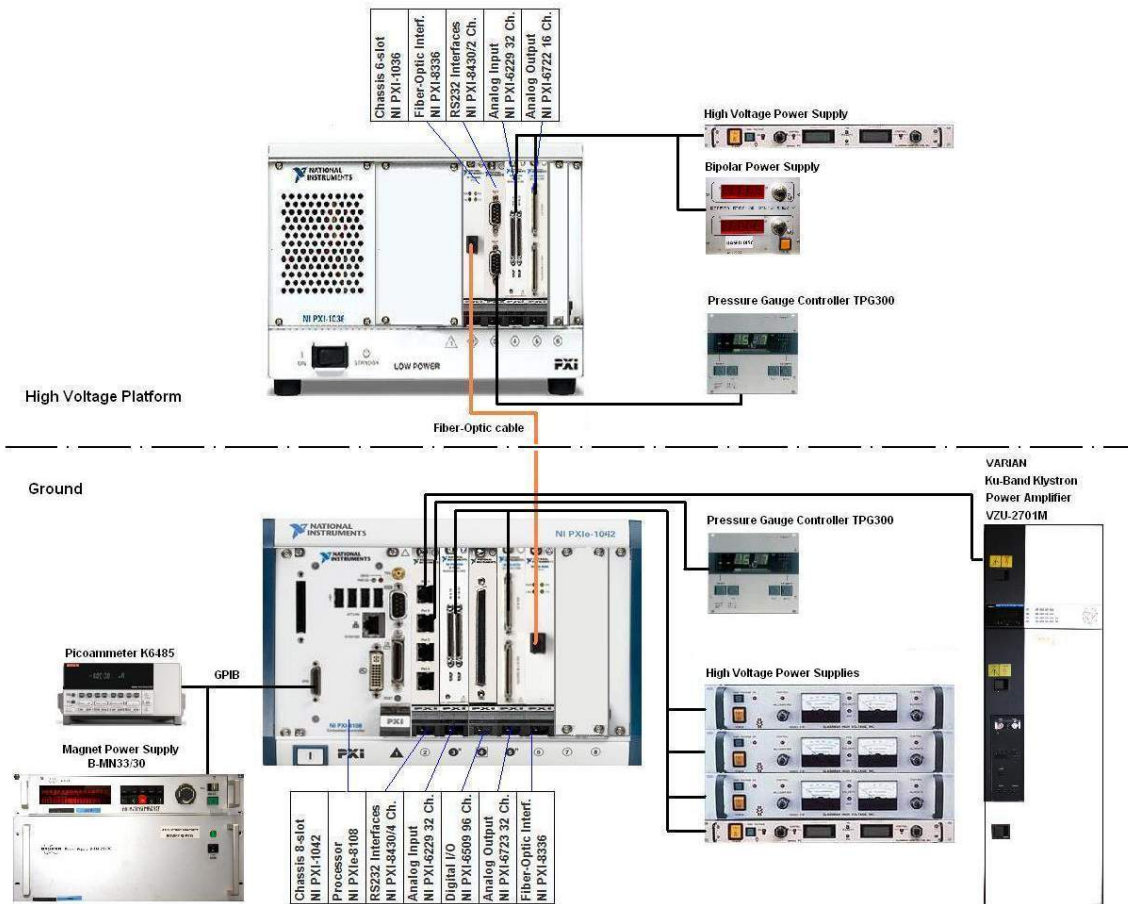


Figure 3. Hardware configuration of the ECRIS control system.

[1] http://www.atomki.hu/atomki/Accelerators/gyorsitoallapot_en.php

[2] <http://www.atomki.hu/atomki/Accelerators/hirek.html>

9.7 Thin target gamma ray yields induced by 0.65–2 MeV deuterons for nitrogen

L. Csedreki, G.Á. Szíki^{a)}, I. Uzonyi, Gy. Gyürky, Z. Szikszai, Á.Z. Kiss

Our laboratory has taken part in the development of the Particle Induced Gamma-ray Emission (PIGE) method since the eighties, using proton and later deuteron beams (p-PIGE and d-PIGE). Concerning d-PIGE, thick target γ -yields, measured for several elements, were published in 1994 [1] and in 2000 [2]. Later on γ -ray production cross-sections were determined from the measured thin target γ -ray yields of deuteron induced nuclear reactions on Li, Be, B, O and F targets [3]. New impetus has been given to our activities in this field since our participation in the coordinated research program (CRP) organized by the IAEA: "Development of a Reference Database for Particle-Induced Gamma-ray Emission (PIGE) Spectroscopy". The aim of this CRP is to create a database of cross-sections to improve the quality and availability of nuclear data for PIGE. Taking advantage of the capability of our electrostatic accelerator to provide deuteron beams and considering the scarcity of the available cross-section data for d-PIGE, we have decided to concentrate our efforts on d-PIGE. The work started with the reconstruction of a small target chamber dedicated to thin target PIGE cross-section measurements, installed at the J30 beam-line of our VdG-5 accelerator. The chamber was equipped with a new port to detect particles simultaneously with γ -rays (for the accurate determination of parameters to be used later in the cross-section calculations). With this setup, a low γ -ray background could be achieved [4]. The first application of this target chamber was the investigation of the nuclear reaction $^{14}\text{N}(\text{d},\text{p}\gamma)^{15}\text{N}$. The target material chosen was a commercially available Si^{3}N^4 thin film with a thickness of 200 ± 14 nm. As a by-product, it also supplies data for silicon simultaneously. Gamma-rays were detected with a coaxial HPGe detector installed on one of the two arms of a turntable at an angle of 55° relative to the incident beam direction. The front face of the detector was at a distance of 9.5 cm from the target. The collected charge var-

ied from 50 to 400 μC to achieve good statistics for all deuteron energy points. From the γ -spectra, the yields of the following γ -lines – not disturbed by escape peaks – could be easily determined: 1885, 2297 and 8310 keV in the case of ^{14}N (see Fig. 1.), and the 1273 and 2028 keV γ -lines in the case of ^{28}Si . The deuteron energy dependence of the γ -ray yield for the sum peak 7299+8310DE keV of nitrogen is also shown in Fig. 1. due to its usefulness for analytical applications. The calculation of cross-sections from the γ -yields using the absolute efficiency of the detector, the number of atoms calculated from the deuteron backscattered (RBS) measurements, etc. is in progress.

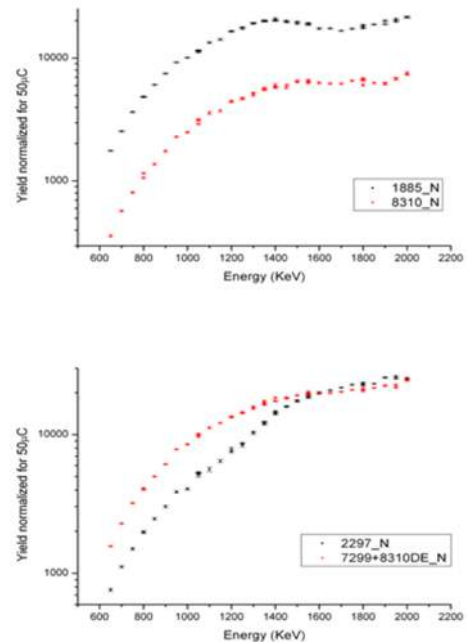


Figure 1. Gamma-ray yield curves in the function of deuteron energy for nitrogen ($Q\approx 50 \mu\text{C}$).

Acknowledgements

This work has been supported by the IAEA CRP Contract No. 16967/R0.

a) Department of Basic Technical Studies, Faculty of Engineering, University of Debrecen

- [1] Kiss Á. Z. et al., Nucl. Instr. and Meth. B **85**, 118-122 (1994)
- [2] Elekes Z. et al., Nucl. Instr. and Meth. B **168**, 305-320 (2000)
- [3] Szíki G. Á. et al., Nucl. Instr. and Meth. B **251**, 343-351 (2006)
- [4] László Csedreki Acta Physica Debrecina **46**, 25-35 (2012).

9.8 Constructing an European Low Energy Neutron Spectrometer (ELENs)

L. Stuhl, A. Krasznahorkay, M. Csatlós, A. Algora, J. Gulyás, G. Kalinka, Zs. I. Kertész, J. Timár

The most exotic nuclei are usually the most interesting nuclei but their production rate decreases exponentially with the increase of the proton-neutron asymmetry. In order to counterbalance this effect, high-efficiency detector setups and thick reaction targets are required. We have developed a neutron ToF setup (ELENs) for studying the (p,n) reaction in inverse kinematics. Using inverse kinematics, the kinetic energy of the neutrons is low and short flight path is sufficient for the time-of-flight measurements. This case one can use at the same time thick targets, without disturbing the energy spectrum of the recoiled neutrons, which has an importance in experiments with rare isotope beams.

The detection efficiency of ELENs has been investigated at the Physikalisch-Technische Bundesanstalt (PTB) accelerator facility, in Braunschweig. The temperature-controlled large experimental hall is well suited for neutron measurements under low-backscatter conditions. Using the ${}^7\text{Li}(p,n){}^8\text{Be}$ reaction at different proton energies quasi-monoenergetic neutrons were created and the detection efficiency of the detector paddles was measured. The energy distribution of neutrons produced in the target was set by using the EnergySet program.

Using dedicated quasi-monoenergetic neutrons at kinetic energies of 240, 471, 925 and 2014 keV the neutron-detection efficiency has been determined. The distance of the ELENs detectors was about 5020 mm from the target (from the target to the front side of the scintillators). The detectors were mounted at 42.5° . Two long neutron counters were mounted as reference counters at 98° and 16° with respect

to the direction of the proton beam.

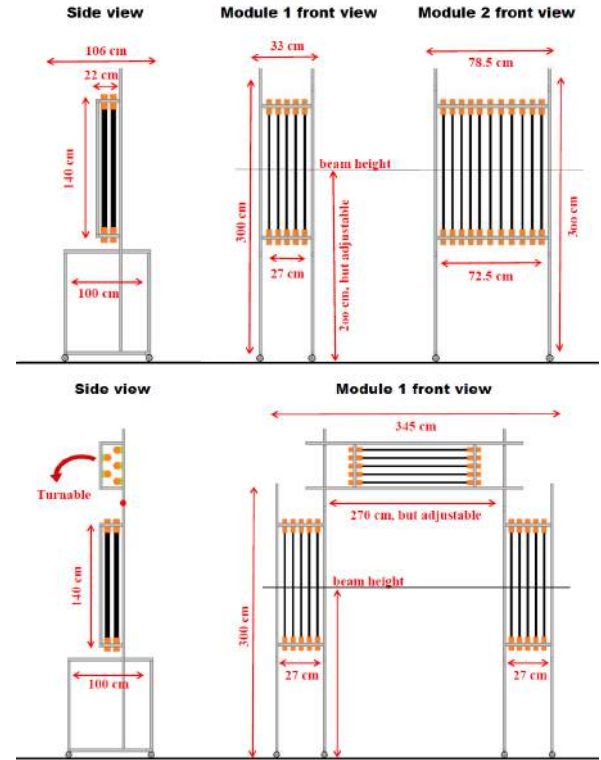


Figure 1. The schematic layout of the ELENs spectrometer. The geometry of ELENs is completely flexible. There are two main configurations, optimized for charge-exchange (p,n) experiments.

The obtained efficiency is 16.9 % at 240 keV, 24.7 % at 471 keV, 42.1 % at 925 keV and 39.2 % at 2.014 MeV. The efficiency of the detector along the scintillator bars is constant within $\pm 5 - 7\%$

Acknowledgements

The work has been supported by the Hungarian OTKA Foundation No. K106035.

9.9 Porting VIRTEX4 data acquisition design to SPARTAN6 FPGA

J. Sütő, G. Hegyesi

The Atomki's Virtex 4 based 4 channel data acquisition card (LIR) card was used in many applications (miniPET-II, miniPET-III, data acquisition system for the multichannel plate installed at the ECR lab). The goal of the work was to improve the LIR using a higher performance FPGA (Spartan6 Trenz module). The Trenz module [1] based system also supports ADC channels up to 16 channels. This work also implied the porting of the Virtex4 based VHDL code to Spartan 6. Further advantage of the proposed system, besides the improvement in the number of ADC channels, that the Spartan6 FPGA is able to run more complex digital signal processing algorithms than the Virtex 4 FPGA. Easy access to the control parameters (via serial interface or Ethernet), flexibility and high performance were considered during the development.

SPARTAN6 FPGA based data acquisition provides more facilities than the VIRTEX4 based. SPARTAN6 is a newer generation of XILINX's FPGAs, which excellent into the high-speed data acquisition.

We ported the HDL code, which runs on LIR module (VIRTEX4 based), to the Trenz module (SPARTAN6 based).

The main parts of the whole program code

```

ATONKI-DSP>
MAC32 l - 2nd byte
MAC34 h - 3rd byte
MAC34 l - 4th byte
MAC56 h - 5th byte
MAC56 l - 6th byte

IPSTAT - the DSP card's static IP address (IPSTAT is enabled if no DHCP server
is available)
IPSTAT = 1.2.3.4:
IPSTAT12 h - 1st byte
IPSTAT12 l - 2nd byte
IPSTAT34 h - 3rd byte
IPSTAT34 l - 4th byte

IPDEST - destination IP to where the data is sent when STARTDEST command
is entered
IPDEST = 1.2.3.4:
IPDEST12 h - 1st byte
IPDEST12 l - 2nd byte
IPDEST34 h - 3rd byte
IPDEST34 l - 4th byte

ATONKI-DSP>
    
```

Figure 1. Command line interpreter.

are the command line interpreter, GMII interface, DHCP process, ARP process and the data read out. Those parts were implemented by picoblaze embedded system. Figure 1 shows the command line interpreter process in the Hyper Terminal.

The command line interpreter communicates with the PC via serial port. In addition, the AdamIOSetting software also use the serial communication, which was created to the VIRTEX FPGA based data collector. In the Wireshark network analyzer software we examined the DHCP and ARP process and using the AdamIOSettings software we tested the data read out from the flash memory of FPGA board. Figure 2 shows the AdamIOSettings program.

Acknowledgements This work was supported by the ENIAC CSI Project (No.120209).

- [1] Trenz electronic Gigabee XC6SLX Serial User Manual Industrial-Grade Xilinx Spartan-6 LX FPGA Micro-modules UM-TE0600 12 June 2012.

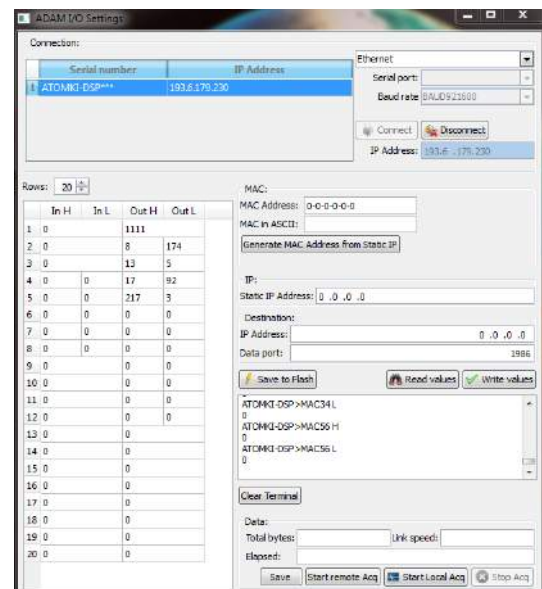


Figure 2. The AdamIOSettings program.

9.10 Time over threshold readout method of SiPM based small animal PET detector

I. Valastyán, J. Gál, G. Hegyesi, G. Kalinka, F. Nagy, B. Király, J. Imrek, J. Molnár

The aim of the work was to design a readout concept for silicon photomultiplier (SiPM) sensor array used in small animal PET scanner. The detector module consist of LYSO 35x35 scintillation crystals, 324 SiPM sensors (arranged in 2x2 blocks and those quads in a 9x9 configuration) and FPGA based readout electronics. The dimensions of the SiPM matrix are area: 48x48 mm² and the size of one SiPM sensor is 1.95x2.2 mm². Due to the high dark current of the SiPM, conventional Anger based readout method does not provide sufficient crystal position maps. Digitizing the 324 SiPM channels is a straightforward way to obtain proper crystal position maps. However handling hundreds of analogue input channels and the required DSP resources cause large racks of data acquisition electronics. Therefore coding of the readout channels is required.

Proposed readout method: The coding of the 324 SiPMs consists two steps: Step 1) Reduction of the channels from 324 to 36: Row-column readout, SiPMs are connected to each other in column by column and row-by row, thus the required channels are 36. The dark current of 18 connected SiPMs is small in off for identifying pulses coming from scintillating events. Step 2) Reduction of the 18 rows and columns to 4 channels: Comparators were connected to each rows and columns, and the level was set above the level of dark noise. Therefore only few comparators are active when scintillation light enters in the tile. The output of the comparator rows and columns are divided to two parts using resistor chains. Then the outputs of the resistor chains are digitized by a 4 channel ADC. However instead of the Anger method, time over threshold (ToT) was used. Figure 1 shows the readout concept of the SiPM matrix.

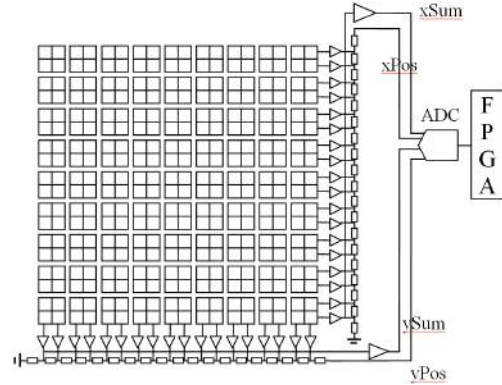


Figure 1. The row-column readout schema of the SiPM matrix.

In order to validate the new method and optimize the front-end electronics of the detector, the analogue signals were digitized before the comparators using a CAEN DT5740 32 channel digitizer, then the comparators, the resistor chains and the position extraction method were implemented in a PC. Position map calculated by the ToT weights is shown in Figure 2.

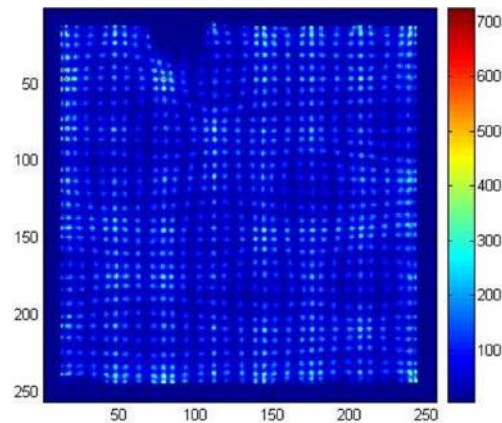
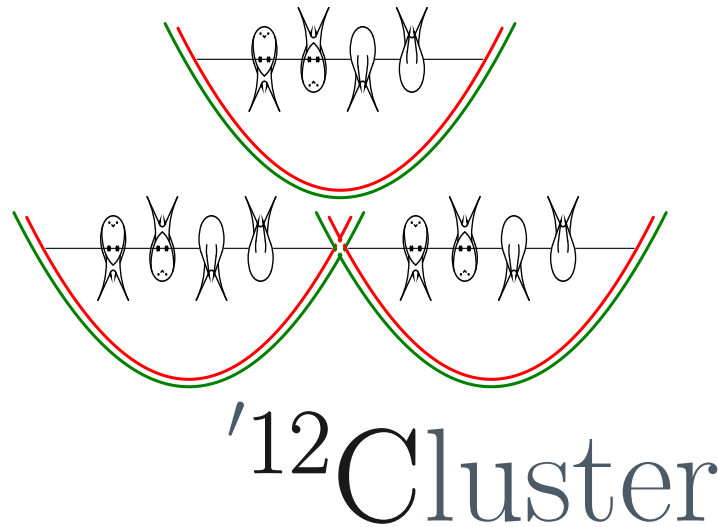


Figure 2. Position map of the SiPM tile and the 35x35 LYSO crystal matrix.

Acknowledgements

This work was supported by the ENIAC CSI Project (No.120209).

10.1 Report on the 10th International Conference on Clustering Aspects of Nuclear Structure and Dynamics



This series of conferences was started in Bochum, 1969, and each number follows the previous one in about four years. The tenth one was organized by Atomki and was held in Kőlcsey Convention Centre, Debrecen, 24–28 September, 2012. The city was chosen as a recognition of the achievements of the members of this Institute in the field of cluster physics.

The conference took stock of the recent progress of research of clustering phenomena, cluster models, reactions with clustered nuclei and the collisions between nuclei described as clusters. The scope now included the following titles:

- Alpha clustering
- Cluster reactions
- Few-body and *ab initio* approaches
- Microscopic approach to cluster structure and reactions
- Algebraic cluster models
- Structure and reactions of exotic nuclei
- Nuclear molecules
- Elongated states, decay and fission; superheavy elements
- Clustering in nuclear matter
- Nuclear reactions for astrophysics

- High-energy and multifragmentation reactions
- Hypernuclei and quark clusters
- Application of cluster theory and clustered nuclei

There were 115 registered participants, representing 22 countries of Europe, Africa, Asia, Central, South and North America. We had 44 plenary talks and 48 talks presented in parallel sessions. All the talks in the plenary sessions were invited talks, but we had some invited talks even in the parallel sessions.

The Proceedings of the Conference is being published by the Institute of Physics and will appear in *Journal of Physics: Conference Series* to be readable both on the internet and as a volume.

Considering that the success of a conference depends primarily on the speakers, in retrospect, we can say that this conference was extremely successful, and that is owing to the great many wonderful talks delivered. This reflects very well on the present status of the field as well as on the work of the International Advisory Board, which proposed us to

invite excellent speakers. The Japanese dominance characteristic of all cluster conferences has only been complained about by some of the Japanese who came to Europe primarily to learn things that they could not learn at home.

Our sponsors have greatly contributed to the success of the conference. They were

the Hungarian Academy of Sciences,
the Paks Nuclear Power Ltd.,
HMP Logic Ltd.
and the International Workshop for Theoretical Physics (Budapest).

We also received indirect support from a JSPS–MTA bilateral cooperation project.

The nucleus ^{12}C , being a paradigmatic example of clustering, of α condensation and of the competition between cluster and shell aspects, was in the focus of the conference. Foreseeing the central role of this nucleus, the logo of the conference was chosen to depict ^{12}C as composed of three α -clusters, each described by a $(0s)^4$ harmonic-oscillator ground state. The nucleons sitting on single-particle levels were visualized as swallows perching on electric wires, with the difference between protons and neutrons as well as between spin-up and spin-down nucleons depicted.

R. G. Lovas

10.2 Events

Physicists' Days – Engineering – play with physics

5-10 March 2012

Péter Závodszky (General Electric Global Research Center): *Great-grandchildren of Edison*

Sándor Mészáros (Atomki): *Nuclear Age or Silicon Age?*

András Pungor (University of Debrecen): *Interpretation of the physics by engineers*

Sándor Soha (MH 59. Szentgyörgyi Dezső Repülőbázis, Kecskemét): *Ironbirds – the miracle of flight*

The European Nuclear Science and Applications Research (ENSAR, FP7) held a Joint Research Activity (JRA) workshop meeting in Atomki. The topic of the meeting was: Advanced Research on Ecr ion Sources (ARES)

19-20 April 2012

"Természet Világa" special issue - MTA Atomki

4 May 2012

Advanced Topics in Nanotechnology - Gábor L. Hornyák

11-22 June 2012

University of Debrecen - MTA Atomki joint courses

We regret to inform you that our unforgettable colleague and friend, director of Atomki between 1976 and 1990, former vice president of the Hungarian Academy of Sciences Professor Dénes Berényi passed away on 27th June, at the age of 84, after a short but fatal illness endured with tolerance. The funeral ceremony was held in Debrecen, on 5th July.

27 June 2012

ENIAC CSI project meeting

6-7 September 2012

20 Years of the ECR Laboratory at Atomki– 60th Birthday celebration of József Pálinkás, the President of the Hungarian Academy of Sciences

10 September 2012

Visit of the Atomki Advisory Board

24-25 September 2012

Cluster'12

24-28 September 2012

10th International Conference on Nuclear Clustering

Researchers' Night

28 September 2012

Kálmán Varga (Vanderbilt University, USA):

Simulation of nanosystems

Nuclear Astrophysics Intensive Course

19-23 November 2012

Thomas Rauscher

LHC T3 Grid Centre in Debrecen (workshop)

22 November 2012

Closing ceremony of the KEOP-5.3.0/A/09-2009-0109 project (Environmental and Energy Operativ Program)

14 December 2012

"Complexity from quantum systems to emergent behavior"

10-14 December 2012

School and workshop

10.3 Hebdomadal Seminars

January 19

How to write FP7 proposals?

Z. Szűcs

February 3

Highlights from the LHC

G. Dissertori (*ETH Zürich*)

February 7

Input of references to MTMT

D. Adomán-Zolnai (*Atomki*)

February 15

Photon and electron induced transformations and pattern formation in amorphous chalcogenide nano-layers

V. Takáts (*Atomki*)

March 13

Functional and structural brain network models

M. Emri (*University of Debrecen*)

March 20

Methods to measure low cross sections for nuclear astrophysics

T. Szűcs (*Atomki*)

March 22

Phase states of matter of strong interaction

T. Fényes (*Atomki*)

March 27

Cluster models and nuclear fission

A. Ventura (*ENEA, Bologna*)

April 5

1. Ion-surface interactions in nanocapillaries 2. Energetic H- emission in collisions of H-bearing molecules and molecular ions

Z. Juhász (*Institute habilitation*)

April 23

State of affairs

Zs. Fülöp, M. Pálinkás (*Atomki*)

April 25

Optically powered sensory system

J. Turán (*Kosice*)

May 4

Application of semiconductor and scintillation detectors for high energy physics experiments

A. Sipos (*Atomki*)

May 10

Study of stability of equilibrium states under constraints

T. Gál (*University of Florida*)

May 16

Transmission of charged particles through a single glass microcapillary

R. J. Berezky (*Atomki*)

May 16

Examination of physical and chemical changes in polymers caused by proton beam irradiation and their applications in proton beam micromachining

Sz. Szilasi (*Atomki*)

May 22

Positron and electron molecule collision calculations using the R-matrix

J. Tennyson (*University College London*)

May 24

Tritium calorimetry - participation in an EFDA training program

A. Bükki-Deme (*Atomki*)

May 31

Neutron stars or quark stars – what do the nuclei say?

A. Krasznahorkay (*Atomki*)

June 7

There is plenty of light at the bottom

N. Kroó (*Wigner Research Centre for Physics, Budapest*)

June 28

Whom the Oxford Institute for Theoretical Physics was named after
Gy. Radnai (*Eötvös Loránd University, Budapest*)

August 23

The observation of the Higgs boson at LHC: workshop secrets
D. Horváth (*Wigner Research Centre for Physics, Budapest*)

August 24

Application of keV and MeV ion microbeams through tapered glass capillaries
T. Ikeda (*Atomic Physics Laboratory RIKEN, Japan*)

August 30

Work and results at Atomki for the ${}^3\text{He}+{}^4\text{He}$ experiment, OTKA **82409** project
C. Bordeanu (*Atomki*)

September 11

Cross section measurements of alpha-captured reactions on Sb isotopes for the astrophysical gamma-process
Z. Korkulu (*Atomki / Kocaeli University, Turkey*)

September 13

In a search for tetrahedral symmetries in ${}^{156}\text{Dy}$
S. N. T. Majola (*iThemba LABS, Cape Town*)

September 14

What can be learned from 20 years of Underground Nuclear Astrophysics?
M. Junker (*Laboratori Nazionali del Gran Sasso*)

September 20

... waiting for a response ... (What is fractional distillation good for?)
L. Zolnai (*Atomki*), Z. Papp (*University of Debrecen*), D. Adomán-Zolnai (*Atomki*)

October 4

Introduction of new colleagues in Atomki
P. Bojtos, Gy. Glodán, A. Horváth, F. Pittler, J. Rácz (*Atomki*)

October 11

Infrared nanoscale spectroscopy
K. Kamarás (*Wigner Research Centre for Physics, Budapest*)

October 18

SU(3) realization of the pairing-plus-quadrupole model in one or more oscillator shells

K. Drumev (*Institute for Nuclear Research and Nuclear Energy, Sofia*)

October 30

Indirect methods in nuclear astrophysics using Rare Isotope Beams

L. Trache (*NIPNE, Bucharest-Magurele and Texas A&M University, College Station*)

November 15

Reports on student-researcher's work in 2011 - 2012

M. Takács, D. Nagy, G. Orsovszki, E. Piros, J. Rácz, K. Szitha (*Atomki*)

November 22

The LHC T3 Grid Center in Debrecen

Z. Trócsányi, O. Feró, Á. Kardos, T. Kovács (*University of Debrecen, Atomki*)

November 29

Radiocarbon dating of lake sediments for understanding of the past 50,000 yrs

I. Hajdas (*Laboratory of Ion Beam Physics, ETH Zurich*)

December 6

Quantum mechanics in work (on the 2012th year's Nobel Prize)

P. Domokos (*Wigner Research Centre for Physics, Budapest*)

December 11

Methods for structural control and dating of hydrothermal solution flows in crystalline rocks considering the example of the Velence Hills

Zs. Benkó (*Karl-Franzens Universität Graz*)

December 12

1. Archaeometry studies with ion beam analytical methods – the CHARISMA FP7 program in Atomki

2. Nuclear microprobe investigation of the penetration of ultrafine TiO₂ and ZnO into human skin

Z. Szikszai (*Institute habilitation*)

December 18

The Borexino experiment

M. Pallavicini (*Università di Genova & INFN*)

December 20

Animations and simulations for science education and information dissemination

S. Nagy (*Eötvös Loránd University, Budapest*)

10.4 Awards

Péter Salamon

Prize of the The Debrecen Committee of the Academy of the MTA

Szabolcs Szilasi and János Farkas

Atomki Young Researcher Award

Gábor Kiss

Young Researcher Award of the Hungarian Academy of Sciences

Dezső Horváth

Széchenyi Prize

Zoltán Elekes and Zsolt Dombrádi

OTKA Prize

Ákos Kövér and Sándor Ricz

Physics Prize of the Hungarian Academy of Sciences

Kadosa Balogh

Szalay Sándor Award

Gábor Kiss

Junior Príma Prize

Sándor Bohátka

Selényi Pál Award of the Roland Eötvös Physical Society

10.5 List of Publications

The total number of publications in 2012 was 451, of which 248 SCI papers, 79 other papers and proceedings, 1 theses, 5 diploma works, 7 books or book chapters and 3 edited work.

The list of the Institute's publications can be found on-line at:
<http://w3.atomki.hu/p2/years/yea02012.htm>

Highlights

In 2012 the following papers have been selected as "Highlights":

Bosonization and functional renormalization group approach in the framework of QED2

I. Nándori, **Physical Review D** 84, 065024 (2011)

Shallow-underground accelerator sites for nuclear astrophysics: Is the background low enough?

T. Szücs, *et. al*, **The European Physics Journal A** 48 (2012) 8

Identification and chemical characterization of particulate matter from wave soldering processes at a printed circuit board manufacturing company

Z. Szoboszlai, *et al.*, **Journal of Hazardous Materials** 203, 308-316 (2012)

Quantum nonlocality does not imply entanglement distillability

Tamás Vértesi and Nicolas Brunner, **Phys. Rev. Lett.** 108 (2012) 030403

Investigation of activation cross-sections of proton induced nuclear reactions on ^{nat}Mo up to 40 MeV: New data and evaluation

F. Tárkányi, *et al.*, **Nucl. Instr. and Meth. B** 280, 45-73 (2012)

Top quark pair production in association with a Z-boson at next-to-leading-order accuracy

A. Kardos, *et. al*, **Physical Review D** 85 (2012) 5:4015

Transmission resonance spectroscopy in the third minimum of ^{232}Pa

L. Csige, *et al.*, **Physical Review C** 85 (2012) 054306

A critical analysis of the experimental L-shell Coster-Kronig and fluorescence yields data

T. Papp, **X-Ray Spectrometry** 41 (2012) 128

Double and transfer ionization in collisions of He with bare ions

L. Gulyás, *et. al*, **Phys. Rev. A.** 86 (2012) 024701

Observation of a new boson at a mass of 125 GeV with the CMS experiment at the LHC

CMS-Collaboration, from Atomki N. Béni, S. Czellár, A. Fenyvesi, J. Molnár, J. Pálkás, Z. Szillási, **Physics Letters B** 716, 30 (2012)

Relation between total cross sections from elastic scattering and α -induced reactions: The example of ^{64}Zn

Gy. Gyürky, *et. al*, **Physical Review C Rapid Communications** 86 (2012) 041601

Gradual spontaneous breakdown of PT symmetry in a solvable potential

G. Lévai, **Journal of Physics A: Mathematical and General** 45 (2012) 444020

A short summary of these papers can be found on the next pages.

Bosonization and functional renormalization group approach in the framework of QED2

I. Nándori

Physical Review D 84, 065024 (2011)

<http://link.aps.org/doi/10.1103/PhysRevD.84.065024>

In particle physics, theories and models are defined at high energies, where symmetry considerations are valid, but the measurements are performed at relatively low energies. Thus one has to determine the low-energy behavior of every model which requires the so called renormalization. Since the invention of the exact renormalization group (RG) method its main goal has been to describe systems where the usual approximations (e.g. perturbation theory) fail. Unfortunately, exact RG equations are functional equations hence one has to use truncations in order to handle them. The truncated RG equations depend on the choice of the so called RG scheme implying that the predicting power of the RG method is weakened and some dependence of physical results on the RG scheme can be observed. Since the functional RG has been developed in order to perform the renormalization non-perturbatively, it is of great importance to optimize the RG scheme-dependence. In order to optimize the scheme-dependence of RG equations a commonly accepted strategy is to consider such models, where other non-perturbative results are available. For example, lattice calculations can provide us physical properties (e.g. critical exponents) of certain models which can be considered as exact values and the RG scheme should be chosen to get the closest

value to the exact one. Then the RG equation optimized in this way can be applied to other models and theories. However, it is an open question whether the RG approach optimized for a particular model can produce the best result for the others. In general, if the RG equation is optimized for scalar type (bosonic) models (which is the usual case) it is rather questionable whether it remains optimized for the more complicated (but more physical) fermionic and gauge theories. The method proposed in the present work is based on the bosonization which opens a new platform to consider the RG scheme-dependence. In low dimensions, exact bosonization rules do exist which enables us to reformulate the gauge and fermionic models in terms of elementary scalar (bosonic) fields. The advantage of this new approach is the usage of bosonization because both the bosonized and the original models can be treated simultaneously by RG methods. Consequently, it is possible to perform optimization for the scalar theory and for its fermionic or gauge counterpart as well. On the one hand, optimizations of the bosonic and fermionic models can be related to each other via the bosonization providing us a tool to consider the validity of the conventional optimization. On the other hand, it has impact on the bosonization.

Shallow-underground accelerator sites for nuclear astrophysics: Is the background low enough?

T. Szücs^{1,2}, D. Bemmerer², T. Cowan^{2,3}, D. Degering⁴, Z. Elekes^{1,2}, Zs. Fülöp¹, Gy. Gyürky¹, A. Junghans², M. Köhler⁴, M. Marta², R. Schwengner², A. Wagner² and K. Zuber³

The European Physical Journal A 48, 8 (2012)

DOI 10.1140/epja/i2012-12008-7

To estimate the rate of a charged particle induced nuclear reaction in a non explosive astrophysical scenario, its cross section must be measured far below the Coulomb barrier. However, at these energies the cross section values are very low, so that the experimental counting rate at the surface of the Earth is dominated by cosmic-ray induced background. This problem can be overcome by working in a deep underground site (> 1000 m of rock cover). In this work a combined approach is proposed, using a shallow underground laboratory and an active shield to veto surviving muons from the cosmic rays, resulting a background level that is not far from that of deep underground sites. Laboratory background measurements were performed at the surface of the Earth, and at underground laboratories with different depth. The shallow underground (47 m depth) location was the Dresden Felsenkeller laboratory in Germany, while the deep underground (1300 m depth) place was the Gran Sasso laboratory in Italy. One and the same detectors have been transported subsequently to each site, to avoid the differences not attributed to the laboratory. Two actively shielded detectors have been used. First a high purity germanium Clover detector equipped with a bismuth germanate (BGO) escape suppression shield, which can also act as a muon veto. The second detector was a lanthanum bromide (LaBr₃) detector placed inside a big BGO antimuon shield. The counting rate difference between the deep underground

and shallow underground sites in the vetoed spectra found to be only a factor of 2.4 in the high energy region (3-8 MeV). Based on the background data, the feasibility of several reaction cross section measurements of astrophysical interest is evaluated, considering the Clover detector in a geometry that have already been used for in-beam cross section measurement of astrophysical interest. It is shown that experiments at the surface of the Earth are not a realistic option for any of the reactions considered here. Instead, an underground setting is needed. Owing to the fact that nuclear reaction experiments require low but not ultra-low background, it is shown that already shallow underground sites offer satisfactory background conditions for a number of in-beam β -spectrometry experiments, if an active shield is applied. As shallow-underground facilities are more easily accessible than deep-underground ones, the present finding holds the promise of greatly accelerated progress in the field of cross section measurements for nuclear astrophysics.

- [1] Institute for Nuclear Research, Hungarian Academy of Sciences (ATOMKI), Debrecen, Hungary
- [2] Helmholtz-Zentrum Dresden-Rossendorf (HZDR), Dresden, Germany
- [3] Technische Universität Dresden, Dresden, Germany
- [4] Verein für Kernverfahrenstechnik und Analytik Rossendorf (VKTA), Dresden, Germany

Identification and chemical characterization of particulate matter from wave soldering processes at a printed circuit board manufacturing company

Z. Szoboszlai¹, Zs. Kertész¹, Z. Szikszai¹, A. Angyal¹, E. Furu¹, Zs. Török¹, L. Daróczy² and Á. Z. Kiss¹

Journal of Hazardous Materials 203, 308 (2012)

doi:10.1016/j.jhazmat.2011.12.030

It is well known that the electronics products industry has exposed workers to high doses of metals. Several studies have reported that the inhalation of metal dust and fumes is associated with adverse health effects such as metal fume fever and other respiratory diseases. In this study, our aim was to investigate indoor aerosol particles in a working environment where the soldering and testing of different kinds of printed circuit boards (PCB) and other electronic components takes place. Wave soldering is one of the main processes used for attaching metal components to the board during the manufacturing of PCBs. (The name is derived from the use of waves of molten solder. The constituents of the solder alloy are dependent on the type of wave solder e.g. leaded (Sn-Pb) or lead free wave solder (Sn-Ag-Cu-Sb). Aerosol samples were collected in a large working hall where approximately 100 people worked. In this study, we have showed that the manufacturing of the PCBs is associated with aerosol emissions. Based on the elemental ratios and correlations, size distribution data and single particle analysis, the creation processes and the indoor sources were identified, e.g. sol-

dering, fluxing, etching and cleaning. The concentration of PM and the elemental components increased at the wave solders. The main constituents of the leaded and the unleaded melt were recognized in the indoor aerosols. Flux-related (Zn, Cl), and etching-related (Fe, Cl) elemental compositions were also identified. It was confirmed that relative to the outdoor atmosphere inside the working hall the air was clean due to supply air ventilators and the low indoor emission rate. Although the concentrations of Pb were less than the limit value of the WHO, there was a maximum in the fine mode in the mass size distributions of Pb and other metals (Ag, Cu, Zn). This fact could be associated with increased risk of the adverse effects, since our stochastic lung model calculations showed higher deposition probability for Pb than for particles of natural origin.

- [1] Institute for Nuclear Research, Hungarian Academy of Sciences (ATOMKI), Debrecen, Hungary
- [2] Department of Solid State Physics, University of Debrecen, H-4010 Debrecen, P.O. Box 2, Hungary

Quantum nonlocality does not imply entanglement distillability

T. Vértesi¹ and N. Brunner²

Phys. Rev. Lett 108, 030403 (2012)

<http://link.aps.org/doi/10.1103/PhysRevLett.108.030403>

Entanglement is a quantum phenomenon in which distinct objects become so deeply linked that they behave as a single entity, no matter how far they are. As a result, once a measurement is carried out on one member of an entangled pair of particles, the state of the other member of this pair is immediately modified. This effect may lead to an even stronger notion of inseparability, which is called nonlocality. This is the strange ability of quantum objects to synchronize actions over large distances in such a strong way which could not have been resulted from any classical mechanism. It turns out that nonlocality cannot happen without entanglement. On the other hand, there exist highly entangled states which do not possess nonlocality. This asymmetric relation has been a strange puzzle for physicist for a long time, and the present work makes a step toward the solution. Namely, it is presented a three-particle system which exhibits

a very weak form of entanglement, so-called undistillable entanglement. In the considered multipartite case, it means that no entanglement can be extracted along any three bipartite cut (A|BC, B|AC, and C|AB) of the system. However, by judiciously chosen measurements, the three-particle state violates a certain Bell inequality, hence the state is nonlocal. This result goes against earlier findings, where states with undistillable entanglement did not show up Bell inequality violation. The present result also disproves a multipartite version of a long-standing conjecture made in 1999 by Asher Peres, who is one of the pioneers of quantum information science. Though, it remains an open question whether the conjecture holds true for two parties or not.

[1] Institute for Nuclear Research, Hungarian Academy of Sciences (ATOMKI), Debrecen, Hungary

[2] H.H. Wills Physics Laboratory, University of Bristol, United Kingdom

Investigation of activation cross-sections of proton induced nuclear reactions on ^{nat}Mo up to 40 MeV: New data and evaluation

F. Tárkányi¹, F. Ditrói¹, A. Hermann², S. Takács¹, A. V. Ignatyuk³

Nucl. Instr. and Meth. B 280, 45 (2012)

<http://dx.doi.org/10.1016/j.nimb.2012.02.029>

Cross-sections of proton induced nuclear reactions on natural molybdenum have been studied in the frame of a systematic investigation of charged particle induced nuclear reactions on metals for different applications and for comparison with theory. Activation cross-section data on molybdenum are important for several practical applications. The nuclear medicine is based on cellular function and physiology, completing other diagnostic methods relying on physical changes in the tissue anatomy (MRI, CT). The primordial role of ^{99m}Tc for nuclear medicine is well known, 80-85% of the nuclear medicine studies are utilizing this nuclide. The proton induced nuclear reactions on ^{100}Mo could be an alternative to the presently used fission method, where recently difficulties in adequate and reliable supply developed. Knowledge of activation cross-sections of proton induced reactions on molybdenum is very important also for other applications, like accelerator - and target-technology and wear measurement by using the thin layer activation (TLA) method. New experimental data have been measured and compared with critically analyzed, evaluated earlier experimental data and with the results of model calculations of the ALICE-

IPPE, EMPIRE-II and TALYS codes. The agreement of the experimental data with the results of the blind calculations is only moderately successful. The comparison shows how the experimental data are still contradicting and how important the reliable experimental data are for developing nuclear reaction theory and improvement of the codes. For a practical production of ^{99m}Tc with accelerators - as a replacement of the reactor based ^{99}Mo - ^{99m}Tc generator - many factors should be taken into account (production yields, energy range, target enrichment, radionuclide impurities, required accelerator, economy, distribution, drug master file, etc.). Our present study proved the possibility of an alternative route for production of the medically important $^{99m}\text{Tc}/^{99}\text{Mo}$ pair by using medium energy charged particle accelerators.

- [1] Institute for Nuclear Research, Hungarian Academy of Sciences (ATOMKI), Debrecen, Hungary
- [2] Cyclotron Laboratory, Vrije Universiteit Brussel (VUB), Laarbeeklaan 103, 1090 Brussels, Belgium
- [3] Institute of Physics and Power Engineering (IPPE), Obninsk 249020, Russia

Top quark pair production in association with a Z-boson at next-to-leading-order accuracy

Á. Kardos¹, Z. Trócsányi¹ C. G. Papadopoulos²

Physical Review D 85, 4015 (2012)

<http://link.aps.org/doi/10.1103/PhysRevD.85.054015>

In high energy physics the cross sections and expectation values for observables are defined through a perturbative expansion in the coupling constant of the theory under consideration. Hence a calculation can be Leading-Order (LO), Next-to-Leading-Order (NLO), etc., where the calculation involves the first and first two terms in the perturbative expansion, respectively. Making predictions at the NLO accuracy is hampered by the presence of one-loop amplitudes, with quickly increasing analytic complexity with increasing the number of particles involved in the scattering process. In the near past the calculation of these contributions has become available by numerical approaches, thus making available processes, which were considered too complex to calculate. One such process is the production of a t-quark pair in association with a Z-boson in hadron collisions (proton-proton in the case of the LHC and proton-antiproton in the case of the TeVatron). Although the first computation with NLO accuracy for this process was published in 2008, it was very limited in scope, only the distribution of transverse momentum for the Z-boson was included. In our paper we computed many more distributions allowing for a much more detailed understanding of the process. We also pointed out a potential problem

in the first computation. This work is part of a large-scale project in which we produce high precision predictions for the hadroproduction of t-quark pairs in association with scalar and gauge bosons. We developed a general framework, called PowHel based upon two publicly available computer programs (the POWHEG-BOX and HELAC-NLO) that enables us to go beyond the NLO accuracy by matching NLO QCD calculations with Shower Monte Carlo programs, that can be used to simulate the complete final state of the processes as seen by the detectors. For this matching we use the POWHEG approach, implemented numerically in the POWHEG-BOX, while all the needed ingredients are taken from the HELAC-NLO code. Within this project we already published predictions for the production of a t-quark pair in association with (i) a jet, (ii) a Higgs boson, (iii) a pseudoscalar Higgs boson, (iv) a Z boson, while the implementation of other processes are in progress. Our predictions are already in use by the TeVatron and LHC experiments.

- [1] Institute for Nuclear Research, Hungarian Academy of Sciences (ATOMKI), Debrecen, Hungary
- [2] NCSR Demokritos, Institute of Nuclear Physics, Athens, Greece

Transmission resonance spectroscopy in the third minimum of ^{232}Pa

L. Csige^{1,2}, *M. Csatlós*¹ *T. Faestermann*³ *J. Gulyás*¹ *D. Habs*² *R. Hertzenberger*² *M. Hunyadi*¹ *A. Krasznahorkay*¹ *H. J. Maier*² *P. G. Thirolf*² *H. F. Wirth*³

Physical Review C 85, 054306 (2012)

<http://link.aps.org/doi/10.1103/PhysRevC.85.054306>

Recently developed, large efficiency germanium 4π detector arrays provided great facilities for high resolution studies of nuclear states associated to extremely elongated nuclear shapes. In the mass region of A 130, more than a hundred superdeformed (axis ratio of 2:1) rotational bands have been identified so far. In this mass region, the centrifugal force (related to the fast rotating motion) is responsible for the large deformation that can be stabilized by the notable shell effects. Contrary to the observations of discrete superdeformed (SD) transitions, the identification of discrete gamma rays from hyperdeformed (HD) nuclear states having an axis ratio of 3:1 represents one of the last frontiers of high-spin physics. Although a large community with 4π gamma arrays have been searching for HD states in very long experiments, no discrete HD states have been identified so far. In the region of the actinides, the formation of the SD and HD states can be explained by the appearance of a second and a third potential minimum in the potential energy surface. In these nuclei, the appearance of fission resonances gives a special possibility for the identification and examination of HD states: observing transmission resonances as a function of the excitation energy caused by resonant tunneling through excited states in the third minimum of the potential barrier allows us to identify the excitation energies of the HD states. Moreover, the observed states could be ordered into rotational bands, with moments of inertia proving that the underlying nuclear shape of these states is a HD configuration indeed. For the identification of the rotational bands the spins and their projections onto the

nuclear symmetry axis (K values) can be obtained by measuring the angular distribution of the fission fragments. The double-odd ^{232}Pa nucleus ($Z=91$) is an especially good candidate for searching HD configurations. Fission resonances of this nucleus have been studied so far only via (n,f) reaction, but due to the limited transfer momentum of the reaction, these experiments showed no conclusive evidence for the existence of HD rotational bands. The aim of our experiment was to investigate the fine structure of the sub-barrier fission resonances of ^{232}Pa and to determine the fission barrier parameters of this nucleus. The experiment was carried out at the Tandem accelerator of LMU (München) employing the reaction $^{231}\text{Pa}(d,pf)$, in which we determined the fission probability of ^{232}Pa as a function of the excitation energy with high resolution by measuring the kinetic energy of the ejectiles with a Q3D magnetic spectrograph in coincidence with the fission fragments. Low-pressure, position sensitive avalanche detectors (developed in ATOMKI) were used to detect the fission fragments with large solid angle and efficiency. As the result of the present experiment, we found, for the first time, convincing evidence on HD configurations in Pa isotopes and, more generally, in an odd-odd nucleus.

- [1] Institute for Nuclear Research, Hungarian Academy of Sciences (ATOMKI), Debrecen, Hungary
- [2] Ludwig-Maximilians-Universität München, D-85748 Garching, Germany
- [3] Technische Universität München, D-85748 Garching, Germany

A critical analysis of the experimental L-shell Coster-Kronig and fluorescence yields data

T. Papp

X-Ray Spectrometry 41, 128 (2012)

DOI: 10.1002/xrs.2367

At the certification of gold and gold jewellery, the composition has to be certified, as opposed to the previous carat system since January of this year. Generally the x-ray fluorescence analysis method is used for characterisation. X-ray irradiation is used to ionise the atom. Outer shell electrons fills the vacancies, and the energy is carried away by x-rays and electrons. The energies of the emitted characteristic x-rays can be used to determine the type of the atoms, while the intensity of the x-ray lines for the quantification of the numbers of atoms. The fluorescence yield is the ratio of the numbers of emitted electrons and x-ray photons, during the decay of the ionised states. If the atomic shell has several sub-shells, like the L or higher shells, then the electron emitting transitions between the sub-shells are called to Coster-Kronig transitions. There are not that many transitions and their transition probabilities are basic atomic parameters, therefore it is expected, that they are well known. They are important at radiation detectors, at radiation transport in biology, used in nuclear physics to determine some of the decay parameters. These parameters are directly used at the quantitative analytical techniques, based on x-ray detection, and the method is named as the fundamental parameter method. All the countries have accepted the RoHS (Restriction of Hazardous Substances) directive, and compliance with the directive is generally verified via x-ray fluorescence analysis. In reality the tables of Manfred O. Krause are used widely. Krause made a visionary work, based on extrapolations of limited number of experimental points with modest accuracy. This was available, and the excellent work of Krause is proven by the use of his tables at basic research for fifty years. We have participated in measuring such parameters for decades, but our goal was not to write another paper, but actually we did need this information. Therefore, we have made measurements with almost all the available methods. In this work we have given a critical analysis, and at each method we call atten-

tion to previously unrecognised systematic errors. We have chosen the L-shell, because there are three sub-shells, and correlations exist between the parameters. We have demonstrated on an example, that the parameters do not comply with basic arithmetic. The situation isn't better for the K-shell. Measurements made in the last ten years yield values differing more than 100%, while the accuracy at each measurement is a few percent. Beyond the description of unrecognized systematic errors, we have called attention to a much more serious problem. In our opinion, the value of the physical parameters should not be determined by polling. The typical procedure followed by the compillators, who creates the tables are to calculate the average and the variance, and this is presented as the physical parameter. We fought for our view that the above method really gives what the next measurement will probably yield, provided that the researchers have similar work ethic and use similar experimental methods. However, this method will not determine the physical parameter. Instead, it is necessary to critically analyze each entry and verify that all the necessary investigations for the determination of the systematic errors have been carried out. The situation is even worse because instead of a critical analysis, the compillators select a theoretical data set, and the experimental data differing by more than five per cent are considered outliers and discarded. The average is calculated on the remaining data set, and the error bar is typically a few percent. This method excludes the possibility of development, because an improved measurement will differ by more than five per cent, and therefore will be discarded. We deliberated on the issue that 'Can a theory-laden observation test the theory?'. Such a critical paper had little chance for acceptance, and we were prepared for a long fight, knowing that the gold price returned to a normal level, and this will require a more precise definition of the data. Surprisingly the paper was easily accepted.

Double and transfer ionization in collisions of He with bare ions

L. Gulyás¹, A. Igarashi² T. Kirchner³

Physical Review A 86, 024701 (2012)

<http://link.aps.org/doi/10.1103/PhysRevA.86.024701>

Electron can be ionized or captured by the projectile when an ion collides with a target atom. Transfer ionization is a two-electron transition, where one of the electron is ionized and the other is captured into the bound state of the projectile ion. This is one of the simplest collision process, where the role of electron correlation can be investigated, and the phenomena receives continuous interest in both experimental and theoretical studies. The electron can be captured into low lying and continuum energy states of the projectile, the process is called electron capture into the continuum (ECC). ECC is considered as a special case of target ionization. Due to the continuity of transition amplitudes into bound and continuum states across the ionization threshold, cross sections for capture into bound states can be derived from those of ionization. In our study the process of transfer ionization is treated as a special case of double ionization in collisions of He atom with energetic bare ion impact. The velocity of one of the electrons was fixed to be identical with that of the projectile ion, and

the charge transfer cross sections was obtained by using the continuity of transition quantities. Only the static correlation was considered in our description, and the role of e-e interaction in the collision (dynamic correlation) was neglected. Our calculations, based on the continuum distorted wave and independent electron approximations, reveal nice agreement with experimental results. These results reveal that the collision mechanism in which the projectile interacts separately with both electrons gives a realistic account of the process only at low impact energies. At high impact energies the shake off mechanism and the initial state correlations were found to be important.

- [1] Institute for Nuclear Research, Hungarian Academy of Sciences (ATOMKI), Debrecen, Hungary
- [2] Department of Applied Physics, Faculty of Engineering, University of Miyazaki, Miyazaki 889-2192, Japan
- [3] Department of Physics and Astronomy, York University, 4700 Keele Street, Toronto, Ontario, Canada M3J

Observation of a new boson at a mass of 125 GeV with the CMS experiment at the LHC

N. Béni¹, S. Czellár¹, A. Fenyvesi¹, J. Molnár¹, J. Pálincás¹, Z. Szillási¹

Physics Letters 716, 30 (2012)

<http://dx.doi.org/10.1016/j.physletb.2012.08.021>

In the Standard Model of particle physics all massive particles acquire their mass via interacting with the Higgs-field. The strength of the Higgs-field is non-zero everywhere even in empty space and its smallest possible excitation is a boson (Higgs-boson). Finding the Higgs boson is crucial for confirming the Standard Model. One of the aims of the Compact Muon Solenoid (CMS) experiment at the Large Hadron Collider (LHC) at CERN (Geneva, Switzerland) is searching for the standard model Higgs boson in proton-proton collisions. The search is performed in five decay modes: $\gamma\gamma$, ZZ , W^+W^- , $\tau^+\tau^-$, and bb . The collected data correspond to integrated luminosities of up to 5.1 fb^{-1} at 7 TeV and 5.3 fb^{-1} at 8 TeV center of mass energies. An excess of events has been observed above the expected background, with a local significance of 5.0σ at a mass near 125 GeV. The observation is interpreted as production of a new particle. The excess is most significant in the two decay modes with the best mass resolution, $\gamma\gamma$ and ZZ ; a fit to these signals gives a mass of $125.3 \pm 0.4(\text{stat.}) \pm 0.5(\text{syst.}) \text{ GeV}$. The decay to two photons indicates that the new particle is a boson with spin different from one. The expected significance for a standard

model Higgs boson of that mass is 5.8 standard deviations. Atomki has been a regular member of the CMS Collaboration since 1997. Atomki participated in the development of the very forward calorimeters (HF-HCAL) of the hadron calorimeter system and in the development of the optical-electromechanical system of the alignment of the barrel muon detectors of CMS (Barrel Alignment Monitor, BAM). Atomki participates in the operation of the system of Modules for the Alignment of the Barrel (MABs) of the muon detection system. Also, in the development phase, Atomki participated in several irradiation tests that aimed at estimating the expected effects induced by energetic gamma photons, electrons, neutrons, protons, electromagnetic and hadronic showers in electronics, electronic-photonic systems and optical systems that were developed for operation in the harsh radiation environment of CMS.

- [1] CMS Collaboration, Co-authors from ATOMKI
- [2] Department of Applied Physics, Faculty of Engineering, University of Miyazaki, Miyazaki 889-2192, Japan
- [3] Department of Physics and Astronomy, York University, 4700 Keele Street, Toronto, Ontario, Canada M3J

Relation between total cross sections from elastic scattering and α -induced reactions: The example of ^{64}Zn

Gy. György¹, P. Mohr^{1,2}, Zs. Fülöp¹, Z. Halász¹, G. G. Kiss¹, T. Szücs¹, E. Somorjai¹

Physical Review C Rapid Communications 86, 041601 (2012)

<http://link.aps.org/doi/10.1103/PhysRevC.86.041601>

There is a basic quantum mechanical relation between the total (nonelastic) cross section of a nuclear reaction and the parameters of the complex scattering matrix $S_L = \eta_L \exp(2i\delta_L)$ obtained from elastic scattering angular distributions:

$$\sigma_{\text{reac}} = \frac{\pi}{k^2} \sum_L (2L+1)(1 - \eta_L^2)$$

where k is the wave number and η_L and δ_L are the reflection coefficients and scattering phase shifts which define the angular distribution of elastic scattering. Surprisingly, in the case of low energy α -induced reactions no experimental justifications of the above relation are available. Moreover, some experiments resulted in significantly different total cross section from the two methods. In certain astrophysical processes, like the p-process, low energy α -induced reactions play an important role. The cross sections of these reactions are typically calculated using the statistical model. One important result of the model calculations is the total cross section, which can be compared with experimental data. It is therefore very important to study experimentally the above relation in order to make the experimental tests of the statistical model more reliable. The $^{64}\text{Zn} + \alpha$ has been chosen for our experimental study since, on one hand, low energy elastic scattering data are available for ^{64}Zn

and, on the other hand, the cross section of the strongest reaction channels can be measured with the activation method. The experiments were carried out with the cyclotron accelerator of ATOMKI. The cross sections of the (α, γ) , (α, n) and (α, p) reaction channels were determined from the measurement of the γ -activity of the reaction products. At 12.4 MeV center of mass energy total cross section was calculated from the measured channels and it was compared with the elastic scattering data at the same energy. Within the overall experimental uncertainty of 17% the result were found to be in agreement and thus the underlying basic quantum mechanical relation was verified for the first time in the case of low energy α -induced reactions. In order to increase the precision of the comparison, a new high precision elastic scattering experiment has been carried out on ^{64}Zn . The analysis of this experiment is still in progress.

- [1] CMS Collaboration, Co-authors from ATOMKI
- [2] 2Department of Applied Physics, Faculty of Engineering, University of Miyazaki, Miyazaki 889-2192, Japan
- [3] Department of Physics and Astronomy, York University, 4700 Keele Street, Toronto, Ontario, Canada M3J

Gradual spontaneous breakdown of PT symmetry in a solvable potential

G. Lévai

Journal of Physics A: Mathematical and General 45, 444020 (2012)

doi:10.1088/1751-8113/45/44/444020

Complex quantum mechanical potentials have been applied successfully in many branches of physics. A more recent development was the discovery of complex PT-symmetric potentials. These are invariant with respect to simultaneous space (P) and time (T) reflection and may possess partly or fully real energy spectrum despite being manifestly non-Hermitian. In one dimension PT symmetry implies that the real and imaginary potential components are even and odd function of the coordinate, respectively. It was also found that increasing the imaginary component the real energy eigenvalues merge pairwise and re-emerge as complex conjugate pairs. The corresponding eigenfunctions cease to be PT-symmetric in the process, so this phenomenon was identified as the spontaneous breakdown of PT symmetry. After ten years of theoretical investigations a significant breakthrough occurred in 2010, when the existence of PT symmetry and its spontaneous breakdown was verified experimentally. Exactly solvable models are useful in studying PT symmetry, because they allow analytical description of the transition through the point of symmetry breaking. The PT-symmetric version of many conventional exactly solvable potential has been derived. The first results concerned the most well-known textbook examples, i.e. shape-invariant potentials, which depend on two or three parameters. However, it turned out that the breakdown of PT symmetry either does not occur in these potentials, or it occurs via the unrealistic "sudden" mechanism, i.e. all the

energy eigenvalues turn into complex at the same value of the control parameter. This is in contrast with the example of some semi-analytically or numerically solvable potentials, where the spontaneous breakdown occurs via the more realistic "gradual" mechanism. Inspired by these results we studied the PT-symmetric version of a wider four-parameter class of solvable potentials that contains all the known shape-invariant potentials that are solved in terms of Jacobi polynomials. Two parameters set the strength of the real and imaginary potential component, while the remaining two (C and δ) set the potential shape. We inspected in detail the domain $C < 0$, $\delta \geq 0$ where the Scarf II and the Rosen-Morse I potentials can be transformed into each other continuously. In the latter one the spontaneous breakdown of PT symmetry does not occur, while in the former one it occurs via the "sudden" mechanism. It turned out that the energy eigenvalues of the general potential can be obtained from the roots of a quartic algebraic equation. The spontaneous breakdown of PT symmetry occurs when two real roots merge and turn into complex as the coupling coefficient of the imaginary potential component is increased. This mechanism can be studied in a controllable way and we found that the breakdown of PT symmetry occurs in this case via the "gradual" mechanism. These studies may be useful in designing further setups in the experimental investigation of PT-symmetric systems.

Index

- Andrási D., 95, 98
Angyal A., 124
Arivuoli D., 77
Attolini G., 77
Aumayr F., 72, 73
Azaiez F., 56
- Baba M., 55
Balkay L., 52
Baran S., 82
Becker F., 56
Beke D.L., 74, 75
Belleguic M., 56
Bemmerer D., 123
Béni N., 1, 131
Benkő I., 96
Benoudia M.C., 75
Bereczky R.J., 71–73, 103
Berzi I., 104
Biri S., 64, 65, 102, 104
Bojtos P., 1
Borbély S., 70
Borcea C., 56
Bosi M., 77
Bourgeois C., 56
Brown B.A., 56
Brunner N., 125
Buffagni E., 77
Bükki-Deme A., 1, 100
Burgdörfer L., 67, 79
- Coster D., 69
Cowan T., 123
Csatlós M., 128
Csedreki L., 108
Csige I., 89
Csige L., 128
Csik A., 74–78, 80
Czébely, 84
Czellár S., 131
- Daróczi L., 124
Degering, 123
Ditrói F., 54, 55, 101, 126
Dlamini N.L., 97
Dlouhy Z., 56
Doblhoff-Dier K., 67
- Dóczi R., 92
Dombrádi Zs., 56
Drentje A.G., 102
DuBois R.D., 63
- Elekes Z., 56, 58, 123
Erdélyi G., 74
Erdélyi Z., 75
- Faestermann T., 128
Farkas J., 53, 58, 60
Feist J., 67
Fenyvesi A., 131
Feró O., 1
Ferrari C., 77
Fossan D.B., 59
Frigeri C., 77, 78
Fülöp Zs., 57, 58, 60, 61, 123, 132
Furu E., 83, 124
Futó I., 82, 84, 85
- Gailhanou M., 75
Gál G.A.B., 64
Gál J., 1, 111
Galaviz D., 58, 61
Gao F., 75
Görres J., 58
Grévy S., 56
Gruber E., 72, 73
Guillemaud-Mueller D., 56
Gulyás J., 128
Gulyás L., 68, 130
Güray R.T., 58, 61
Gyürky Gy., 53, 57, 58, 60, 61, 108, 123, 132
- Habs D., 128
Hakl J., 80
Halas S., 82
Halász Z., 53, 57, 60, 61, 132
Haszpra L., 83
Hegyesi G., 1, 110, 111
Heim E., 84
Herczku P., 64–66, 68
Hermanne A., 54, 55, 126
Hertenberger R., 128
Horváth A., 81, 85
Hunyadi M., 128

Ibrahim F., 56
 Igarashi A., 130
 Ignatyuk A.V., 54, 55, 126
 Iliadis C., 51
 Imrek J., 111

 Janovics R., 86–88, 91
 Joice Sophia P., 77
 Juhász Z., 64–66
 Jull A.J.T., 87, 88, 90, 91
 Junghans A., 123

 Kalinka G., 111
 Kamarás K., 78
 Kardos Á., 127
 Kertész Zs., 1
 Kertész Zs., 83, 124
 Khánh N.Q., 78
 Khaydukov Yu.N., 76
 Király B., 111
 Kirchner T., 130
 Kis-Varga M., 75
 Kiss Á.Z., 108, 124
 Kiss G.G., 57, 58, 61, 132
 Kiss K., 1
 Köhler M., 123
 Koike T., 59
 Koltai G., 82
 Korkulu Z., 57, 61
 Kormány Z., 104
 Kovács B., 95, 98
 Kovacevic M., 71
 Kovács S.T.S., 64–66, 68
 Kovács T.G., 47
 Kövér Á., 68
 Kowarik G., 72, 73
 Krasznahorkay A., 128
 Kuti I., 59

 Labat S., 75
 Ladinig F., 72
 Lahiri S., 98
 Lakatos A., 74
 Langer G.A., 74, 75
 Lee I.Y., 59
 Lemell C., 67, 79
 Leonard A.G., 88
 Lévai G., 45, 133
 Lewitowicz M., 56
 Lukyanov S.M., 56

 Machiavelli A.O., 59
 Maier H. J., 128
 Maiti M., 98
 Major I., 83, 90
 Major Z., 82
 Makovec A., 1, 74
 Mandal S., 56
 Marinkovic B. P., 71
 Marta M., 123
 Mayet P., 56
 Mbianda X.Y., 97
 Milosavljevic A. R., 71
 Mohr P., 50, 51, 58, 61, 132
 Molnár J., 1, 111, 131
 Molnár A., 86
 Molnár M., 81–83, 86–88, 90, 91
 Mrázek J., 56

 Nagele S., 67
 Nagy D., 1
 Nagy F., 1, 111
 Nagy G.U.L., 103
 Nagy L., 70
 Nándori I., 46, 122
 Nasi L., 78
 Negoita F., 56

 Ornelas A., 61
 Orsovszki G., 81
 Orsovszki J., 86, 91
 Özkan N., 58, 61

 Palcsu L., 82, 84, 85
 Pálincás J., 64, 131
 Papadopoulos C. G., 127
 Papp L., 82
 Papp T., 129
 Pazourek R., 67
 Penionzhkevich Yu.-E., 56
 Perduk Z., 104
 Perov N.S., 76
 Pintér G., 1
 Pittler F., 47
 Podolyák Zs., 56
 Pulker T., 93

 Rácz R., 64, 65, 102, 104
 Rajta I., 64, 103
 Rauscher T., 57, 60
 Rinyu L., 81

Roussel J.-M., 75
 Roussel-Chomaz P., 56
 Rubovszky B., 1

 Saint-Laurent M.G., 56
 Salamon P., 46, 52, 69
 Sarkadi L., 68
 Sarkadi-Pribóczky É., 81
 Sass V., 1
 Sathekge M., 93
 Savajols H., 56
 Schrempf D., 72, 73
 Schwengner R., 123
 Sello T., 93
 Serényi M., 78
 Sipos A., 1
 Shinpaugh J.L., 62
 Sohler D., 56, 59
 Somorjai E., 57, 58, 60, 61, 132
 Sorlin O., 56
 Stanoiu M., 56
 Starosta K., 59
 Sulik B., 64–66
 Sütő J., 1, 110
 Szücs T., 53, 57, 60, 61, 123, 132
 Szücs Z., 92, 93, 95, 97–99
 Szíki G.Á., 108
 Szabó B., 1
 Szabó Cs., 89
 Szabó Zs., 89
 Szádai J., 1
 Szalka J., 1
 Székely G., 1
 Szekrényes Zs., 78
 Szikszai Z., 108, 124
 Szilasi S.Z., 64
 Szillási Z., 1, 131
 Szoboszlai Z., 124

 Tárkányi F., 54, 55, 101, 126
 Takács M.P., 61
 Takács S., 54, 55, 95, 99, 101, 126
 Takáts V., 80
 Thierolf P. G., 128
 Thomas O., 75
 Timár J., 56, 59
 Timis C., 56
 Toburen L.H., 62
 Tőkési K., 1, 62, 63, 67, 69–73, 79, 96, 103
 Török Zs., 57, 124

 Tóth A., 70
 Tóth J., 97
 Trócsányi Z., 127
 Tskhakaya D., 69

 Uzonyi I., 108

 Vad K., 74, 77, 80
 Vajda I., 104
 Vajta Zs., 56
 Valastyán I., 1, 111
 Vaman C., 59
 Veres M., 81
 Vértesi T., 125
 Vertse T., 46, 52
 Vodila G., 84, 85
 Vos M., 96

 Waclawek J.P., 72, 73
 Wagner A., 123
 Wirth H.F., 128

 Yalcin C., 58, 61

 Zeevaart J.R., 93, 97
 Znojil M., 45
 Zolnai Z., 77
 Zuber K., 123